Physical Controls on Extremes of Oceanic Carbon and Oxygen in Coastal Waters

by

Zelalem M. Engida
M.Sc., Dalhousie University, 2012
PgD., the International Center for Theoretical Physics, 2008
BSc, Arba Minch University, 2005

A Dissertation Submitted in Partial Fulfillment of the
Requirements for the Degree of

DOCTOR OF PHILOSOPHY

in the School of Earth and Ocean Sciences

Physical Controls on Extremes of Oceanic Carbon and Oxygen in Coastal Waters

by

Zelalem M. Engida
M.Sc., Dalhousie University, 2012
PgD., the International Center for Theoretical Physics, 2008
BSc, Arba Minch University, 2005

Supervisory Committee

Dr. Debby Ianson, Co-Supervisor
(School of Earth and Ocean Sciences)

Dr. Adam Monahan, Co-Supervisor
(School of Earth and Ocean Sciences)

Dr. Mike Foreman, Departmental Member
(School of Earth and Ocean Sciences)

Dr. Karen Kohfeld, Additional Member
(Simon Fraser University)

ABSTRACT

The west coast of Vancouver Island is located at the northern end of the California Current System, one of the world's Eastern Boundary Current Systems. The region is characterized by wind driven coastal upwelling and high productivity, which supports fisheries and related industries. Climate change poses a challenge to these industries by increasing seawater acidity and decreasing dissolved oxygen levels, which are two of the multi-stressors of marine organisms. This thesis explores the relative importance of different physical and biological mechanisms that affect oxygen and carbon extremes in the region.

The relatively weak local wind in the region is not well-correlated with local currents and temperature. Results of coherence analyses between multi-depth current and temperature measured at a single mooring site (48.5° N, 126° W) in the west coast of southern Vancouver Island and coincident time series of North America Regional Reanalysis (NARR) 10 m wind stress in the geographic domain 36 – 54° N, 120 – 132° W are presented. The two-decade long (1989 – 2008) current records from the three shallowest depths (35, 100 and 175 m) show a remote response to winds from as far south as 36° N. In contrast, temperature only at the deepest depth (400 m) show strong coherences with remote winds. The frequency window of maximum coherence and the estimated average time-lags are consistent with the frequencies and pole-ward propagating phase speeds of coastal trapped waves. Lack of coherence between remote winds and the 400 m currents suggests that the temperature variations at that depth are driven by vertical motion resulting from poleward travelling coastal trapped waves (CTWs).

In order to study the relative roles of physical and biological processes on controlling oxygen and carbon tendencies, oxygen cycle has been successfully added to an existing biogeochemical model of the west coast of Vancouver Island. This idealized model then was forced with a long synthetic record of present-day conditions, specifically 1017 years of stochastically generated daily resolved forcing including local and remote winds. The seasonal cycles of the modelled DIC and O_2 compare well with

depth averaged observational data. They are also found to be strongly coupled in the lower layers, where biological processes are more important. In the upper layer, physical processes such as the differing gas exchange rates partially decouple DIC and O_2.

Robust statistics on DIC and oxygen extreme events were calculated by using the long realizations of the model baseline experiment. In the upper mixed layer, O_2 extreme events occur 2–3 times more frequently than DIC extreme events. Both extreme events show a much larger interannual variability in the lower layer. In this layer, oxygen extreme events events occur late in the summer, following intense upwelling events early in the upwelling season. Counter-intuitively, within the summer upwelling season, when sporadic upwelling events are expected to cause extreme conditions, the fraction of days with joint DIC–O_2 extreme events is negligible.

Sensitivity analysis shows that increased primary production, via increased phytoplankton growth rate, decreases the small fraction of days with joint DIC–O_2 extreme events in the upper layers during the summer upwelling season but increases it in the winter downwelling season. Lowering upwelling intensities lowers the fraction of days with joint DIC–O_2 extreme events. Increasing the upwelling intensities had the opposite effect on this fraction. Changes in up/downwelling intensity did not change this fraction within the summer upwelling season. A non-monotonic response by oxygen extreme events in the lower layer is observed when phytoplankton growth rate was increased. Generally, a moderate decrease in growth rate increases the chances of model lower layer O_2 extreme events, while near-zero growth rate does not. In some cases, the same parameter perturbation results in different responses by the mean and the extreme events of DIC and O_2, suggesting that results of studies focusing on physical and biological forcing of the mean state may not directly translate result to extremes.

This thesis has identified relative locations within the study domain of priority for effective monitoring of dissolved oxygen and carbon extremes in the study region. Finally, joint DIC- O_2 extreme events are found to be common at the end of the sum-

mer. This information can be used to inform adaptation and mitigation plans aimed at protecting the economic and bequest value of the coast from potential hazards associated with oxygen and carbon extremes.

Contents

List of Tables

List of Figures

ACKNOWLEDGEMENTS

I would like to thank my supervisors: Drs. Debby Ianson and Adam Monahan. I cannot imagine this thesis ever being completed without your continuous mentoring, and patience. Drs. Karen Kohfeld and Mike Foreman, thank you for sharing your precious times by being on my supervisory committee. Dr. Richard Matear, thanks for your thorough assessment of this work.

I would also like to go back and acknowledge Ian Folkins and other former supervisors and professors, for inspiring me to do research and recommending me to graduate schools.

I acknowledge the multiple financial supports I received through the University of Victoria fellowships and awards, NSERC-CREAT program, Dr. Arne H. Lane Graduate Fellowships in Marine Sciences, Edward Bassett Family Scholarship, research grants to Debby Ianson, and Adam Monahan.

A special thank you to Debby Ianson for providing me the source codes for her original model. Thanks to Richard Thomson for kindly providing the currentmeter data used in this thesis, and his co-authorship. Other data used in this thesis have been obtained from DFO maintained cruises and several NOAA affiliated agencies.

Allison Rose and Kalisa Valenzuela, you made my journey through this program easier by keeping me organized. Ed Wiebe, you were extremely helpful with my computational needs.

Thanks to Hakase Hayashida, Eric Mortenson, Carsten Abraham, and the many past colleagues I shared ideas with throughout my PhD program.

James Bowen and Liana, thank you for your hospitality during the last days of writing this thesis. James Bowen, John Callinder, John Brett and Lloyd Bartholomew, your friendship kept my sanity intact.

To my colleagues at ONC, specially data team members, thanks for reminding me the magnitude of this achievement.

To my mother and my children, who paid the utmost sacrifice for my success, thank you!

DEDICATION

To my mom, Etaba.

&

To Nathan and Mikiyas.

Chapter 1

Introduction

Introduction

Coastal upwelling regions are among the most variable regions of the global ocean within which extreme environmental conditions are common (Feely et al., 2008). These regions are also characterized by high primary production, which supports abundant marine life (Ware and Thomson, 2005). This thesis investigates drivers of carbon and oxygen extremes and the relationship between two extremes. For this investigation the west coast of southern Vancouver Island is chosen.

1.1 The Study Region

Southern Vancouver Island is located at the northern end of the California Current System (CalCS) where the North Pacific current bifurcates into subtropical and subpolar gyres (Figure 1.1). The CalCS is characterized by a slow moving current that stretches from the west coast of North America to about 1000 km offshore. Meridionaly, it extends from about 20°N to 50°N (Hickey, 1979, 1998). Seasonal reversal of winds generates the upward displacement of mid-depth (100-200 m), nutrient-rich, high carbon, low oxygen water during the summer upwelling season (Smith, 1994). Near southern Vancouver Island the upwelling intensity and duration are often less

than at locations farther south within the CalCS (Thomson and Ware, 1996). The region has a 'temperate' type climate with light-limited primary productivity in the relatively long winter season (Hickey and Banas, 2008). Upwelling occurs at the shelf break (Crawford and Thomson, 1991). In the inner shelf (water depth of 75–100 m), the summertime surface circulation is dominated by buoyancy fluxes (Freeland et al., 1984; Crawford and Thomson, 1991). The poleward-flowing, buoyancy-driven Vancouver Island Coastal Current (VICC) is a distinct feature of the inner shelf. The bulk of the alongshore local wind stress impact is on the mid-shelf and slope currents (Crawford and Thomson, 1991).

1.2 Carbon and O_2 Extremes

1.2.1 Drivers of Oxygen and Carbon Extremes

Biological and physical processes control oxygen and carbon cycles in the ocean (Sarmiento and Gruber, 2006). Biogeochemical models are, useful tools for characterizing the relative contribution of these processes in controlling low oxygen (e.g., Deutsch et al. (2005, 2006)) and high carbon events (e.g., Ianson and Allen (2002); Bianucci et al. (2011); Bianucci and Denman (2012)). To my knowledge, there are no models that exclusively considered these extremes in the study region. While there are hindcasts and future projections for mean carbon trajectories in the southern CalCS (e.g. Claudine Hauri (2015), Gruber et al. (2012)) , there are no studies of extremes.

The combined effect of high carbon and low oxygen in the ocean has long been recognized (Hofmann and Schellnhuber, 2009). However, there are only a few modelling efforts that studied carbon and oxygen cycles simultaneously in the study region (Bianucci et al., 2011; Bianucci and Denman, 2012).

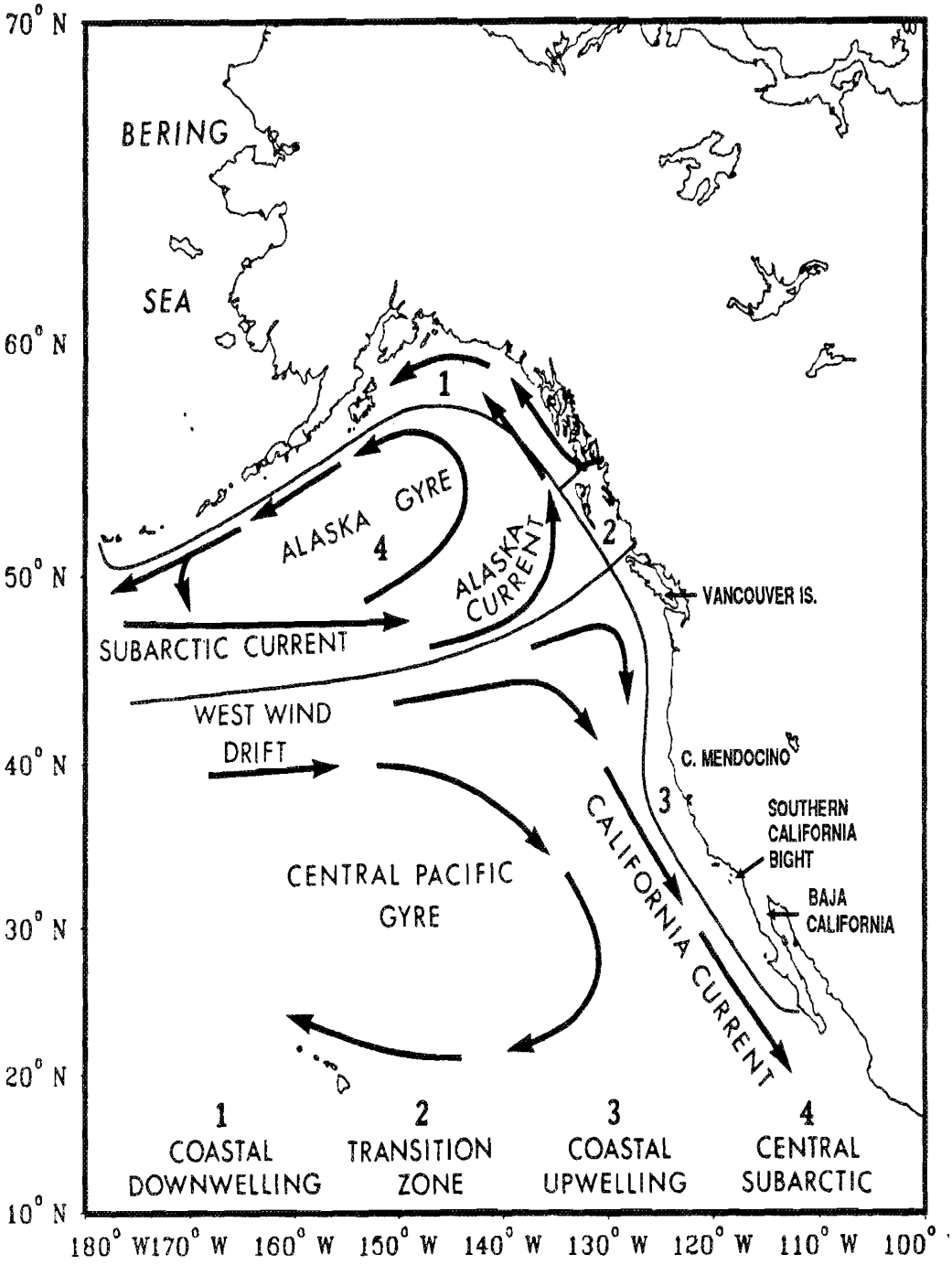

Figure 1.1: Map showing general circulation in the northeast Pacific Ocean (From Ware and Thomson (1991)). Vancouver Island is located at the northern end of the California current system.

1.2.2 Carbon

Due to its reactive nature CO_2 exists in more than one form in the ocean (Zeebe and Wolf-Gladrow, 2001). The total carbon in sea water is represented as $\sum CO_2 = [CO_{2(aq)}] + [H_2CO_3] + [HCO_3^-] + [CO_3^{2-}]$, which is referred to as dissolved inorganic carbon (DIC) (Edmond and Gieskes, 1970). A benefit of defining DIC in this way is that it is conservative with respect to mixing and changes in temperature and pressure. Therefore DIC, along with total alkalinity, is one of the most appropriate quantities for oceanic carbon cycle models.

Exchange of gaseous CO_2 between the atmosphere and the ocean is a continuous process where the net flux and flux direction depend on multiple factors that control the availability of excess CO_2 in either of the two reservoirs (Volk and Hoffert, 1985). The bicarbonate (HCO_3^-) and carbonate (CO_3^{2-}) ions make up more than 90% of DIC at present day atmospheric partial pressure (pCO_2). This speciation of DIC enhances the ocean's carbon storage capacity (Emerson and Hedges, 2008; Williams and Follows, 2011). At present the ocean is one of the biggest carbon reservoirs, storing roughly 60 times more carbon than the Earth's atmosphere (Williams and Follows, 2011). The oceanic mixed layer (50–100 m thick) alone contains as much carbon as there is in the whole atmosphere (Williams and Follows, 2011). This layer serves as the carbon flux exchange conduit between the deeper ocean, which stores more carbon due to biological export, and the atmosphere (Williams and Follows, 2011).

Increased CO_2 uptake by the ocean due to its increased release into the atmosphere from fossil fuel burning has been observed. Some estimates find that about one third of the anthropogenic CO_2 released during the last two centuries was absorbed by the ocean and caused ocean acidity to increase (Sabine et al., 2004; Raven et al., 2005; Canadell et al., 2007). Ocean acidification is now considered as the other global problem of fossil fuel burning, along with climate change (Doney et al., 2009). The present day global average ocean surface pH (measure of acidity) is 0.1 units lower,

at 8.1 units, relative to the pre-industrial times (1850) solely due to the increased CO uptake by the ocean (Sabine et al., 2004; Canadell et al., 2007). Compared to the pH ranges due to natural variability in coastal upwelling regions the 0.1 unit decrease is small (e.g., Figure 2 of Haigh et al. (2015)). Ocean pH values were much lower in the planet's distant past. However, the rate of decrease during the last 250 years is believed to be the fastest in the past several thousand years (Hoegh-Guldberg et al., 2007; Hönisch et al., 2012). This fast rate of increase in ocean acidity has become more concerning as we begin to understand how marine organisms, especially those in coastal upwelling regions, will be affected by these pH changes (e.g., Haigh et al. (2015)).

Recent model projections from the Coupled Model Intercomparison Project Phase 5 (CMIP5) project a global mean sea surface pH decrease of 0.145 (RCP2.6) – 0.31 (RCP8.5) units by the end of the 21st century (Ciais et al., 2013). Regional projections show even faster rates of pH decline (e.g., Gruber et al. (2012)). This decrease in the baseline pH will no doubt worsen seasonal occurrences of acidic waters in coastal upwelling regions such as the Vancouver Island west coast. Hence, there is a need to understanding how this long term change will interact with short term pH fluctuations coastal upwelling regions, where the time scales of variability range from hours to seasons (Waldbusser and Salisbury, 2014). The first step towards this understanding is studying what mechanisms primarily control variability of DIC in these regions.

1.2.3 Oxygen

Similar to ocean acidification, ocean deoxygenation has become of concern in recent years (e.g., Gruber (2011); Breitburg et al. (2018)). Keeling et al. (2010) projects that about 7% of dissolved oxygen will be lost from the global ocean by the end of the 21st century. Most of this oxygen loss is expected to occur in mid to high latitude regions where oxygen demand is high due to large biological production and the subsequent export of organic matter to below the mixed layer (Sarmiento et al., 1998; Gruber, 2011).

In coastal upwelling regions low levels of oxygen are often experienced as oxygen-poor subsurface water rises seasonally to the ocean surface. The level of oxygen in the ocean's interior is determined by biological processes (particularly remineralization of sinking organic matter) and physical processes (such as the strength of ventilation through new water formation and local vertical mixing) (Emerson et al., 2004). Increased stratification, which makes resupply of oxygen to the ocean's interior difficult, and reduced solubility of gases are the two consequences of rising ocean surface temperature (Matear and Hirst, 2003; Gruber, 2011).

The mid-depth water in the northeast Pacific ocean is relatively old due to the long circulation pathway (Feely et al., 2004). Since the age of water is inversely proportional to its dissolved oxygen content (Emerson and Hedges (2008)), this water has poor oxygen levels (Figure 1.2). Upwelling of such old water during upwelling seasons can cause severely low oxygen concentrations in shallow depths along the west coast. Because the majority of upwelling takes place in the summer productive season, the low oxygen level in upwelled water is often followed (within few days) by photosynthetic production and/or invasion of the gas from the atmosphere (Teeter et al., 2018). The subsurface oxygen levels, however, gradually decline during the course of the productive summer season due to remineralization of organic matter exported from shallower depths.

Recent observations show a marked increase in occurrences of extremely low dissolved O_2 concentrations in coastal upwelling regions in general and the expansion of the oxygen minimum zone in the northeast Pacific in particular (Bograd et al., 2008). Chan et al. (2008) reported a complete absence of dissolved oxygen near the inner shelf of central Oregon coast following local upwelling favourable winds in 2006. Simultaneous data from monitored transect lines showed a complete absence of certain fish types and near complete mortality of some microscopic invertebrates (Chan et al., 2008). Previous to this extreme oxygen event, a similar oxygen extreme event and subsequent mass die-off of fish and invertebrates were reported by Grantham et al. (2004). Coastal regions in the northern CalCS have been generally less prone

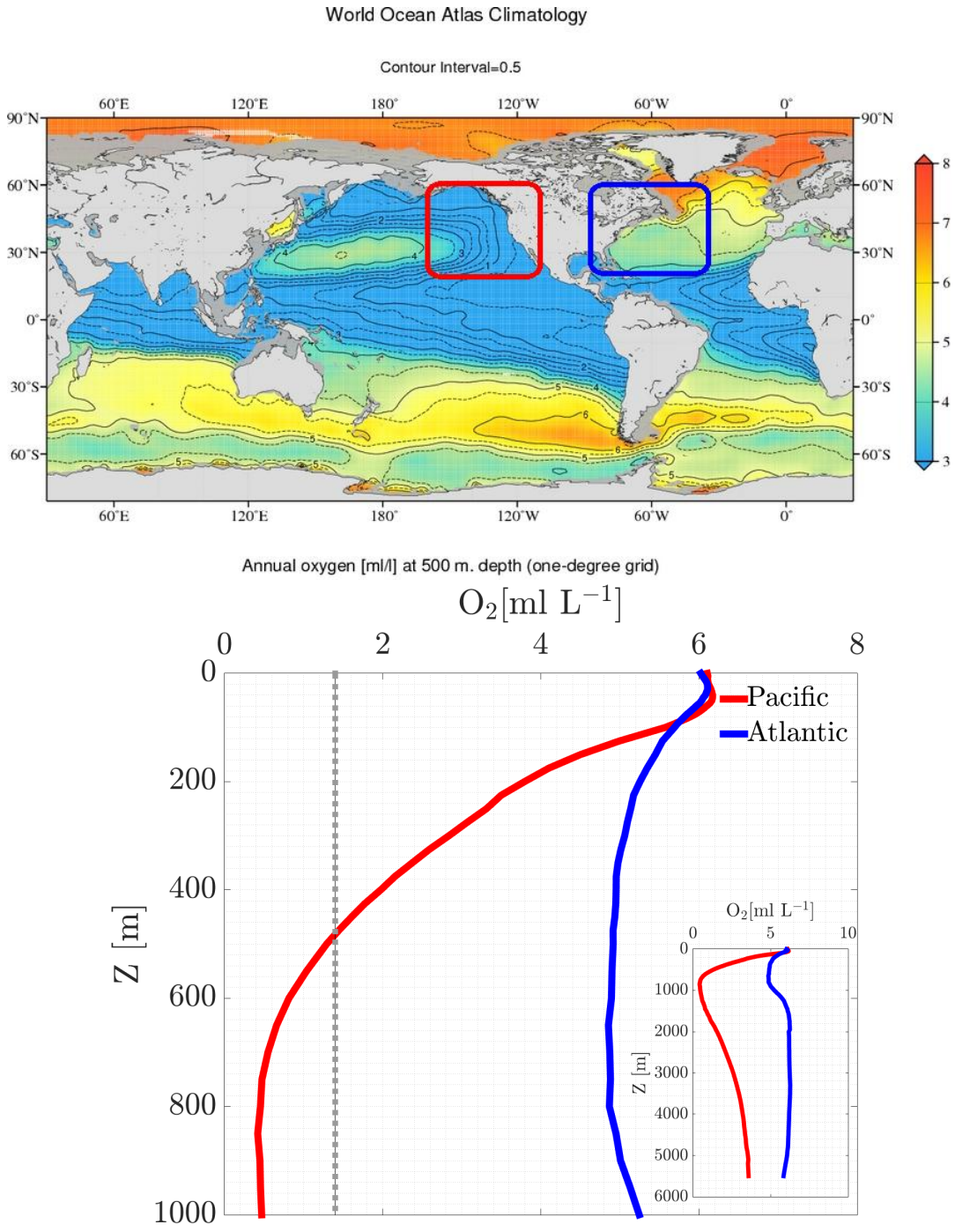

Figure 1.2: Top panel: Global map of annual dissolved oxygen at 500 m depth from the World Ocean Atlas 2013. Bottom panel: Spatially (colored boxes in top panel) averaged profiles of dissolved oxygen in the northeast Pacific and northwest Atlantic. The colors of the profile plots match the color of the boxes in top panel. (Data source: https://data.nodc.noaa.gov/)

to extremely low oxygen events compared to regions in the southern portion. Notable exceptions include the occurrence of hypoxic and anoxic surface waters over the Washington and southern Vancouver Island shelves during the summers of 2003–2006 reported by Connolly et al. (2010).

There is a limited knowledge of the combined effects of multiple stressors such as ocean acidification, deoxygenation, and warming ocean temperatures at the level of individual organisms. Fully understanding the net impact of multiple stressors on marine ecosystems (or even an organism) remains a challenging task (Pörtner and Farrell, 2008; Pörtner, 2009; Bopp et al., 2013; Hoshijima et al., 2017).

The west coast of Vancouver Island supports lucrative fisheries, tourism and related industries that depend on the health of the coastal water (Ware and Thomson, 1991, 2005; Haigh et al., 2015). The wide shelf and relatively slow bottom currents increase the residence time of upwelled acidic, oxygen-poor water before it mixes with offshore waters. The lack of efficient mechanisms for flushing this water (Hickey and Banas, 2008; Ianson et al., 2009) may negatively affect organisms in the region (Feely et al., 2010). Due to its unique physical set up, the area could be at risk in a changing climate, which could pose an economic challenge to industries relying on the health of the coastal ocean (Ekstrom et al., 2011; Billé et al., 2013).

1.3 Physical Forcing of Carbon and O_2 Extremes

Upwelling of nutrient-rich sub-surface water to the well-lit euphotic zone is one of the main physical mechanisms influencing photosynthetic primary production in the ocean Wind-driven Ekman upwelling is the most common type of upwelling in coastal regions. The Ekman theory assumes steady balance between the Coriolis force and turbulent momentum fluxes (Cushman-Roisin and Beckers, 2011).

Due to strengthening of land-to-ocean temperature gradients, the intensification of upwelling favourable winds in the Eastern Boundary Current Systems is expected to occur in response to global warming (e.g., Bakun (1990)). Lachkar (2014) found

the intensification of upwelling favourable winds in the CCS and the Canary Current Systems has contrasting effects on oceanic carbon, due to the differences in the relative contributions of physical and biological processes in the two coastal upwelling regions.

Bakun (1990) hypothesized an early onset and late termination of intense upwelling seasons in the Eastern Boundary Current Systems in the future warm climate. While this hypothesis seems to hold in most parts of the Eastern Boundary Current Systems, it does not seem to hold at the northern California Current system (CCS). Recent studies (Bograd et al., 2009; Foreman et al., 2011; Wang et al., 2015) have suggested late onset, early termination and no change (or weakening) in the intensity of upwelling favourable conditions in the northern CCS. Upwelling in the northern CCS is also influenced by the El Niño/Southern Oscillation (ENSO) (Hsieh et al., 1995), North Pacific Gyre Oscillation (Di Lorenzo et al., 2008) and Pacific Decadal Oscillation (Mantua et al., 1997). The impact of low frequency ENSO related waves on upwelling variability in the northern CCS has been studied by Frischknecht et al. (2015).

Upwelling mediated by coastal trapped waves has been less appreciated but it may be an important may be an important mechanism for bringing nutrients into the sunlit zone in some coastal regions, including the west coast of southern Vancouver Island. Coastal trapped waves, with amplitudes that decay offshore, have been found to impact upwelling variability in areas like the northern Gulf of Guinea (Moore et al., 1978; Clarke, 1979). The role of these waves in driving variability of carbon and oxygen in seawater has not received much attention. Their role, along with local physical forcing mechanisms, and biological mechanisms in defining the responses of carbon and oxygen extremes to changes in climate is not fully understood.

1.4 Thesis objectives

This thesis will investigate the physical and biological drivers of carbon and oxygen extremes on the west coast of southern Vancouver island. First, the relative con-

tributions of local and remote forcing of upwelling will be investigated by analyzing atmospheric and oceanographic datasets and the link between them. These results will then be used to study DIC and O_2 extreme events in a biogeochemical model.

This thesis will focus on the statistical aspects of DIC and O_2, with the model results assessed by comparison to observations. To estimate robust model statistics, I will use a stochastic model that will allow generation of arbitrarily long model forcing quantities. The estimated statistics will be used to understand how frequent DIC and O_2 extreme events are in the study region, and the extent to which they co-occur. I will also investigate the different time scales of the different mechanisms that control DIC and O_2 extremes. The main objectives are to:

1. Study the main drivers of coastal upwelling in the study region and their relative importance.

2. Incorporate all relevant physical forcing mechanisms, including the drivers of coastal upwelling identified above, into a coupled physical-biogeochemical model and study the relative effects of each process on O_2 and carbon extremes in the study region.

3. Characterize carbon and O_2 extreme events by their timing and frequency of occurrence, including the nature of joint carbon–O_2 extreme events .

1.5 Thesis Outline

1. Chapter 1 gives a general introduction.

2. Chapter 2 addresses part of objective 1. An observationally-based study on how wind controls vertical velocity variations in the study area has been conducted. From this study, the time scales of local and remote wind forcing on upwelling variability in the study region (the latter via coastally-trapped waves) were identified.

3. Chapter 3 addresses objective 2. The physical factors identified as drivers of biogeochemical cycles in the study region were applied to my updated version of the coupled physical-biogeochemical model of Ianson and Allen (2002). This chapter describes these updates to the model and includes an extensive model evaluation conducted using observational data collected from approximately two decades.

4. Chapter 4 addresses objective 3. It presents results of statistical analyses of modelled oxygen and carbon. The exceedance probabilities, return periods, and conditional cumulative density functions of oxygen and DIC were computed. The timing of individual and joint DIC - O_2 extremes were investigated for the baseline model run.

5. Chapter 5 discusses model sensitivity experiments. Selected results from a total of over 400 model sensitivity experiments conducted on selected model parameters, initial and boundary conditions are presented. The timing of joint DIC - O_2 extremes were investigated by using various model parameters.

6. Chapter 6 summarizes major findings of the work done, provides conclusions and future work to be done.

Chapter 2

Remote Forcing of Subsurface Currents and Temperatures near the Northern Limit of the California Current System

The contents of this chapter, except subsection 2.3.4, have been published under the title "Remote Forcing of Subsurface Currents and Temperatures near the Northern Limit of the California Current System." at the Journal of Geophysical Research: Oceans, 121(10):7244–7262 (Engida et al. (2016)).

2.1 Introduction

Summer coastal winds in the northern portion of the California Current System (CalCS) (southern Vancouver Island, 48.5° N) are weaker and more directionally variable than winds in the southern CalCS on the west coast of North America. Based only on these wind patterns, Ekman theory would predict cross-shore circulation resulting in stronger upwelling and consequently higher coastal productivity at southern coastal locations. However, observations of chlorophyll-a and other primary

productivity proxies indicate that the opposite is true (Ware and Thomson, 2005). Two explanations for this apparent paradox are: (a) physical features promote the retention of upwelled nutrient rich water, which gives enough time for strong phytoplankton blooms to form (Ianson and Allen, 2002), or (b) other physical mechanisms contribute to the upwelling itself.

In the northern CalCS, poleward propagating coastal trapped waves (CTWs) can influence upwelling (Hickey and Banas, 2008). The arrival of remotely forced CTWs modifies the intensity of summer upwelling generated by local winds (Leth and Middleton, 2006). CTWs are a hybrid of internal Kelvin and shelf waves (LeBlond and Mysak, 1978) whose propagation in the ocean is manifested as sea level, current and temperature fluctuations (Enfield and Allen, 1980). It has been shown that even in areas where application of regional Ekman theory fails, the theory of CTWs successfully reproduced observed coastal circulation features (e.g., Clarke, 1979).

Wind stress provides a generating mechanism for CTWs (e.g., Buchwald and Adams, 1968; Gill and Schumann, 1974; Clarke, 1977). A large volume of work exists on the statistical relationships between winds and oceanic variables (e.g., Battisti and Hickey, 1984; Allen and Denbo, 1984; Denbo and Allen, 1987; Pringle and Riser, 2003; Frischknecht et al., 2015) with a general consensus that CTWs are partially responsible for circulation features within the northern section of the CalCS.

Battisti and Hickey (1984) demonstrated a wave mediated connection between sea level at stations along the west coast of North America and wind stress records further south. Using current measurements from the Coastal Ocean Dynamics Experiment, Denbo and Allen (1987) found strong coherences between the remote wind stress along the west coast of North America and the amplitudes of the first time domain empirical orthogonal functions of longshore currents across multiple depths at various coastal locations in the CalCS. However, their results from the two years they considered (1981 and 1982) were not consistent. Part of the reason for this inconsistency is likely the occurrence of the major El Niño event in 1982 and the relatively short data record used. A recent analysis by Thomson and Krassovski (2015) using an intermediate-

length current record (2010–2014) from southern Vancouver Island found evidence for CTW variability at 10 to 40 day periods but little evidence of direct CTW variability beyond a period of 40 days. Pringle and Riser (2003) presented one of the very few observationally based works relating ocean temperatures and remote wind stress with regard to CTWs. Recently, Frischknecht et al. (2015) have shown the relative importance of local and remote forcing through CTW on average boundary layer temperatures throughout the CalCS. In the northern portion of the CalCS they found lower temperature response to remote forcing than to local forcing and attributed this observation to the more dissipative nature of temperature (more local sources and sinks) relative to other variables such as sea surface height.

CTWs arriving at a coastal upwelling location lift the pycnocline, which can then bring nutrients into the euphotic zone, stimulating primary productivity (Hickey and Banas, 2008). It has been observed in recent years that coastal locations in the northeast Pacific experience extreme carbon and oxygen conditions following strong upwelling events (Feely et al., 2008; Connolly et al., 2010). Therefore, characterizing the CTW generating wind field at remote locations can improve the understanding of sub-seasonal changes in primary productivity and extreme oceanic conditions in the northeast Pacific coast.

In contrast to the central CalCS, the northern extent of the CalCS, along southern Vancouver Island, has received less attention with respect to CTW influence. Noteworthy exceptions include Crawford and Thomson (1982), Yao et al. (1984), Denbo and Allen (1987), Connolly et al. (2014) and Thomson and Krassovski (2015). Crawford and Thomson (1982) showed that the continental shelf and slope off southern Vancouver Island allow first mode diurnal frequency barotropic shelf waves and attributed fluctuations in diurnal currents to them. Yao et al. (1984) attempted to interpret low frequency current variability off west coast of Canada in terms of CTW theory, but they concluded that the unique coastline geometry (and other factors) limited the success of their analysis.

The record length used in Yao et al. (1984) is relatively short ($\sim$ 7 months)

and contains data only for October–April. Denbo and Allen (1987) found modest coherences at low frequencies over a distance stretching between 300–1400 km in longshore direction from southern Vancouver Island, just south of mooring site A1 (Figure 2.1). However, the record length in their study was less than two months long, even shorter than the one used by Yao et al. (1984). The more recent studies of Connolly et al. (2014) and Thomson and Krassovski (2015) investigated low frequency CTWs using moderately long (2–4 years) records.

In the present study, I characterize the influence of remote winds on ocean currents and temperatures throughout the water column near the northern limit of the CalCS off of southern Vancouver Island. Specifically, I use multi-year multitapered coherence analysis of concurrent 20-year long observational records to estimate the statistical relationship of wind stress with both currents and temperatures at multiple depths (35–400 m) on the continental slope. By making use of recently-available high-resolution reanalysis surface wind products, I can characterize the structure of the statistical relationship between winds across the northeast Pacific ocean and variability of currents and temperatures at southern Vancouver Island. My results are less sensitive to interannual variability or sampling bias than those of previous studies because of my use of long observational records.

2.2 Data and Method

2.2.1 Data

I consider hourly ocean current and temperature data at depths of 35, 100, 175, and 400 m from the continental slope off western Canada, 60 km offshore of the southern Vancouver Island where the mean water depth is roughly 500 m (A1, in Figure 2.1). These data were obtained from a mooring at which data have been collected from 1985 to the present. The currents are measured by single-point Aanderaa RCM4/5 mechanical current meters, which have a sensitivity threshold of 0.015 m s^{-1}. When

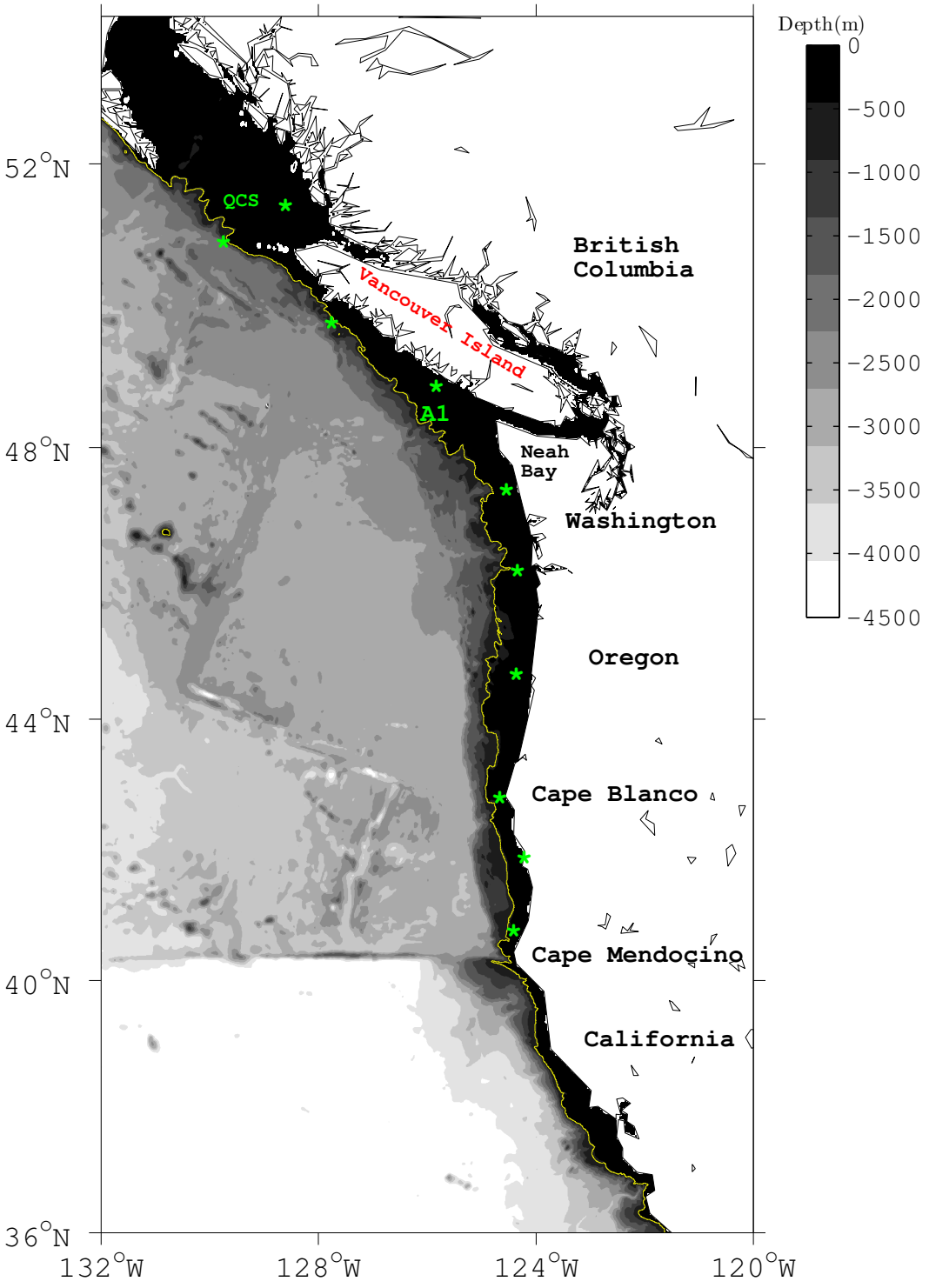

Figure 2.1: Study domain showing Vancouver Island and adjacent geographic locations, mooring A1 location (A1), buoy locations to which NARR winds interpolated (green stars), and bathymetry (downloaded from the 1 Arc-Minute ETOPO1 Global Relief Model, https://www.ngdc.noaa.gov/). The yellow line denotes the 500 m depth contour.

currents are above this threshold, their accuracy is the greater of ± 0.01 m s^{-1} or 2% of the measured speed. The thermistors can record temperatures as low as 0.05^{o}C and have accuracy of ± 0.3 ^{o}C (Krassovski, 2008; Thomson and Emery, 2014) . The longshore and cross-shore directions of current velocity at each depth are defined based on the principal axes of the current ellipses (Thomson and Krassovski, 2010). Based on a visual inspection of data gaps I decided to use records from the years 1989–2008 for this work. Where there is a significant loss of data within a given selected year (Figure A.2), I ignored data from those years at a later stage of my analysis (Table A.1).

The eight times per day (3-hourly) wind data used are from the North America Regional Reanalysis (NARR) product (Mesinger et al., 2006). NARR assimilates atmospheric observations into a high-resolution model (32 km horizontally with 45 vertical layers) of the National Center for Environmental Prediction (NCEP). The relatively low noise level and absence of data gaps makes NARR winds more convenient than buoy records for this work. More importantly, NARR provides broad spatial coverage allowing us to estimate the large-scale spatial structure of the wind forcing. NARR winds do not perfectly compare with buoy winds. For example, the 10 m wind speeds have a slight negative bias in both winter and summer (Mesinger et al., 2006). However, at the sub-daily frequencies, which are the focus of this work, NARR winds are well correlated with buoy winds along the west coast of North America (Moore et al., 2008; Bylhouwer et al., 2013). Comparisons between coherence analyses using buoy data and co-located NARR wind products indicate that the modest NARR biases in the mean or standard deviation of the winds have only small effects on my results.

2.2.2 Methods

I defined anomalies in the current and temperature data by first subtracting the overall mean from the record and then using harmonic regression to remove the annual cycles from the residual time series at each depth. Subsequently, I used the Unified

Tidal Analysis and Prediction (UTide) package (Codiga, 2011) to remove the tidal components. Lanczos cosine band pass filtering (with cutoff periods of 12–14 hr and 23–25 hr) was used to complete the removal of the diurnal and semidiurnal tidal components, which are not stationary at the mooring location. As a sensitivity analysis, I repeated the analyses shown in this paper using 35 hr low pass Kaiser-Bessel and Lanczos filtered time series and removing the annual and seasonal cycles from the filtered data. I found that the results of the second analysis are statistically indistinguishable from the ones presented here.

After defining the anomalies, I extracted the anomaly time series for the upwelling (June–September) and downwelling (November–February) seasons. The choice of these months is based on the typically observed upwelling and downwelling seasons off of southern Vancouver Island (Thomson and Ware, 1996; Bylhouwer et al., 2013). The upwelling and downwelling seasons used in the present study fall within those recently estimated by Thomson et al. (2014) using a record of seismic data. To be consistent with the wording in previous studies, upwelling and downwelling seasons will be referred to respectively as summertime and wintertime. Onshore and poleword current directions are defined as positive.

The NARR (10 m) winds were taken from the domain 228°W–240°W, 36°N–54°N. There are a total of 2948 grid points in this domain and about 2000 of them are over the ocean. Using the time series of the 3 hourly wind components at each grid point, I calculated the neutral wind stress vector components following Yelland and Taylor (1996) with air density ρ=1.2 kg m^{-3}. The choice of drag coefficients had only a small effect on the wind stress magnitudes (not shown). The wind stresses were then deseasonalized using the same technique used for the current records. I denote the eastward wind stress anomalies τ_x and and the northward anomalies τ_y and use the right hand sign convention of eastward and northward as positive. The NARR winds interpolated to the ten coastal buoy locations shown in Figure 2.1 have principal axes nearly parallel to the local coastline and hence no effort is made redefine the longshore wind direction for the scalar coherence analysis part of this work. The

hourly current and temperature anomalies were sub-sampled to 3 hourly to match the time resolution of the winds.

It has been documented that the effect of coastal winds can extend over a thousand km horizontally and into the ocean interior (e.g., Wang and Mooers, 1977). As these non-local wind effects are mediated by propagating waves, they are most naturally studied in the frequency domain. To this end, I calculate scalar coherences between meridional winds and longshore currents and extend this analysis using rotary coherences (Gonella, 1972) to show spatial structures of coherences between wind stress vectors and components of currents. These calculations are then repeated for the coherence of the winds with temperatures at the four depths. I computed the coherences using the multitaper method of estimating power spectral densities and other quantities in the frequency domain (Thomson, 1982). In the following, I briefly outline how I used this method to estimate coherences and time lags.

First, I grouped the data into blocks, each consisting of a single season in a single year. Then, for a given season, I smoothed each data block using 7 window (taper) functions (Appendix A) to improve the accuracy of the spectral estimates. I then computed the power spectra and cross spectra (between wind and currents, and wind and temperature) for each block. Next, I averaged spectral and cross-spectral estimates across all years in the record. I then calculated the scalar coherences and phase lags. Finally, I calculated the mean rotary coherence, $\bar{\kappa} \in [0, 1]$, over a specified frequency band by adapting the method of Oliver and Thompson (2010). The quantity $\bar{\kappa}$ represents the fraction of variance of a current or temperature time series that is linearly related to the wind stress vector component at a given location over the specified range of frequencies. I also calculated mean time lags by converting phase lags.

Before carrying out the coherence calculations, I analyzed the correlation between the two components of the currents and several rotated wind stress components at buoys near the mooring site (the nearest two stars just north of A1, Figure 2.1). The aim of the wind stress rotations was to find the one rotation that gives the highest

correlation with the current components. However, all the correlations were small and not generally statistically significant (not shown). There was also no correlation between current shear and the local wind stress. This lack of correlation occurs in part because the shallowest depth of the current observations (35 m) is near the bottom of, or below, the Ekman layer in which the flow responds directly to surface wind stress (Lentz, 1992). Specifically, using a typical value of diffusive eddy viscosity ($K_m = 2 \times 10^{-4}$ m^2 s^{-1}) (Cushman-Roisin and Beckers, 2011) and observed mean wind speeds at the mooring location (48.5° N, Figure 2.1) the depth of the upper Ekman layer is roughly 20 m.

2.3 Results and Discussion

2.3.1 Currents

To determine the frequency ranges over which coherences between winds and currents are largest, I first consider coherence patterns between meridional wind stress (τ_y) and longshore currents at all depths (Figure 2.2). Similarly, I consider coherence patterns between meridional wind stress (τ_y) and temperatures at all depths (Figure 2.3). Where the coherences are significant (Appendix A) the associated phase lags, ϕ, are shown as a function of frequency (panel–II of Figures 2.2 and 2.3).

Summertime squared coherence between NARR τ_y interpolated to ten coastal locations (Figure 2.1) and longshore currents at 35, 100, and 175 m show maxima at locations a few hundred kms south of the mooring, concentrated in the ∼7–20 day period window (panel–I of Figure 2.2). The maximum squared coherence values increase slightly with depth between 35 and 175 m. Based on the number of gap-free time blocks (Table A.1) used in the spectral averaging, the 95% significance levels for the squared coherence values at 35, 100, 175 and 400 m depths are 0.19, 0.21, 0.22, and 0.22. At the 95% significance level, only the 400 m currents show no significant coherence with wind stress at any of the ten locations. The coherences gradually

decrease to the north of the mooring location.

Time lags (lag $= \frac{\Delta\phi(f)}{2\pi f}$) are positive when winds lead the currents (temperatures) and negative when the winds lag currents (temperatures). At 35 m the currents lag the winds to the south of the mooring (Figure 2.2 (panel–II)). The phase lags are higher for locations a greater distance to the south as seen in the progressive increase in the y-intercepts at each wind location in Figure 2.2 (panel–II). A positive slope in the phase-vs-frequency plots, which represents northward phase speed, is found for all wind locations south of the mooring. I interpret the positive slopes found at locations north of the mooring as a consequence of the spatial correlations within the wind field, rather than indicating a causal connection between winds at these locations and currents at the mooring. The clear progression of phase with latitude to the south of the mooring (where coherences are much larger) is considerably less clear to the north.

I expect multiple wave modes are present in the frequency band of maximum coherence. My method is not capable of identifying the different wave modes. However, the primary concern of this study is determining which winds drive the current and temperature fluctuations at the location of the mooring. Therefore, for each surface wind location, I use the average lag over all 13 frequencies between $\frac{1}{20}$ and $\frac{1}{7}$ cycle per day (cpd) as a measure of the time separation between forcing and response. For example, I found the mean time lag between 35 m currents and winds at 40.7° N to be 3.23 days. Similarly, at 100 and 175 m the currents have mean time lags of 3.24 and 3.19 days, respectively (Figure A.3). These time lags are in agreement with the approximately 3 days time lag (space-time lagged correlation derived) obtained by Denbo and Allen (1987). Their Figure 13 shows longshore currents at southern Vancouver Island lag winds at about 35° N by about 5 days and winds at about 47° N by about 0.5 days such that the lags are monotonically decreasing towards the mooring location (48° N).

At all depths, phase speeds (calculated from the time lags and an estimate of longshore distances from each wind location to the mooring site) range between about

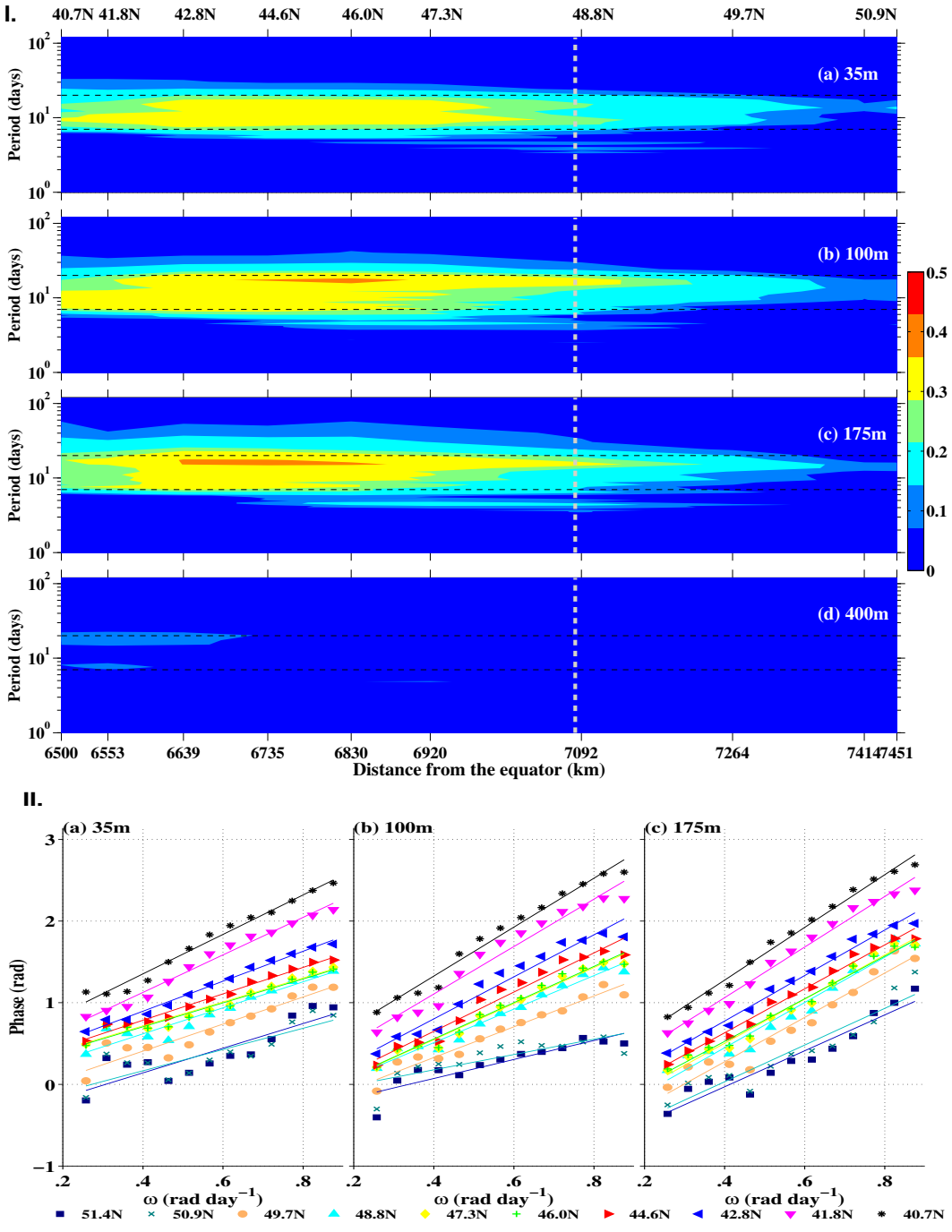

Figure 2.2: **Panel-I.** Coherence squared between longshore currents at depths from 35 to 400 m on the southern Vancouver Island shelf break and 10 m meridional wind stress along west coast of North America. The vertical dashed line indicates the location of the mooring (48.5° N). Horizontal dashed lines show the periods of 7 and 20 days between which maximum coherence is seen. **Panel-II.** Phase difference between the longshore currents and meridional wind stresses (markers). Only phases for periods (7–25 day) where coherences are highest are shown. Least square fit lines for each location are shown in the same color as the markers. A positive phase indicates that the wind leads the current.

$\sim$100–400 km day^{-1}. These values fall in the range of phase speeds reported in previous studies (Table 3.1), most of which considered sea surface elevation.

2.3.2 Temperature

In contrast to the currents, summertime temperatures at depths between 35 m and 175 m show no significant coherences with remote (or local) wind stress (panel–I of Figure 2.3). At 400 m, the squared coherences (panel–I of Figure 2.3d) are comparable in magnitude to those for the currents at shallower depths (Figure 2.2). Peak squared coherence values for temperature are found at a slightly longer period band (10–25 days) than for currents. Time lag estimates based on calculated phase lags (Figure 2.3 (panel–II)) indicate mean propagation times of up to 4 days (Figure A.3). These time lags are slightly longer than the time lags for currents.

2.3.3 Rotary Coherence Results

It is clear that there is a response to remote meridional wind stresses by the longshore currents between the depths of 35 and 175 m at the mooring and by the temperature field at 400 m. The oscillation periods where these responses are highest are consistent with the periods of previously-documented CTWs in this region. The phase relations (panel–II of Figures 2.2 and 2.3) and propagation speed calculations further support this interpretation. In order to characterize the spatial structure of the statistical relationship between current and temperature variability at the mooring and the winds, I adapted a method introduced by Oliver and Thompson (2010). At each NARR grid-point in my domain (Figure 2.1), I computed rotary coherence (Gonella, 1972) values and averaged them across frequency bands to define a band averaged mean coherence ($\overline{\kappa}$). I chose to use rotary coherence analysis in order to characterize the spatial structure of the wind field that affects current and temperatures at the mooring for all wind directions. The choice of the longshore wind direction for NARR grid-points is ambiguous near the coast, and increasingly so for grid points further

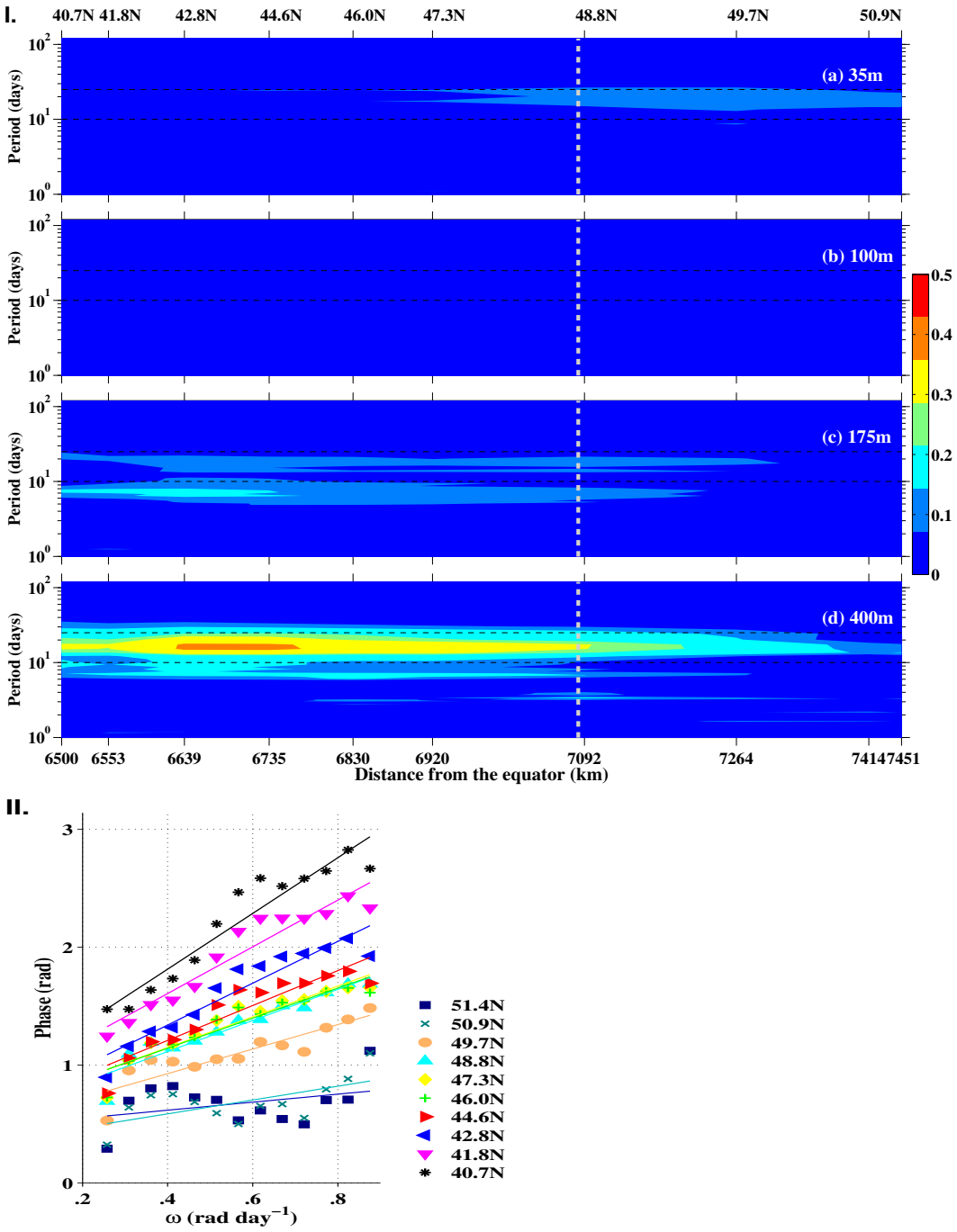

Figure 2.3: As in Fig 2, for temperature at the mooring site. Horizontal dashed lines show 10–25 days period interval. Phase difference as a function of frequency are shown only at 400 m.

offshore. Another option, defining the longshore wind stress components based on the principal axes of the wind ellipses, gave less meaningful longshore wind direction as we go further offshore because the major axes of the ellipses no longer align themselves with the coastline. Thus, I consider the full vector winds and computed their rotary coherences with components of current vectors (and temperatures). Average time lags were computed for the same frequency window where the coherences were averaged (Equation A.12).

Currents

The cross-shore currents are not significantly coherent with the wind vectors (not shown). Therefore, I present the longshore current results. Values of clockwise (CW) $\overline{\kappa}$ computed for the upper (35, 100, and 175 m) mooring depths over the period window between 7 and 20 days further indicate that winds from remote south latitudes exert significant influence on the longshore currents at these depths Figure 2.4. As in my scalar coherence results (Figure 2.2) the rotary coherence results at 35 m are slightly lower than those at 100 and 175 m (Figure 2.4). The lower maximum coherence at 35 m may be due to a larger contribution of local near-surface processes that are not associated with CTWs. It is also possible that the CTWs may have different effects on currents at different depths, although there is a strong barotropic nature in the current records from the upper three depths. The single black contour in all coherence maps shows the 95% significance level. The 400 m longshore currents are not significantly related to the wind at any location (Figure 2.4d & h). The winter CW coherences between 100 and 175 m longshore currents and wind stress vectors have a resemblance to the summer results but the 35 m winter CW coherence is slightly (about 0.1 lower) weaker than its summer counterpart. This last result is consistent with a deeper winter mixed layer, increasing the influence of local near-surface processes at 35 m (Thomson and Fine, 2003). As expected, coherence decays offshore since longshore coastal winds dominate the generation of CTWs. However, the maximum coherence occurs at locations south of the mooring site , extending to

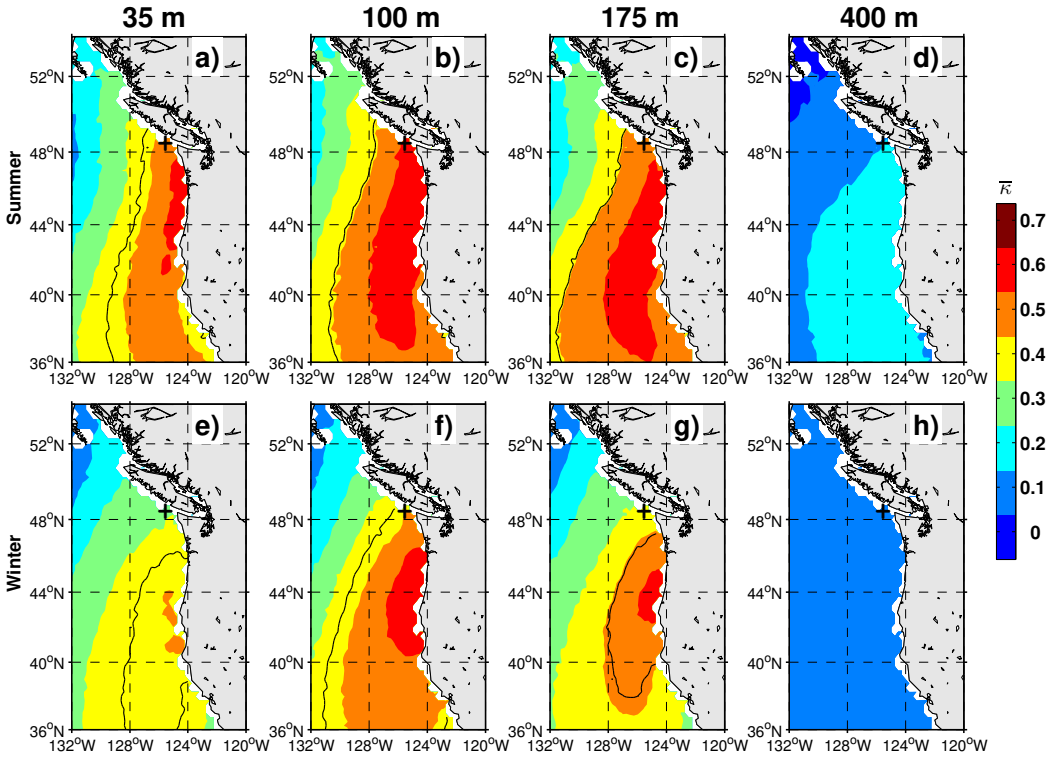

Figure 2.4: CW band averaged mean rotary coherence ($\bar{\kappa}$) over the 7–20 day period window between 10 m NARR wind stress across the study domain and moored current observations at the mooring site (shown by the dark cross). Panels (a-d) are for the summer, while (e-h) are for the winter. The 95% significance levels for $\bar{\kappa}$ are shown by a heavy contour.

at least a 1000 km.

I also used the corresponding phase information from the CW rotary coherence calculations to estimate mean time lags (Figure 2.5). Only mean time lags corresponding to coherences above the 95% significance level are shown. The summertime CW mean time lags clearly show a northward phase propagation at 35, 100, and 175 m. In the winter we see a similar northward phase propagation, although it is not as distinct as it is during the summer, except that the winter time lags are generally shorter (Figure 2.5d–f). The shorter mean time lags here are in agreement with the increased mode 1 CTW phase speeds during the winter (Battisti and Hickey, 1984). The mean time lags together with estimates of longshore distance between a given NARR wind location and the mooring site give phase speeds of CTWs (Table

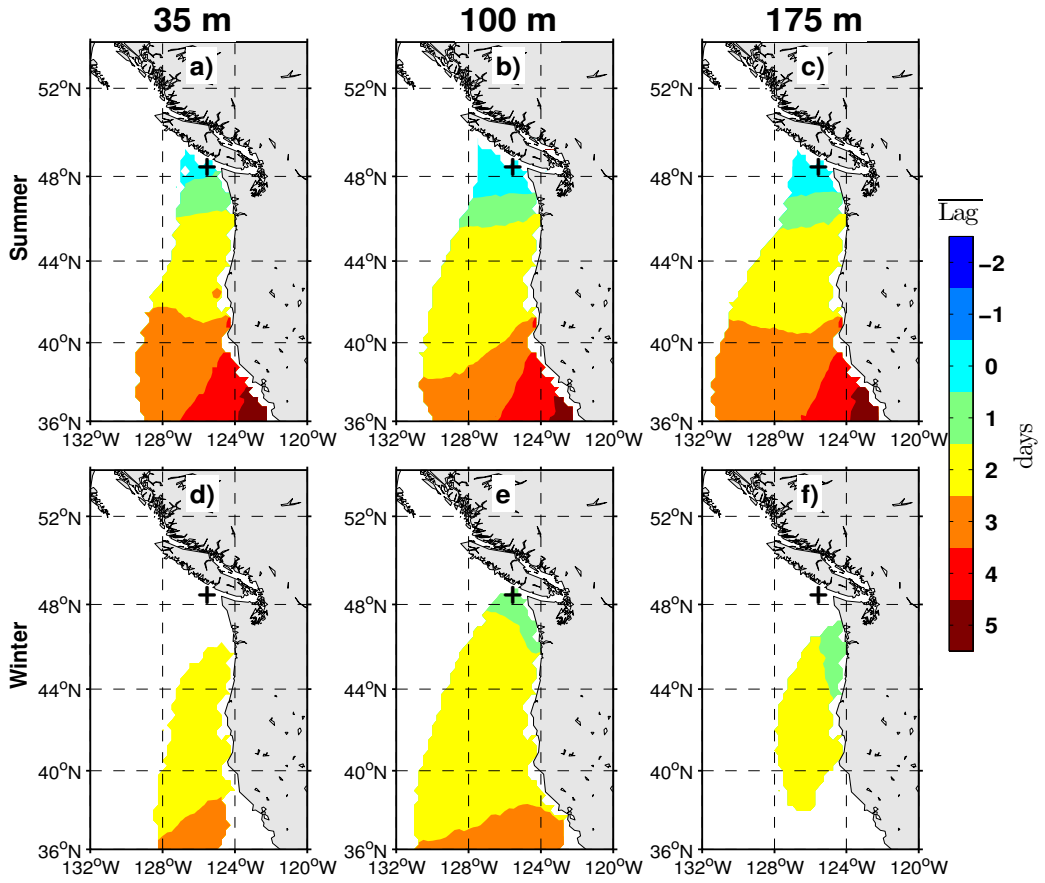

Figure 2.5: Summer (a-c) and winter (d-f) CW mean time lags ($\overline{\text{Lag}}$) corresponding to the CW band averaged mean rotary coherences shown in Figure 2.4 over those depths where significant coherences are found. Positive values show the winds lead the currents. Only time lags associated with $\bar{\kappa}$ above the 95% significance level are shown.

3.1).

The counter-clockwise (CCW) coherences are slightly weaker than the CW coherences (Figure 2.6). The offshore decay of coherences is still observed. Similar to the CW coherence results, the CCW coherences at 400 m are not significant in either season (Figure 2.6d &h). The winter CCW significant coherences do not extend to the location of the mooring site. During the summer, the highest CCW coherences are generally found between Cape Mendocino and southern Washington while the highest summer CW coherences extend from the mooring location to southern California. During the winter this marked difference in the latitudinal extent of co-

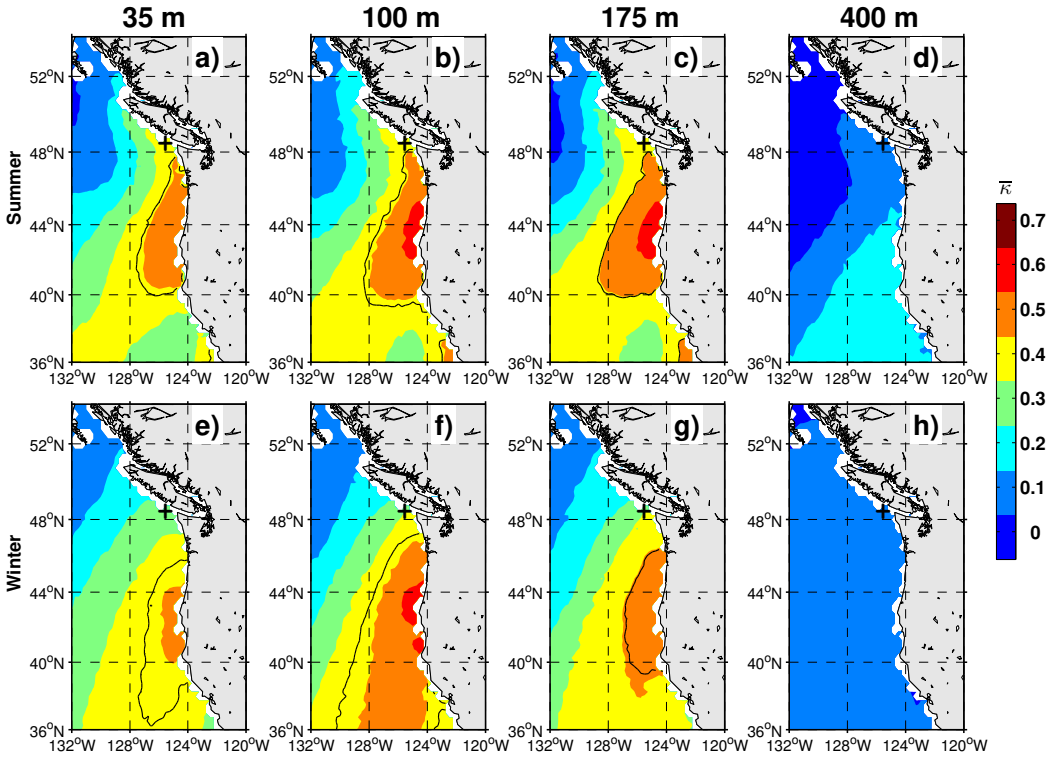

Figure 2.6: As in Figure 2.4 for the CCW polarization.

herences between the two polarizations is less pronounced , most likely due to the reduced stratification and the resulting increased lateral length scale of motion in winter.

The summer CCW mean time lags (Figure 2.7a–c) are almost the same as the summer CW mean time lags (Figure 2.5a–c). The winter CCW mean time lags (Figure 2.7d–f) are longer than the winter CW (Figure 2.5d–f) and summer CCW mean time lags (Figure 2.5a–c) by about 0.5–1 day.

The wind data used for each depth are slightly different due to different gaps at different depths of the current-meter records (Figure S1 and Table A.1). For example, winds from 1995 and 2003 are not included for the 35 m depth record but are included for the 100 m depth coherence calculations. Similarly, 1992 and 1997 are included in the 100 m coherence but not in the 35 m coherence calculations. Coherence and mean time lag patterns obtained by removing the same years at all depths (not shown) are qualitatively similar to those presented above. However, the former had fewer degrees

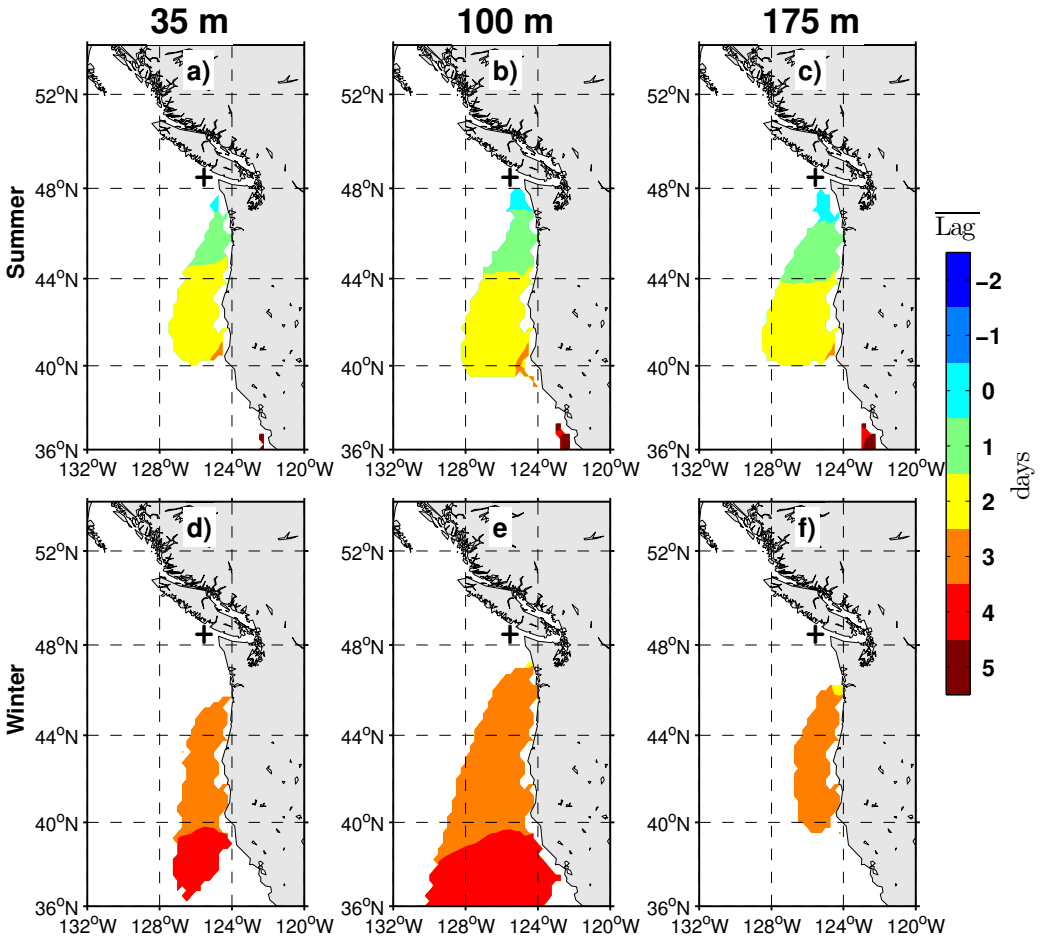

Figure 2.7: As in Figure 2.5 for the CCW polarization.

of freedom. Therefore, I decided to remove wind data based on data gaps at each mooring depth.

Temperatures

I showed in sub section 3.2 that only temperatures at 400 m are coherent with the meridional wind stress along the west coast of North America (panel–I of Figure 2.3). The highest coherence between wind stress vectors and temperatures at this depth is found at a slightly lower frequency band (10–25 days period). Using this result as a guide I computed the rotary coherences and the associated time lags between 400 m temperature and wind stresses across the domain, averaged over the the 10–25 days period band. Only the summertime CW components show significant coherences (Figure 2.8). There is a region of strong coherence along the coast, similar to the coherence pattern between wind stress and longshore currents (e.g., Figure 2.4). The associated mean time lag distributions also suggest a northward phase propagation.

Processes in the deeper water column depth are expected to be near-adiabatic, so temperature changes will be associated with either horizontal or vertical advection. As the 400 m horizontal currents are not coherent with the winds, horizontal advection is unlikely to be responsible for the wave-mediated temperature variations. Rather, I interpret the 400 m temperature variability as resulting from CTW-generated vertical motion displacing isotherms relative to the time-mean state. I will elaborate on this interpretation in the following subsection.

Comparison to Previous Results

The time lags that I have presented and phase speed associated with the peak coherences are consistent with previous results documenting the connection between the oceanic variables and remote winds mediated by CTWs. For example, Wang and Mooers (1977) found peak coherences between summertime adjusted sea level heights at Neah Bay, Washington (Figure 2.1) and winds from over a ∼1000 km south of this location at a period of ∼10 days. These peak coherences were interpreted as resulting

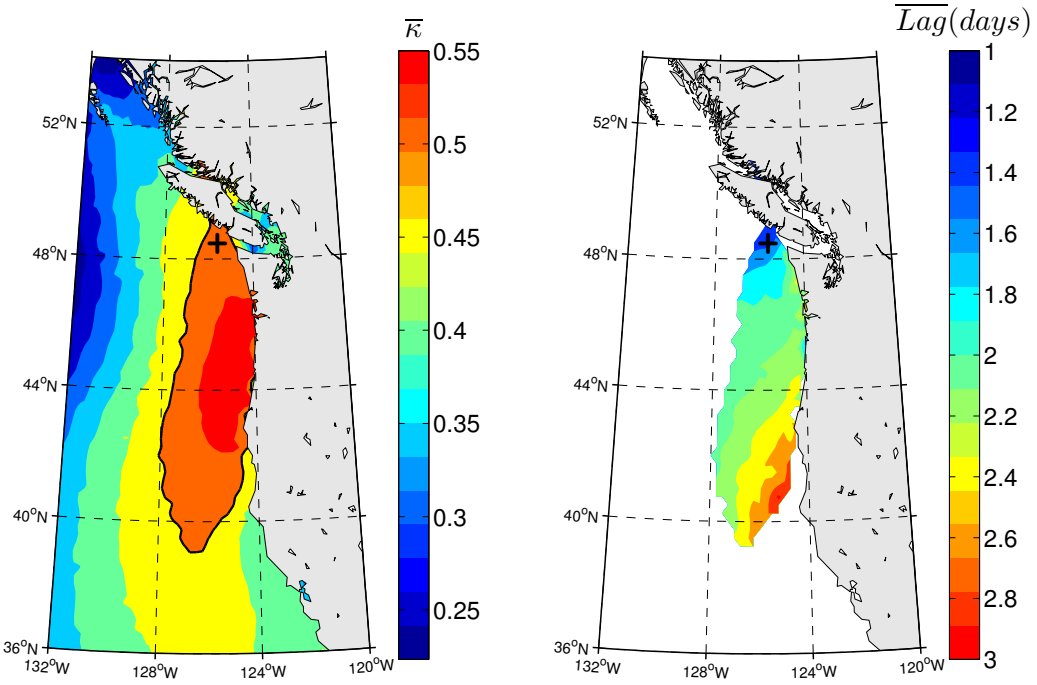

Figure 2.8: Left: CW band averaged mean rotary coherence ($\bar{\kappa}$) for the 10–25 day period between 10 m NARR wind stress in the study domain and 400 m temperatures at the mooring site (shown by the dark cross). The 95% significance level (0.49) for $\bar{\kappa}$ is shown by a heavy contour. Right: Associated mean time lags ($\overline{\text{Lag}}$). Only time lags associated with $\bar{\kappa}$ above the 95% significance level are shown.

from a northward propagation of CTWs with propagation speeds between ∼460 and ∼560 km day^{-1}. Battisti and Hickey (1984) used the CTW model of Clarke [1977] to estimate the arrival time at Oregon and Washington shelves of the mode-1 CTW generated by winds between San Francisco and Cape Mendocino (Figure 2.1). Their first barotropic mode CTW (periods longer than ∼5 days) phase speed estimates were between ∼225 and ∼433 km day^{-1}. Using sea level height and buoy wind data from a number of stations between 60° N and 33° S, Enfield and Allen (1980) reported phase speeds of 180±100 km day^{-1} based on correlation calculations and 60–100 km day^{-1} using cross spectral estimates.

Pringle and Riser (2003) estimated a phase speed of ∼220 km day^{-1} from lagged correlations between winds off Baja California and nearshore (bottom depths of 33 and 15 m) temperatures off San Diego. My work, which uses a much longer record

length, estimates a phase speed of 270 km day^{-1} based on coherence phase estimates between winds off Cape Mendocino and temperature records at a 400 m depth of a ∼500 m water column at the shelf break of British Columbia. Both these phase estimates are within the range of the theoretical phase speeds of mode-1 CTW for the respective regions. The main difference between my results and those of Pringle and Riser (2003) is that while they find significant correlations with lags as long as a year, my significant coherences are bounded in the 10-25 day period. I cannot see coherences out beyond a season because of the way I analyzed my data, and there may be differences because of the different environments of the two works.

Only periods within the daily to seasonal band are resolvable with my analysis because the calculations are done separately for each season and then averaged. Hence, the longest period that I can resolve is 122 days (corresponding to 4 months). I do not find significant coherences between the 25 and 122 day periods. It is possible that if the wind domain were expanded southward that longer period waves would become significant at my study site because waves with periods longer than 25 days are most likely generated in the tropical Pacific region and slowly propagate northward. Such waves have been shown to be important in the south-central CalCS (e.g., Frischknecht et al., 2015).

My results are in broad agreement with those of previous studies but do not show the high frequency coherences found during summer by Wang and Mooers (1977) and during winter by Denbo and Allen (1987). Similarly, Thomson and Krassovski (2015), using a more recent and shorter dataset at A1 than I am considering here, found weak coherences at high frequencies (period $<$ 10 days) between longshore currents and NARR winds only near the mooring site. In all three studies, the high frequency weak coherences were interpreted as being due to local wind forcing. My analysis in this paper is based on record lengths between 12 and 19 seasons (as missing data differ between depths and variables), with a corresponding increase in statistical robustness relative to all previous studies (which typically used one or two - and no more than 4 - years of data). The absence of those high-frequency weak coherences in

my results suggests that the previously found coherences at these frequencies might be less robust.

My results also show lower, but significant, coherence between local wind stress and current/temperature (Figures 2.4, 2.6 and 2.8). These local coherences may not actually represent local influences because the spatial low frequency coherence length scale of the wind stress field ($L_c \simeq 500$ km) is relatively long (Denbo and Allen, 1987).

My rotary coherence and mean time lag distributions clearly show the presence of CTW signals at southern Vancouver Island. Phase speeds computed using these mean time lags fall within the range of speeds reported by other studies (Table 3.1). For the CW mean time lags, the main difference between summer and winter is that the time lags for winter are shorter at the same locations. This difference in mean time lags (phase speeds) has most likely to do with seasonal changes in the ocean stratification. A detailed explanation of these results requires further study using CTW models.

Generally, at the mooring site the 400 m currents are relatively less energetic than currents at the shallower depths. However, the ratio between the 400 m and 35 m current variances is roughly the same as the ratio between the 400 m and 35 m temperature variances. Therefore, I argue that lower variance in 400 m current or temperature does not preclude the occurrence of high coherences with the winds. Only the 400 m temperatures are coherent with the wind stresses for the potential reason discussed below.

The absence of significant coherence between the wind and the water temperature at 35 – 175 m depth, while the currents from the same depths are significantly coherent with the winds, shows that CTWs can influence currents and temperatures differently. The relative magnitudes of vertical and horizontal temperature gradients and the phases of different velocity components also play a role in how the winds affect temperatures at the given depth. For example, consider the horizontal advection of warm water by a passing wave, associated with vertical raising of colder water. In this example the net effect on temperature at a given point will be small.

Table 2.1: A compilation of coastal trapped wave phase speeds (sub-seasonal) along the west Pacific coast from previous studies.

Authors	**Speed(km/day)**	**Obs/Mod?**	**Data used**	**Time period**	**Statistical method**
This work	100–400	Obs.	currents, & T	1989–2008	Coherence
Meyers et al (1998)	170–260	Obs.	SSH	1991–93	Lagged correlation
Enfield and Allen (1980)	80–280	Obs.	SSH	1950–1974	Lagged correlation
Wang and Mooers (1977)	460–560	Obs.	SSH	1973	Lagged corr.
Lyman and Johnson (2008)	185–225	Obs.	SSH (Altimeter)	1982–1999	Lagged correlation
Hermann et al (2009)	150	Mod.	SSH,CSL	1997–2002	Lagged correlation
Strub and James (2002b)	100–240	Mod	SSH (Altimeter)	1982-83	Lagged correlation
Batisitti and Hickey (1984)	240–410	Mod.	SSH &,currents	1972,1977 & 1978	Coherence
Frischknecht et al (2015)	210–250	Obs., Mod.	SSH	1979–2013	Lagged correlation

Mod.: Model

Obs.: Observation

SSH: Sea surface height

CSL: Coastal Sea Level

T: temperature

Where the statistical relationship between horizontal currents and remote winds is weak, wind-driven temperature variations can still result from vertical displacements of isotherms by the CTW. While this result may seem counter-intuitive given the continuity equation, which relates horizontal gradients of horizontal velocity components to the vertical gradient of the vertical velocity, I analyze the actual currents. The statistical relationship between winds and a velocity component field will generally differ from that between winds and derivatives of this field.

The above argument is also supported by CTW theory. When the effects of stratification cannot be neglected, the offshore structure of long CTWs is such that near the coast the cross-shore flow is depth-independent, and near the shelf-break the cross-shore and vertical motion are bottom trapped (Wang and Mooers, 1976). Wave-induced upwelling near the shelf break is, therefore, expected to be stronger near the bottom than higher up in the water column. The mooring is located immediately seaward of the shelf break and the deepest current meter at 400 m (∼100 m above the bottom) shows a signal consistent with upwelling. This signal is only seen during summer when the cross-slope stratification in the upper 500 m is the strongest. In contrast, during winter downwelling stratification is reduced. I am unable to identify specific wave modes in this analysis. The broad frequency band over which coherences are significant, and the differences of these bands between horizontal currents and temperatures, suggests that more than a single mode is mediating the remote response. However, the phase speed range and vertical structure of the perturbations suggest mode 1 CTWs are important contributors.

Seasonal change in stratification also explains the differing spatial extent of significant CW and CCW coherences between summer and winter. Stratification is greater in summer in the upper ocean, so the lateral scale of the motions (the internal Rossby radius of deformation) is reduced, yielding greater differences between CW and CCW motions as a result of geostrophy (Figure 2.4a–c vs Figure 2.6a–c). The scale is larger in winter and the difference locally between CW and CCW is reduced ((Figure 2.4e–g vs Figure 2.6e–g).

Near the coast the wind is predominantly longshore, meaning that the vectors are rectilinear. This linear polarization tends to make the CW and CCW coherence values nearly equal at same latitude. Further offshore, wind vectors are more elliptical and in the northern hemisphere the CW component dominates, making the CW coherence values higher (e.g., Figure 2.4b–c vs Figure 2.6b–c). Finally, I note that generally higher coherences occur in coastal locations where the winds are stronger and more effective at exciting CTWs, in this case the winds south of the mooring. Similar results have been found by previous statistical investigations of CTWs in the CalCS (e.g., Pringle and Riser, 2003; Thomson and Krassovski, 2015).

2.3.4 Wavelet Coherence

The Fourier decomposition of a signal provides only the frequency content of a signal and does not tell at what time a given signal of specific frequency occurs. For this same reason the rotary coherence analysis does not tell us at what time and for how long a typical oscillation occurs. Wavelet coherence analysis is a useful tool to find the correlation between two signals and display them in time-frequency (or period) plane. The phase lag calculated from the wavelet cross-spectrum are usually used to estimate the time lag between the two signals.

I apply this technique to the summertime (June, July, August and September: JJAS) northward NARR wind stresses at selected locations along the west coast and the 100 m longshore current speeds from the mooring A1. The phase arrows on wavelet coherence plots are interpreted such that arrows in the 3^{rd} and 4^{th} quadrants of the Cartesian coordinate plane are always telling the wind stresses lead the currents. These orientations are of importance as far as my main goal of finding evidences for a wave mediated remote windstress – current interactions. The arrows in 1^{st} and 2^{nd} Cartesian coordinate plane are always telling the windstresses lag the currents. Arrows heading to the right show the winds and currents are in phase and those heading to the left show the winds and currents are out of phase. The cone of influence (parabolic curve in each wavelet coherence plot) sets a boundary outside of

which a coherence peak is not reliable due to the effect of end points of a finite length data. Even if there are 95% confidence contour lines running across these cones I do not trust the coherences between these contours and part of the cone of influence.

Figure 2.9 results of wavelet coherence analysis for a normal ENSO (1996), strong El Niño (1997) and strong La Niña (2007) years. I have done these quick calculations (a)to see how robust my rotary coherence results are. As can be noted from my results, the remote wave forcing is a dominant and persistent feature at the periods ranging between a week to a month. As we go north, these features fade out and become completely absent at latitudes north of the mooring site A1 (48.8°N) (b) because wavelets help visualize both coherence and phase differences between two vectors more easily (on the same plot), and (c) wavelets give us an idea of for how long a typical oscillation persisted which the rotary coherence calculations do not. For example, during 1996 and 2007 the low frequency wave forcing from 41.8°N lasted for the whole summer season, while in 2008 the activity ended around mid August (Figure not shown). The coherences at the relatively higher frequencies (4-8 days period in these figures) are not easy to interpret because the phase arrows switch often from year to year (ie. in some years winds lead currents and in some years currents lead currents). Another reason for constructing the wavelets is to look at how ENSO affects remote wind forcing. The wavelet results suggest during summer of a strong El Niño year remote wind forcing nearly collapses and during the summer of a strong La Niña year remote forcing intensifies. The weak coherences between the windstress from north of the mooring site and the 100 m longshore current are independent of the ENSO states. Finally, I highlight that the connection between the remote wind and current is stronger during early June and mid September (could be considered the edges of the upwelling season). This particular timing of remote forcing may explain the cause for higher fraction of days ($\mathcal{F}$) with extreme carbon and oxygen.

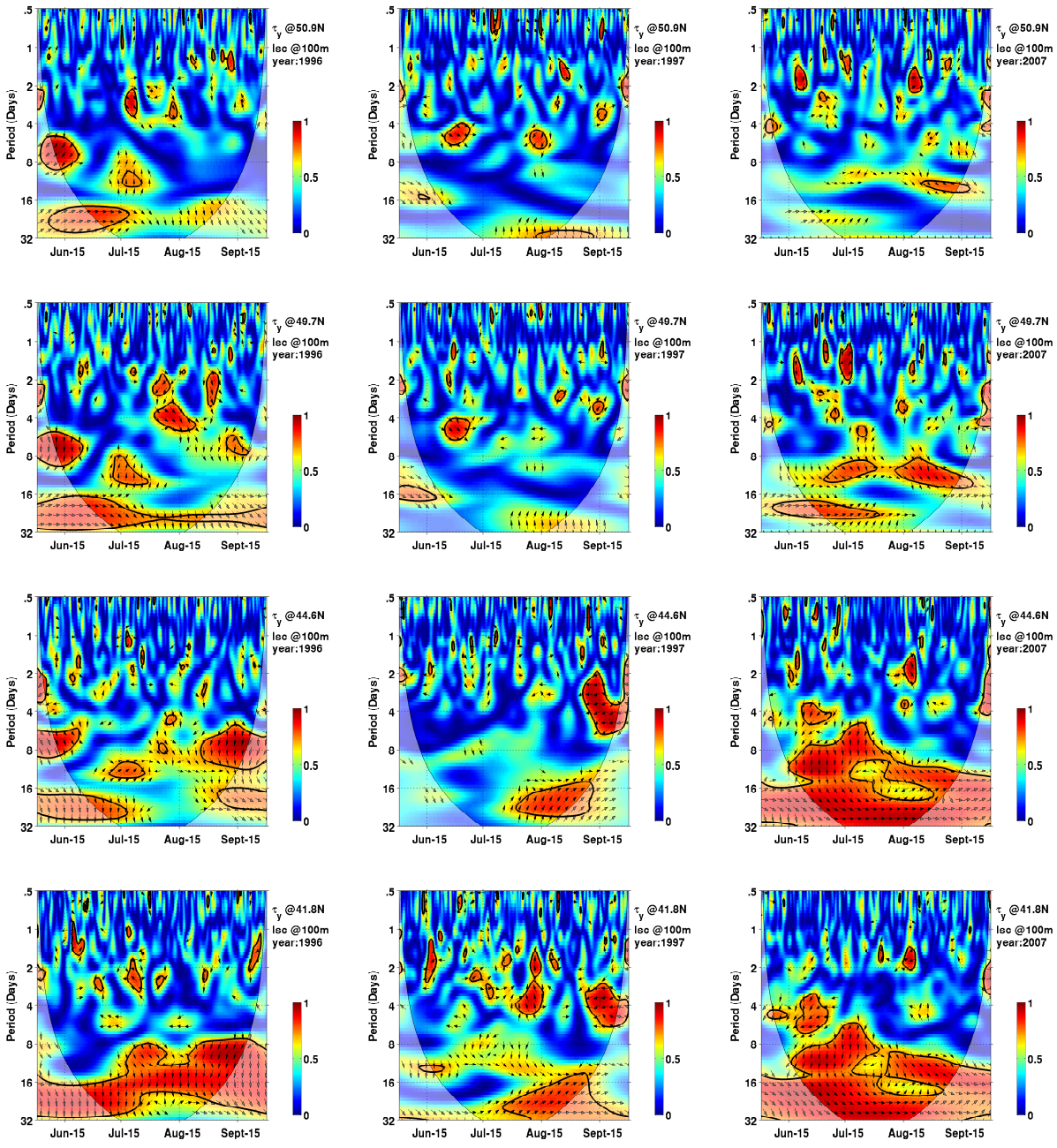

Figure 2.9: Wavelet coherences between summertime (JJAS) northward NARR wind stresses (τ_y) at selected locations along the west coast of North America and the 100 m longshore current speeds (lsc) from the mooring A1.

2.4 Summary and Conclusion

I have shown that longshore currents at depths between 35-175 m and temperatures at 400 m are significantly coherent with remote winds hundreds of km south of southern Vancouver Island. Generally, both rotary and scalar coherence calculations show winds off Cape Mendocino have the strongest connection with the currents at this location. Temperatures, on the other hand, show the strongest connection with winds between Cape Blanco and southern Washington. The footprint in both temperature and current results is large so the peak coherence zone is broadly distributed.

My time lag estimates show in almost all cases that the winds south of southern Vancouver Island lead the currents and temperatures, with lags of up to 6 days. The distribution of these time lags with latitude suggests the connection is mediated by slow-moving, low-frequency (7–25 day period) CTWs.

Temperature variability at 400 m is most likely a result of variations in vertical advection only. Because the horizontal currents at this depth are not significantly coherent with the winds (local or remote), the coherence between the same winds and temperatures at 400 m is interpreted as resulting from fluctuations in vertical advection caused by CTW driven variability in upwelling and downwelling.

I have presented rotary coherence estimates between wind stress vectors and current components and 400 m temperatures. Generally speaking, the CW and CCW coherences for the currents are similar in both summer and winter seasons. The only coherence values found to be significant for the 400 m temperature are those for CW polarization in the summer. In general, the mean coherence and time lag results are suggestive of CTW involvement as a link between the remote winds and currents and temperatures. A detailed understanding of the dynamical reasons for any preference in polarization and season represents an interesting direction for a future study. Also, further work remains to be done using CTW models to clarify the role of wave-driven upwelling in the temperature field.

Representation of time-dependent upwelling in the northern limit of the CalCS

requires the appropriate characterization of the generating mechanism, including remote coastal winds to the south. These winds can be represented using historical observations or as synthetically-generated stochastic processes with specified statistical features. Both approaches allow a statistical representation of coastal upwelling as an oceanic response to surface winds (Carton and Philander, 1984).

Understanding the effects of remote forcing on local upwelling helps to better understand the timing (Bylhouwer et al., 2013) and relative frequency of extreme conditions over the continental shelf such as hypoxia and low pH that are a direct consequence of upwelling as has been observed in the CalCS (Feely et al., 2008; Connolly et al., 2010). Although the causes of these extremes include multiple factors, including biological processes such as local remineralization (Ianson et al., 2003; Connolly et al., 2010), physical mechanisms remain essential contributors (Siedlecki et al., 2015). Future work will systematically investigate the relationship between physical, biological, and chemical processes in controlling carbon and oxygen extremes in this region.

Chapter 3

Forcing of Dissolved Inorganic Carbon and Oxygen on the Continental Margin of Southern Vancouver Island

3.1 Introduction

Coastal upwelling regions such as the west coast of Vancouver Island are characterised by a highly variable environment where extreme events are expected to be common given the dynamic circulation (Smith, 1994; Haigh et al., 2015). The drivers of extreme events of carbon and oxygen in this region have physical and biological origin. The physical processes include wind driven up/downwelling (Bakun, 1973, 1990). Changes in the strength and patterns of coastal winds in response to global scale changes affect coastal circulation (Bakun, 1990). The timing and strength of up-/downwelling in coastal upwelling regions may control the occurrence of high carbon and low oxygen conditions in both surface and subsurface waters, affecting marine organisms (Mackas et al., 2001; Barth et al., 2007). Biological processes also play a

role in the modulation of dissolved oxygen in the ocean through elevated production by photosynthesis or consumption by respiration.

Growth and survival of species at certain sensitive life stages could be directly affected by exposure to high carbon conditions (e.g., Haigh et al. (2015)). Adults and those in higher trophic levels could also be affected by changes in the food web dynamics and altered nutrient cycling. Low dissolved oxygen levels impact organisms at any trophic level (McCormick and Levin, 2017).

The impact of co-occurrence of high carbon-low dissolved O_2 conditions on organisms has been given little attention until recently (Burnett, 1997; Pörtner and Farrell, 2008; Gobler et al., 2014; Gobler and Baumann, 2016; DePasquale et al., 2015; Feely et al., 2018). Gobler and Baumann (2016) argue that measures to keep coastal dissolved oxygen levels are not enough. The effects of high carbon and its interaction with oxygen must be taken into consideration. This thesis will focus on both high carbon and low dissolved oxygen (both individual and joint extremes) and seeks to understand the physical and biological mechanisms that drive them. The modelled state variables are dissolved O_2 and Dissolved Inorganic Carbon (DIC). DIC is used as the carbon state variable for the following reasons:

- It is conservative with respect to mixing and changes in temperature and pressure, facilitating modelling of its budget.
- With well constrained total alkalinity modelled DIC can be used to estimate other parameters of the carbon system such as pCO_2 and pH.
- The scope of this thesis does not directly address the details of how organisms respond to extremes such as aragonite saturation state. As such, it is sufficient to focus on DIC.

In this chapter I characterize the physical processes that lead to extreme DIC and oxygen conditions in the study region. For this purpose I extended the 2D biogeochemical model originally developed by Ianson and Allen (2002) (IA02 henceforth).

The updated model has prognostic equations for modeling the O_2 cycle, has a physically based (accounting for all surface fluxes), time-varying mixed layer, and remotely- and locally-forced upwelling velocities. Descriptions of data used, methods applied, and the necessary model updates are given. Model evaluation using observations from multiple cruises conducted in the study region will be given towards this chapter.

Short Summary

One of the two model variables of interest, oxygen, was successfully added to the process model. This model was further improved by introducing a more mechanistic mixed layer depth and allowing it to handle multiple time dependent forcing components. The key results of this modelling exercise which are extensively evaluated by using observational data collected from the past two decades are listed below:

1. Including remote wind forcing of upwelling variability in the model improved model-observation agreements.

2. A prognostic oxygen cycle has been successfully added to the original model.

3. Modelled DIC and O_2 show larger interannual variability at the start and end of the upwelling season, due to variability in the start and end of upwelling season itself. The winter downwelling season shows the least interannual variability.

4. Model simulations show relatively high DIC during winter and a minimum late in the productive summer upwelling season. This seasonal cycle matches with depth averaged observed data. The modellded dissolved oxygen shows an opposite signed seasonal cycle as DIC and also agrees well with data.

5. The time varying model forcing allowed for the representation of seasonal cycles and variability in modelled DIC and O_2, whose climatology is useful for filling in time periods where observational data are scarce.

6. The modelled DIC and O_2 are better coupled in the lower layers, where biological processes are more important than physical processes.

3.2 Data and Methods

I use hydrographic and water chemistry data collected from the study region for the last two decades (1996–2017) to initialize, set boundary conditions for, and asses the model. The chemistry (bottle) data are comprised of at least 1500 profiles taken during 109 individual cruises. The CTD data are comprised of a much larger number of profiles collected during 107 cruises. These data were collected by the Department of Fisheries and Oceans (DFO) of Canada (La Perouse program: Mackas (1992); Line P program: Whitney and Tortell (2006)) and the Pacific Marine Environmental Laboratory of the National Oceanic and Atmospheric Administration (NOAA). A summary of the temporal and spatial information on these cruise data are available upon request.

Six years(1997 – 2002) of daily National Centers for Environmental Prediction (NCEP) reanalysis wind products from the 2.5×2.5 degrees spatial resolution, downloaded from http://www.esrl.noaa.gov/psd/data/gridded/data.ncep.reanalysis.html, were used. The wind vector components (u_x and u_y) were interpolated to key locations inside the model domain and used in the construction of the bulk mixed layer depth, forcing gas fluxes, and vertical velocities. The wind products were also interpolated to a southern location (125.5° W, 42.5° N) for remote forcing of up/-downwelling intensity in the model. The wind stress vector, parallel to the wind and of magnitude $\tau = \rho_a C_D U_{10}^2$, used in the model was calculated using air density ρ_a=1.2 kg m^{-3}, the 10 m wind speed, $U_{10} = \sqrt{u_{x10}^2 + u_{y10}^2}$, and the neutrally stable boundary layer drag coefficients, C_D, of Yelland and Taylor (1996)

$$1000C_D = \begin{cases} 0.29 + \frac{3.1}{U_{10}} + \frac{7.7}{U_{10}^2}, & (3 \leq U_{10} \geq 6\ m/s) \\ 0.60 + 0.071U_{10}, & (6 \leq U_{10} \geq 26\ m/s) \end{cases} \tag{3.1}$$

In all cases, instead of computing the alongshore wind stresses I used the northward components of the calculated wind stresses. This choice was made because the interpolated wind had a principal axis that is nearly parallel to the local coastline at

both the local and remote locations.

Similarly, the $1^\circ \times 1^\circ$ gridded daily net surface heat flux (Q_{net}) and evaporation rate (E) for the time period 1997–2002 were interpolated to the model domain. The Q_{net} and E products used are archived at the Woods Holes Oceanographic Institution's global datasets website http://oaflux.whoi.edu. Precipitation (P) data were interpolated from the $1^\circ \times 1^\circ$ gridded daily Global Precipitation Campaign Program (GPCP) datasets for the time period 1997–2002 (Huffman et al., 2001) . This time period is used as it is the period in which data for all forcings are available .

After I set up the model using the forcing datasets from the time period 1997 – 2002, I generated a 1020 year long time series for each atmospheric forcing variable using a stochastic technique that is designed to capture the annual cycles of means and standard deviations of each variable, as well as correlations between them. A detailed description of this technique is given in Appendix D.1. By using results from the 1020 year long model run, forced with the these synthetic datasets, I was able to produce robust seasonal cycles of means, variances and extremes of the model variables under present day conditions.

Relatively few inorganic carbon samples were collected from the model region prior to 2010. These data are now collected more regularly, but the available data are still far fewer than other water property samples (Table C.3). For use in model assessment, I used a linear regression to predict DIC from apparent oxygen utilization (AOU), which is a function of the commonly sampled temperature and oxygen, using multiple linear regression . An example of the relationship between DIC and AOU is shown in Figure 3.1.

This technique was adapted from that developed by Lara-Espinosa (2013) for the study region . She used a smaller subset of the data used in this thesis. With these updated data, the technique increased the DIC record by more than seven-fold (bottom panel of Figure 3.1).

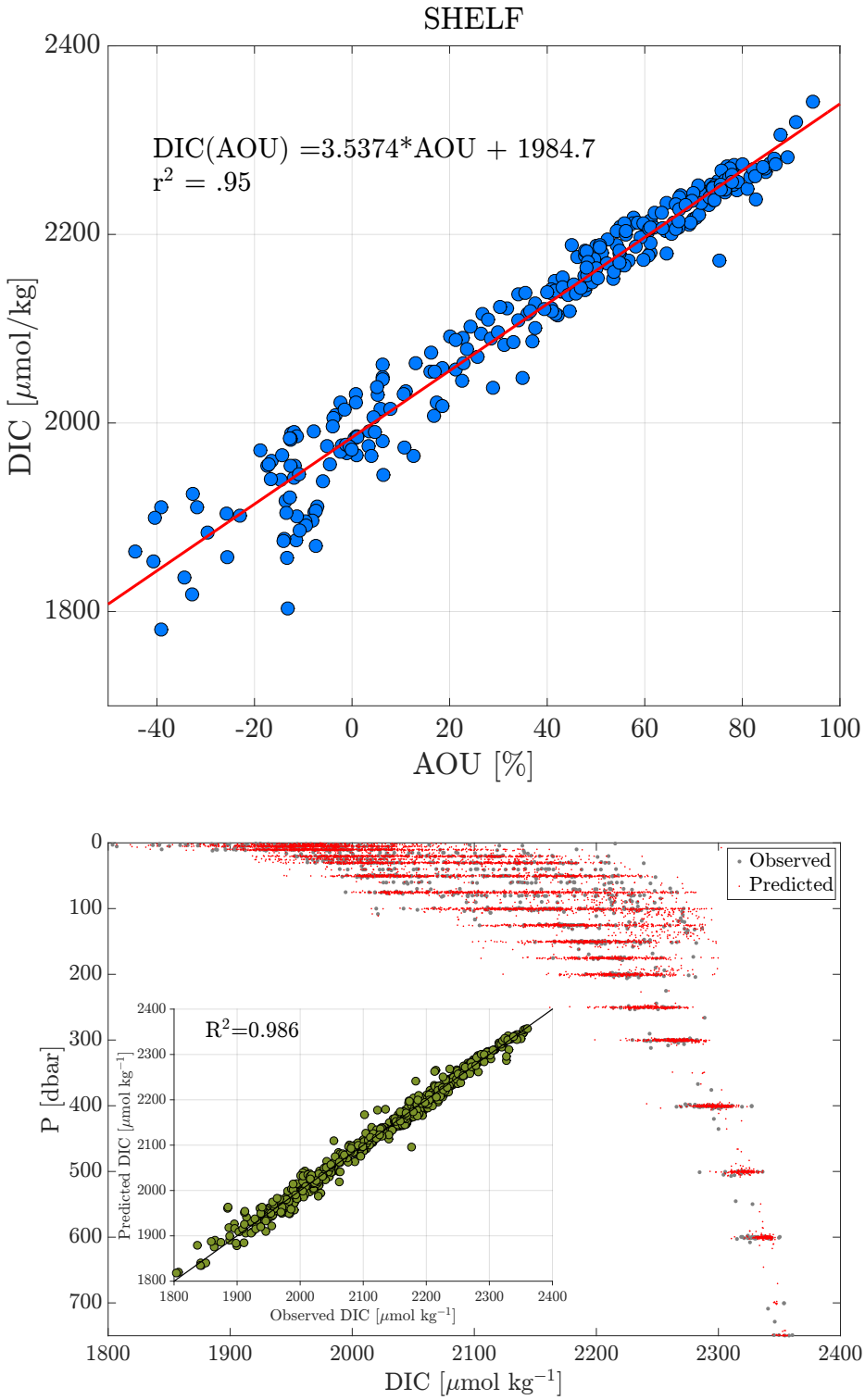

Figure 3.1: Top panel: Scatter plot showing DIC as a function of AOU for the model upper shelf. The red line is the least square fit whose equation is shown inside the figure panel. Bottom panel: Shows profiles of observed DIC (gray) and predicted DIC (red). The inset figure shows the scatter diagram of observed vs predicted DIC (top panel). The measure of agreement between observed and predicted DIC is high (R^2 = 0.986).

3.2.1 The Model

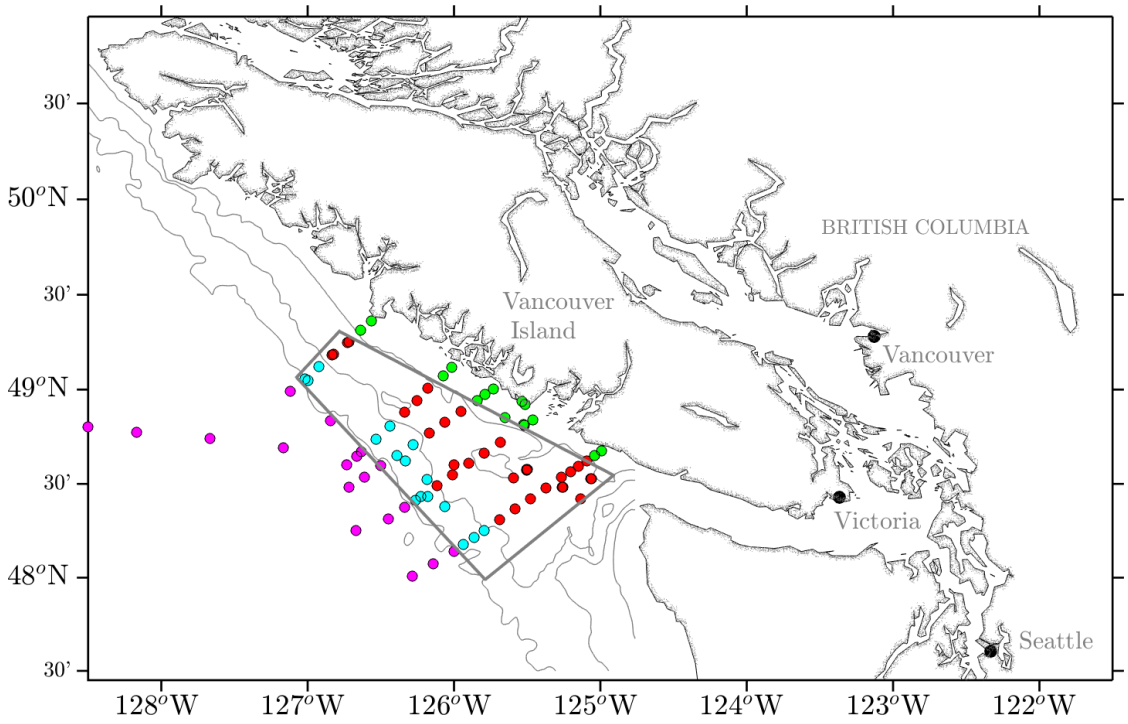

Figure 3.2: Model domain (gray box) showing stations (colored) in each sub-region of the model. Stations in the inner shelf (VICC region) stations are labeled in green colors. Red dots represent outer shelf stations. Dots in cyan and magenta represent stations over slope and the open ocean transition regions, respectively.

The study domain is the west coast of southern Vancouver Island, near the northern limit of the California Current System (grey polygon in Figure 3.2). The model used in this study is based on the 2D nitrogen based biogeochemical model of IA02 which was designed to estimate seasonal to decadal fluxes. Since I am interested in extreme conditions over periods of days, I have added a more realistic physical forcing that captures the important impacts of mixed layer depth variations, coastal trapped waves and extends the capability of AI02 model to these shorter time scales.

Carbon and nitrogen are the two currencies in the original model. Carbon exists in the model as either dissolved inorganic carbon (DIC), dissolved organic carbon (DOC) or particulate organic carbon (POC). Nitrogen similarly has the three forms, ie., DIN, DON and PON. Dissolved oxygen has been added as a third model currency.

The representation of the oxygen budget is simplified by making oxygen to depend only on the carbon budget, and it does not feedback on the carbon and nitrogen budgets. Salinity is modelled, forced by the net evaporation minus precipitation flux. Temperature is specified diagnostically as in Ianson and Allen (2002).

The model has two main layers in the vertical (Figure 3.3). Horizontally, it represents the outer shelf (10 km wide) and slope (20 km wide). The inner shelf is dominated by the buoyancy-driven Vancouver Island Coastal Current (VICC) that is not modelled. The VICC flows northward throughout the year with peak volume during spring. Fluxes from the VICC region are prescribed at the inner boundary for the upper shelf layer. I define the VICC region (the area containing the green dots in Figure 3.2) for modeling purpose as the region between the 75 m isobath and the coastline. Along the coast the VICC region is defined from the mouth of Juan de Fuca strait (located southeast of the model domain) to the northernmost boundary of the model domain .

Vertical diffusive mixing between the lower and upper model boxes is mediated by a pycnocline layer specified between the two layers. Since my interest is in time scales longer than a day, I do not explicitly model high frequency processes such as tidal mixing. Instead, the effects of this process are represented by a tunable vertical mixing coefficient (Appendix B.1) . The model also couples the boxes in the vertical using externally-determined time series of vertical velocities. A complete set of the ordinary differential equations (ODEs) and other equations of the model used in this thesis are given in Appendix B.1. In the following, I present in more detail the key aspects of the work done to extend the original model.

- The air-sea gas transfer coefficient and upwelling/downwelling velocities have been obtained from observationally-based products (reanalysis and a stochastic model), instead of using a smoothly-varying idealized wind.

- The effect of remote, in addition to local, wind forcing on vertical velocities have been included (based on the results of Chapter 2).

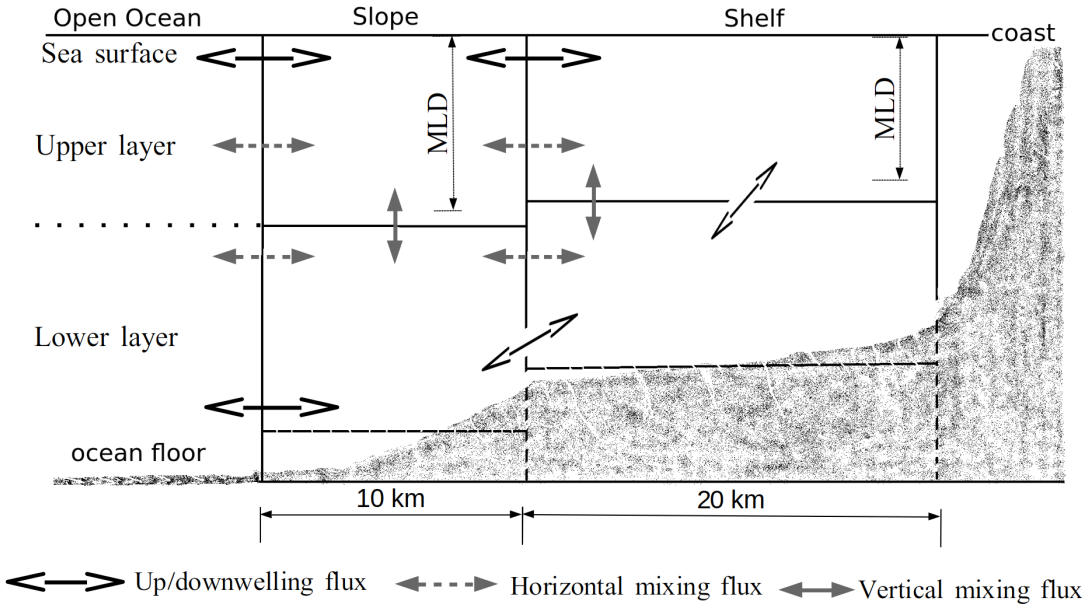

Figure 3.3: Model geometry modified from IA02.

- The model mixed layer variability is transformed from one with a simple prescribed seasonal cycle to one that is estimated from local surface fluxes.
- Oxygen has been added as a prognostic model currency.
- Extensive model evaluation and tuning have been done using observations collected during the last two decades.

In the following subsections I present a detailed description of the model changes listed above. New or modified model parameter values are listed in Table 3.1, while boundary conditions are given in Table 3.2.

Model Mixed Layer

The model upper box is treated as well-mixed irrespective of season, with a time-evolving depth. IA02 prescribed this depth using a smooth seasonally-varying curve, with added higher frequency cycles to mimic the effects of storm mixing, to study carbon fluxes mainly on seasonal time scales. In the current study, I am interested in extremes over significantly shorter time scales (days to weeks). Therefore, it was essential to redefine the model mixed layer so that primary atmospheric and oceanic factors contributing to key fluxes act in synchrony. The simplest bulk mixed layer formulation that is appropriate for the upgraded version of the model is one that responds to varying surface fluxes assuming a constant depth two layer ocean where the fluid densities in the two layers are slightly different. This mixed layer model is a simplified version of the Price et al. (1986) model with no velocity shear in the water column. An overview of the model mixed layer dynamics is given in Appendix C.1.

Up/downwelling Velocity

Upward water motion, upwelling, delivers nutrients to fuel primary production in the well-lit upper layers. Downward motion, downwelling, on the other hand, depresses the nutricline which may reduce primary production. Direct measurements of the vertical velocity in the ocean are usually not practical. Rather, it is customary to estimate this velocity from other quantities (e.g., the upwelling index based on the rate of baroclinic energy conversion used in Ware and Thomson (1991)). In this work, I develop proxy-based estimates of upwelling velocity, which will be denoted by the symbol w_l when the forcing is local and w_r when the forcing is remote. The net sum of the locally and remotely forced vertical velocities is denoted by the symbol W. To differentiate between upward and downward velocities I use the superscripts $^+$ and $^-$, respectively, to each velocity symbol (Eg., W^+ and W^- refer to the upward and downward net velocities).

The goal here is to construct a continuous time series of vertical velocity for use in

the model. To simplify my approach, I consider only the dominant type of upwelling, wind driven coastal upwelling. The locally generated (Ekman) upwelling is due to alongshore wind stress. The local winds, however, do not show strong coherence with upwelling proxies such as sea surface temperature and subsurface currents, suggesting the need for additional forcing to explain the observed upwelling and its effect on the biogeochemical cycles in the study region. As shown in Chapter 2, upwelling in this region is partially controlled by northward propagating coastal trapped waves. This wave-mediated remote wind forcing explained nearly half the variance of the near bottom temperature in a mooring location inside the model domain. In this study I combine both local and remote wind forcing to represent the net vertical velocities.

The locally forced vertical velocity ($w_l(t)$) in the model is expressed using the Ekman transport theory as

$$w_l(t) = \frac{\tau_l^y(t)}{\rho f R_d} \tag{3.2}$$

where τ_l^y, ρ, f and R_d are local alongshore wind stress, density of sea water, Coriolis parameter and internal Rossby radius of deformation, respectively. R_d is used to approximate the cross-shelf extent of the upwelling cell (Marchesiello and Estrade, 2010). I estimate R_d in the study region using $\sqrt{\frac{v^2}{f^2}}$ with an average internal wave phase speed of $v = 2$ m s^{-1} and $f = 10^{-4}$ s^{-1} to be roughly 20 km, which is the same as the model shelf width (Figure 3.3). In the calculation of the local upwelling velocity, τ_l^y is 7-day high pass filtered based on the results of Thomson and Krassovski (2015), who found that the local wind is more important on timescales shorter than a week.

I showed in Chapter 2 that near bottom (400 m) temperature at a long term mooring deployed off the west coast of southern Vancouver Island (125°W, 48.5°N) is strongly coherent (in the 7–25 days period window) with northward wind stresses at locations as far south as 36°N. This remote coherence was interpreted as the result of heaving of isotherms due to northward propagating waves generated by coastal winds

south of the study region. Since the horizontal temperature gradients are much smaller than vertical gradients near the bottom, the primary source of temperature variability there is due to the vertical undulation of density surfaces by passing waves. This motion corresponds to a vertical velocity contribution that is remotely forced. I estimate the remotely-forced contribution to the vertical velocity, $w_r(t)$, as follows

Assuming that the only source of temperature variability at 400 m depth is vertical advection, I ignored the horizontal advection and diabatic terms in the internal energy conservation equation

$$\frac{dT(t)}{dt}|_{z=400m} = u\frac{\partial T(t)}{\partial x} + v\frac{\partial T(t)}{\partial y} + w\frac{\partial T(t)}{\partial z} \tag{3.3}$$

After excluding the horizontal components and re-arranging terms in Equation 3.3, the remotely forced w (w_r) is given by

$$w_r(t) = \left(\frac{\partial T(t)}{\partial z}\right)^{-1}\left[\frac{dT(t)}{dt}|_{z=400m}\right] \tag{3.4}$$

The ubiquitous gaps in the temperature record at the 400 m depth did not allow for the direct calculation of the temperature time tendency in Equation 3.4 from these data (Figure 3.4). In order to calculate this term in Equation 3.4, I fit a linear model to the temperature record using a 7 day low pass filtered northward wind stress (τ_r^y) calculated from a reanalysis wind product at a remote location (42.5°N, 125°W), where the northward wind stress was found to have the highest coherence with the 400 m temperature at the above mooring location (Chapter 2).

I then defined the net upwelling velocity, $W(t)$, as a sum of the locally and remotely generated vertical velocities as

$$W(t) = \epsilon\frac{\tau_l^y(t)}{\rho f R_d} + w_r(t) \tag{3.5}$$

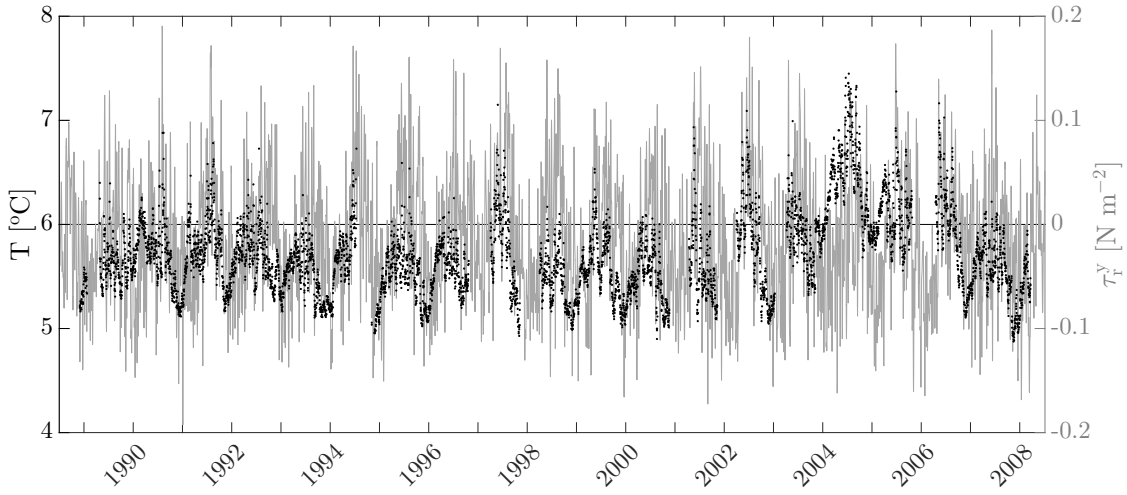

Figure 3.4: Time series of 400m temperature (black dots) at a mooring site inside the model domain and seven day low pass filtered northward wind stress, τ_r^y (at 42.5°N, 125°W) used to fit a linear model to the temperature record.

where the factor

$$\epsilon = \begin{cases} 2, & \text{if } \tau_l^y \leq 0 \\ 3, & \text{otherwise.} \end{cases} \tag{3.6}$$

is used to adjust the local Ekman upwelling such that the Ekman downwelling is slightly stronger than upwelling because the wind is stronger in the winter (Bakun, 1973). This adjustment is used to offset the bias of the seasonal cycle in the local upwelling forcing due to the highpass filtering.

The correlation length scale for the wind field is large (hundreds of km), particularly during the winter season (Denbo and Allen, 1987). Therefore, the remote and local winds are closely related. An important distinction between the local and remote contributions to vertical velocity is thus their frequency content. Local wind forcing is more important at higher frequencies while remote wind forcing is more important at lower frequencies (including the annual cycle). That is not to say the two types of wind forcing have fundamentally different frequency contents, but rather the ocean acts as a low pass filter to the remote wind forcing. When isopycnals are brought up into the mixed layer, irreversible transport does occur. Therefore, it is assumed in the derivation of the remotely generated upwelling that the CTWs cause

instantaneous mass transport through the model box interfaces.

3.2.2 Oxygen cycle

A complete set of the ordinary differential equations (ODEs) and other equations of the model used in this thesis are given in Appendix B.1. In the following, I specify the ODEs to represent oxygen tendencies in each model box.

$$\frac{dO_{2_u}}{dt} = PQ_n(PP + \sigma_C PC) - RQ(r_d DOC_u) + \frac{G^*}{h_u} + X + V + H \tag{3.7}$$

$$\frac{dO_{2_l}}{dt} = -RQ(r_p POC_l - r_d DOC_l) + X + V + H \tag{3.8}$$

These ODEs were solved using the canonical Runge-Kutta Order 4 (RK4) scheme with an adaptive time step (maximum time step is 0.1 day).

A schematic of the model oxygen cycle is presented in Figure 3.5. In the model upper layers, oxygen is produced as a byproduct of primary production (PP, expressed here in nitrogen units, corresponding to green arrow from POC_u to $[O_2]_u$ in Figure 3.5). The total number of moles of oxygen produced per mole of carbon assimilated, PQ_n, is set to 1.4. This value corresponds to the uptake of nitrate (NO_3^-) (Laws, 1991), which is assumed the dominant form of nitrogen in the model. The only biological sink of oxygen in the upper layer is oxidation of DOC_u (upper layer DOC), with the specific remineralization rate of r_d. In the lower layers, oxygen is consumed during remineralization of both DOC and POC. The value of the respiratory quotient (RQ), corresponding to the number of moles of CO_2 produced per mole of O_2 consumed during oxidation of organic matter, reflects the type of organic substrate that is preferentially oxidized (Tcherkez et al., 2003). When carbohydrates are primarily oxidized, RQ takes the value 1 (Ghashghaie et al., 2003). However, different authors have used values of RQ ranging between 0.5 to 1.33 depending on the substrate respired. Hernández-León and Ikeda (2005) discussed the scarcity of

data to accurately estimate the value and used a value of 0.97. Since RQ depends on temperature, it is one of the parameters that is relevant to future climate where ocean temperature is projected to increase. In this work I set the baseline value of RQ to 1 and in Chapter 5 test the sensitivity of the model results to this value.

When nutrients are limiting but light is not, excess inorganic carbon (PC) is converted into the semi-labile DOC (Anderson and Williams, 1998; Ianson and Allen, 2002; Druon et al., 2010; Bianucci and Denman, 2012). The fraction of PC, $\sigma_C = 0.45$, is used to include the production of O_2 during this process (Druon et al., 2010; Bianucci and Denman, 2012).

Bubble injection is not explicitly modelled. It is possible for model oxygen concentrations in the model lower layers can become negative as I do not include denitrification (Bianucci and Denman, 2012). The model is intended to be primarily used outside of regions where oxygen levels do not become too low for nitrate oxidation to start. In the study region at present anoxia has not been observed (Crawford and Peña, 2013).

The advective term, X, in Equations 3.7 and 3.8 includes the buoyancy fluxes, which include precipitation, terrigenous runoff and mixing with the outflow from the Juan de Fuca strait (VICC) as described in IA02. The terms V and H represent conservative vertical and horizontal mixing between boxes, respectively.

Gas Flux

The term G^* in Equation 3.7 represents the gas flux in units of μmole kg^{-1} day^{-1} per meter coastline. Air-sea gas exchange acts as a source or sink to the oxygen pool depending on the oxygen saturation value (O_{2sat}) in the 'surface' layer and oxygen available (O_{2a}) in it:

$$G^* = -K_{O_2}(O_{2a} - O_{2sat}) \tag{3.9}$$

$$K_{O_2} = 0.266U_{10}^2(Sc/600)^{-0.5} * 0.24 \tag{3.10}$$

$$Sc = 1953.4 - 128.00T_s + 3.9918T_s^2 - 0.050091T_s^3 \tag{3.11}$$

The rate of gas exchange is influenced by the level of turbulence at the surface, as represented by the gas transfer coefficient, K_{O_2}.

The O_{2sat} value was determined using the corrected equation of Garcia and Gordon (1992,1993). The K_{O_2} value (Equation 3.10, in units of m d^{-1}) in this work was determined following Ho et al. (2006) (Equation 3.10) where U_{10} is wind speed at 10 m height. The Schmidt number (Sc) was calculated from the prescribed sea surface temperature (T_s) using coefficients from Wanninkhof (1992).

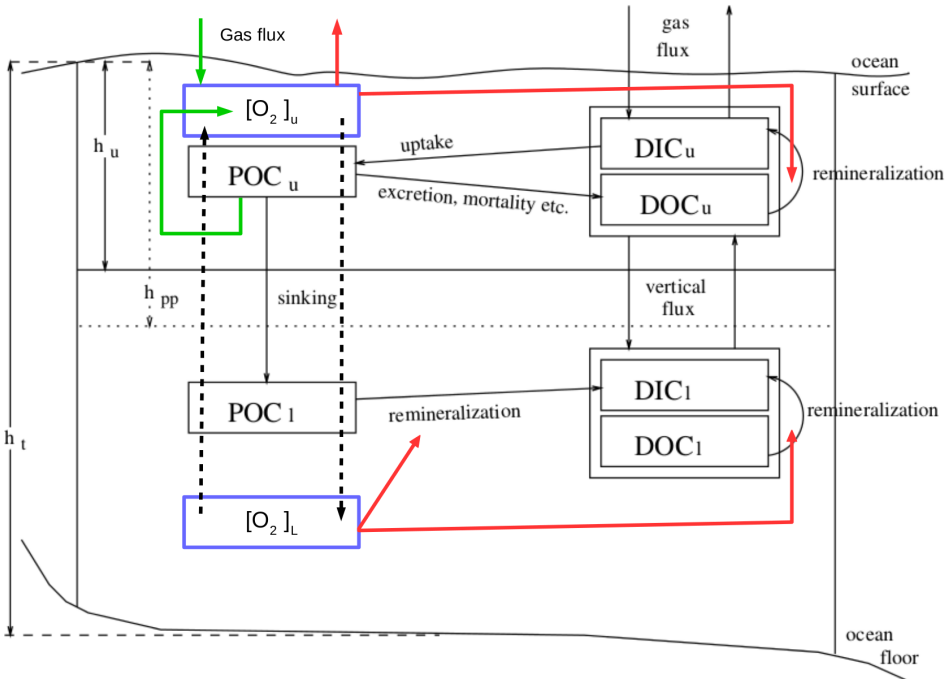

Figure 3.5: Model biological fluxes shown using carbon as a currency (Figure modified from IA02). Each box in either layer represents a state variable pool. Arrows show fluxes into and out of these pools. Purple boxes are for the added oxygen variable. Oxygen sources are shown by green arrows. Oxygen losses are indicated by red arrows.

For clarity I include the equations for model air-sea CO_2 flux, which already existed in the original model.

$$G^* = K_{CO_2} * sol * (pCO_{2a} - pCO_{2w}) \tag{3.12}$$

$$K_{CO_2} = 0.39U_{10}^2(Sc/660)^{-0.5} * 0.24 \tag{3.13}$$

$$Sc = 2073.1 - 125.62T_s + 3.9918T_s + 3.6276T_s^2 - 0.043219T_s^3 \tag{3.14}$$

The gas transfer coefficient (K_{CO_2}) using Ho et al. (2006) using Schmidt number coefficients from Wanninkhof (1992). CO_2 solubility (sol) was calculated following Weiss (1974). Annual variability of pCO_{2a} was prescribed (Manning, 1993). I considered surface stratification diluting DIC and TA following IA02. Partial pressure of CO_2 in seawater (pCO_{2w}) is calculated from an empirically derived TA-S relationship given in Equation B.26.

Table 3.1: Physical parameters. Only new or updated model parameters are listed. The average velocities were computed from the 1017 year long (present-day) forcing data.

Parameter	Description	Value	Unit
h_u	mixed layer depth: shelf, slope	10 – 45, 10 – 65	m
h_{pp}	permanent pycnocline depth: shelf, slope	50, 70	m
M_V	vertical mixing coefficient	0.1	m d^{-1}
d_m	depth of mixing	5	m
$\overline{w^+}_l$	average local upwelling velocity	1.96	m d^{-1}
$\overline{w^-}_l$	average local downwelling velocity	1.28	m d^{-1}
$\overline{w^+}_r$	average remote upwelling velocity	7.53	m d^{-1}
$\overline{w^-}_r$	average remote downwelling velocity	4.98	m d^{-1}

3.2.3 Observational Data Analysis

The cruise data used to develop and evaluate the model were analyzed as follows. First, the stations were grouped into four regions, based on a mixture of hydrographic properties and bathymetry: inner shelf (VICC), outer shelf, slope and the open ocean

Table 3.2: Range of boundary conditions to all model runs in parenthesis. The baseline (see definition in subsection 3.2.3) is given before the ranges.

Pool	Description	Baseline value (range)	Unit
River_{DIC}	DIC in fresh (river) water	200(0 – 400)	μM
VICC_{DIC}	DIC in VICC	2144 (0 – 4289)	μM
VICC_{DOC}	DOC in VICC	30 (0 – 60)	μM
VICC_{POC}	POC in VICC	2.7 (0 – 5.4)	μM
VICC_{DIN}	DIN in VICC	22 (0 – 44)	μM
VICC_{DON}	DON in VICC	3 (0 – 6)	μM
VICC_{PON}	PON in VICC	0.45 (0 – 0.9)	μM
VICC_{O_2}	O_2 in VICC	244 (0 – 489)	μM
Open Ocean Surf_{DIC}	DIC in open ocean surface water	2000 (0 – 4000)	μM
Open Ocean Surf_{DOC}	DOC in open ocean surface water	40 (0 – 80)	μM
Open Ocean Surf_{POC}	POC in open ocean surface water	1.2 (0 – 2.4)	μM
Open Ocean Surf_{DIN}	DIN in open ocean surface water	6.75 (0 – 13.5)	μM
Open Ocean Surf_{DON}	DON in open ocean surface water	20 (0 – 40)	μM
Open Ocean Surf_{PON}	PON in open ocean surface water	0.18 (0 – 0.36)	μM
Open Ocean Surf_{O_2}	O_2 in open ocean surface water	300 (0 – 600)	μM

(Figure 3.2). To relate property profiles to the vertically-integrated model variables, I depth-averaged each profile measured at each station within the model domain. For the upper layers, the depth averaging was done from the surface to the base of the average model mixed layer depth during the month the profile was measured. Data were extrapolated to the surface or to the model mixed layer base when data at these depths were not available. Depth averaging for the lower layers was carried out between the model's permanent pycnocline depth and the model bottom for each region. The depth-averaged values from each month and year were then averaged across stations within the same region. Finally, a time series of monthly mean values were created across the twenty years of the record.

Data from stations outside the model domain were analyzed differently. Profiles from the inner shelf region used for setting the inner model boundary conditions were depth averaged between surface and the time-mean observed mixed layer depth. I then computed the overall spatial and temporal mean of the depth averages to represent inventories. Considering the offshore boundary conditions, a careful inspection of the observed data indicated that the potential density $\sigma_\theta = 26.6$ surface is the density surface most often reaching the base of shelf upper layer during the upwelling season. For the outer model boundary, I took spatial and temporal averages of variables on this density surface (Table C.1). These average values may be influenced by the phase of the 18.6-year tidal cycle which has been shown to influence oxygen on the isopycnals of interest (Crawford and Peña, 2013). Agreement between the model and observations suggests that this sampling bias is likely not large. Extensive model analysis subsequently showed that use of this density surface for offshore boundary conditions produced best agreement between model simulations and observations, among all density surfaces considered (not shown).

3.2.4 Model Evaluation

In this section, I present results from a (present-day) 1017 year long baseline model run and compare them with observations. The baseline model run is a reference model run for 1017 years with standard model parameters, forcing, geometry and boundary conditions using a time step of 0.1 day. A fact that should be kept in mind in all model-observation comparisons is that most of the observed data come from time periods other than the winter season. It is also important to remember that the direct model-observation comparisons are dependent not only on the accuracy of the model, but also on the spatial and temporal resolutions of the cruise data and the averaging process. In general, under-sampling tends to reduce the range of observed variability of observations while spatial heterogeneity increases it.

Before I embark on the comparison of individual time series, I consider the probability distributions of model quantities over the entire simulation, without accounting for seasonal variations. Where the annual cycles are larger than the interannual or intraannual variability, the probability distributions tend to be bimodal, as is the case with the upper shelf DIC and O_2 and upper slope DIC . Otherwise, the distributions are in general unimodal. DIC and O_2 in the lower layers and O_2 in the upper slope follow a unimodal distribution, reflecting a lack of strong seasonal cycles (Figure 3.6).

In the upper slope, the observed O_2 histogram agrees well with the modelled O_2 histogram, especially considering the large spatial variation in the observed O_2. The lack of strong seasonal cycles in the lower shelf and slope is also evident in the unimodal observed O_2 histograms. The main difference between the lower layer modelled and observed O_2 is that while the modelled O_2 value never falls below 50 μmole kg^{-1} such values occur in observations. One reason that the modelled histograms are narrower than the observed histograms is because the model is representing spatially averaged quantities.

The observed O_2 histogram for the upper shelf is positively skewed, but does not clearly show a bimodal shape, unlike the modelled upper shelf O_2. Much of this

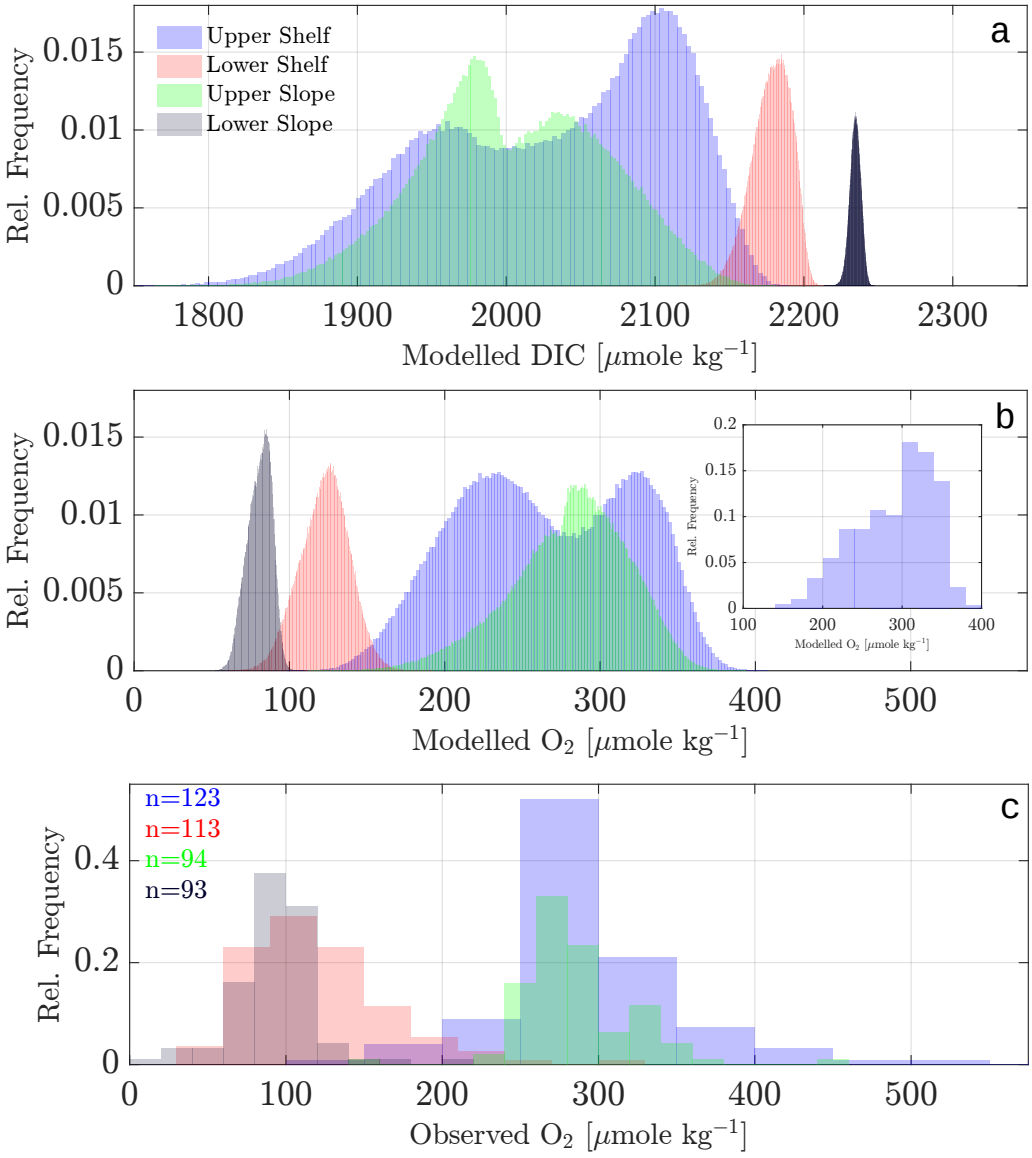

Figure 3.6: Histograms of modelled (a) DIC and (b) O_2 and (c) histograms of depth averaged O_2 data are shown. All the daily realizations of the (present-day) 1017 year simulation are used to construct the modelled histograms. The number of depth averaged data points used to construct observed oxygen histograms are shown in the same color as the histograms. The observed DIC are not used to generate histograms because there are not enough of the data. A histogram of sub-sampled (based on Julian days where O_2 data were available over the shelf) modelled O_2 in the upper shelf box are shown in inset in panel b.

difference between observed and simulated distributions results from sampling bias due to the relatively small number of winter observations. To demonstrate this fact, I subsampled the modelled O_2 based on observed sampling times and built the histogram shown as inset in panel b of Figure 3.6. Although the skewness differs between modelled and observed shelf O_2, this figure shows that the unimodal distribution in the observed O_2 is due to lack of enough observation in the winter season.

Box-and-whisker plots of modelled and observed DIN, DIC and O_2 (Figures 3.7, 3.8 3.9) show their mean seasonal cycles and the seasonally-evolving median, quartiles, and extremes. A detailed comparison of modelled and observed quantities will be presented in the following sections.

DIN

I compare modelled DIN with observed nitrate concentrations, which I simply call observed DIN. In the model upper shelf, the median DIN for January and February is 18±2 μM (Figure 3.7). However, modelled DIN values at this time can extend as low as 10μM. This high wintertime upper layer DIN then decreases towards early spring. The upwelling season in the model region runs from mid-April through mid-October (Thomson et al., 2014). The modelled interannual variability of DIN is stronger at the start and end of this season, as indicated by the larger interquartile ranges and the extreme DIN values. Possible reasons for this strong interannual variability are variations in the upwelling start/end dates and its intensity (Schwing et al., 2006). During May to early September the modelled upper layer median DIN values are essentially zero except in some episodic intense upwelling events where more DIN is brought from below. The observed DIN for the upper shelf layer is shown in open red box plots (Figure 3.7). In the lower shelf the modelled DIN shows a weaker seasonal cycle than observations, but the difference between their medians is only ±2.5 μM. The model DIN also has more frequent outliers (extremely low values in this case) throughout the years while the observations do not. In terms of the upper shelf, the agreement is better, particularly during the spring. During

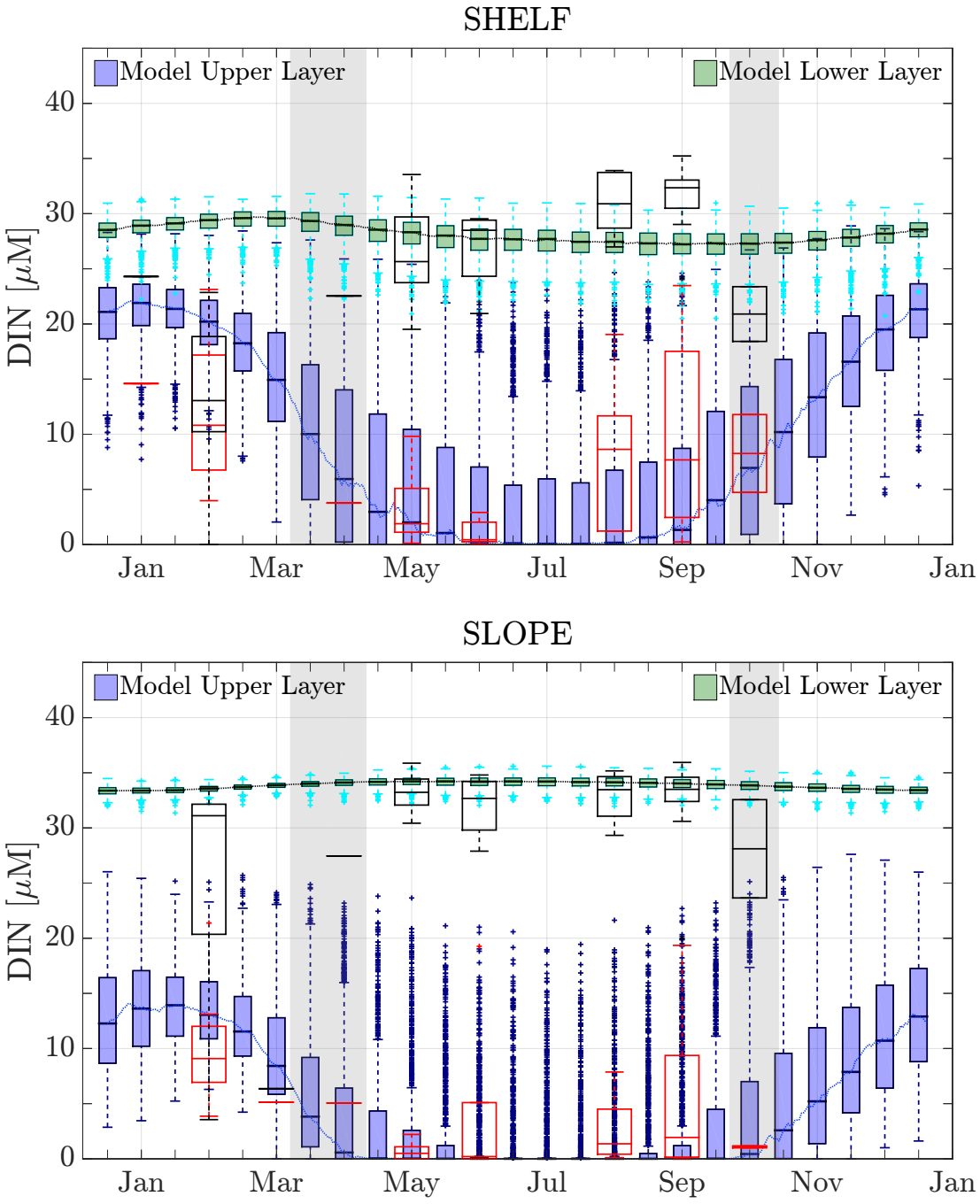

Figure 3.7: Model DIN for baseline run: Results for shelf and slope are shown in top and bottom panels, respectively. Upper (blue) and lower (green) layer results are indicated by bi-weekly shaded box-plots. Depth averaged observed values for each month are shown by unshaded box-plots. Dark and red box-plots are for upper and lower layer depth averaged values. The dashed lines connect the model median values. The plus signed markers represent outliers.

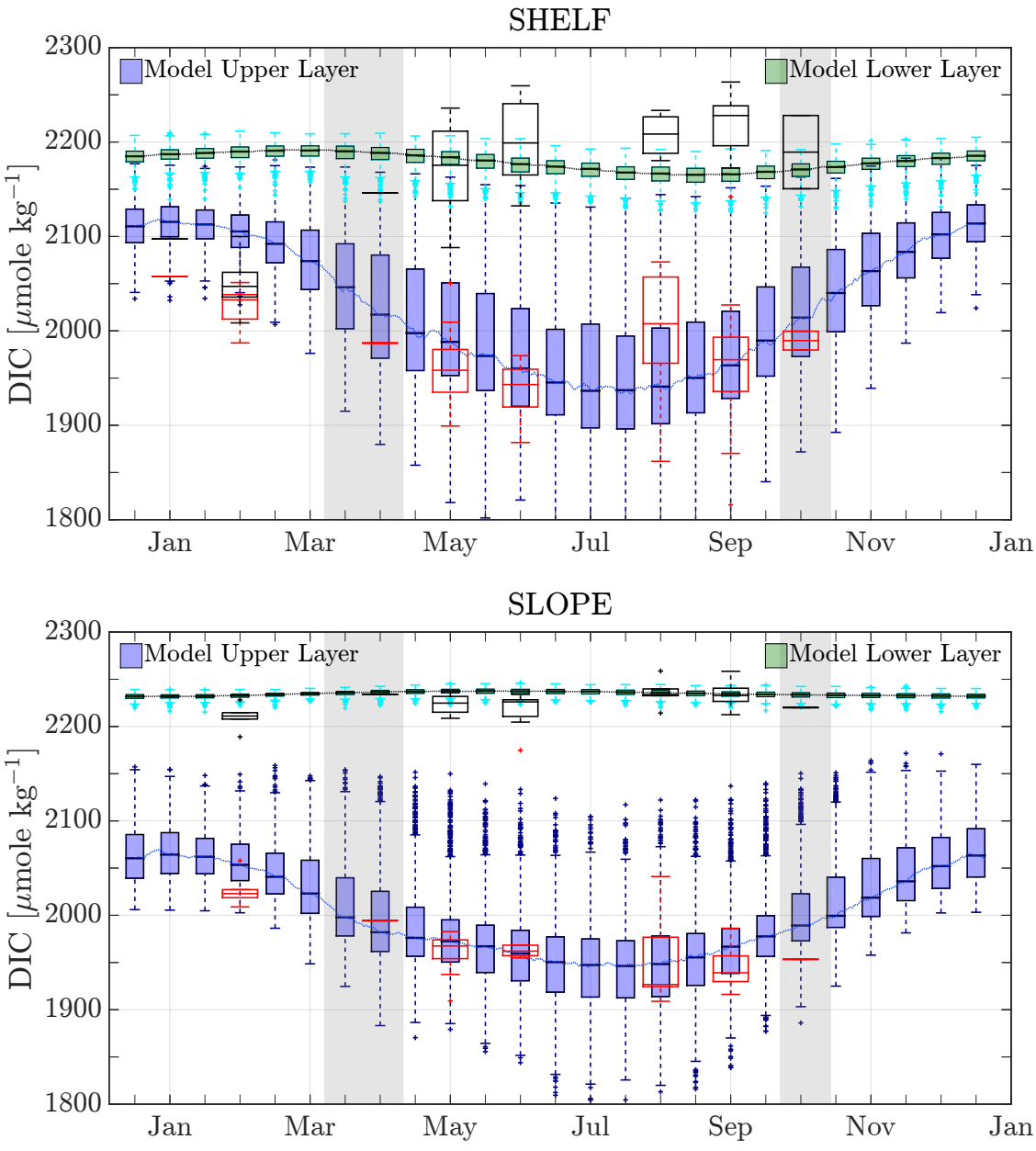

Figure 3.8: Same as Figure 3.7 but for DIC.

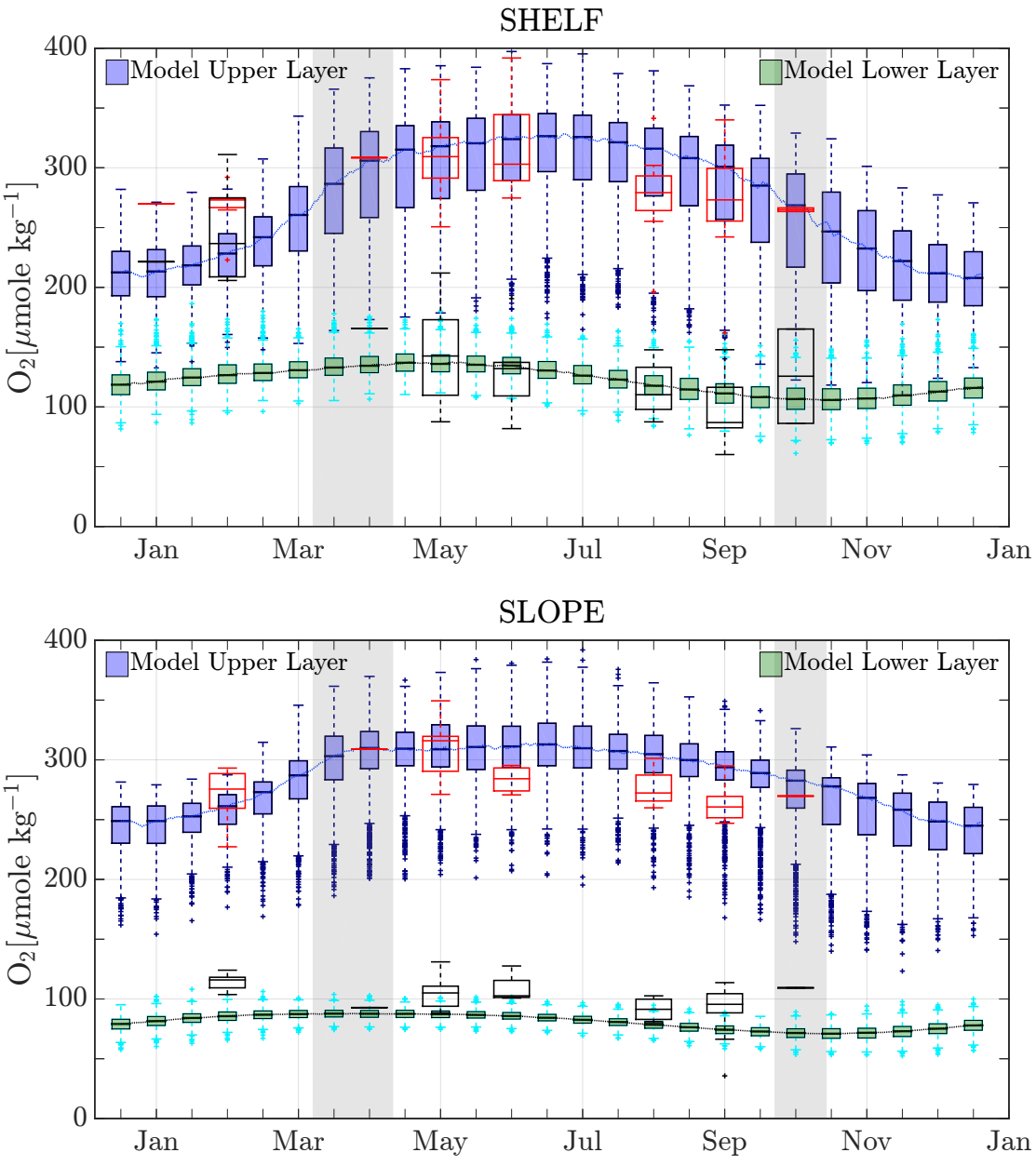

Figure 3.9: Same as Figure 3.7 but for oxygen.

Month	# of years available			# of profiles			depth and spatial averages			stdev. across years		
	DIN	DIC	O_2	DIN	DIC	O_2	DIN	DIC	O_2	DIN	DIC	O_2
1	1	1	1	1	1	1	14.59	2057.51	270.05	0.00	0.00	0.00
2	7	7	7	9	8	9	12.05	2025.78	267.66	6.89	21.57	21.38
3	0	0	0	0	0	0	-	-	-	-	-	-
4	1	1	1	3	1	1	3.77	1987.06	308.46	0.00	0.00	0.00
5	11	13	13	31	43	41	3.02	1961.56	311.53	3.05	40.73	32.12
6	5	6	7	6	10	11	1.08	1936.75	318.88	1.21	33.79	40.96
7	0	0	0	0	0	0	-	-	-	-	-	-
8	6	7	8	9	14	18	8.40	2301.26	276.38	6.94	840.72	41.17
9	9	13	13	18	37	38	10.06	1965.62	279.04	8.63	77.48	58.47
10	2	2	2	5	4	4	8.26	1989.66	264.96	4.99	14.09	2.15
1	1	1	1	1	1	1	24.30	2097.66	221.40	0.00	0.00	0.00
2	7	5	5	7	5	5	13.35	2049.97	245.21	7.51	32.63	43.40
3	0	0	0	0	0	0	-	-	-	-	-	-
4	1	1	1	3	1	1	22.54	2145.91	165.56	0.00	0.00	0.00
5	10	13	13	33	42	42	26.09	2171.22	143.66	4.56	47.01	39.31
6	4	6	6	7	8	7	26.87	2199.28	130.48	4.03	47.59	36.11
7	0	0	0	0	0	0	-	-	-	-	-	-
8	6	6	6	13	15	17	30.85	2207.57	114.46	2.78	20.98	23.02
9	8	12	12	21	36	36	31.39	2220.95	97.05	3.40	30.61	27.42
10	2	2	2	5	4	4	20.90	2189.32	125.69	3.51	54.86	55.78
1	0	0	0	0	0	0	-	-	-	-	-	-
2	8	6	5	10	6	5	10.16	2026.44	270.63	5.38	16.64	25.86
3	1	0	0	1	0	0	5.12	-	-	0.00	-	-
4	1	1	1	11	2	1	5.06	1994.27	308.90	0.00	0.00	0.00
5	13	15	13	34	62	48	0.63	1960.93	307.01	0.72	19.34	21.42
6	6	6	4	9	8	6	4.13	1996.56	283.62	7.68	87.45	11.54
7	0	0	0	0	0	0	-	-	-	-	-	-
8	7	7	4	13	10	8	2.62	1951.35	276.45	2.90	46.86	17.60
9	12	15	15	26	66	56	5.08	1944.51	262.35	6.41	19.86	12.84
10	2	1	1	5	1	1	1.08	1953.37	269.70	0.13	0.00	0.00
1	0	0	0	0	0	0	-	-	-	-	-	-
2	7	6	5	8	6	5	25.62	2210.27	114.22	11.20	12.63	7.48
3	1	0	0	1	0	0	6.36	-	-	0.00	-	-
4	1	1	1	11	2	1	27.46	2233.76	92.82	0.00	0.00	0.00
5	14	15	13	38	63	48	33.18	2223.81	105.17	1.72	9.54	12.51
6	4	7	4	7	9	6	32.01	2220.98	108.43	3.03	11.04	12.83
7	0	0	0	0	0	0	-	-	-	-	-	-
8	4	6	3	9	10	7	32.86	2235.47	91.38	2.55	14.35	11.27
9	14	15	15	32	69	57	32.54	2233.16	92.22	3.87	12.65	19.62
10	2	1	1	4	1	1	28.11	2219.98	109.33	6.30	0.00	0.00

Table 3.3: Statistics of observed data used to compare with model results (Figures 3.7, 3.8 & 3.9). From top, the first and second set of 10 rows are for the upper and lower shelf region, respectively. The third and last set of 10 rows are for the upper and lower slope region, respectively.

late summer, the interannual variability in the observations is larger than in the modelled DIN, but the differences are still within an acceptable range considering the extra variance introduced into the observations by the multiple profiles included from multiple stations. In January, not many DIN profiles are available on the shelf. The biannual La Perouse cruise, which runs every spring and late summer/early fall, covers a wider area of the shelf and provides observational data from several stations. As a result, the model observation comparisons are more meaningful in the spring and summer seasons.

The model median DIN in the upper slope shows a similar seasonal progression as in the upper shelf with main difference that the values are smaller. During the upwelling season, the median values are nearly zero although the individual DIN values can reach as high as 20μM. The reason for the low median DIN values over the upper slope is that the upwelled water, has lost much of its nutrients by the time it reaches the slope region, mainly through biological uptake. In terms of the seasonal cycle, both the model and observations show higher DIN in the winter downwelling season and lower in the summer upwelling season. Unlike the upper shelf, the upper slope model DIN compares well with observations in all seasons.

The modelled DIN in the lower layer, especially over the slope, shows a much weaker seasonal cycle. The lower shelf median value stays around 30μM for much of the winter season and becomes slightly lower during spring and summer. This reduction results from biological uptake in the upper layer. This nutrient depleted water is mixed downward by vertical mixing. Generally, there is good agreement between modelled and observed DIN in the upper layers. In the lower layers the comparison was not as good as in the upper layers for only a couple of months.

DIC

Similar to DIN, the model upper shelf median DIC reaches its maximum during the winter months and gradually declines towards the spring season (Figure 3.8). Increased biological uptake, driven by increased availability of nutrients and sunlight,

causes further depletion of DIC from the upper layer until about mid-to-late July. By then, the median DIC becomes about 100 μmole kg^{-1} lower than the wintertime maximum. Although upwelling may continue until mid-October, the median DIC starts to increase around late August due to vertical mixing, the remineralization of a larger volume of organic matter and a decrease in biological uptake of DIC. After September the rate of increase becomes even faster. DIC uptake in the upper layer is limited by either light or nitrate (DIN). Towards the end of the upwelling season upper layer DIN is large enough to not limit DIC uptake, but light becomes a limiting factor due to reduced intensity at this time of the year in the study region. Throughout the year the upper shelf model and observed data (open red box plots) agree well. The upper slope DIC shows a similar seasonal cycle as in the upper shelf and the agreement with data is satisfactory.

With regard to the median values, the lower shelf modelled DIC is slightly lower than 2200 μmole kg^{-1} and shows little change with season. The observed median DIN also lingers around the value 2200 μmole kg^{-1} except in February when the value is lower. In the lower slope there is almost a constant DIC median value of about 2240 μmole kg^{-1} throughout the year. The model-observation agreement here is even better than in the lower shelf region. In contrast to the modelled DIC, there are almost no outliers in the observed DIC (likely because of depth averaging).

Oxygen

In the upper shelf, median oxygen increases starting from early March and reaches its peak in early June as a result of primary production (Figure 3.9). The lower shelf shows a similar increase as the upper shelf, due to vertical mixing. Unlike DIC, the oxygen budget in the upper layers are strongly affected by air-sea gas fluxes (Figure 3.10). These fluxes are controlled by physical mechanisms influencing oxygen saturation, which is a function of temperature and salinity. The temperature, a greater control on the gas fluxes than salinity, is not warm enough in the spring to cause a strong out-gassing. This small temperature effect is offset by increased O_2

production and lack of large organic matter pool to be remineralized. Progressing into the middle of summer, oxygen levels start to decline in response to both warmer temperatures (enhancing out-gassing) and increased levels of respiration. The slope region shows slightly weaker O_2 seasonal cycles and interannual variability, especially in the lower layer. Although slightly poorer relative to the shelf region, the model-observational data agreement in the slope region generally remains good. One notable difference between the upper shelf and slope modelled O_2 results is the number of outliers (most of which qualify for my definitions of extremes in subsequent sections). In the upper shelf they are found between May and September, but they are found throughout the year in the upper slope. In both regions the pronounced outliers exist as the lowest values.

Despite the low level of complexity of the model, where data are available the model and observation values are generally in good agreement. The model is able to capture both the seasonal cycles and interannual variability of DIN, DIC and O_2 when appropriately varying physical forcing is used.

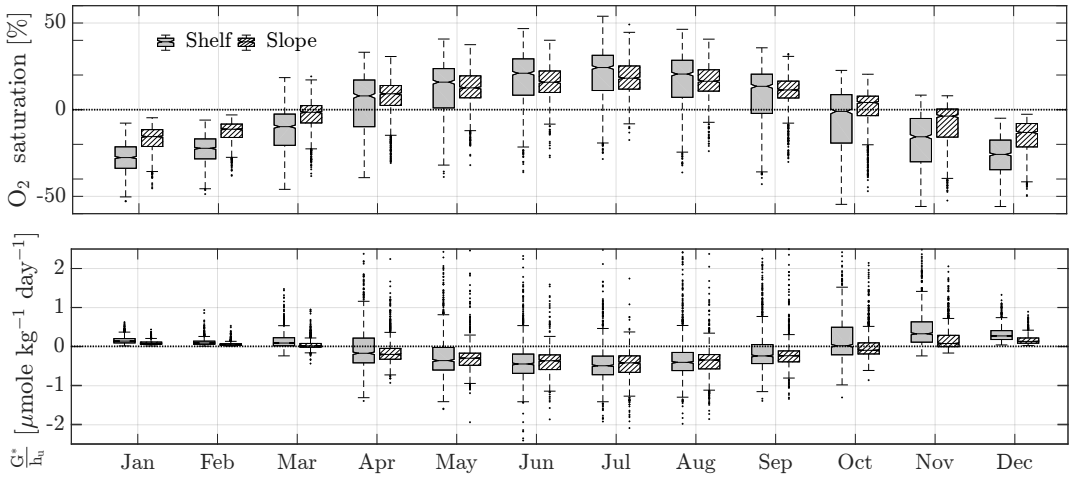

Figure 3.10: Top: Model oxygen percent saturation , $(\frac{O_2}{O_{2sat}} - 1) \times 100\%$, in the surface layer. Bottom: Model O_2 gas flux contributions to the upper layers' O_2 tendency (Equation 3.7). G^* and h_u are as described in the main text. Solid box-plots are for shelf and hatched ones for slope. The box-plots represent all the daily values centered at each month. All of the (present-day) 1017 year base run realizations used.

Chapter 4

Extreme Dissolved Inorganic Carbon and Oxygen on the Continental Margin of Southern Vancouver Island

4.1 Introduction

The previous chapter introduced the model used to study carbon and oxygen extremes and presented the model climatology. The following questions will be addressed in this chapter.

- What are the timing and frequency of occurrence of DIC and O_2 extreme events in the study region?
- Are DIC and O_2 extreme events similar in terms of their timing and frequency of occurrence?
- What mechanisms drive timing and frequency of occurrence of DIC and O_2 extreme events?

To answer the above questions I use the long model simulation, obtained by using the stochastically generated forcing, to calculate robust statistics regarding the present day system. This analysis identifies drivers of extreme events. Although this analysis is focused on the present climate, it provides insight about possible changes in DIC and oxygen extreme events in the study region in the future. Extremes will be defined by the upwelling season 95^{th} percentile of DIC and 5^{th} percentile of O_2.

The main statistical techniques applied to the model generated data include exeedance probabilities and return periods of extremes, conditional cumulative distribution functions, and the fraction of days with individual and joint extreme events of carbon and oxygen. Unless otherwise stated, the data analyzed in this chapter are obtained from the baseline model run.

Short Summary

The application of stochastically-generated, daily-resolution, long-record model forcing enabled the estimation of robust statistics on DIC and O_2 extremes. The following key results were found:

1. In the upper mixed layer O_2 extreme events occur more frequently than DIC extreme events.

2. Oxygen and DIC extreme events show a much larger interannual variability in the lower layer than in the upper layer.

3. Physical processes control O_2 and DIC extreme events mainly in the upper layers, while biological processes are more important in subsurface layers.

4. Early season intense upwelling leads to late season O_2 extreme events in the lower layer.

5. Joint DIC – O_2 extreme events are rare in the summer upwelling season. These joint extreme events are more rare than the marginal probability distributions of DIC and O_2 would suggest.

4.2 Data and Methods

In order to study the potential for and frequency of DIC and O_2 extremes in any particular region of the model, I calculated the individual probability of exceedance and return period (the inverse of the frequency of exceedance of a pre-defined value).

The probability of exceedance at a given time gives the likelihoods of upcrossing a threshold at least once over a given time. It does not specify for how long the random process have had values above (below in the case of oxygen) the threshold. Nor does it specify the highest value above the threshold for a given time interval. For a stationary Gaussian random process, the number of upcrossing of a threshold is given by Rice's Equation (Rice, 1945). After defining the thresholds for extremes of DIC and O_2, I apply Rice's equation to estimate both the probability of exceedance and return periods relevant to the model results.

Model DIC extremes for any model run are defined as DIC values larger than the overall 95$^{\text{th}}$ percentile of DIC for that model run. For model O_2 extremes I use values smaller than the overall 5$^{\text{th}}$ percentile O_2 of the model run. The symbols $q_{95(DIC)}$ and $q_{05(O_2)}$ are used for these percentiles. The same quantile definitions will be used whether I focus on the full year or a subset (season) of the model results; the meaning will be clear from context.

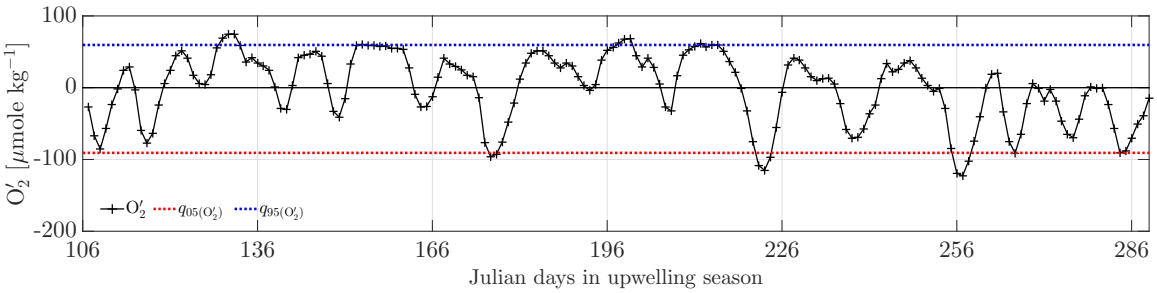

Figure 4.1: A) Time series of mean (298.3 μmole kg^{-1}, Table 4.1) removed model oxygen (O_2') in the upper shelf of a randomly selected upwelling season. The 5$^{\text{th}}$ ($q_{05(O_2')}$) and 95$^{\text{th}}$ ($q_{95(O_2')}$) percentiles of the mean removed oxygen from the baseline model run are shown in dashed red and blue lines, respectively. Upwelling season is considered to be the time period from mid-April through mid-October (Thomson et al., 2014). The absolute values of $q_{05(O_2')}$ for each model box is given in Table 4.1.

I focus on the upwelling season, as DIC and O_2 extremes are relatively more common around this season (cf., Figure 3.8). In the following I describe the calculations of the exceedance probabilities and return periods of extremes using $q_{95(DIC)}$. Probabilities of down-crossings are obtained using the same calculations as the $q_{95(DIC)}$ exceedance to O_2 multiplied by -1. That is, I calculate the exceedance probability of the sign changed 95^{th} percentile of O_2.

If the time series of the O_2 or DIC had a zero auto-correlation, the frequencies of exceedance of a quantile threshold would be determined by a Bernoulli process and the return period would simply be defined by the compliment of the quantile threshold. For example, for a sample size of 100 there will be on average 5 peaks above the 95^{th} percentile threshold. The number of threshold crossings may differ from the number of local maxima above the threshold if the time series does not cross the threshold between successive peaks. The threshold upcrossing is usually a good approximation to the number of peaks above the threshold for a Gaussian process where the threshold is at least twice larger than the standard deviation of the Gaussian process (Hoblit, 1988). I consider moderately large thresholds (95^{th} for DIC and 5^{th} percentiles for O_2) which satisfy this criterion. I have defined the exceedance probabilities in terms of internally-defined quantile thresholds rather than physically or biologically determined absolute thresholds. This definition facilitates comparison of results among the model regions.

The DIC and O_2 time series I consider are serially dependent and I do not expect the number of crossings to approximate the number of data points across the threshold. For example, in Figure 4.1 there are 5 occasions the oxygen values fall below the 5^{th} percentile of O_2, but the total count of data points below this threshold is 9 ($\sim$4.9% of the total 183 points, close to the expected value of 5%). The frequency of threshold crossing can change with time as will be clear from the results when using individual seasons to calculate exceedance probabilities and return periods. This difference in exceedance probabilities and return periods gives a sense for variations in these statistics. The statistics computed from a small number of data points such

as from one season are otherwise misleading and illustrate the value of using long records for such calculations (either observational or model-based)

Table 4.1: The 5^{th} O_2 and 95^{th} DIC percentiles of the baseline run for upwelling season only. The first column under O_2 and DIC is the percentiles computed from mean removed (note that these are the values used in exceedance probability calculations of the mean removed O_2 and DIC. Also note that the absolutes values are given for $q_{05(O_2')}$). The second column under O_2 and DIC contains the percentiles computed from the mean retained values in the upwelling season. The last column under O_2 and DIC is the mean of the O_2 and DIC values computed from the (present-day) 1017 upwelling seasons. All units are μmole kg^{-1}.

Region	O_2			DIC		
	$\lvert q_{05(O_2')} \rvert$	$q_{05(O_2)}$	$\overline{O_2}$	$q_{95(DIC')}$	$q_{95(DIC)}$	$\overline{DIC}$
Upper shelf	92.35	205.49	298.30	125.62	1978.93	2106.39
Lower shelf	24.49	97.49	124.94	19.70	2172.49	2193.30
Upper slope	55.61	245.07	301.52	97.81	1966.71	2066.80
Lower slope	10.84	68.79	81.27	4.03	2235.91	2241.30

DIC and O_2 thresholds for calculating exceedance probabilities for the upwelling seasons are given in Table 4.1. Since exceeding the anomaly based percentiles ($q_{05(O_2')}$ and $q_{95(DIC')}$) by the anomaly (O_2' and DIC') timeseries is the same as exceeding the percentiles ($q_{05(O_2)}$ and $q_{95(DIC)}$) of the mean retained values by (O_2 and DIC), I will drop the apostrophe in referring to the percentiles and DIC and O_2 throughout this section.

The model results are prepared to be used in calculating exceedance probabilities and return periods as follows. First, I removed the annual cycle from each of the (present-day) 1017 years of model timeseries and sub-sampled the data to the upwelling seasons. Then I computed the power spectral density, $\Phi_{DIC}(f)$, of DIC for each upwelling season to be used in Equation 4.2 using the multitaper method of Thomson (1982). Following Rice (1945) and Hoblit (1988), I define the frequency of

exceeding $q_{95(DIC)}$ as,

$$N(q_{95(DIC)}) = N_0 e^{-\frac{1}{2}(\frac{q_{95(DIC)}}{\sigma_{DIC}})^2} \tag{4.1}$$

$$\text{where, } N_0 = \sqrt{\frac{\sum_{k=1}^{n} f_k^2 \Phi_{DIC}(f_k)}{\sum_{k=1}^{n} \Phi_{DIC}(f_k)}} \tag{4.2}$$

is the upcrossing frequency of the zero line (Rice, 1945; Hoblit, 1988). The standard deviation σ_{DIC} is calculated from the same data used to compute $q_{95(DIC)}$. Since the number of times $q_{95(DIC)}$ is exceeded increases with time as a Poisson process,

$$P(t) = \frac{(-N(q_{95(DIC)})t)^r}{r!} e^{-N(q_{95(DIC)})t} \tag{4.3}$$

where r is the number of times the exceedance has occurred, the probability that there was no exceedance (r=0) at a given time, t, is given by $e^{-N(q_{95(DIC)})t}$ (Feller, 1966). Hence, the probability that exceedance has occurred at least once at time, t, is

$$P^{ex}_{q_{95(DIC)}}(t) = 1 - e^{-N(q_{95(DIC)})t} \tag{4.4}$$

The mean time between threshold crossings ($> q_{95(DIC)}$) called the return period, ($\tau^{ret}_{q_{95(DIC)}}$), is the inverse of the frequency of exceedance

$$\tau^{ret}_{q_{95(DIC)}} = \frac{1}{N(q_{95(DIC)})} \tag{4.5}$$

The same calculations were used to find the exceedance probability ($P^{ex}_{q_{05(O_2)}}(t)$), and return period ($\tau^{ret}_{q_{05(O_2)}}$)

The exceedance probability can also be thought of as the equivalent of the fraction of times, over a long sample duration, a threshold is crossed. By definition values above the 95^{th} percentile occur $1/20^{th}$ of the time. For uncorrelated daily data, a 95^{th} or 5^{th} percentile threshold crossing should occur on average once every 20 days.

The relationship between threshold crossing frequency and quantiles is less clear for serially correlated time series. For a fixed quantile threshold, more frequent crossings imply a shorter duration of events. For example, if there were 5 threshold crossings in a 100 daily data points, the average duration of each event will be 1 day. On the other hand, for a serially correlated data the probability increases of a smaller number of longer events: for example, of a single threshold crossing of 5 days. A further factor to consider is that in my calculations the thresholds are defined based on the quantiles of all upwelling seasons of the baseline run (Table 4.1). For the upwelling seasons of individual years, since the threshold is still a globally defined quantile, there may not be any points across this threshold throughout the season. However, even if there are not any points above this threshold, the computed waiting time distribution indicates how long one would have to wait before a crossing would occur. The waiting time in this case could be longer than the length of a season. Conversely, in an individual season there may be more than 5% of all the data points in a given season across the globally defined threshold.

4.3 Results

4.3.1 Exceedance Probability

The exceedance probability curves for data from each upwelling season individually and all upwelling seasons together are shown in Figure 4.2 (DIC) and 4.3 (O_2). The exceedance probabilities show a strong interannual variability in all the four model boxes. The exceedance probability calculated using all the upwelling seasons together is shown using thick black curves in Figure 4.2. Individual years with lower than the long-term value $P^{ex}_{q_{95(DIC)}}$ are associated with a substantially reduced likelihood of relatively high DIC events. On the other hand, those years showing higher $P^{ex}_{q_{95(DIC)}}$ than the all-year exceedance probabilities are associated with years of elevated probability of relatively high DIC events.

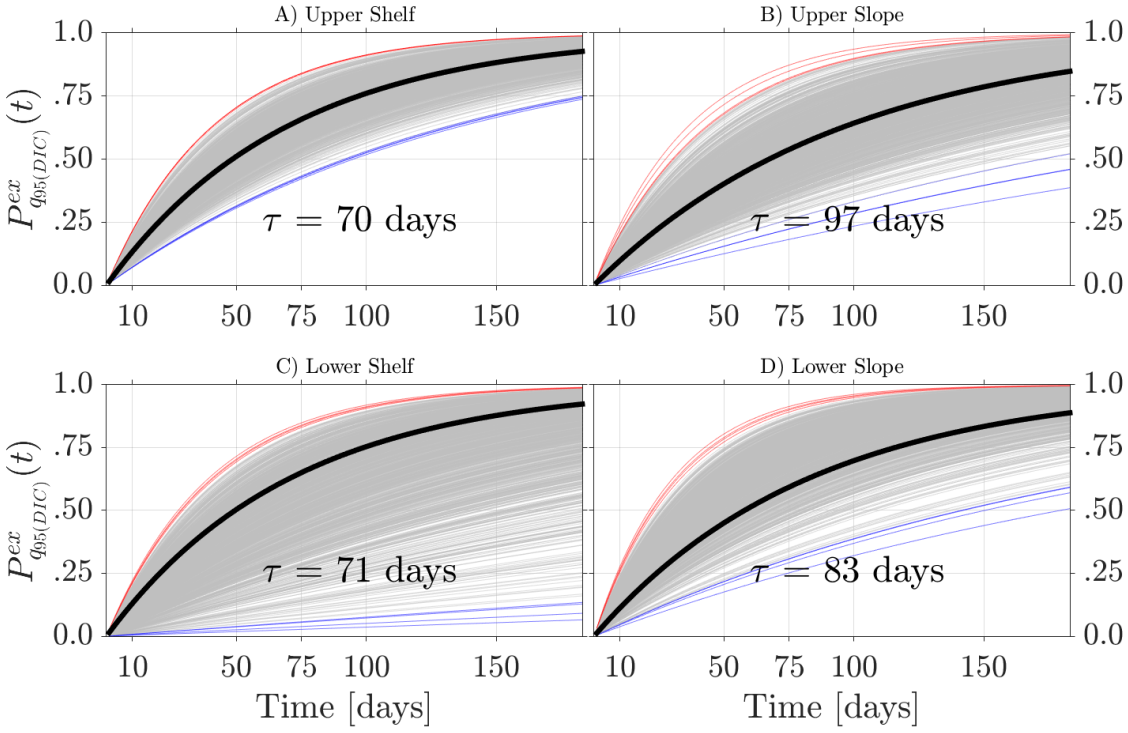

Figure 4.2: A) The exceedance probability, $P^{ex}_{q_{95(DIC)}}$, for the upper shelf. B), C) and D) are the same as A) but for the upper slope; lower shelf; and lower slope. The heavy line in each panel shows the exceedance probabilities computed from all the upwelling seasons. The return period, $\tau^{ret}_{q_{95(DIC)}}$, for each of these curves is shown in these figures. Each light grey curve represents $P^{ex}_{q_{95(DIC)}}$ of a single upwelling season. Seasons with the four shortest and four longest return periods, whose $P^{ex}_{q_{95(DIC)}}$ highlighted in red and blue respectively will be used to investigate the timeseries of DIC.

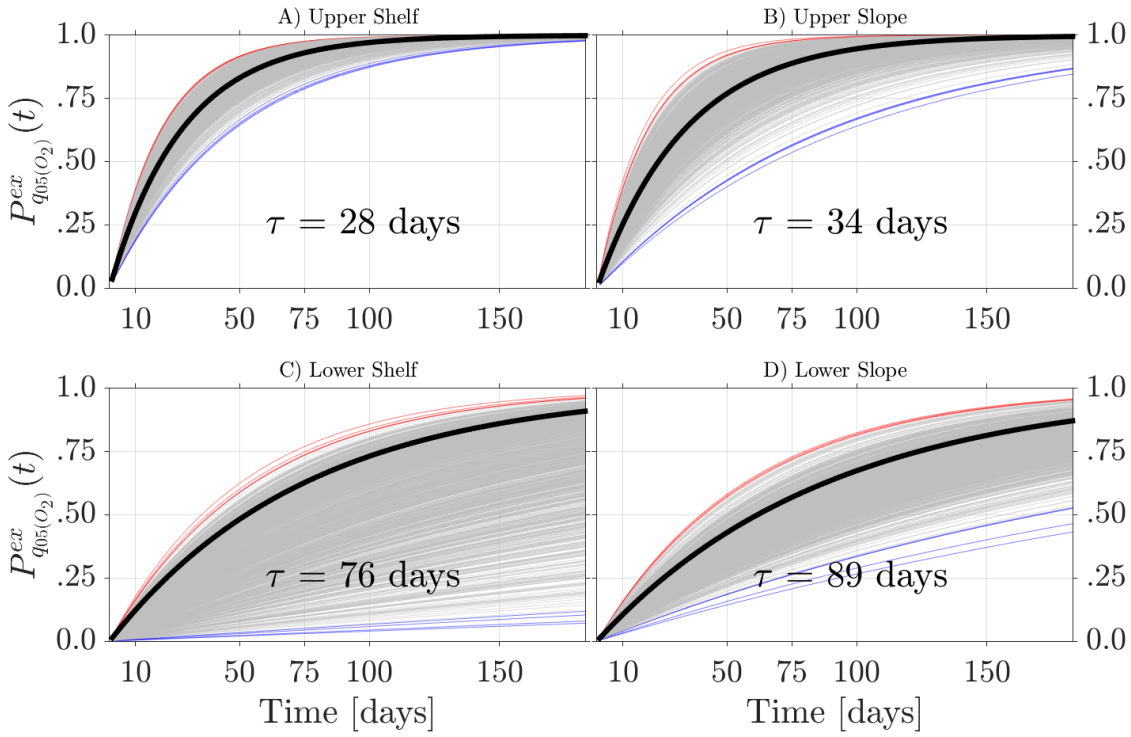

Figure 4.3: A) The exceedance probability, $P^{ex}_{q_{05(O_2)}}$, for the upper shelf. B), C) and D) are the same as A) but for the upper slope; lower shelf; and lower slope. The heavy line in each panel shows the exceedance probabilities computed from all the upwelling seasons. The return period, $\tau^{ret}_{q_{05(O_2)}}$, for each of these curves is shown in these figures. Each light grey curve represents $P^{ex}_{q_{05(O_2)}}$ of a single upwelling season. Seasons with the four shortest and four longest return periods, whose $P^{ex}_{q_{05(O_2)}}$ highlighted in red and blue respectively will be used to investigate the timeseries of O_2.

The $P^{ex}_{q05(O_2)}$ in each of the upwelling seasons and the $P^{ex}_{q05(O_2)}$ calculated from the overall upwelling time series (heavy black curves) are shown in Figure 4.3. Similar to $P^{ex}_{q95(DIC)}$, there is a strong interannual variability of $P^{ex}_{q05(O_2)}$. The $P^{ex}_{q95(DIC)}$ curves in the upper shelf $P^{ex}_{q05(O_2)}$ show the least spread, and those in the lower shelf show the largest spread. A more quantitative discussion of the similarities and differences among these curves is presented in terms of return periods in the next subsection.

4.3.2 Return periods

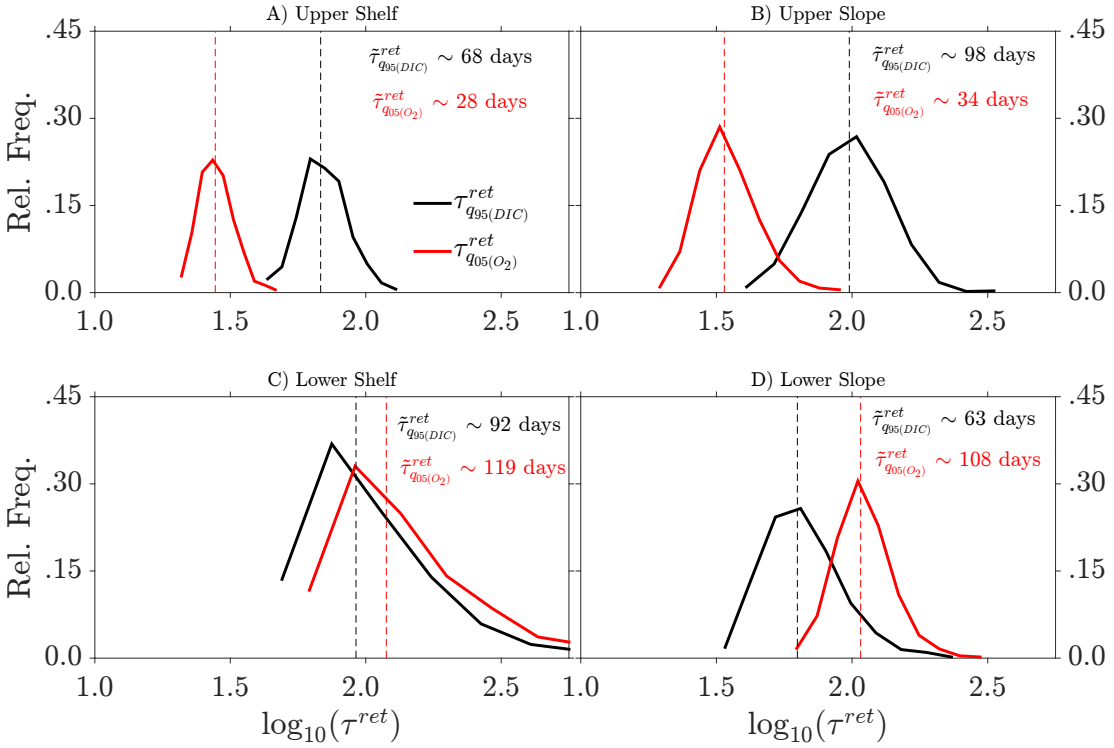

Figure 4.4: Relative frequencies of return periods. The median values of return periods $\tilde{\tau}^{ret}_{q95(DIC)}$ and $\tilde{\tau}^{ret}_{q05(O_2)}$ for each model region are shown in the corresponding panels (The vertical lines in the same color as these curves also show where the medians are).

The $\tau^{ret}_{q95(DIC)}$ distributions, except in the lower shelf, are near log-normal with median values of 68, 98, 92, and 63 days for upper shelf, upper slope, lower shelf, and lower slope, respectively (Figure 4.4). The most robust $\tau^{ret}_{q95(DIC)}$ values are obtained

from the exceedance probabilities calculated based on the entire (present-day) 1017 upwelling seasons record (heavy black curves in Figure 4.2). The values are 70, 97, 71, and 83 days for upper shelf, upper slope, lower shelf, and lower slope respectively. These values are almost the same as the medians of individual season $\tau^{ret}_{q95(DIC)}$ values. In the lower shelf the $\tilde{\tau}^{ret}_{q_{95(DIC)}}$ is 21 days longer than the all-year derived return period (Figure 4.2), but the lower slope $\tilde{\tau}^{ret}_{q_{95(DIC)}}$ is 20 days shorter.

Comparison of the full record derived $\tau^{ret}_{q95(DIC)}$ values from the different regions shows there is only a very small difference in the frequency of DIC threshold crossings between the upper and lower shelf (Figure 4.2). In the slope region, the upper layer $\tau^{ret}_{q95(DIC)}$ is about two weeks longer than the lower layer $\tau^{ret}_{q95(DIC)}$. The $\tau^{ret}_{q95(DIC)}$ values indicate the shelf region generally experiences more frequent threshold crossings than does the slope. Because of the way the threshold is defined the more frequent extreme events have shorter duration than less frequent events. For DIC it is not clear how long the duration of extreme events needs to be to have impact on organisms. However, oxygen extreme events of even a day or two could be problematic for individual organisms or an ecosystem as a whole.

Similar to $\tau^{ret}_{q95(DIC)}$, the $\tau^{ret}_{q05(O_2)}$ shows a near log-normal distribution with median, $\tilde{\tau}^{ret}_{q_{05(O_2)}}$, values of 28, 34, 119, and 108 days for the upper shelf, upper slope, lower shelf, and lower slope, respectively (Figure 4.4). In the upper layers these values are close to those $\tau^{ret}_{q05(O_2)}$ values calculated from the overall time series (Figure 4.3). In the lower layers, the $\tilde{\tau}^{ret}_{q_{05(O_2)}}$ values are 2 – 4 weeks larger than values calculated from the overall time series. Oxygen threshold crossings are more frequent in the shelf than in the slope region, as suggested by the return periods (Figure 4.3). The upper layers show substantially more frequent oxygen threshold crossings than the lower layers.

Comparing the return periods of DIC and O_2 extremes, based on full record calculations, indicates the upper layer O_2 threshold crossings are more than twice as frequent as DIC threshold crossings. In the lower layers O_2 threshold crossings occur at a slightly lower rate than do the DIC threshold crossings (Figures 4.2, 4.3). These results and return period distributions in Figure 4.4 indicate that carbon and O_2 ex-

treme events are not fully coupled in the upper layers. This behaviour is most likely due to physical processes, whose impact on either of these extreme events can be different, being more important the upper layer. In the lower layers, where biological processes dominate DIC and O_2 extremes, the evidence indicates stronger coupling. Based on the interquartile ranges (IQR) of the return period distributions, the upper layer DIC return periods are more variable than are the O_2 return periods (Table 4.2). In the lower layers, the opposite is true.

Region	$\tilde{\tau}^{ret}_{q_{95(DIC)}}$		$\tilde{\tau}^{ret}_{q_{05(O_2)}}$	
	Median	IQR	Median	IQR
Upper shelf	68	19	28	6
Upper slope	98	45	34	11
Lower shelf	92	69	119	96
Lower slope	63	28	108	34

Table 4.2: The median and interquartile range (IQR) of return periods (in units of days) of extreme DIC and O_2 events.

4.3.3 Composites of net upwelling forcing

In order to investigate the effects of interannual variability of the net upwelling forcing (W) on the return periods discussed above, for each of DIC and O_2 I consider two sets of four upwelling season W time series normalized by their globally defined standard deviation. The first set corresponds to the four upwelling seasons with the shortest return periods (red $P^{ex}_{q_{95(DIC)}}$ and $P^{ex}_{q_{05(O_2)}}$ curves in Figures 4.2 and 4.3), and the second corresponds to the longest return periods (blue $P^{ex}_{q_{95(DIC)}}$ and $P^{ex}_{q_{05(O_2)}}$ curves in Figures 4.2 and 4.3). The goal is to investigate how W impacts return periods of O_2 and DIC extremes.

Because the individual upwelling seasons are selected separately for each box, the set of W or $\frac{W}{\sigma_W}$ is unique to each model box. In Figures 4.5 – 4.8. I show three day running mean smoothed model variables (O_2 and DIC) and $\frac{W}{\sigma_W}$. As expected most values of W lie with in 1 standard deviation from the mean. In the upper shelf and slope there are not substantial qualitative differences between the normalized

upwelling velocities between the large-τ and small-τ sets (solid dark curves in Figures 4.5 and 4.7, results for slope not shown). In both sets of seasons there is a clear upwelling response where DIC maxima and O_2 minima follow $\frac{W}{\sigma_W}$ maxima after about two days. Similarly, DIC minima and O_2 maxima follow $\frac{W}{\sigma_W}$ minima. Given the relatively narrow distributions of $\tau^{ret}_{q_{95(DIC)}}$ and $\tau^{ret}_{q_{05(O_2)}}$ in the upper layers (Figure 4.4), it is not surprising that the $\frac{W}{\sigma_W}$, the DIC and O_2 are not substantially different between the two sets of upwelling seasons.

Unlike the upper layers, in the lower layers there is a strong difference between the wind patterns ($\frac{W}{\sigma_W}$) in the two sets. The values of $\frac{W}{\sigma_W}$ corresponding to short return period seasons in the lower shelf are generally larger than those corresponding to the long return periods (Figures 4.6 and 4.8). Short $\tau^{ret}_{q_{95(DIC)}}$ seasons usually start with high amount of DIC and exhibit frequent threshold crossing early in the season.

The difference in lower shelf DIC between the two sets of upwelling seasons increases as the season progresses (Figure 4.6). This feature is mainly because in the long $\tau^{ret}_{q_{95(DIC)}}$ seasons DIC remains stable due in part to the nearly uniform $\frac{W}{\sigma_W}$ throughout the season. In the short $\tau^{ret}_{q_{95(DIC)}}$ seasons, the $\frac{W}{\sigma_W}$ amplitude is larger and more variable with time. The strong upwelling early in the season is strong enough to drag high DIC water from the lower slope region, thereby causing the threshold crossing in the lower shelf early in the season. Late in the upwelling season individual downwelling events become more important to the lower layer DIC budget because (a) it flushes the lower layer with lower DIC water from above and (b) at this time the lower layers have weak horizontal gradient of DIC between them. This weak gradient is not strong enough to result in changes in the lower shelf DIC when occasional upwelling brings water from outside. The relatively strong frequent downwelling in the later half of the upwelling season in short $\tau^{ret}_{q_{95(DIC)}}$ seasons decreases the DIC by offsetting the DIC increase from organic carbon downward export and the subsequent reminiralization to DIC (Figure 4.6). These interactions between the physics and biology will be discussed again in Chapter 5.

The time evolution of $\frac{W}{\sigma_W}$ associated with the short $\tau^{ret}_{q_{05(O_2)}}$ seasons in the lower

shelf (Figure 4.8) and slope (not shown) is such that the number of strong upwelling events is larger in the earlier part of the season than in the late part. The normalized upwelling $\frac{W}{\sigma_W}$ behaves oppositely in the long $\tau^{ret}_{q_{05(O_2)}}$ seasons. The strong early upwelling causes higher O_2 production in the upper layers. Then, vertical mixing and the occasional downwelling increase the lower layer O_2. Once the upwelling weakens, the physically maintained lower layer O_2 starts to decline as high organic matter fall out from the upper layer continues. At some point in time (usually the second half of the upwelling season) oxygen loss to reminiralization becomes a dominant factor to the lower layer O_2.

Weak early season upwelling followed by strong late season upwelling tends to maintain relatively high O_2 in the lower layer. Early in the upwelling season there is little organic matter export due to lack of primary production. Later in the upwelling season vertical mixing and the occasional downwelling of O_2 produced, as a result of the strong late season upwelling, maintains the lower layer O_2 from falling (Eg., 4.8). As expected from the very low values of $P^{ex}_{q_{05(O_2)}}$ (Blue curves in Figures 4.3C and D) in all the four selected long $\tau^{ret}_{q_{05(O_2)}}$ seasons there was no O_2 threshold crossing (Eg., 4.8).

	Short $\tau^{ret}_{q_{95(DIC)}}$				Long $\tau^{ret}_{q_{95(DIC)}}$				Short $\tau^{ret}_{q_{05(O_2)}}$				Long $\tau^{ret}_{q_{05(O_2)}}$			
Region	$\widetilde{W^+}$	$\widetilde{W^-}$	σ_{W+}	σ_{W-}	$\widetilde{W^+}$	$\widetilde{W^-}$	σ_{W+}	σ_{W-}	$\widetilde{W^+}$	$\widetilde{W^-}$	σ_{W+}	σ_{W-}	$\widetilde{W^+}$	$\widetilde{W^-}$	σ_{W+}	σ_{W-}
Upper shelf	13	-9	2	1	14	-9	2	1	14	-8	2	1	14	-9	2	2
Upper slope	12	-8	2	1	15	-9	2	1	14	-9	2	1	13	-9	2	1
Lower shelf	18	-11	2	1	12	-8	1	1	14	-8	2	2	15	-9	2	1
Lower slope	14	-9	2	1	16	-10	2	1	15	-9	2	1	15	-9	2	1

Table 4.3: Summary statistics for PDF curves shown in Figure 4.9: The median and standard deviations of the 95th percentiles of upwelling velocities (in units of m d^{-1}) from selected 50 upwelling seasons. The selection is based on the lengths of return periods of DIC and O_2 thresholds, $q_{95(DIC)}$ & $q_{05(O_2)}$ respectively. The median and standard deviations are rounded to the nearest integer.

As a final analysis of the relationships between the exceedance probabilities and the upwelling forcing in all the four model regions, I consider the probability distributions of the 95th percentiles of the upwelling ($q_{95(W^+)}$) and downwelling ($q_{95(W^-)}$) strengths from seasons with the shortest and longest fifty return periods (Figure 4.9).

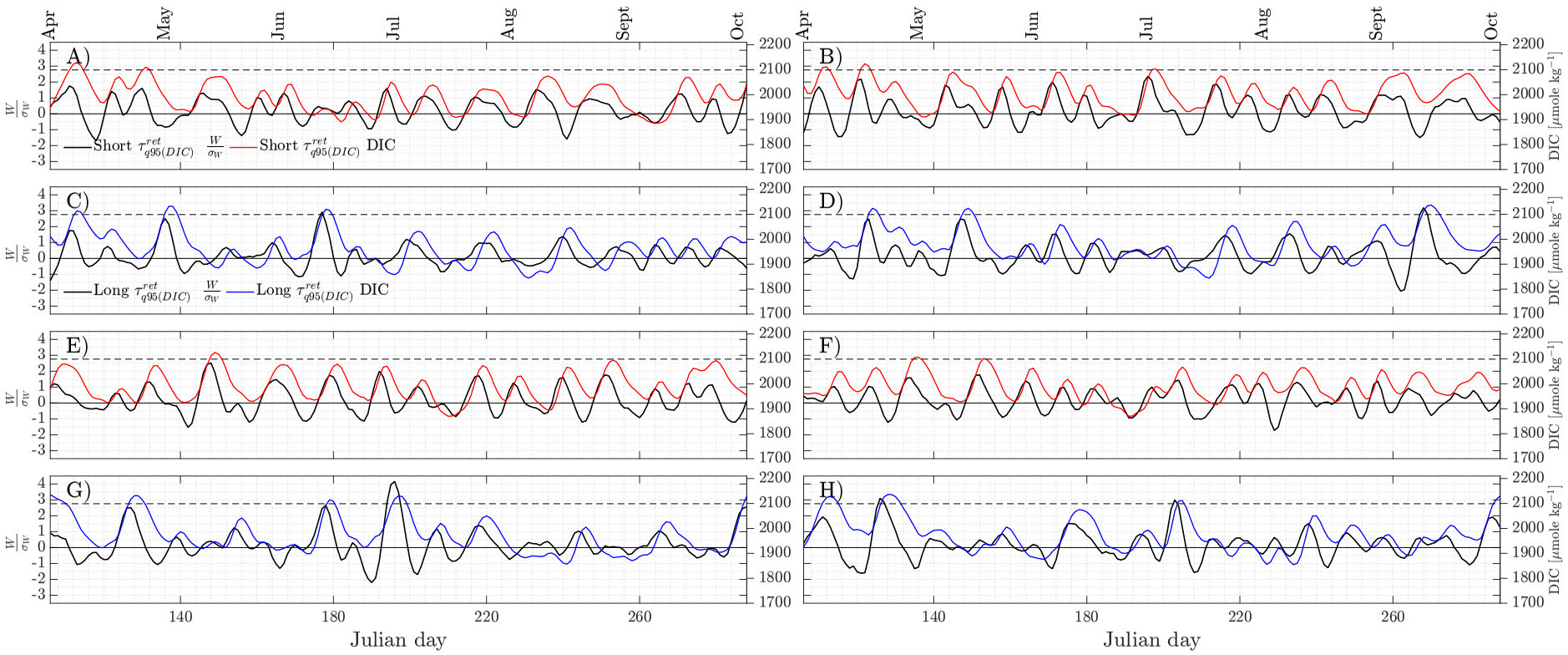

Figure 4.5: Three-day running mean smoothed time series for **upper shelf**. In each panel solid dark lines represent normalized net up/downwelling velocities corresponding to years with short and long average return periods of modelled DIC extremes, which are shown by red and blue solid lines. Globally defined $q_{95(DIC)}$ (Table 4.1) are represented by dark dashed lines. The pairing in each subplot is as follows: panel A) and C) show time series of upwelling season of the years with the shortest and longest $\tau^{ret}_{q95(DIC)}$; panels B) and D) show time series of upwelling season of the years with the 2$^{\text{nd}}$ shortest and the 2$^{\text{nd}}$ longest $\tau^{ret}_{q95(DIC)}$; panels E) and G) show time series of upwelling season of the years with the 3$^{\text{rd}}$ shortest and the 3$^{\text{rd}}$ longest $\tau^{ret}_{q95(DIC)}$; panels F) and H) show time series of upwelling season of the years with the 4$^{\text{th}}$ shortest and the 4$^{\text{th}}$ longest $\tau^{ret}_{q95(DIC)}$. The y axes on the left are always scaled for $\frac{W}{\sigma_W}$ and y axes on the right are always scaled for DIC.

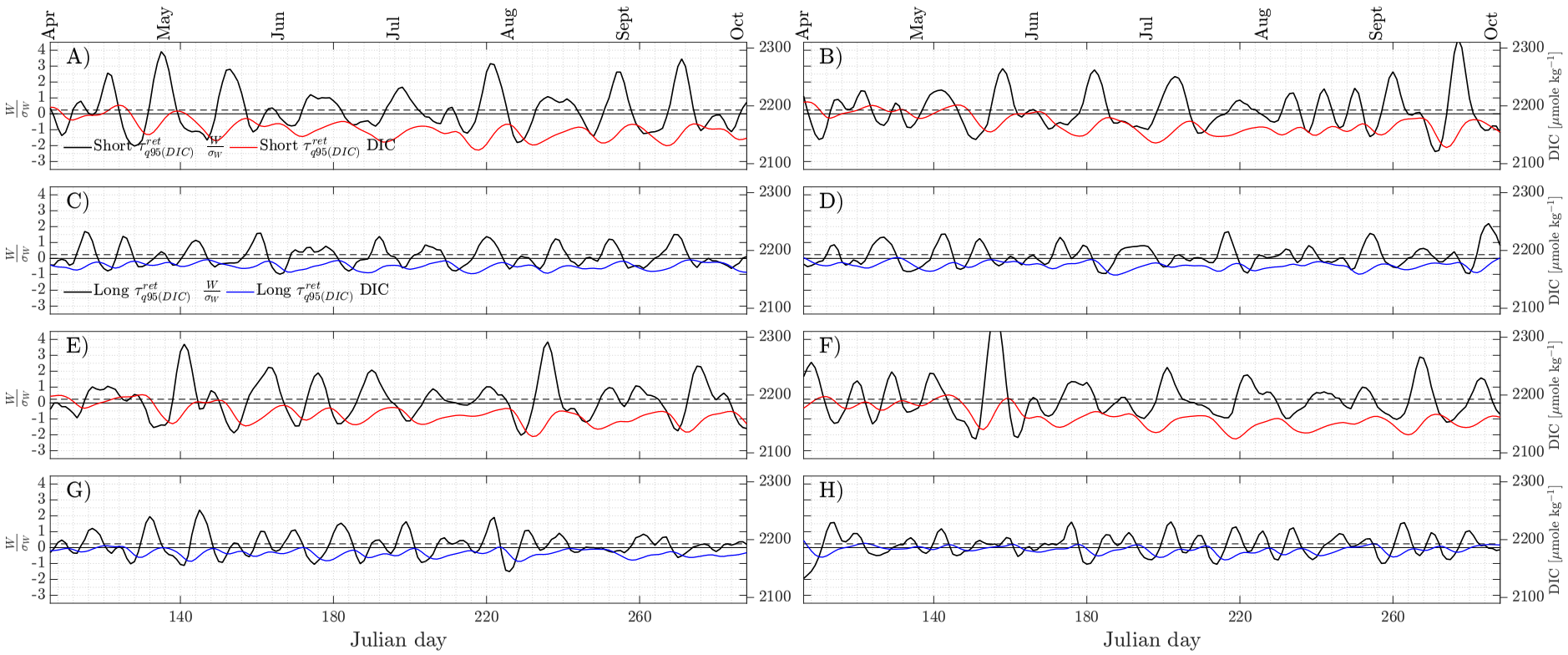

Figure 4.6: Three-day running mean smoothed time series for **lower shelf**. In each panel solid dark lines represent normalized net up/downwelling velocities corresponding to years with short and long average return periods of modelled DIC extremes, which are shown by red and blue solid lines, respectively. Globally defined $q_{95(DIC)}$ (Table 4.1) are represented by dark dashed lines. The pairing in each subplot is as follows: panel A) and C) show time series of upwelling season of the years with the shortest and longest $\tau^{ret}_{q95(DIC)}$; panels B) and D) show time series of upwelling season of the years with the 2$^{\text{nd}}$ shortest and the 2$^{\text{nd}}$ longest $\tau^{ret}_{q95(DIC)}$; panels E) and G) show time series of upwelling season of the years with the 3$^{\text{rd}}$ shortest and the 3$^{\text{rd}}$ longest $\tau^{ret}_{q95(DIC)}$; panels F) and H) show time series of upwelling season of the years with the 4$^{\text{th}}$ shortest and the 4$^{\text{th}}$ longest $\tau^{ret}_{q95(DIC)}$. The y axes on the left are always scaled for $\frac{W}{\sigma_W}$ and y axes on the right are always scaled for DIC.

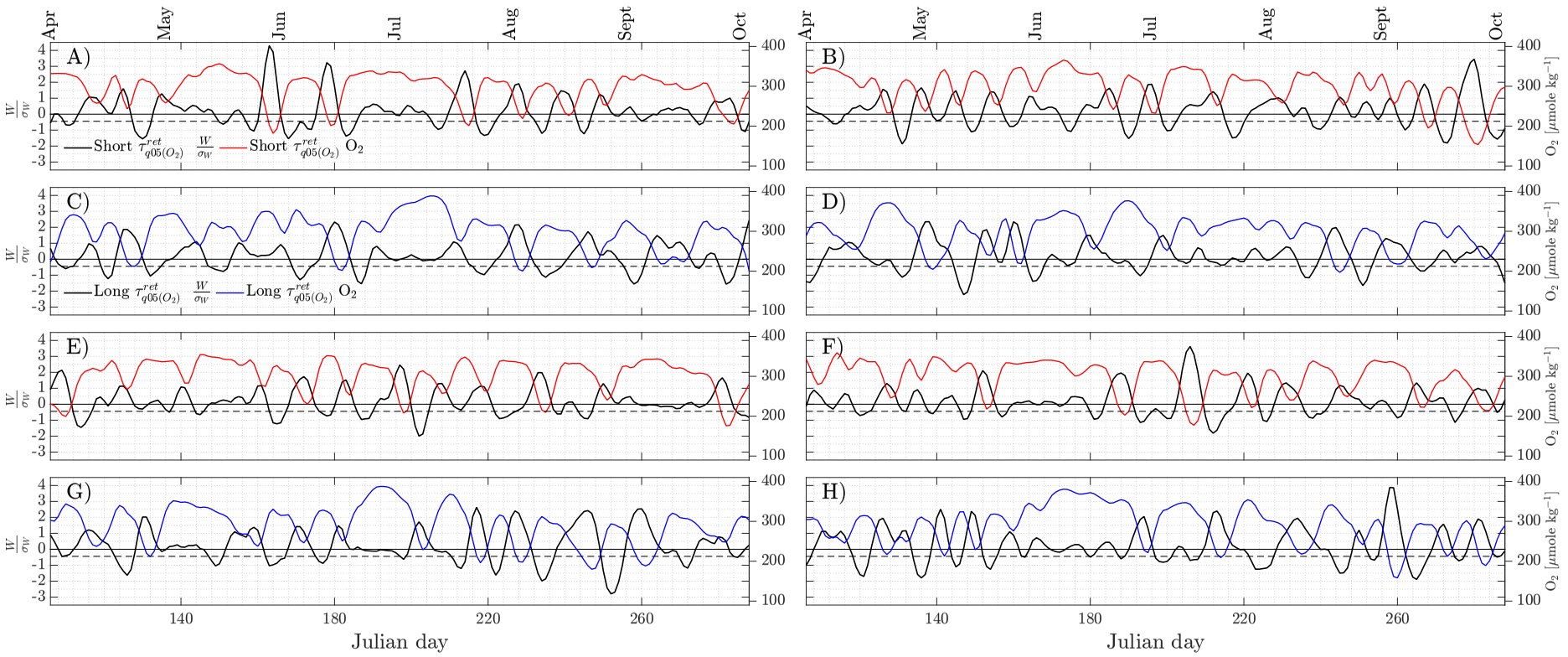

Figure 4.7: Three-day running mean smoothed time series for **upper shelf**. In each panel solid dark lines represent normalized net up/downwelling velocities corresponding to years with short and long average return periods of modelled O_2 extremes, which are shown by red and blue solid lines, respectively. Globally defined $q_{05(O_2)}$ (Table 4.1) are represented by dark dashed lines. The pairing in each subplot is as follows: panel A) and C) show time series of upwelling season of the years with the shortest and longest $\tau^{ret}_{q05(O_2)}$; panels B) and D) show time series of upwelling season of the years with the 2$^{\text{nd}}$ shortest and the 2$^{\text{nd}}$ longest $\tau^{ret}_{q05(O_2)}$; panels E) and G) show time series of upwelling season of the years with the 3$^{\text{rd}}$ shortest and the 3$^{\text{rd}}$ longest $\tau^{ret}_{q05(O_2)}$; panels F) and H) show time series of upwelling season of the years with the 4$^{\text{th}}$ shortest and the 4$^{\text{th}}$ longest $\tau^{ret}_{q05(O_2)}$. The y axes on the left are always scaled for $\frac{W}{\sigma_W}$ and y axes on the right are always scaled for O_2.

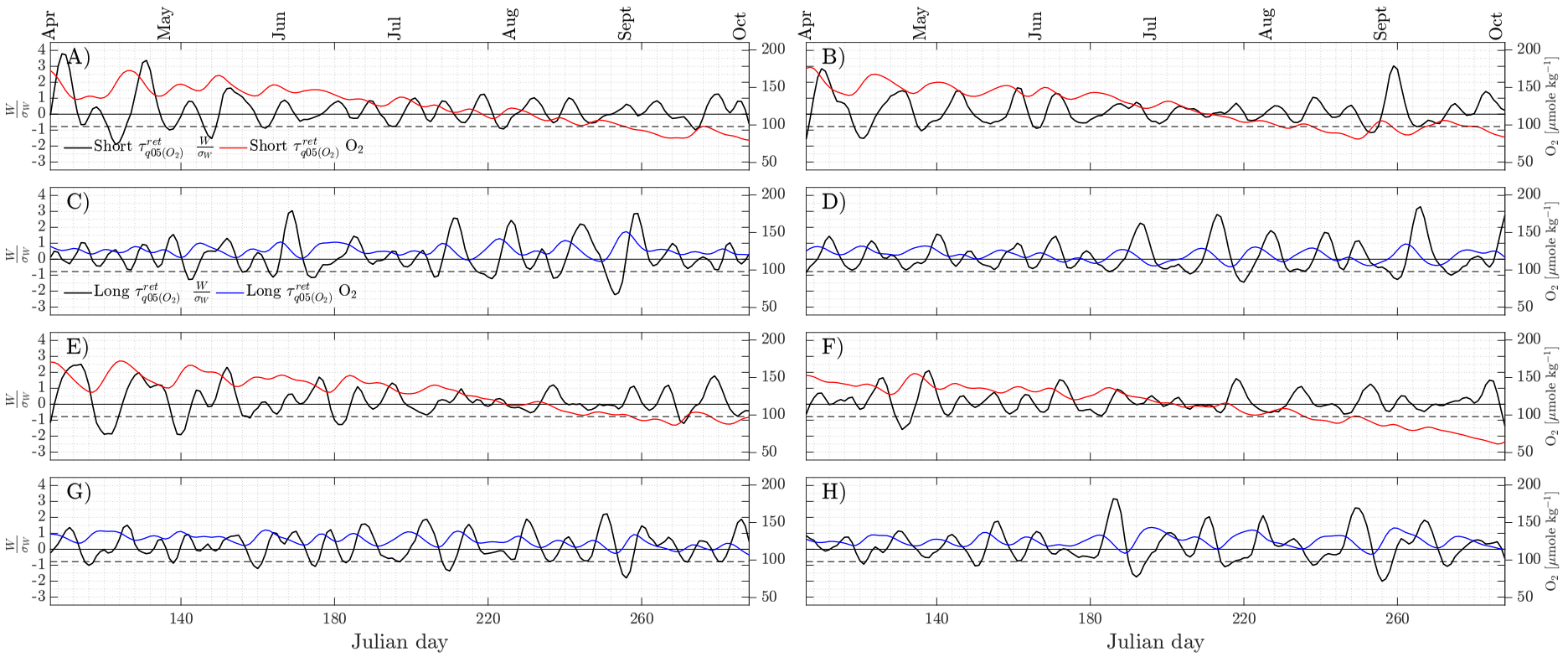

Figure 4.8: Three-day running mean smoothed time series for **lower shelf**. In each panel solid dark lines represent normalized net up/downwelling velocities corresponding to years with short and long average return periods of modelled O_2 extremes, which are shown by red and blue solid lines, respectively. Globally defined $q_{05(O_2)}$ (Table 4.1) are represented by dark dashed lines. The pairing in each subplot is as follows: panel A) and C) show time series of upwelling season of the years with the shortest and longest $\tau^{ret}_{q05(O_2)}$; panels B) and D) show time series of upwelling season of the years with the 2$^{\text{nd}}$ shortest and the 2$^{\text{nd}}$ longest $\tau^{ret}_{q05(O_2)}$; panels E) and G) show time series of upwelling season of the years with the 3$^{\text{rd}}$ shortest and the 3$^{\text{rd}}$ longest $\tau^{ret}_{q05(O_2)}$; panels F) and H) show time series of upwelling season of the years with the 4$^{\text{th}}$ shortest and the 4$^{\text{th}}$ longest $\tau^{ret}_{q05(O_2)}$. The y axes on the left are always scaled for $\frac{W}{\sigma_W}$ and y axes on the right are always scaled for O_2.

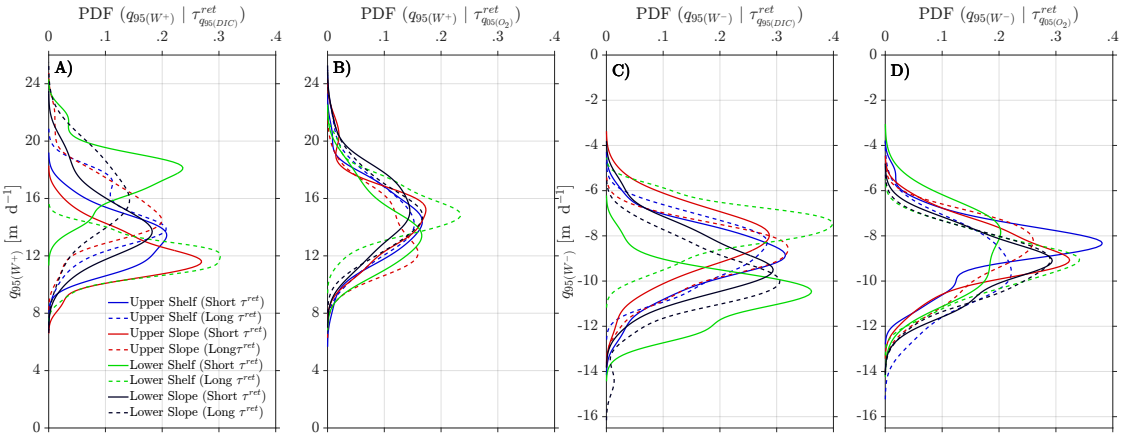

Figure 4.9: Probability density functions (PDF) of the 95$^{\text{th}}$ percentiles of upwelling ($q_{95(W^+)}$) and downwelling ($q_{95(W^-)}$) selected from the years with the shortest and longest 50 return periods. A) PDF of $q_{95(W^+)}$ given $\tau^{ret}_{q_{95(DIC)}}$; B) PDF of $q_{95(W^+)}$ given $\tau^{ret}_{q_{05(O_2)}}$. C) and D) are the same as A) and B) except downwelling ($q_{95(W^-)}$) is considered. For each model region the PDFs from years of short return periods are represented by unique colored solid lines and those PDFs from years with long return periods are represented by the same colored dashed lines.

Because, the subset is limited to the upwelling season, the extreme upwelling velocities (W^+) generally have larger median and standard deviations than the extreme downwelling velocities (Table 4.3).

The distinction between subsets of intense up/downwelling velocities ($q_{95(W^+)}$ or $q_{95(W^-)}$) from short and long return period seasons in the upper shelf is small (blue curves in Figure 4.9). In the upper slope there is a slight difference between the medians from the two seasons, with short $\tau^{ret}_{q_{95(DIC)}}$ seasons having lower $q_{95(W^+)}$.

One of the biggest differences between the two sets of $q_{95(W^+)}$ is found in the lower shelf when return periods of DIC extremes are considered (4.9A). The median of $q_{95(W^+)}$ from the short $\tau^{ret}_{q_{95(DIC)}}$ seasons is about 6 m day^{-1} larger than the median from long $\tau^{ret}_{q_{95(DIC)}}$ seasons.

Generally, the differences between intense up/downwelling values from short and long $\tau^{ret}_{q_{05(O_2)}}$ seasons are less than the differences between intense up/downwelling values from short and long $\tau^{ret}_{q_{95(DIC)}}$ seasons (Table 4.3). This result is another indication of how physical forcing affect carbon and O_2 extremes differently. The difference in

the exceedance frequencies in the lower layers must be driven by processes at the surface, where there is a clear difference between $\tau^{ret}_{q_{05}(O_2)}$ and $\tau^{ret}_{q_{95}(DIC)}$ values (Figure 4.4).

4.3.4 Effects of Upwelling and Downwelling on Extremes

In the previous subsection, I showed that the character of up/downwelling forcing, plays a key role in driving the occurrence of carbon and O_2 extremes by considering representative examples of $\frac{W}{\sigma_W}$ for short and long return periods. To further investigate and quantify the effects of instantaneous upwelling and downwelling strengths on DIC and oxygen distributions, I calculated the cumulative distribution functions (CDFs) of DIC and O_2 conditioned on the upwelling and downwelling strengths falling in specified percentile intervals of width 5%. I call the CDFs in this section conditional cumulative distribution functions (CCDFs) to reflect their dependence on another factor. The up/downwelling percentile intervals were chosen from the percentiles of the overall up/downwelling velocity used in the baseline run (Table 4.4). The symbols W^+ and W^- are used to refer to the magnitudes of positive (upwelling) and negative (downwelling) velocities, respectively, of the full year model results.

In the previous section I focused on the relationships between up/downwelling strength and time evolution of DIC and O_2 by examining composites of return periods of extremes. In this section I investigate the instantaneous relationships between up/downwelling strength and probability distributions of DIC and O_2. One advantage of considering the instantaneous relationships between up/downwelling and the CCDFs of DIC/ O_2 is that it allows us to investigate how the different time scales of physical and biological processes determine the net DIC/ O_2 response. Although the focus will still be on extremes, I also consider the full cumulative distribution functions.

After defining the set containing the up/downwelling velocities ($\mathbf{q}_j$) based on the j^{th} percentile interval, we computed the CCDFs for DIC and O_2 as

Table 4.4: Percentiles of the magnitudes of baseline model run upwelling and downwelling velocities used to calculate CCDFs of O_2 and DIC.

W	$\mathbf{q}_1(2.5\%)$	$\mathbf{q}_2(25\%)$	$\mathbf{q}_3(50\%)$	$\mathbf{q}_4(75\%)$	$\mathbf{q}_5(97.5\%)$
W^+(m d^{-1})	0 – 0.51	2.43 – 3.03	5.73 – 6.52	10.31 – 11.56	19.90 – 52.61
W^-(m d^{-1})	0 – 0.43	1.87 – 2.28	4.03 – 4.54	6.94 – 7.76	13.27 – 40.05

$$CCDF_{O_2,j} = P(O_2 \leq x_{O_2} |\ W \in \mathbf{q}_j) \tag{4.6}$$

$$CCDF_{DIC,j} = P(DIC \geq x_{DIC} |\ W \in \mathbf{q}_j) \tag{4.7}$$

where $j = 1, 2.., 5$ refers to the index for the five percentile intervals whose centers are given in bracket in Table 4.4. Note that the the mid-points of the 5% intervals are shown in Table 4.4. For example, 50% is the mid point of the interval 47.5% to 52.5%. The right-hand side of Equation 4.6 represents the probability that the random variable O_2 takes on a value less than or equal to x_{O_2} given the up/downwelling (W) velocity falls in the j^{th} percentile interval (Table 4.4). The definition of $CDF_{\text{DIC},j}$ (and, therefore, that of $CCDF_{\text{DIC},j}$) differs from a conventional cumulative distribution function, whose values are the probabilities of a random variable being less than or equal to the argument given to the function.

A range of different kinds of probabilistic information can be extracted from Figures 4.10 and 4.11, which show CCDFs of O_2 and DIC. For example, the probability of upper shelf DIC being larger than 2050 μmole kg^{-1} is 0.5 when W^+ lies in the 47.5% – 52.5% range (Table 4.4). In other words, about 50% of the time the upper shelf DIC values are larger than 2050 μmole kg^{-1} given that the upwelling strength falls near to the median W^+ value (Figure 4.10B). Similarly, we can say about 99% of the time the value of O_2 is less than or equal to $x_{O_2} = 250$ μmole kg^{-1} when W^+ lies in the range 95% – 100% (Figure 4.10A). I will describe the general features of these CCDFs for both the shelf and slope regions before I focus on the low-probability extreme events (CCDFs<0.1).

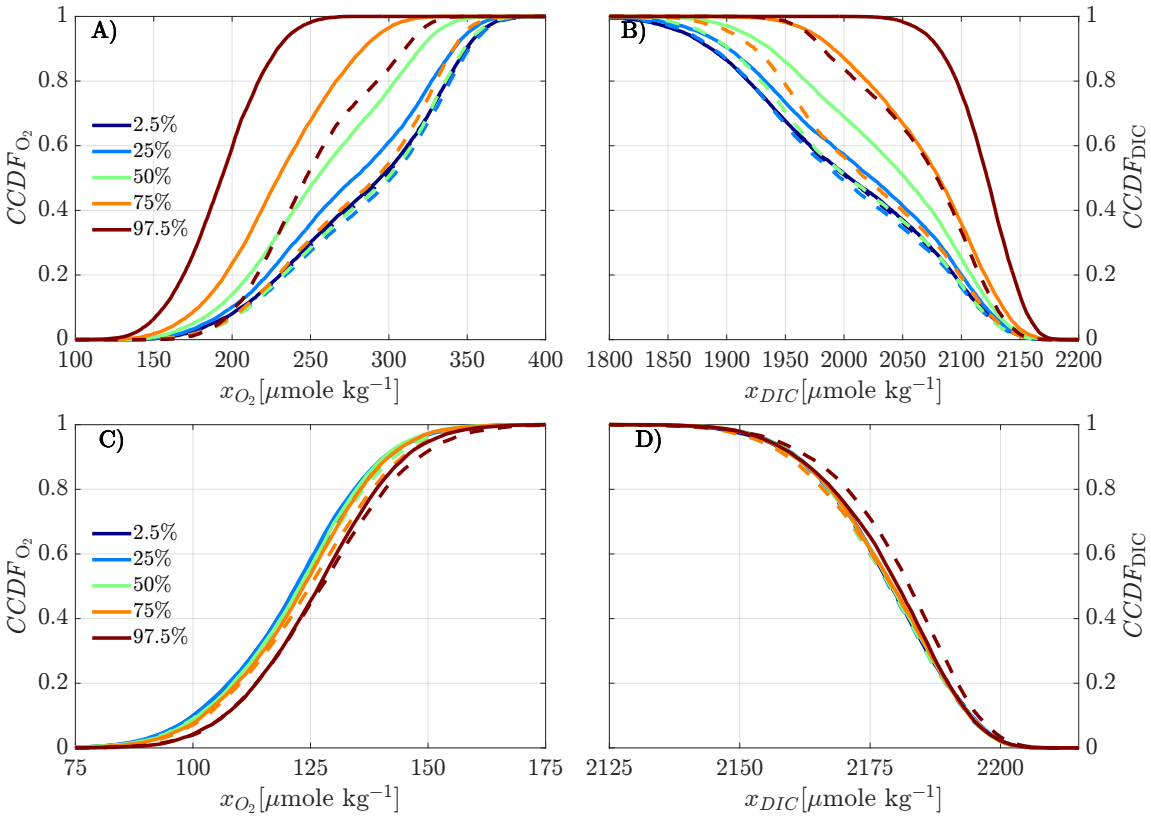

Figure 4.10: Cumulative distribution functions for the upper shelf oxygen (A) and DIC (B); lower shelf oxygen (C) and DIC (D) given the magnitude of the total up/-downwelling velocities lie in one of the five percentile intervals in the baseline forcing (Table 4.4). Solid and dashed lines represent the cumulative distribution function for upwelling (W^+) and downwelling (W^-) velocity magnitudes, respectively.

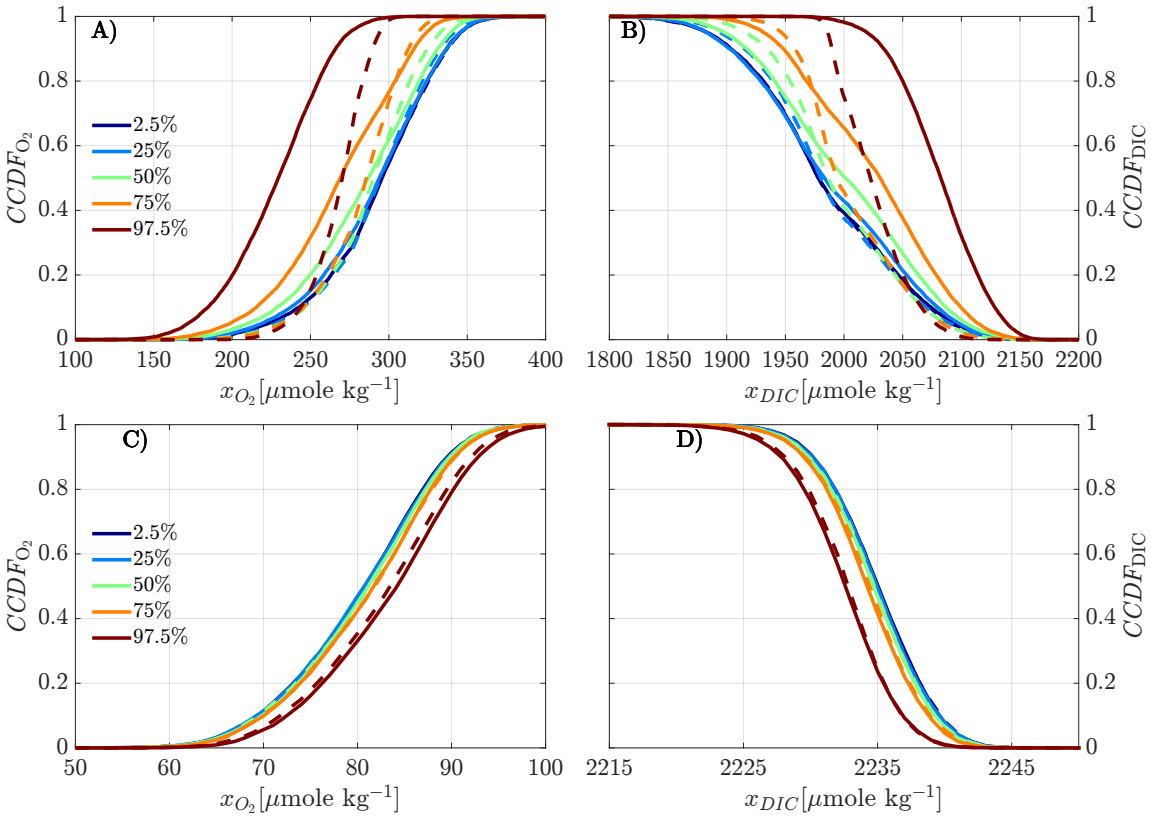

Figure 4.11: Cumulative distribution functions for the upper slope oxygen (A) and DIC (B); lower slope oxygen (C) and DIC (D) given the magnitude of the total up/-downwelling velocities lie in one of the five percentile intervals in the baseline forcing (Table 4.4). Solid and dashed lines represent the cumulative distribution function for upwelling (W^+) and downwelling (W^-) velocity magnitudes, respectively.

Upper Layers

In the upper shelf, unless the upwelling strength is extremely high, the probability of the oxygen value falling below 150 μmole kg^{-1} is small (<0.1). Even for the most extreme upwelling, the $P(O_2 \leq x_{O_2} | W^+ \in \mathbf{q}_5)$ associated with 150 μmole kg^{-1} oxygen is small (about 0.1). For a given value of the CCDF, stronger upwelling strength corresponds to smaller values of upper shelf oxygen (Figure 4.10A). For example, at the CCDF value of 0.4 oxygen threshold corresponding to $P(O_2 \leq x_{O_2} | W^+ \in \mathbf{q}_1)$ is ~275 μmole kg^{-1}, the oxygen threshold for $P(O_2 \leq x_{O_2} | W^+ \in \mathbf{q}_4)$ is ~230 μmole kg^{-1}, and oxygen threshold for $P(O_2 \leq x_{O_2} | W^+ \in \mathbf{q}_5)$ is ~190 μmole kg^{-1} (Figure 4.10). These results quantify how stronger upwelling is associated with smaller instantaneous O_2 concentrations.

As expected, for the same percentile bin, CDFs conditioned on downwelling are generally associated with larger oxygen values than CDFs conditioned on upwelling, because upwelling brings up lower oxygen. For example, the value of x_{O_2} is ~200 μmole kg^{-1} for $P(O_2 \leq x_{O_2} | W^- \in \mathbf{q}_5) = 0.1$ while it is ~160 μmole kg^{-1} for $P(O_2 \leq x_{O_2} | W^+ \in \mathbf{q}_5) = 0.1$ (Figure 4.10A). In other words, there is 40 μmole kg^{-1} more oxygen during the extreme downwelling than during the extreme upwelling. At higher probabilities, the difference in x_{O_2} between W^+ and W^- for a fixed CCDF value becomes larger as can be seen in the spread between any pair of W^+ and W^- CCDF curves (Figure 4.10A). For example, there is about 20 μmole kg^{-1} larger difference at CCDF = 0.6 than at CCDF = 0.1. This because 60% of the time upper shelf oxygen is below x_{O_2} = 200 μmole kg^{-1} for W^+ in the bin that contains the 97.5$^{\text{th}}$ percentile, while the same percentage of oxygen is below x_{O_2} = ~260 μmole kg^{-1} for W^- in the bin that contains the 97.5$^{\text{th}}$ percentile. For the most part, the CCDFs of DIC are mirror images of that of oxygen (Figure 4.10B).

For the most part, the spread of the CCDFs for changes in downwelling intensity is much smaller than that of the spread in the upwelling CCDFs. Similar to the CCDF of the W^+, the CCDF for the W^- in the 97.5$^{\text{th}}$ percentile bin is separated from the

rest of the CCDFs. At probabilities higher than 0.4, the W^- curve for the 97.5th percentile bin is associated with smaller x_{O_2} values than the moderate and lower W^- CCDF curves (Figure 4.10A). This result, which implies that very strong downwelling is also associated with relatively low oxygen levels, compliments the result I found using W^- from upwelling season only (Figure 4.9D). One mechanism that leads to this low oxygen-intense downwelling relationship is that when downwelling is too intense, it brings in nutrient poor offshore water to the shelf and reduces oxygen production, by slowing down primary production. Another mechanism is the slowing down of inshore-offshore exchange by strong downwelling that leads to increased residence time of water, which in turn leads to elevated local oxygen consumption. These processes, of course, apply to upwelling season only. One possibility of low oxygen-intense downwelling relationship occurring in the downwelling season is if the downwelling season follows a highly productive upwelling season. The wintertime subsurface O_2 following a highly productive summer is usually low. Intense winds (which also drive strong downwelling) mix this low O_2 water with surface water thereby reducing the surface O_2. So, it is not the downwelling that is directly affecting O_2 (reduce it in the upper shelf) but also the co-occurrence of low O_2 at depth and strong mixing.

The CCDF$_{O_2}$ and CCDF$_{DIC}$ result show that in the upper layer physical processes dominate. I found a similar result in section 4.3.3 when I computed the return period composited PDFs of w^+ and w^- for both DIC and O_2 (Table 4.3). Both results imply that in the upper layers physical processes, which are relatively of short time scale, dominate over biological processes, with strong upwelling events leading to low-O_2, high-DIC events and weak upwelling events leading to high-O_2, low-DIC events. As can be expected, the physical response to up/downwelling is more rapid than responses to biological processes.

In the upper slope, the oxygen CCDF curves look similar to those in the upper shelf except that all the W^- curves cross the W^+ curves (Figure 4.11). In the upper shelf, only the 97.5% W^- CCDF crosses the W^+ curves. The steepness of the slopes of the W^- CCDF curves in the upper slope reflects the fact that DIC and O_2 are less

variable over the slope relative to the high variability seen on the shelf.

Lower Layers

Since the lower shelf oxygen and DIC are mostly controlled by biological processes, their CDFs conditioned on instantaneous upwelling/downwelling intensity are clustered together (Figure 4.10C, D). Oxygen values in the lower shelf are relatively low and a small difference in the CCDF curves can be as important biologically as the larger changes in the upper shelf. A more interesting contrast between the upper and lower shelf CCDF_{O_2} curves is that the order reversal between the two layers (Figure 4.10A, C). This order reversal shows that an intense up/downwelling is associated with lower O_2 in the upper shelf while it is associated with higher O_2 in the lower shelf (cf., Figures 4.9B, and 4.9D). The opposite response by oxygen at different depths to the same forcing shown by the above reversal of CCDF_{O_2} curves shows that we cannot generalize to the entire water column the response at a given depth to forcing.

The $P(DIC \geq x_{DIC} |\ W \in \mathbf{q}_i)$ curves in the lower slope also show switching in order relative to the upper slope. For example, the probability that the DIC is below 2235 μmole kg^{-1} is 0.25 for the 97.5% W^+ whereas the probability of the same condition under the 2.5% W^+ is twice as large (Figure 4.11). In the shelf, only the $P(O_2 \leq x_{O_2} |\ W \in \mathbf{q}_i)$ curves show order switching. Unlike in the upper layers, a stronger upwelling in the lower slope is associated with lower DIC. Since the CCDFs here do not show a clear distinction between W^+ and W^- percentiles, I conclude that both intense upwelling and downwelling have a decreasing effect on the level of DIC in the lower slope. The effect of intense downwelling on the lower slope DIC is due to increased flushing with lower DIC water from the upper layer.

The reason why intense upwelling is associated with low DIC in the lower slope is not obvious. One possibility is the effect of short residence time of the upwelled water in that region. During intense upwelling, the upwelled water stays for too short in this narrow slope to allow increased production in the surface and also for reminiralization to increase its DIC concentration. This mechanism makes the DIC concentration to at

least remain the same. The small decrease in DIC could be caused by other processes. The average difference between the 2.5% UI and 97.5% DIC CCDFs are only about 5 μmole kg^{-1}, which can be caused by vertical mixing alone.

In the lower shelf both intense upwelling and downwelling are associated with high DIC. In the lower slope they are associated with low DIC. The differing responses to up/downwelling intensities suggest that the responses in one of the boxes cannot be generalized to the lower layer in general. In other words, both regions need to be monitored for DIC changes.

4.3.5 The CCDFs of extreme DIC and O_2

The analysis above indicated that the changes of the CCDFs with up/downwelling are different for the relatively low-probability events than for the bulk of the distribution. I now focus on CCDFs with values below 0.1 to further investigate the effects of upwelling/downwelling strengths on the O_2 and DIC extremes (that by construction occur only less than 10% of the time).

In the baseline model run, the spread (differences in the means) among these CCDF curves is for the most part larger for O_2 than DIC (solid lines in Figures 4.12, 4.13). Physical forcing is generally more important for the upper layer oxygen extremes than the DIC extremes. Since biological processes also influence the conditions for these extremes, I calculated the CCDFs for model simulations where the specific growth rate was set to zero. The results show biological uptake not only contributes to the CCDF spreads but also to their slopes (the probability density) (dashed lines in Figures 4.12, 4.13).

Sensitivity of the CCDFs to up/downwelling intensity is highly reduced when the specific growth rate is zero, indicating that biology strongly affects the response of the O_2 and DIC extremes to different up/downwelling intensities. Also when biological uptake was turned off, the slopes of the CCDF curves became steeper, which indicates the variance loss that is normally added to the extremes by biological processes (when organic matter is not produced within the system reminiralization fluxes are

also significantly reduced even though these rate parameters are unchanged). While physical processes are more important for the bulk of the DIC/ O_2 distributions (previous subsection), the importance of biological processes increases at the lower ends of the CCDFs (rare events).

In both lower shelf and slope regions, where local biological processes are expected to dominate over advection, the solid CCDF curves are almost always associated with low O_2 and high DIC (Figures 4.12E–H and 4.13E–H). In the upper slope downwelling seems to be relatively more important than upwelling when there is no growth, because the spread among the W^+ CCDF curves is (Figure 4.13A–B) less than the spread among the W^- CCDF curves is (Figure 4.13C–D).

Strong downwelling decreases the mean and larger quantiles of O_2 in the upper layers as it slows down primary production (Figures 4.10A and 4.11A). The decreasing effect on mean oxygen is clearly seen in Figure 3.9. Downwelling, however, also tends to reduce the probability of extremely low O_2 values (Figure 4.12 and 4.13). In other words, downwelling prevents the upper shelf and slope from becoming hypoxic by flushing with offshore surface water that are well-ventilated.

The intermittent downwelling events in summer effectively increase the residence time in the system by pausing the 'upwelling conveyor belt', or pushing the subsurface water back down and preventing it from coming up to the surface where it would be oxygenated. The net effect of this mechanism is reducing O_2 in the lower layers. When biological uptake is turned off, the above mechanism will have no effect on the lower layer O_2. The increased residence time of water alone does not change O_2 as there is no downward export of organic matter to consume oxygen. The main effect of a strong downwelling in the lower layer, however, is still to increase O_2 because of the nature of the O_2 vertical profile.

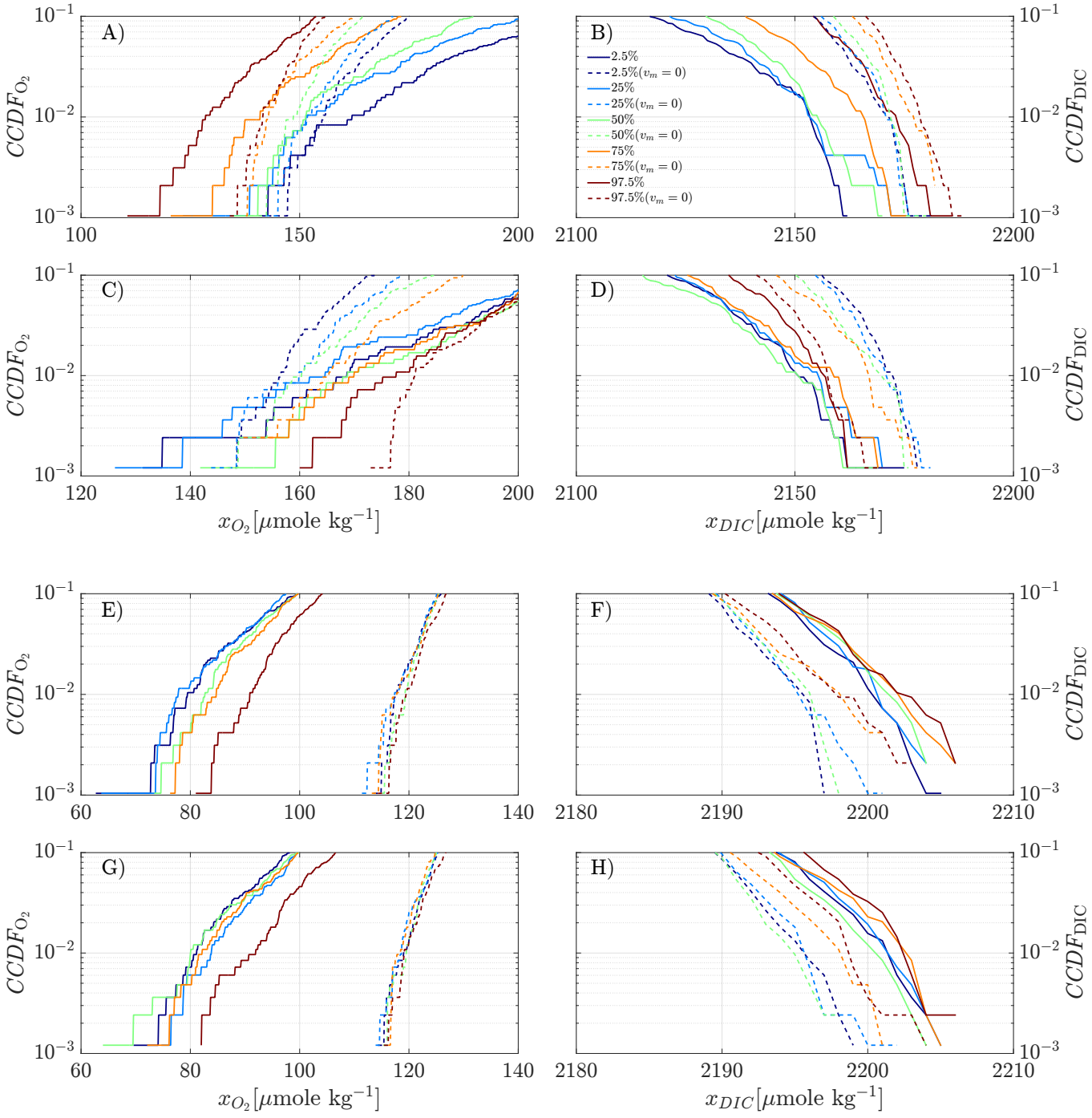

Figure 4.12: The lowest CCDFs of O_2 and DIC for baseline (solid lines) and $v_m = 0$ run (dashed lines). The CCDFs in A)– D) are for upper shelf; CCDFs in E) – H) are for lower shelf. A), B), E) and F) are based on percentiles of W^+; C), D), G) and H) are based on percentiles of W^-.

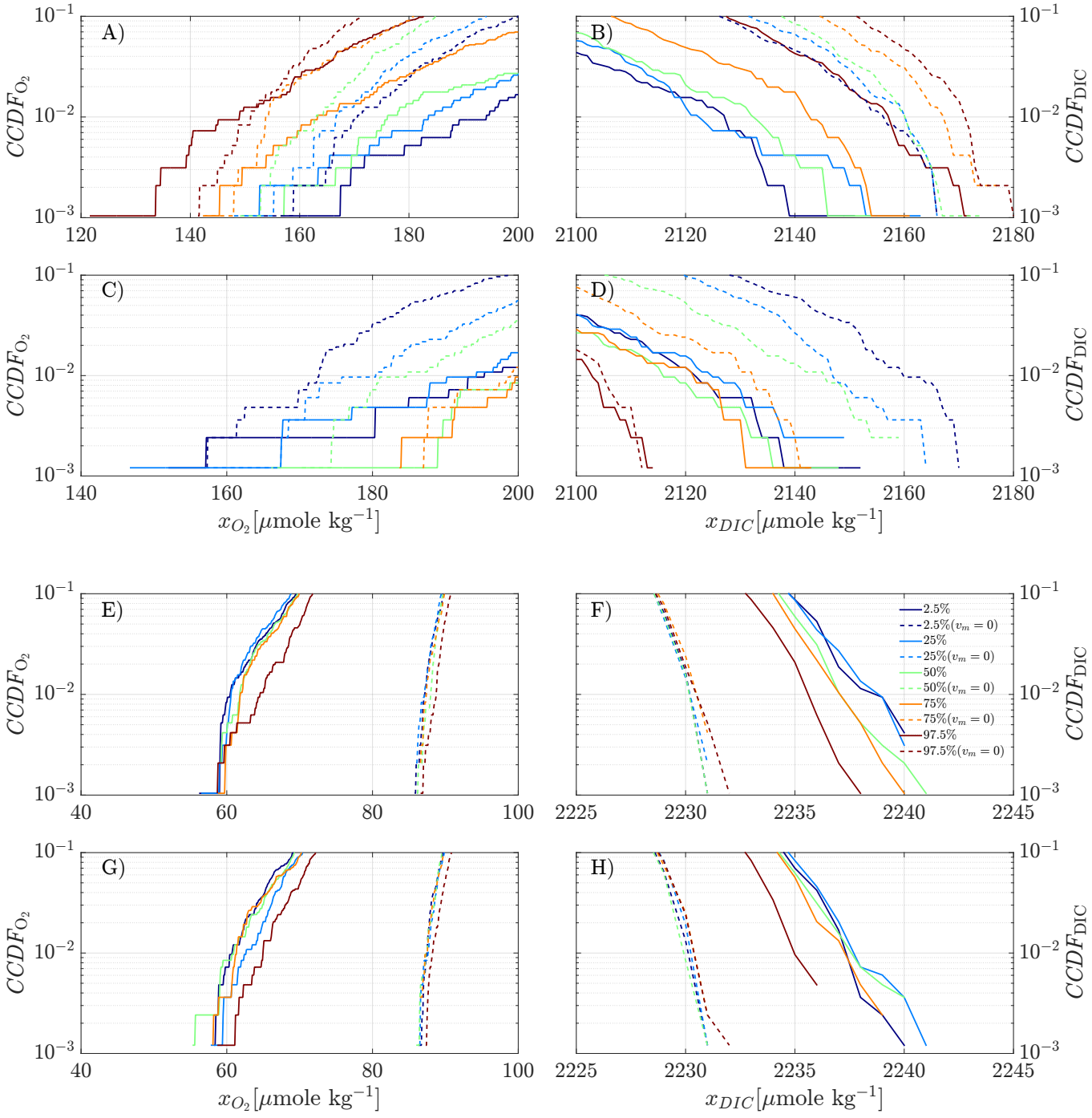

Figure 4.13: The lowest CCDFs of O_2 and DIC for baseline (solid lines) and $v_m = 0$ run (no biological production, dashed lines). The CDFs in A)– D) are for upper slope; CDFs in E) – H) are for lower slope. A), B), E) and F) are based on percentiles of W^+; C), D), G) and H) are based on percentiles of W^-.

4.3.6 Timing of Extremes of DIC and O_2

The timing of carbon and oxygen extremes can be as important as the values of the extremes themselves for understanding their effects on marine organisms at their various life stages (Haigh et al., 2015). Different species respond to carbon and oxygen extremes differently and even within a species the responses are dependent on life stages of the organisms (Pörtner et al., 2005). The aim of this section is to characterize the seasonal variations in the extremes using the baseline model results for the whole year.

As in the previous chapters, I will refer to oxygen values below the long-term $q_{05(O_2)}$ as extreme values. The points below the dashed lines in the O_2 panels of Figure 4.14 represent these extremes for the four model boxes. DIC values exceeding the $q_{95(DIC)}$ are considered extreme values corresponding to the points above the dashed lines in DIC panels of Figure 4.14. Since O_2 and DIC are biologically coupled their extremes can and are likely to co-occur. The simultaneous occurrence of carbon and oxygen extremes represents a particularly strong hazard to oceanic organisms (Burnett, 1997; Pörtner, 2009; Pörtner and Farrell, 2008; Gobler et al., 2014; Gobler and Baumann, 2016; DePasquale et al., 2015; Feely et al., 2018; Bopp et al., 2013).

In this section I investigate the factors that may change the timing and frequency of DIC and O_2 individually and their simultaneous occurrence. For this purpose I use a simple metric that for each Julian day computes the fraction, $\mathcal{F}$, of days, D, as

$$\mathcal{F}_{DIC} = \frac{D(DIC > q_{95(DIC)})}{N} \tag{4.8}$$

$$\mathcal{F}_{O_2} = \frac{D(O_2 < q_{05(O_2)})}{N} \tag{4.9}$$

where $N = 1017$ is the number of times each Julian day occurs (e.g.,. 1017 Julian day 01).

For the fraction of days where DIC and O_2 extremes simultaneously occur, I use

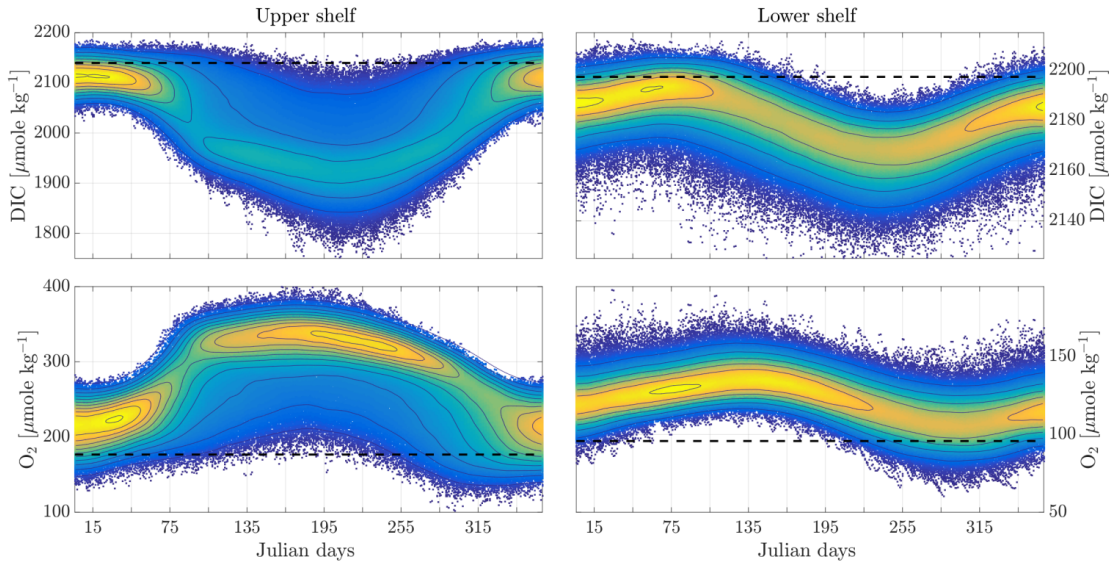

(a) shelf

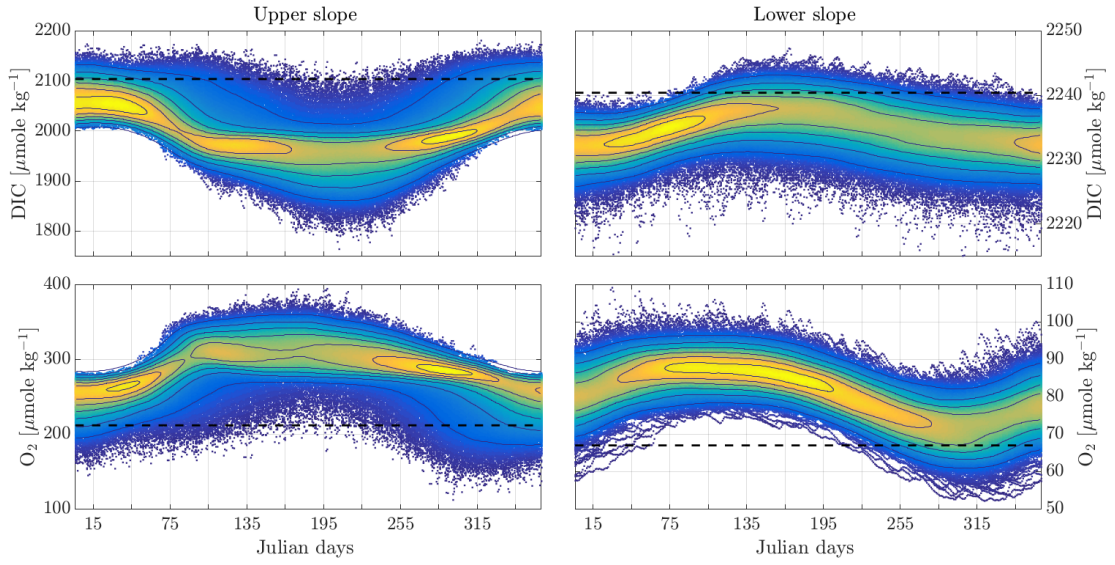

(b) slope

Figure 4.14: The baseline run DIC and O_2 results. The $q_{05(O_2)}$ and $q_{95(DIC)}$ calculated from all the (present-day) 1017 years DIC and O_2 are shown in dashed lines. The probability density function plots show the most likely value ranges in warm colors and the less likely value ranges (including the extremes) in cold colors.

the metric

$$\mathcal{F} = \frac{D(O_2 < q_{05(O_2)} \ \& \ DIC > q_{95(DIC)})}{N} \tag{4.10}$$

First, I show the individual timing and frequencies of DIC and O_2 during the course of the year (Figure 4.15A). Lower slope DIC extremes are most likely in late May and least likely in the later part of the downwelling season. In late October the slope region is most likely to experiences O_2 extremes, while the shelf region faces the most likely O_2 extremes about a month later. DIC extremes are most likely in January in all but the lower shelf boxes, which shows a peak in $\mathcal{F}_{DIC}$ in mid March. As expected, the fractions of days with DIC or O_2 extremes in each of the model boxes showed peaks that correspond to the seasonal cycles shown in Figure 4.14. What is more interesting is how the fraction of days with both DIC and O_2 extremes evolves with time.

If the occurrence of DIC and O_2 extremes were perfectly independent, then the product $\mathcal{F}_{DIC} \cdot \mathcal{F}_{O_2}$ must be the same as $\mathcal{F}$. Time series of $\mathcal{F}$, and $\mathcal{F}_{DIC} \cdot \mathcal{F}_{O_2}$ are shown in Figure 4.15B. From comparison of these curves DIC and O_2 are dependent on each other outside of the upwelling season (days 106 – 288), providing a further quantification of the extent to which extremes are coupled. During the upwelling season, the product $\mathcal{F}_{DIC} \cdot \mathcal{F}_{O_2}$ in the upper layers converge to the corresponding $\mathcal{F}$'s which are small- further quantifying the weak coupling of extremes in the upper layers during this season. The probabilities of DIC – O_2 joint extremes, especially those in the upper layers, grow from either edges of the upwelling season.

Figure 4.15B shows that simultaneous extreme O_2 and DIC events are relatively less common in the middle of the upwelling season than at the start and end of the season. In the lower layers, the chance of the two extremes occurring on the same day is much lower than it is in the upper layers. Part of the reason may be the time delay between remineralization and physical processes that control oxygen and DIC fluxes.

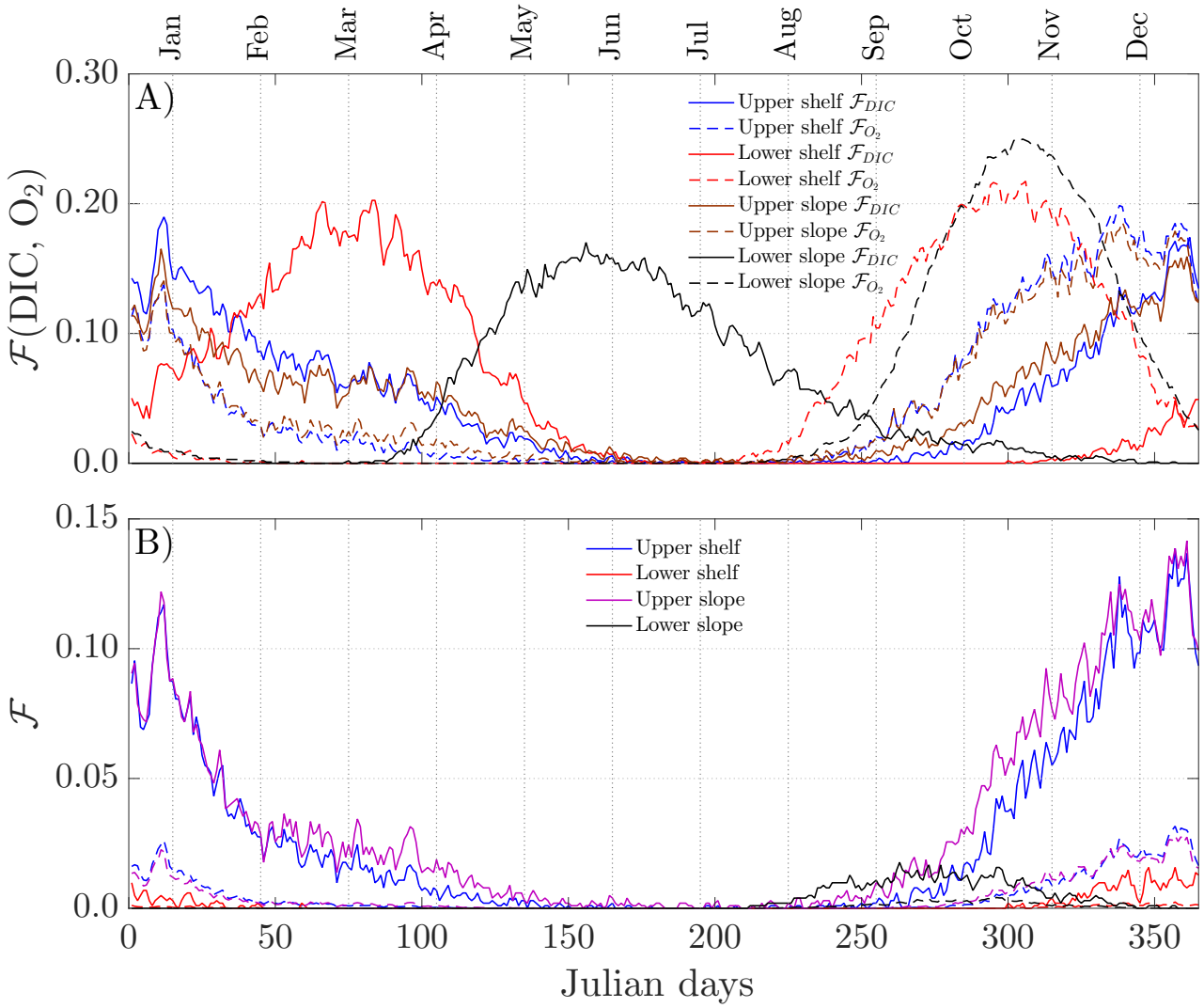

Figure 4.15: Fraction of days (D) that meet the condition A) $DIC > q_{95(DIC)}$ percentile (Solid lines) $O_2 < q_{05(O_2)}$ percentile (dashed lines); B) Fraction of days ($\mathcal{F}$) that satisfy both conditions in A) as defined in the text. The dashed lines in panel B) represent the products of the pair of same colored curves in A). Color codes represent the different model regions.

The factors that control the timing of co-occurrence of oxygen and DIC extremes will be investigated using sensitivity analyses in chapter 5.

4.4 Conclusion

My model simulation shows that O_2 extreme events in the upper layer are more than twice as frequent (but of shorter duration) as DIC extreme events. Based on the exceedance probabilities calculated, in the upper layers most of the (present-day) 1017 upwelling seasons are likely to experience O_2 extreme events while years with and without DIC extreme events are both common (Figures 4.2 and 4.3). This frequent occurrence of extreme O_2 conditions does not necessarily mean the oxygen levels fall below hypoxic thresholds. It simply means the O_2 values below the lowest 5^{th} percentile of the baseline model run O_2 distribution occur at higher frequencies. In fact, in the upper layers the probabilities of occurrence of O_2 values below hypoxic thresholds are negligible (Figures 4.2 and 4.3).

The oxygen values in the upper layer are nearly out of phase relative to that of the upwelling forcing as upwelling brings low oxygen water from the lower layer (e.g., Figure 4.7). DIC curves follow the same pattern as upwelling curves but they rarely cross the threshold (e.g., Figure 4.5). In the upper layer both oxygen and DIC show a time lag of about two days relative to upwelling events. A key consequence of the difference in the return periods of DIC and O_2 is that it demonstrates partial decoupling of DIC and O_2.

The lower shelf has the highest interannual variability of O_2 and DIC extremes (Figures 4.2 and 4.3). Unlike the upper layer where multiple fluxes (e.g., gas flux, precipitation, evaporation, river runoff) determine the variability of O_2 and DIC, the lower layer is mainly influenced by the interannual variability in the upwelling forcing. This highly variable region is poorly observed and the limited available data, especially with regard to the carbonate system, could result in misleading estimates about the presence of years with extremes (Haigh et al., 2015).

The connection between upwelling behaviour and O_2 and DIC extremes is not always straightforward. Each model box responds to upwelling differently. One of the factors in the variations of responses is the time characteristics of the upwelling. Generally, less variable upwelling strength throughout the season tends to be related to stable conditions (long return periods of extremes). Frequent DIC extremes (short return periods) are associated with frequent and intense upwelling events, specifically in the early part of the upwelling season. Early season weak upwelling followed by late season strong upwelling tends to keep the lower layer O_2 above the minimum threshold. In contrast, strong early upwelling followed by weak late season upwelling causes O_2 values to fall below the lowest threshold (e.g., Figure 4.8). Therefore, upwelling timing is as important as its intensity.

In the upper layers there is higher contrast among up/downwelling intensities and higher contrast among upwelling and downwelling effects on DIC and O_2 extremes (e.g., Figure 4.10). This response to physical forcing suggest both DIC and O_2 extremes in the upper layer are mainly controlled by physical processes. The effect of varying up/downwelling intensities on lower layer DIC and O_2 extreme events is relatively small, which suggests they are mainly controlled by biological processes. Further evidence of this behaviour was found when biological uptake was set to zero. In this case, the difference between the effects of up/downwelling forcing on DIC and O_2 extremes was substantially reduced from when the baseline uptake rate was used.

Finally, joint DIC–O_2 extreme events were found to be less likely in the summer upwelling season than at other times of the year. These joint extreme events are more rare than the marginal probability distributions of DIC and O_2 suggest, demonstrating that although DIC and O_2 variations are not perfectly coupled neither are they entirely decoupled.

Chapter 5

Sensitivity Analysis

5.1 Introduction

The purpose of this chapter is to understand the results discussed in this thesis in a broader context, and to assess how the results would change had I used model parameter values different than those used in the model baseline run.

Short Summary

Sensitivity analysis results reveal some details on how DIC and O_2 extreme events respond to selected model parameters and in some cases corroborated results found by statistical analysis. For example, increasing the strength of upwelling favoured more changes in the upper layer DIC and O_2 extreme events than it did in the lower layer. Key results of the sensitivity analysis are

1. The model's lower layer DIC extreme values showed unexpected increase of up to 20 μmol kg^{-1} when atmospheric pCO_2 was substantially (75 – 100%) increased. The increase in the mean DIC was slightly lower (up to 15 μmol kg^{-1})

2. The effect of fluxes from the inner shelf (VICC) region on modelled DIC and

O_2 extremes are minor compared to other fluxes of both physical and biological origin.

3. DIC and O_2 extremes are more sensitive to biological parameters such as growth rate during upwelling season than across a year.

4. A moderate decrease in phytoplankton growth rate increases the chances of model lower layer O_2 extremes, while near-zero growth rate does not.

5. DIC and O_2 extremes showed more sensitivity to certain model parameters than their mean/median values did.

6. Increased primary production, via increased phytoplankton growth rate, decreased the frequency of joint DIC–O_2 extreme events in the upper layers, during the summer upwelling season but increased it in the winter downwelling season.

7. Changes in up/downwelling intensity do not change the frequency of joint DIC–O_2 extreme events within the upwelling season.

8. Lowering upwelling intensities lowered the frequency of wintertime joint DIC–O_2 extreme events. Increasing the upwelling intensities had the opposite effect on the frequency of joint extremes.

9. A narrow shelf experiences frequent wintertime joint DIC–O_2 extreme events in both upper and lower layers.

5.2 Method

A total of 420 sensitivity experiments were conducted on 35 model parameters (including some boundary conditions). The criteria to chose these parameters were based on (1) high uncertainties in their measurements (2) high impact on modelled

quantities during preliminary inspections (3) being more likely to change in future climate.

Table 5.1: The 5^{th} O_2 and 95^{th} DIC percentiles of the baseline run.

Region	O_2 [μmole kg^{-1}]	DIC [μmole kg^{-1}]
Upper shelf	175.14	2142.5
Lower shelf	93.54	2196.6
Upper slope	209.76	2107.40
Lower slope	66.60	2235.30

Through these sensitivity analyses, I investigate the strength of physical and biological controls on DIC and O_2 extremes in the model. Similar to other sensitivity studies, this analysis also identifies parameters and boundary values that need more field measurements and those that are most important to track in a changing climate. A more detailed discussion of those important parameters/boundary values and their effect on both the magnitude and frequency of occurrences of the extremes follows in the next sub sections. The main statistics I use are the 95$^{\text{th}}$ percentile of DIC ($q_{95(DIC)}$) and 5$^{\text{th}}$ percentile O_2 ($q_{05(O_2)}$) (Chapter 4). For comparison I also discuss results based on the medians ($q_{50(DIC)}$ and $q_{50(O_2)}$).

Twelve values of each of the selected parameters were generated by changing the baseline values by -100, -97.5, -75, -50, -25, -2.5, 2.5, 25, 50, 75, 97.5, and 100 % (Figures 5.1 – 5.4). Since many different parameters and boundary conditions are considered here, the same ranges were used for each to avoid an analysis that was too finely-tuned on any particular subset of parameters. Not all of the resulting parameter values are realistic.. For the same reason of a faster computation, I also run the sensitivity tests only for 100 years. Some of the changes I made to the parameters were unrealistically big, in which case the model either crashed or produced results that are not realistic. These instances are shown by blank white spaces in the figures (see Table 5.2 for details). One unrealistic result of some of the large parameter changes was negative oxygen concentration. Such values can occur in the model due to lack of denitrification process, which I do not model (subsection 3.2.2).

In some cases the ranges were too large and results that correspond to unrealistic scenarios were discarded. For example, to estimate the shelf width range to be used in this study I looked at the global average shelf width of 67.6 km and the Oregon shelf, one of the narrowest along the west coast of North America, which is 14km wide at its narrowest (Byrne, 1963). Since the shelf width in the model is 20km the 50% change gives a reasonable 10 – 30 km range.

Another parameter whose range was limited was the respiratory quotient, RQ. As mentioned elsewhere in this study, when the dissolved oxygen is too low in the real world, microbes in the ocean use nitrate (NO_3^{-2}) as a substitute oxidant. Due to the model lacking this denitrification mechanism, the lower layer can run out of O_2 and I get negative O_2 values when model parameters such as RQ are too large. The most likely range for this parameter appears to be 0.5 – 1.33 (Ghashghaie et al., 2003; Tcherkez et al., 2003; Hernández-León and Ikeda, 2005). The model runs with unrealistic parameter range were excluded from further analyses. Finally, the values of w_r^+ and w_r^- that caused the model to crash are unrealistically large but do not linearly translate to very large wind speed increases. Since the relationship between the upwelling forcing and the wind speed is quadratic, doubling the w_r^+ or w_r^- for example, would be associated with wind speed increases of roughly 40%.

5.3 Results

Table 5.2: Reasons for blank spaces in Figures 5.1 and 5.2. The model crashed for values corresponding to the first three rows in this table.

Parameter	Parameter changes [%] (new values)	Comments
w_{sh}	-100 – -75 (0 – 5 km); 75 – 100 (25 – 40 km)	Geometry problem; Lower layer O_2 used up
W_r^+	75 – 100 (77 – 88 m d^{-1})	Amplitude too big and sharp for ODE solver
W_r^-	-100 – -97.5 (64 m d^{-1})	Amplitude too big and sharp for ODE solver
RQ	50 – 100 (1.5 – 2.0)	Lower layer O_2 used up

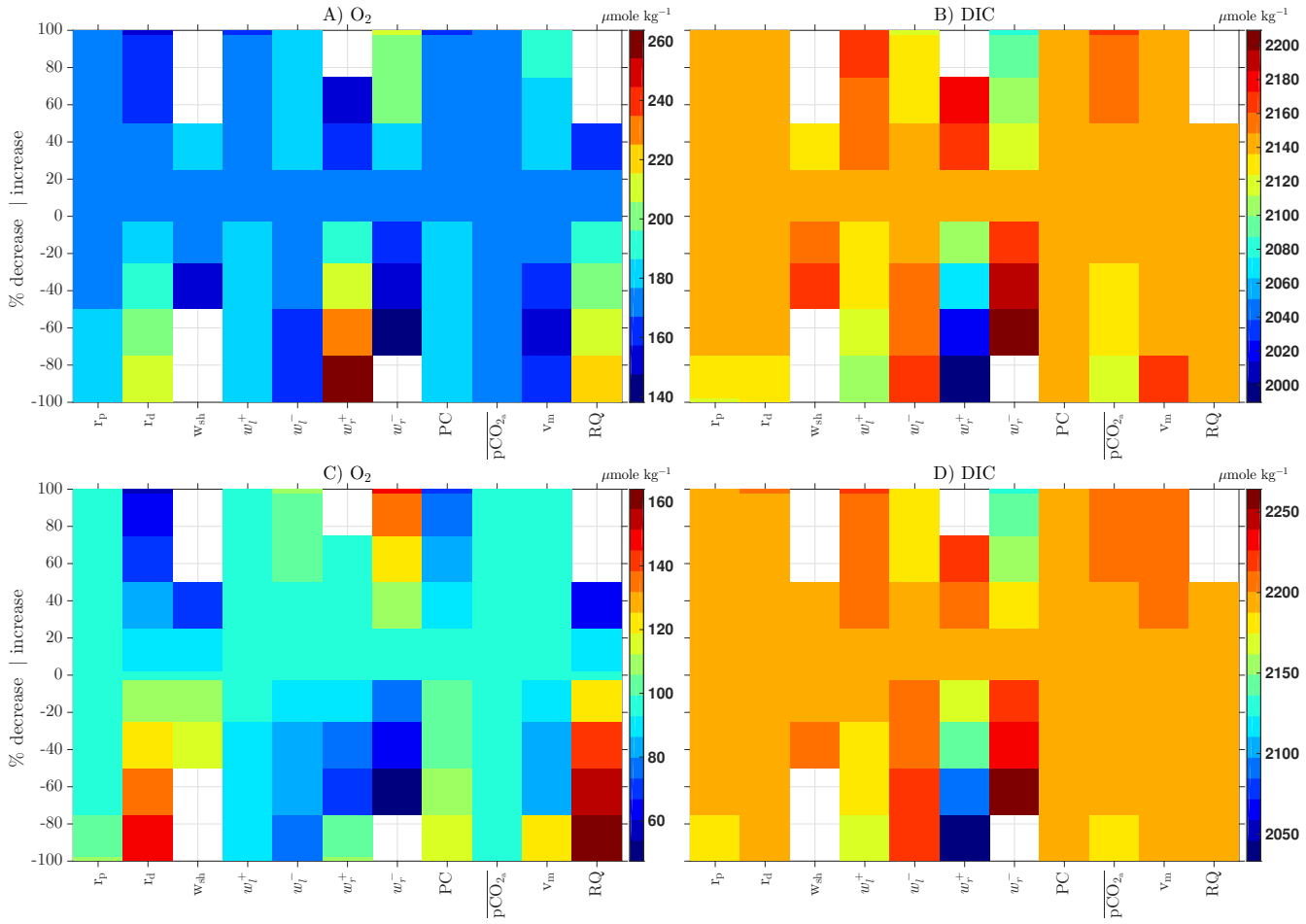

Figure 5.1: The low tail (5^{th} percentile, $q_{05(O_2)}$) and high tail (95^{th} percentile, $q_{95(DIC)}$) of the O_2 and DIC probability distributions, respectively, from the upper shelf (A - O_2; B - DIC) and lower shelf (C - O_2; B - DIC). Each distribution is the result of 100 years model run for 12 sensitivity runs (specifically varying single parameters or boundary conditions by -100 – 100% of its baseline value) on the y-axis, for each of the parameters on the x-axis.

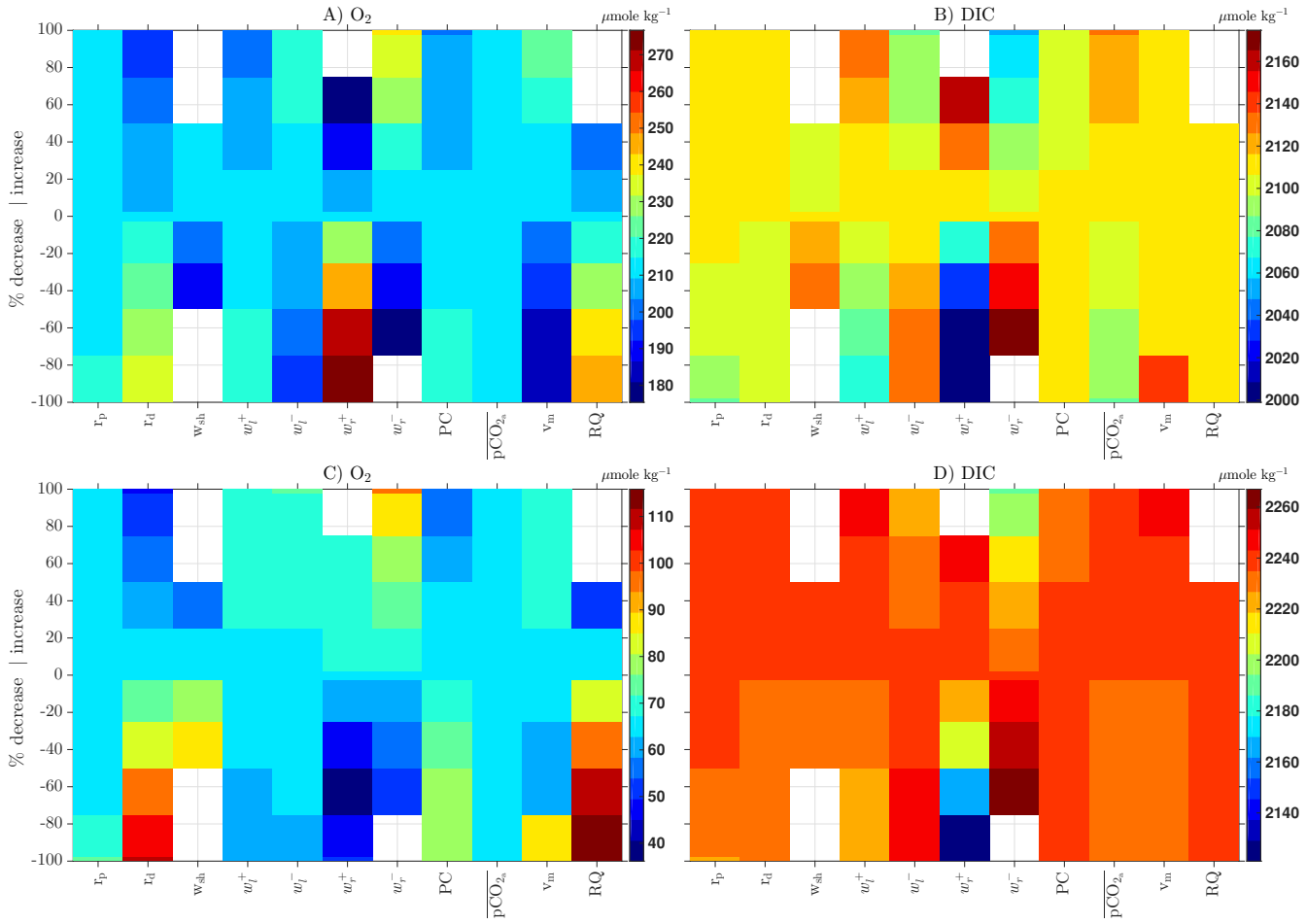

Figure 5.2: The low tail (5^{th} percentile, $q_{05(O_2)}$) and high tail (95^{th} percentile, $q_{95(DIC)}$) of the O_2 and DIC probability distributions, respectively, from the upper slope (A - O_2; B - DIC) and lower slope (C - O_2; B - DIC). Each distribution is the result of 100 years model run for 12 sensitivity runs (specifically varying single parameters or boundary conditions by -100 – 100% of its baseline value) on the y-axis, for each of the parameters on the x-axis.

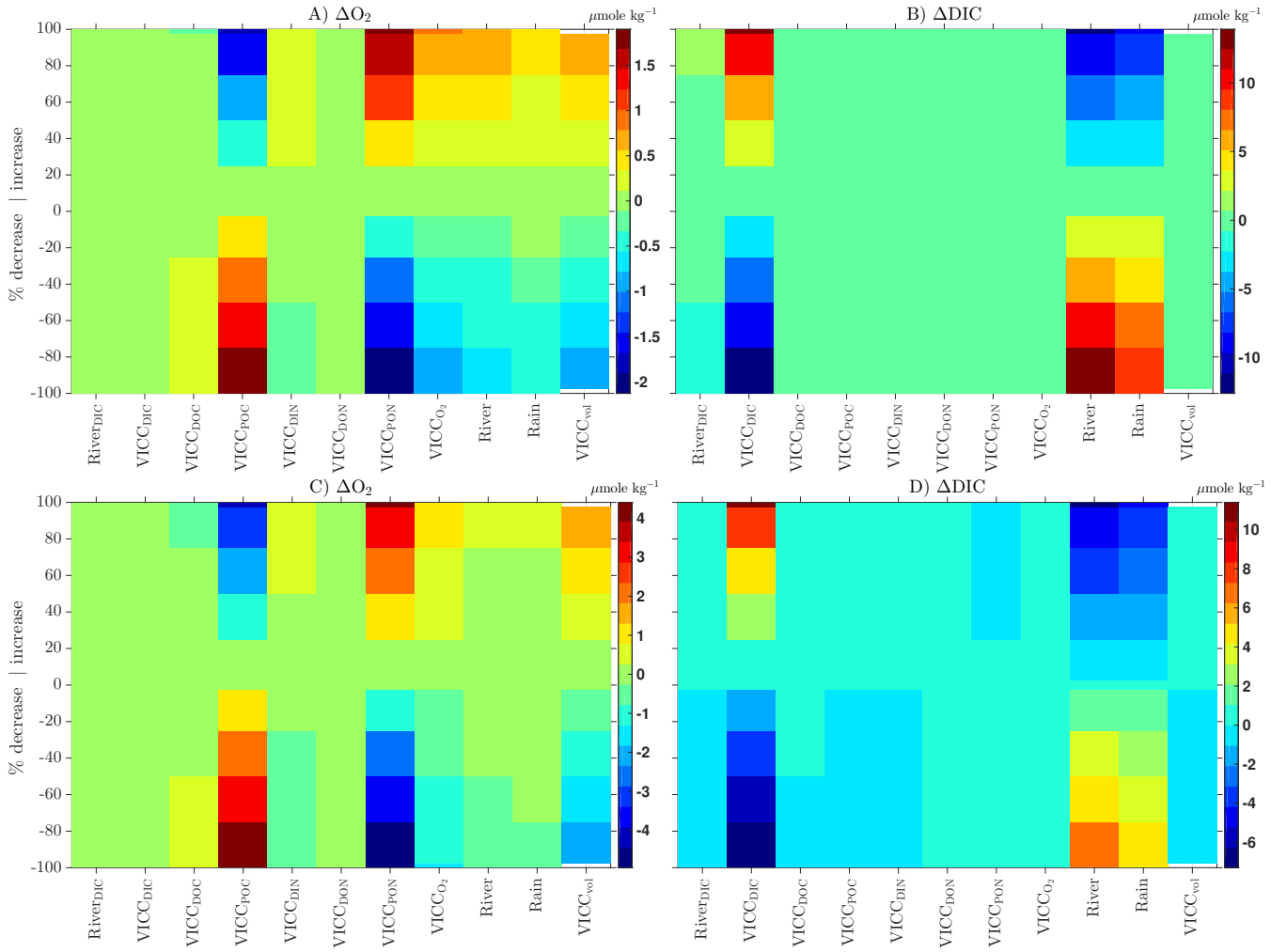

Figure 5.3: Differences between the 5^{th} O_2 (95^{th} DIC) percentiles of the 12 sensitivity runs and the baseline run 5^{th} O_2 (95^{th} DIC) percentiles (Table 5.1). A) Upper shelf O_2. B) Upper shelf DIC. C) Lower shelf O_2. D) Lower shelf DIC. Here the sensitivity tests done on model inner boundary values.

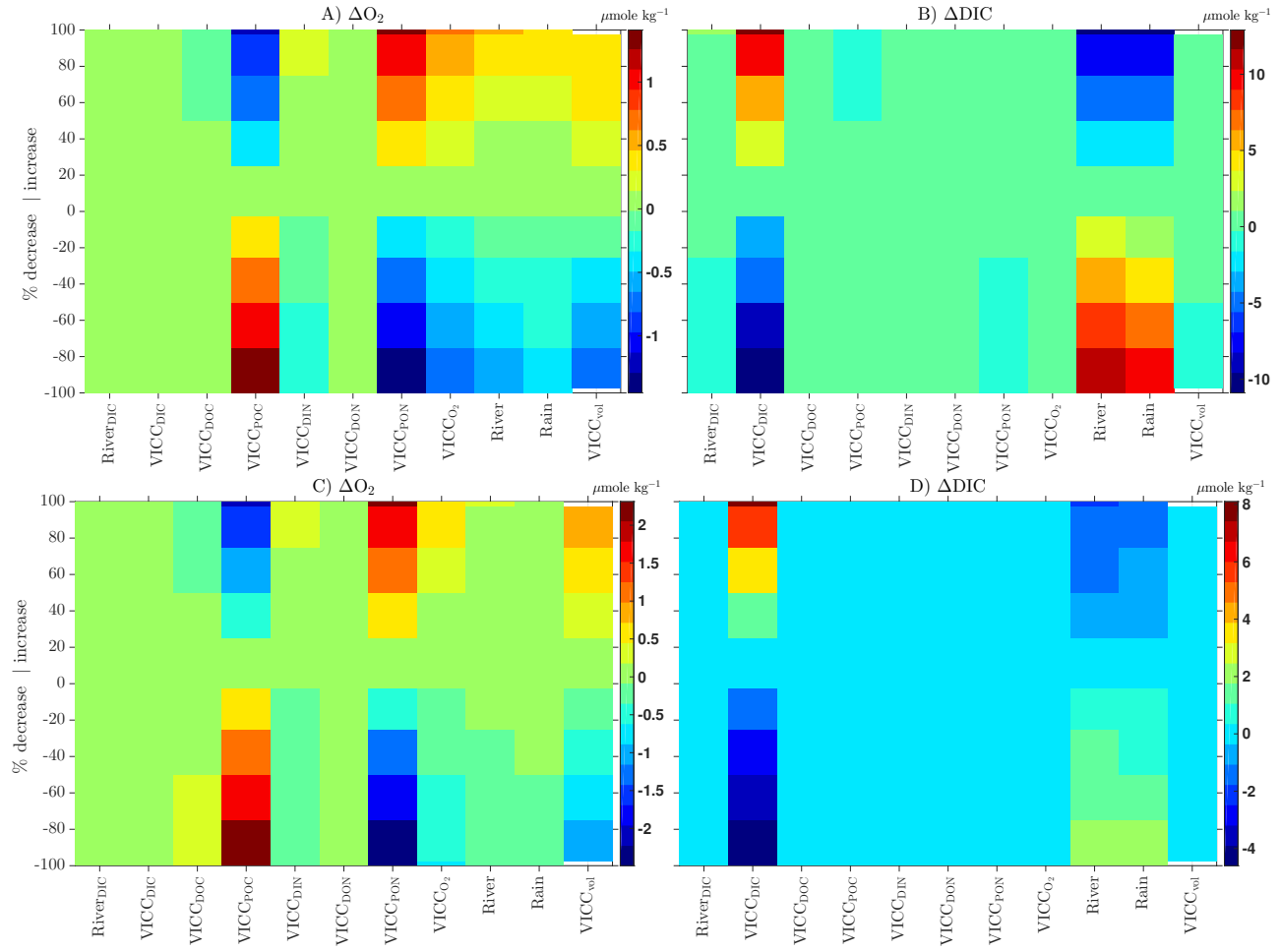

Figure 5.4: Differences between the 5^{th} O_2 (95^{th} DIC) percentiles of the 12 sensitivity runs and the baseline run 5^{th} O_2 (95^{th} DIC) percentiles (Table 5.1). A) Upper slope O_2. B) Upper slope DIC. C) Lower slope O_2. D) Lower slope DIC. The parameters labeled in the x-axes were varied by 12 different percentages (see main text). Here the sensitivity tests done on model inner boundary values.

5.3.1 Biological parameters:

POC remineralization rate, r_p

Remineralization of particulate organic matter does not occur in the model's upper layers (Ianson and Allen, 2002). Any effect of a change in the value of r_p on either $q_{05(O_2)}$ or $q_{95(DIC)}$ in the upper layers is, therefore, indirect. Generally, the model $q_{05(O_2)}$ is not strongly sensitive to r_p for the range of values considered.

A 50 – 100% decrease in r_p was responsible for only 5 – 10 μmole kg^{-1} increase in $q_{05(O_2)}$ in all model boxes. The lower layer boxes showed a slightly higher increase because that is where r_p is directly affecting $q_{05(O_2)}$. Increasing r_p by any amount did not change $q_{05(O_2)}$ in any of the boxes. The sensitivity of $q_{95(DIC)}$ to r_p is similar to that of $q_{05(O_2)}$ except the sign of the $q_{95(DIC)}$ change is reversed (Figures 5.1 and 5.2).

DOC remineralization rate, r_d

Remineralization of DOC occurs in all model layers. The model $q_{05(O_2)}$ and $q_{95(DIC)}$ are more sensitive to r_d than to r_p. A 50 – 100% decrease in r_d caused a roughly 4 times larger (20 – 40 μmole kg^{-1}) $q_{05(O_2)}$ increase in the upper shelf and slope than the same change in r_p. The corresponding $q_{05(O_2)}$ increase in the lower shelf and slope was 30 – 50 μmole kg^{-1}. This change is to be compared with no change when r_p decreased by 50 – 100% in the lower shelf and slope. The main difference here is simply caused by the presence of a higher amount of DOC than POC in the lower layers.

When r_d increased by 50 – 100%, the model $q_{05(O_2)}$ dropped by 20 – 30 μmole kg^{-1} in all the four model boxes. As expected, increasing (decreasing) r_d increased (decreased) $q_{95(DIC)}$. However, the change in $q_{95(DIC)}$ was less than ± 10 μmole kg^{-1} in all boxes except the lower slope, where the $q_{95(DIC)}$ increase was slightly higher.

Specific growth rate, v_m

A faster specific growth rate leads to quicker DIC uptake in the upper layer and export to the lower layer as DOC. Therefore, for a given value of available nutrients, $q_{95(DIC)}$ decreases in the upper layers and increases in the lower layers when v_m is higher. Even when nutrients are limiting, as long as there is enough light, DIC uptake and subsequent export of DOC increases DIC in the lower layers, while DIC decreases in the upper layers. The effect of varying v_m on oxygen is complicated by its nonlinear response. The immediate effect of increased v_m is increasing primary production, which produces more O_2. However, after some time the increased biomass will degrade and consume more O_2, leading to net O_2 reduction. This reduction shifts the O_2 distribution curve to the left (i.e., lowered $q_{05(O_2)}$). There is more influence of air-sea gas exchange on oxygen than on DIC because the former has faster exchange rate (Emerson and Hedges, 2008).

When I reduced v_m by 97.5%, the upper layers' $q_{95(DIC)}$ had a maximum increase of ≈ 45 μmole kg^{-1}. Decreasing v_m by less than 97.5% or increasing it further (100%) did not change $q_{95(DIC)}$ substantially. When I increased v_m by 25 – 100%, the lower shelf, $q_{95(DIC)}$ increased by 5 – 10 μmole kg^{-1}. In the lower slope, the $q_{95(DIC)}$ increase was slightly higher. When v_m was decreased by 25 – 100% the $q_{95(DIC)}$ in the lower layers decreased by about 10 μmole kg^{-1}.

Low v_m leads to low primary production, and reduces upper layer O_2. Considering only biological processes, it should also increase subsurface O_2 due to a reduction in organic matter exported from the upper layers and its eventual reminiralization. However, in the model this sequence is true only when v_m is reduced by 97.5% (Figures 5.1, 5.2). A moderately low v_m actually decreased the lower layers' $q_{05(O_2)}$. This decrease is due to reduction of upper-layer oxygen production and subsequent physical mixing that normally offsets the oxygen deficit following upwelling.

The $q_{95(DIC)}$ in the upper layers is not sensitive to v_m. The upper layers' $q_{95(DIC)}$ was expected to decrease with increasing v_m and vice versa. The median DIC

($q_{50(DIC)}$) shows the expected response to v_m changes (Appendix E.1, Figures E.3 & E.4). Similarly, the lower shelf $q_{95(DIC)}$ was expected to decrease with decreasing v_m, due to reduced downward export of organic matter, but this change was not observed. The $q_{50(DIC)}$ showed this response. The difference between the responses of the median and extremes to v_m indicates that the relative importance of biological and physical factors in controlling median values can be different from that of extremes. For example, transport of DIC to the surface during a strong upwelling may dominate over the effects of the higher/lower uptake rates.

Respiratory quotient, RQ

Only the oxygen budget is affected by RQ. A large (small) value of RQ is related to more (less) oxygen consumption. The impact of changing RQ on O_2 occurs primarily in the lower layers, where the largest physical forcing is mixing and/or advection. For example, for the same 25 – 50 % increase in RQ, $q_{05(O_2)}$ in the upper shelf decreased by 15 – 25 μmole kg^{-1} while in the lower shelf it decreased by 35 – 45 μmole kg^{-1}. When RQ was reduced by only 2.5 – 25%, $q_{05(O_2)}$ in the upper shelf increased by up to 15 – 25 μmole kg^{-1}. In the upper slope, the increase was only about 10 μmole kg^{-1}. When RQ was reduced by 97.5%, the largest increase in $q_{05(O_2)}$ was found in the lower shelf (about 60 μmole kg^{-1}) , followed by the lower slope (40 μmole kg^{-1}).

5.3.2 Atmospheric CO_2

The rise of atmospheric CO_2 (represented here as the partial pressure, $\overline{pCO_{2a}}$) and its impact on climate and the ocean carbon cycle have been studied in great detail (e.g., Kleypas et al. (1999); Feely et al. (2004); Orr et al. (2005); Doney et al. (2009); Vargas et al. (2013)). In this study the atmospheric CO_2 sensitivity experiment is not strictly speaking a climate change simulation, as all other physical forcing kept the same. It is included to show what happens to the carbon system if $\overline{pCO_{2a}}$ changes while everything else remains at the current condition.

The global mean $\overline{pCO_{2a}}$ during the year 2015 of 400 ppm and a seasonal cycle amplitude of 17ppm (from https://www.co2.earth/) was used in the base run. This mean value was varied in the sensitivity runs between 200 ppm (CO_2 level 20 thousand years ago, Ward and Kelly (2004)) and 800 ppm (CO_2 level beyond which even if CO_2 emissions become zero the quasi-equilibrium CO_2 concentration reaches $\sim$ 500 ppm, Solomon et al. (2009)).

Doubling $\overline{pCO_{2a}}$ increased $q_{95(DIC)}$ in the upper layers by 50 μmole kg^{-1} (the $q_{50(DIC)}$ increased by about 20 μmole kg^{-1}), while reducing $\overline{pCO_{2a}}$ by half decreased $q_{95(DIC)}$ by about 25 μmole kg^{-1} (decreased $q_{50(DIC)}$ by about 15 μmole kg^{-1}). The $q_{95(DIC)}$, in any of the model boxes, showed almost no response to $\overline{pCO_{2a}}$ changes between -25% and 50%.

The response of the upper layer DIC to varying $\overline{pCO_{2a}}$ is expected. Since the lower layer is not directly involved in gas exchange, the effect of changing $\overline{pCO_{2a}}$ in the layer was indirect and was not necessarily expected (Figures 5.1, 5.2, 5.3, and 5.4). Increasing (decreasing) $\overline{pCO_{2a}}$ by 75% – 100% increased (decreased) $q_{95(DIC)}$ in the lower layers by 10 – 20 μmole kg^{-1}. This change in $q_{50(DIC)}$ is slightly smaller (10 – 15 μmole kg^{-1}). These changes in the lower layer DIC are caused by present day levels of vertical mixing and downwelling, mechanisms which are likely to change with a changing climate (Bograd et al., 2009; Foreman et al., 2011; Wang et al., 2015).

5.3.3 Physical Parameters

Up/downwelling velocity:

The general effects of upwelling and downwelling on the mean states of DIC and oxygen have been examined by Connolly et al. (2010); Crawford and Peña (2013); Booth et al. (2014); Lachkar (2014) and others. To my knowledge, previous work has not quantitatively assessed the relative effects of locally and remotely generated upwelling velocities on DIC and oxygen extremes in the study region, or elsewhere. In the study region these two forcing mechanisms contribute to up/downwelling over

different frequency ranges. It is therefore important to establish a clear understanding of the impact of each forcing on oxygen and carbon extremes.

Oxygen

Increasing the upwelling strength decreased $q_{05(O_2)}$ in the upper layers and increased it in the lower layers although the increase was small (Figures 5.1, 5.2). The upper layer $q_{05(O_2)}$ decrease is either a direct response to the upwelling of oxygen-poor water or a delayed response to higher production (and subsequent remineralization) following strong upwelling. A challenge in associating a change in forcing to a particular response in my analysis in this section is that the response of the distribution of O_2 to a change of a parameter involves contributions from physical and biological processes across a range of timescales. Let us say the upwelling strength is increased throughout the year. Since most of the upwelling occurs in the spring and summer, the response of $q_{05(O_2)}$ to increased early summer upwelling could be immediate, or could occur a few days later, or even later in the summer (Chapter 4). The immediate and late summer responses would tend to reduce the $q_{05(O_2)}$ throughout the water column (by advection and respiration, respectively). In contrast, the response at the intermediate timescale would tend to increase $q_{05(O_2)}$ in the upper layer given other conditions also contribute to primary production. The small increase in $q_{05(O_2)}$ in the lower layers could be explained by the intermediate timescale response where the low oxygen in the upwelled water is offset by mixing with high oxygen upper layer water.

There is no large difference in the timing of local vs remote upwelling forcing in the model partly because the foot-print of the wind forcing is large. These two forcing also do not show large differences in frequency content. Their effect on local upwelling is what is frequency dependent as the ocean acts as a low pass filter to the remote wind forcing. So, the differences in the responses to local vs remote forcing lies in the differences in the frequencies at which each is relevant and magnitude of the forcing. A 50 – 75% stronger w_l^+ decreased $q_{05(O_2)}$ by 10 – 20 μmole kg^{-1} in the upper shelf and by 5 – 15 μmole kg^{-1} in the upper slope (Figures 5.1, 5.2). In the lower layers, $q_{05(O_2)}$ increased by about 5 μmole kg^{-1}. A 50 – 75% stronger w_r^+ decreased $q_{05(O_2)}$

by 25 – 35 μmole kg^{-1} in the upper layers. The lower layers' $q_{05(O_2)}$ did not change. The lower layers' $q_{05(O_2)}$ sensitivity to either w_l^+ or w_r^+ is offset by remineralization which is particularly strong for very large upwelling.

The relatively strong winter offshore winds keep the offshore surface water saturated with O_2. Since downwelling is more common in the winter, the strong onshore flow flushes both the upper and lower model boxes with oxygen-rich water. The changes in extremes due to changes in downwelling seen in Figures 5.1 and 5.2 are, therefore, mainly due to winter conditions.

A 50 – 75% increase in w_l^- increased $q_{05(O_2)}$ by 10 – 20 μmole kg^{-1} in the upper layers while the same levels of increase in w_r^- increased $q_{05(O_2)}$ by 25 – 35 μmole kg^{-1}. The lower layer $q_{05(O_2)}$ also increased by a similar amount. When I decreased w_l^- and w_r^- by 50 – 75%, the changes in $q_{05(O_2)}$ were similar in magnitude but opposite to the changes we saw above for the 50 – 75% increase in downwelling. The similar responses in the upper and lower layers are further evidence of wintertime, physically-dominated responses.

The same level of changes in w_l^+ (or w_r^+) and w_l^- (or w_r^-) did not produce equal magnitude changes of opposite sign. For example, a 50 – 75% weaker w_r^+ increased the upper shelf $q_{05(O_2)}$ by 55 – 65 μmole kg^{-1} while a 50 – 75% weaker w_r^- decreased it by 25 – 35 μmole kg^{-1}. In the lower layers, the effect of occasional downwelling events during the summer upwelling season is complicated by two competing processes. Since the lower layer oxygen level is always lower than it is in the upper layer (in the model depth range), downwelling almost always ventilates the lower layers. On the other hand, nutrient poor offshore water brought by downwelling reduces photosynthesis. As a result, oxygen levels in the upper layers and, by vertical mixing, the lower layers will be reduced. During the wintertime, downwelling brings water that has higher levels of oxygen into the upper shelf and slope regions. The lower layers are ventilated by vertical advection and mixing with the upper layers.

DIC

Intense (25 – 75% more) local or remote upwelling increased the value of $q_{95(DIC)}$

in both the upper and lower shelf (Figure 5.1). Because the local Ekman upwelling is weaker, w_r^+ is normally higher in magnitude than w_l^+. The effect of w_r^+ on $q_{95(DIC)}$ is about twice as large as that of w_l^+ when both increased by the same amount. Increasing w_r^+ by more than 75% caused the model to crash (Table 5.2). Increasing the upwelling strength had a similar effect on both the upper shelf and slope $q_{95(DIC)}$ (Figure 5.2). For example, a 25 – 75% higher w_r^+ caused 45 – 55 μmole kg^{-1} more $q_{95(DIC)}$. The $q_{95(DIC)}$ increase from a 25 – 75% higher w_l^+ was only 15 – 25 μmole kg^{-1}. The lower slope, however, showed lower sensitivity to upwelling when compared with the lower shelf. A 25 – 75% higher w_r^+ caused the lower shelf $q_{95(DIC)}$ increase by 40 – 50 μmole kg^{-1} while it increased the lower slope $q_{95(DIC)}$ by 15 – 25 μmole kg^{-1}.

When the local and remote upwelling velocities were made weaker, $q_{95(DIC)}$ in both the upper and lower shelf boxes dropped. In all the model boxes, the $q_{95(DIC)}$ drop associated with 25 – 75% reduced w_r^+ was much larger (115 – 125 μmole kg^{-1}) than the one associated with 25 – 75% reduced w_l^+ (15 – 25 μmole kg^{-1}). When w_r^+ was reduced by 97.5%, the $q_{95(DIC)}$ became about 140 μmole kg^{-1} lower. The same level of reduction in w_l^+ caused only about 40 μmole kg^{-1} lower $q_{95(DIC)}$ in both the upper and lower shelf. $q_{95(DIC)}$ in the slope boxes dropped by 90 – 110 μmole kg^{-1} when a 97.5% lower w_r^+ was used. The $q_{95(DIC)}$ decrease associated with a 97.5% reduced w_l^+ was about twice as large in the upper slope than in the lower slope ($\sim$15 μmole kg^{-1}).

Increasing w_r^+ (w_l^+) by 97.5% had a net effect of increasing the lower shelf $q_{95(DIC)}$ by 50 μmole kg^{-1} (25 μmole kg^{-1}), while decreasing w_r^+ (w_l^+) by 97.5% had a net effect of decreasing $q_{95(DIC)}$ by 140 μmole kg^{-1} (40 μmole kg^{-1}). In this particular example, the difference between the effects of decreased w_r^+ and w_l^+ is 100 μmole kg^{-1} while the difference between the effects of increased w_r^+ and w_l^+ is only 25 μmole kg^{-1}. The difference in $q_{95(DIC)}$ responses to changed w_r^+ and w_l^+ arises from the fact that the baseline run w_r^+ is already large and decreasing it has a stronger effect on $q_{95(DIC)}$ than increasing it.

When w_l^- was increased by 25–75%, $q_{95(DIC)}$ in the upper shelf decreased by about 10 – 20 μmole kg^{-1}. A similar increase in the w_r^- caused the $q_{95(DIC)}$ in the upper shelf to decrease by 25 – 45 μmole kg^{-1}. When w_l^- was reduced by 25 – 75%, $q_{95(DIC)}$ increased by 15 – 25 μmole kg^{-1} in the upper shelf and by 10 – 20 μmole kg^{-1} in the lower shelf. $q_{95(DIC)}$ increased by 30 μmole kg^{-1} in the upper slope and by only 10 μmole kg^{-1} in the lower slope. A similar decrease in w_r^- caused 40 – 60 μmole kg^{-1} more in the upper shelf and slope, and 30 – 50 μmole kg^{-1} more in lower shelf. In the lower slope the increase was 10 – 20 μmole kg^{-1}.

One of the most important lessons from the up/downwelling sensitivity analysis is that the relatively low frequency remote forcing cannot be neglected. In fact, the DIC/O_2 responses to remote forcing, which by construction in this model is larger in magnitude and lower in frequency, is larger than relatively high frequency local forcing. The analysis also showed DIC is more sensitive to remote forcing than O_2 is, because the latter is influenced more by high frequency processes such as local gas exchange.

Shelf width:

Oxygen

Changes in the shelf width have contrasting effects on $q_{05(O_2)}$ in the upper and lower layers (Figures 5.1, 5.2). A 25 – 50 % wider shelf increased the upper shelf $q_{05(O_2)}$ by 5 – 10 μmole kg^{-1}, but did not change the upper slope $q_{05(O_2)}$. In the lower shelf, the $q_{05(O_2)}$ level dropped by about 25 – 35 μmole kg^{-1}. In the lower slope the $q_{05(O_2)}$ drop was 10 – 20 μmole kg^{-1}. When the shelf width was narrowed by 25 – 50 %, the upper shelf and slope $q_{05(O_2)}$ decreased by 15 – 25 μmole kg^{-1}, and the lower shelf and slope $q_{05(O_2)}$ increased by the same amount.

DIC

DIC in the upper layers is quite sensitive to the shelf width (Figures 5.1, 5.2). When the shallow and relatively wide (120 m deep and 10 km wide) shelf is made narrower, values of $q_{95(DIC)}$ in both the upper shelf and slope increase. A 25 – 50 %

narrower shelf had 25 – 35 μmole kg^{-1} more $q_{95(DIC)}$ in the upper shelf and slope. However, the lower shelf and slope $q_{95(DIC)}$ did not change. A 25 – 50 % wider shelf, on the other hand, had about 10 μmole kg^{-1} less $q_{95(DIC)}$ in the upper shelf and slope.

Decreasing the shelf width has a similar effect on $q_{05(O_2)}$ and $q_{95(DIC)}$ as increasing upwelling strength. In a narrow shelf, the upwelled water quickly leaves the shelf region, as it does when upwelling is relatively stronger. The amount of time the upwelled nutrient rich water stays (residence time) in the shelf region becomes lower in these two cases. In the upper shelf, this phenomenon lowers oxygen production as local primary producers cannot use all the nutrients before its rapid offshore transport. This relatively low oxygen water gets mixed with water in the upper slope region. Oxygen levels in the upper slope also drop due to offshore transport of the shelf water that has failed to produce more oxygen. Only a fraction of the nutrient that is transported offshore could actually stay in the slope region and fuel more oxygen production. The majority of the nutrients end up leaving the model box(out side slope) and fail to cause oxygen production within the model boxes. This reduced residence time has an opposite effect in the lower layer oxygen pool since there will be less biological export of organic matter, which consumes oxygen during remineralization.

The biological uptake of DIC depends on the availability of nutrients, which are flushed out quickly in narrower shelves. A lower DIC uptake results in the subsequent reduction in biological export to the lower layer. With a narrower shelf the nutrients in the upper layers are quickly driven offshore, a process which slows down DIC uptake and results in increases of both the mean and $q_{95(DIC)}$. In the lower layers, DIC is not directly affected by changes in the shelf width because there is no DIC uptake. Also, the horizontal DIC gradients between the lower slope and the deep ocean are not as strong as they are between the open ocean and the upper slope. Changes in the shelf width have a stronger effect on $q_{95(DIC)}$ where there is already a strong DIC gradient which in this case is the upper layers.

5.3.4 Effects of the Vancouver Island Current

The main source of the Vancouver Island Coastal current is the outflow from the Juan de Fuca Strait. During the snow melt season, the outflow volume increases (Pawlowicz and Farmer, 1998). However, due to the strong tidal mixing within the narrow straits and passages, the water at the seaward mouth of the strait is relatively salty and rich in nutrients (Masson, 2006). In order to assess the impacts of this current on the model oxygen and DIC extremes, I conducted sensitivity experiments on both the discharge volume as well as the amount of carbon and oxygen in this water (Figures 5.3, 5.4).

Unlike the parameters I have so far considered, the sensitivity of extremes in the model to quantities related to the VICC was weak. This weak sensitivity is independent of shelf and slope or the upper and lower layers. Therefore, I describe the main features of the model sensitivity results related to VICC without referring to a particular region of the model. In reality, the response in the upper shelf is expected to be the strongest due to its proximity to the JDF but the sensitivity is small across the model regions.

The VICC volume has a relatively small effect on the model $q_{95(DIC)}$ and $q_{05(O_2)}$ (Figures 5.3, 5.4). Removing all the POC in the VICC increased $q_{05(O_2)}$ by a maximum of 4 μmole kg^{-1}. When I doubled the POC, the maximum decrease in $q_{05(O_2)}$ was only 4 μmole kg^{-1}. The same experiment with PON gave similar but opposing results. Neither POC nor PON in the VICC affected $q_{95(DIC)}$. In fact, the only quantity in the VICC that affected $q_{95(DIC)}$ was DIC itself. Doubling the DIC in the VICC increased $q_{95(DIC)}$ by 10 μmole kg^{-1} and omitting it reduced $q_{95(DIC)}$ by the same amount. Finally, the effect of VICC on $q_{05(O_2)}$ and $q_{95(DIC)}$ slightly increased when upwelling was weaker (results not shown). This result suggests the lack of strong sensitivity to quantities in the VICC is due to the relatively small total VICC flux compared to other fluxes such as upwelling and gas fluxes.

5.3.5 Effects of fresh water input

Fresh water input in the model, represented by river runoff and precipitation, affect DIC through dilution (IA02). The upper shelf $q_{95(DIC)}$ was about 10 μmole kg^{-1} more and about 10 μmole kg^{-1} less when runoff was turned off and doubled, respectively (Figures 5.3 and 5.4). As expected, the upper slope $q_{95(DIC)}$ sensitivity to runoff was slightly lower than the upper shelf $q_{95(DIC)}$ because the effect on it is indirect. Identical relative changes in precipitation, which remained the same in both shelf and slope, gave nearly identical effects in both upper shelf and slope. Doubling the precipitation rate decreased $q_{95(DIC)}$ by about 10 μmole kg^{-1} and turning precipitation off increased $q_{95(DIC)}$ by about 10 μmole kg^{-1} in both upper shelf and slope. The effects of runoff and precipitation on $q_{95(DIC)}$ in the lower layers was about half of the effects in the upper layers.

5.3.6 Sensitivity During Upwelling Season

The sensitivity to certain parameters, especially biological ones, was substantially higher when I restricted my analyses to the upwelling season (Year days 183 – 206). For example, when v_m was reduced by 75 – 100%, the decrease of $q_{05(O_2)}$ in the upper layers during the upwelling season (Figures E.1 & E.2) was twice as large as in the full year result (Figures 5.1 & 5.2). The change in sensitivity of $q_{05(O_2)}$ to RQ was similar. The main reason for the sensitivity to some biological parameters is higher in the upwelling season is because it is in this season that these parameters matter the most.

Unlike the sensitivity to the biological parameters, the sensitivity of $q_{05(O_2)}$ in the upper layers to the physical parameters did not systematically increase in the upwelling season. For example, a 50 – 75% weaker w_r^+ increased the upper shelf $q_{05(O_2)}$ in the full-year by 55 – 65 μmole kg^{-1} while the same percent change in w_r^+ increased the upper shelf $q_{05(O_2)}$ in the upwelling season by 40 – 50 μmole kg^{-1}. Similarly, the $q_{05(O_2)}$ sensitivity to reducing w_r^+ by 75 – 100% was about 10 – 20 μmole kg^{-1} less

in the upwelling subset than in the full year. The reduced sensitivity to upwelling in the upwelling season could be due to the more active biological activity offsetting the effect of intense upwelling, which lifts oxygen-poor water to the upper layer. The upper shelf $q_{95(DIC)}$ sensitivity to most parameters was always larger in the upwelling season except for the slightly lower (< 2 μmole kg^{-1}) sensitivity to $\overline{pCO_{2a}}$.

In the lower shelf, the upwelling season $q_{05(O_2)}$ sensitivity was higher to almost all the parameters considered than the sensitivity of the full year $q_{05(O_2)}$. In the upwelling season both physical (advection) and biological process work in the same way to primarily lower oxygen. Therefore, $q_{05(O_2)}$ sensitivity during upwelling season must be stronger than it is during the full year. Upwelling affects both upper and lower layer $q_{05(O_2)}$ in the same way by lowering it. Biological processes, on the other hand, affect the upper and lower layer $q_{05(O_2)}$ in opposite way. They increase $q_{05(O_2)}$ in the upper layer and decrease it in the lower layer. Therefore, the sensitivity decrease in the upper layer and increase in the lower layer of $q_{05(O_2)}$ to upwelling during the upwelling seasons is mostly a consequence of biological processes reducing the effects of physical processes in the upper layers and reinforcing them in the lower layers.

The largest sensitivity change in the lower layers was to RQ, increased by about 50%. The change in sensitivity to v_m, in contrast, was quite small as it does not directly affect the lower layer $q_{05(O_2)}$. The lower shelf $q_{95(DIC)}$ sensitivity to almost all parameters was larger in the upwelling season, with the largest change being about 45% more for a 75 – 100% reduced r_p. In the lower slope, neither of the $q_{05(O_2)}$ and $q_{95(DIC)}$ show change in sensitivity when the model results were subset to the upwelling season (Figure E.2).

5.3.7 Sensitivity of Timing of Extremes

In addition to the sensitivity of actual values of DIC and O_2 extremes, I investigate the sensitivity of their timing (as defined in chapter 4) by defining

$$\Delta\mathcal{F} = \mathcal{F}_i - \mathcal{F}, \tag{5.1}$$

where $\mathcal{F}_i$ is the $\mathcal{F}$ associated with the i^{th} sensitivity run of the 12 perturbation runs (for each parameter when applicable) and $\mathcal{F}$ is the baseline $\mathcal{F}$. As noted above, model runs other than the baseline are limited to 100 years. To avoid sampling bias when comparing the baseline $\mathcal{F}$ results with another model run $\mathcal{F}$, I limited the standard baseline run to the same 100 years for this purpose. The $\mathcal{F}$ curves from this baseline run are shown on top of each $\Delta\mathcal{F}$ plot (Figures 5.5 – 5.7). These curves are similar to those of $\mathcal{F}$ from the (present-day) 1017 year baseline run (Figure 4.15).

Effects of locally generated upwelling/downwelling on $\mathcal{F}$

In the upper layers, the sensitivity of $\mathcal{F}$ to local upwelling is either dampened by biological processes or air-sea gas exchange keeps the number of extreme events constant. Given that air-sea gas exchange is more important for O_2 than it is for DIC, it is likely the biological fluxes are responsible for keeping the number of days with the joint O_2 - DIC extremes near constant as the value of w_l^+ changes (Figure 5.5aA–B). In the main upwelling season (mid-April – mid-October) $\mathcal{F}$ in any of the model boxes did not change in response to changes in w_l^+. In addition to possible influence from biological processes to maintain lower number of days with joint extremes, the fact that the local upwelling strength is relatively small likely contributes to the absence of $\mathcal{F}$ sensitivity in the upwelling season.

Locally forced upwelling has the biggest impact on $\mathcal{F}$ during late fall to winter in the lower shelf and only during late fall in the lower slope (Figure 5.5aC–D). Local upwelling (w_l^+) at this time of the year, although less frequent than in the main upwelling season, is stronger and the change in its magnitude impacts $\mathcal{F}$. A similar but much weaker sensitivity is observed in the upper layers.

The changes in $\mathcal{F}$ corresponding to increased and decreased local downwelling

(w_l^+), which mostly occurs during winter with isolated events in summer, were nearly mirror images of one other. The $\Delta\mathcal{F}$ results for w_l^+ and those for w_l^-, are also the mirror images of one another (Figures 5.5a and 5.5b).

Effects of remotely generated upwelling/downwelling on $\mathcal{F}$

When remotely generated upwelling is decreased, there is a general decrease in the number of days with the joint DIC-O_2 extremes. Increasing this upwelling forcing has a minor effect of increasing the fraction of days with the extremes. Similarly to locally generated up/downwelling changes in remotely-forced upwelling do not affect $\mathcal{F}$ in the upwelling season (Figure 5.6a). Outside the upwelling season, changes in w_r^+ caused stronger responses by $\mathcal{F}$. For some year days, the change in $\mathcal{F}$ due to w_r^+ was more than twice the change in $\mathcal{F}$ due to w_l^+. Unlike in the w_l^+ changes, the w_r^+ changes are felt more in the upper than in the lower layers. The contrasting responses of $\mathcal{F}$ to local and remote upwelling can be explained by the relative strengths of the local and remote forcing in the model. Why the effect of changing w_r^+ matters more in the upper layer $\mathcal{F}$ than it does in the lower layers is not clear. One factor in the difference of responses may be the differences in timescales of the local and remote forcing.

The w_r^- appears to be important only in the lower layer during the late fall to winter seasons. Decreasing it by 25 – 75% changes $\Delta\mathcal{F}$ values up to 0.1. Since $\mathcal{F}$ values for the lower layers are below 0.05, the 0.1 value of $\Delta\mathcal{F}$ represents about doubling of days with combined DIC and O_2 extremes.

Effects of Specific Growth Rate, v_m, on $\mathcal{F}$

During the summer, decreasing v_m by more than 75% increased $\mathcal{F}$ in the upper layers but did not change $\mathcal{F}$ in the lower layers (Figure 5.7a). Increasing v_m (even doubling it) in the summer had no effect on $\mathcal{F}$. The lack of response to increased v_m or a decrease by less than 75% of v_m during summer is a result of competing physical and biological processes, which act in opposite direction in the upper layers.

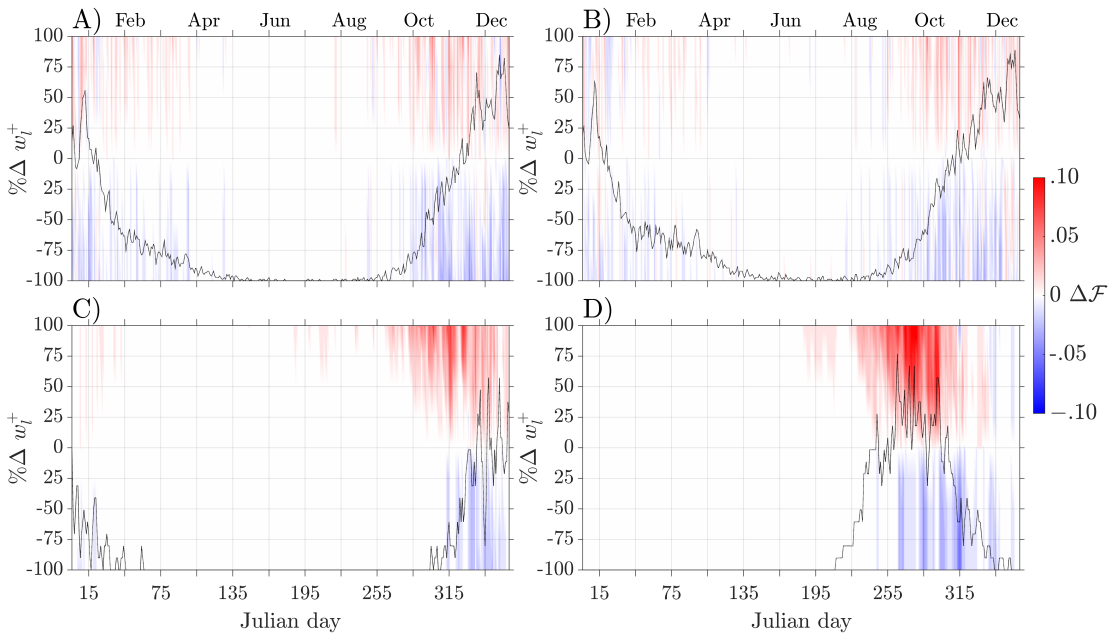

(a) $\Delta\mathcal{F}$ of local upwelling sensitivity runs. A) upper shelf. B) upper slope. C) lower shelf. D) lower slope.

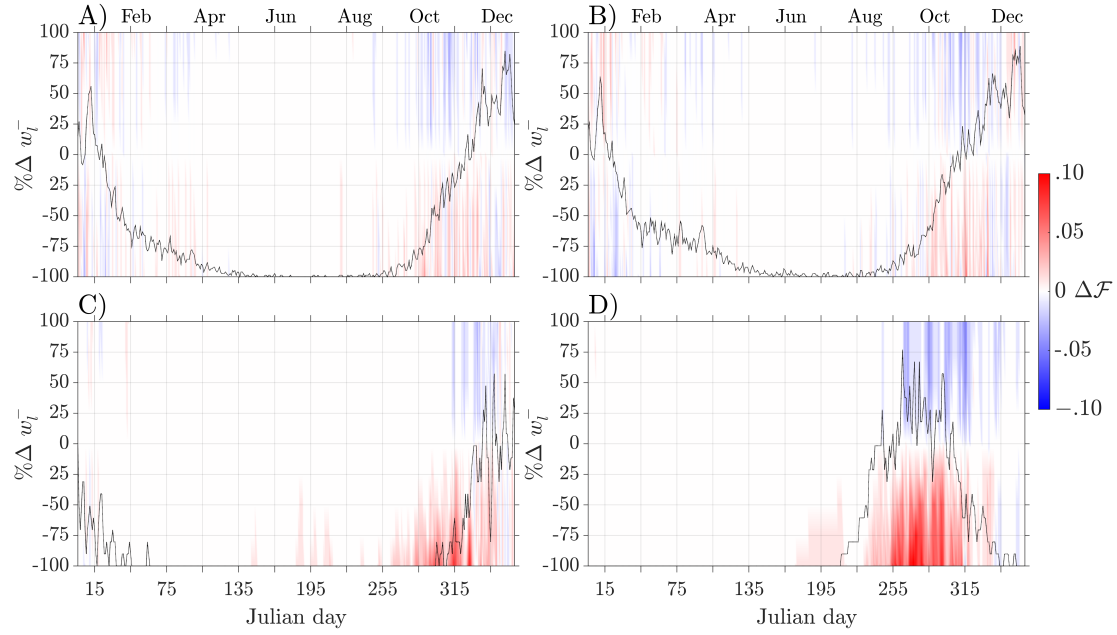

(b) $\Delta\mathcal{F}$ of local downwelling sensitivity runs. A) upper shelf. B) upper slope. C) lower shelf. D) lower slope.

Figure 5.5: The difference in the number of days with joint DIC – O_2 extremes in the baseline and that of the sensitivity model runs. The $\mathcal{F}$ curves from the baseline run are shown on top of each plot.

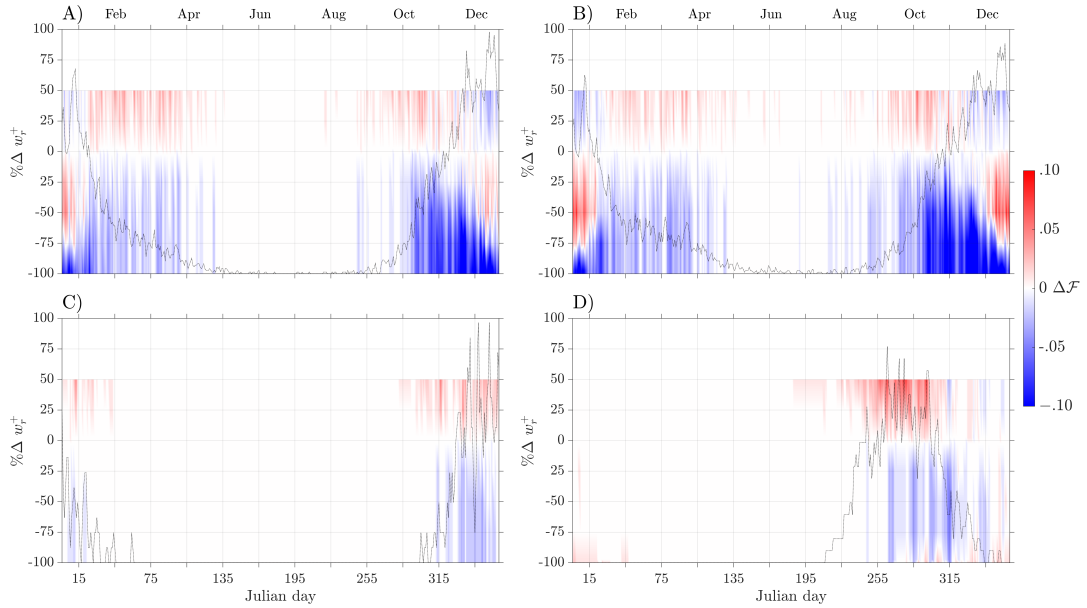

(a) $\Delta\mathcal{F}$ of remote upwelling sensitivity runs. A) upper shelf. B) upper slope. C) lower shelf. D) lower slope.

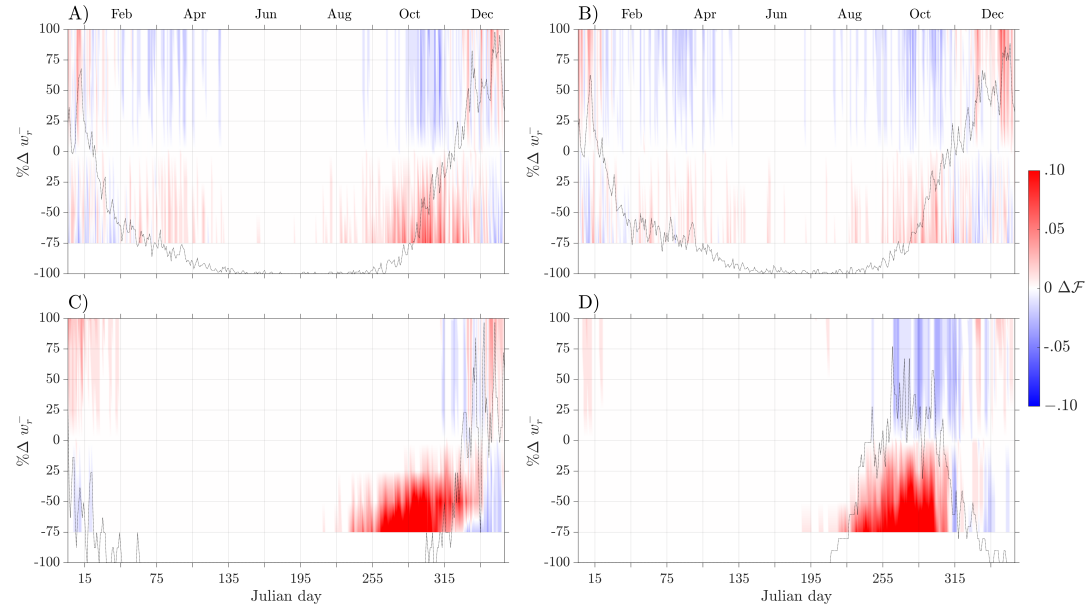

(b) $\Delta\mathcal{F}$ of remote downwelling sensitivity runs. A) upper shelf. B) upper slope. C) lower shelf. D) lower slope.

Figure 5.6: The difference in the number of days with joint DIC – O_2 extremes in the baseline and that of the sensitivity model runs. The $\mathcal{F}$ curves from the baseline run are shown on top of each plot.

During the winter, the upper layer $\mathcal{F}$ values increased with increasing v_m and decreased with decreasing v_m. Since v_m is less important in the winter, this relatively strong response in the upper layers to v_m was not expected. It could be a delayed response to strong/weak productive summer caused be increased/decreased v_m. Another explanation of the strong sensitivity to v_m during winter is that the upper layers, where biological and physical processes act in opposite ways, are dominated by physical processes that drive the DIC – O_2 joint extremes. The lower layers showed only negligible changes in $\mathcal{F}$.

Effects of Shelf Width, w_{sh}, on $\mathcal{F}$

As long as the specific growth rate is constant, the shorter residence time in a narrow shelf decreases $q_{05(O_2)}$ and increases $q_{95(DIC)}$ in the upper layers (both consistent with a reduction in the strength of biological processes relative to physical ones, Figures 5.1 & 5.2). Whether the frequency of the joint DIC – O_2 extremes change with shelf width or not is independently determined by examining the $\Delta\mathcal{F}$ results. Except for the slight winter time $\mathcal{F}$ increase (~ 0.05) with shelf width decrease and slight decrease (~ -0.05) with shelf width increase, $\mathcal{F}$ is not affected by changes in shelf width (Figures 5.7bA & B). The lack of change in the upper layer $\mathcal{F}$ with shelf width during the summer and the small changes in the winter show the shelf width effect on the upper layer extremes is mainly through changes in the values of these extremes values of ($q_{95(DIC)}$ and $q_{05(O_2)}$) and not through changes in the frequency at which the extremes occur.

5.4 Conclusion

In this Chapter, I considered the sensitivity of extremes of DIC and O_2 to variations in model parameters. This thesis has, for the first time, quantified the relative importance of local and remote wind forcing to carbon and oxygen extreme events, specifically in the southern Vancouver Island region. In this chapter I considered the

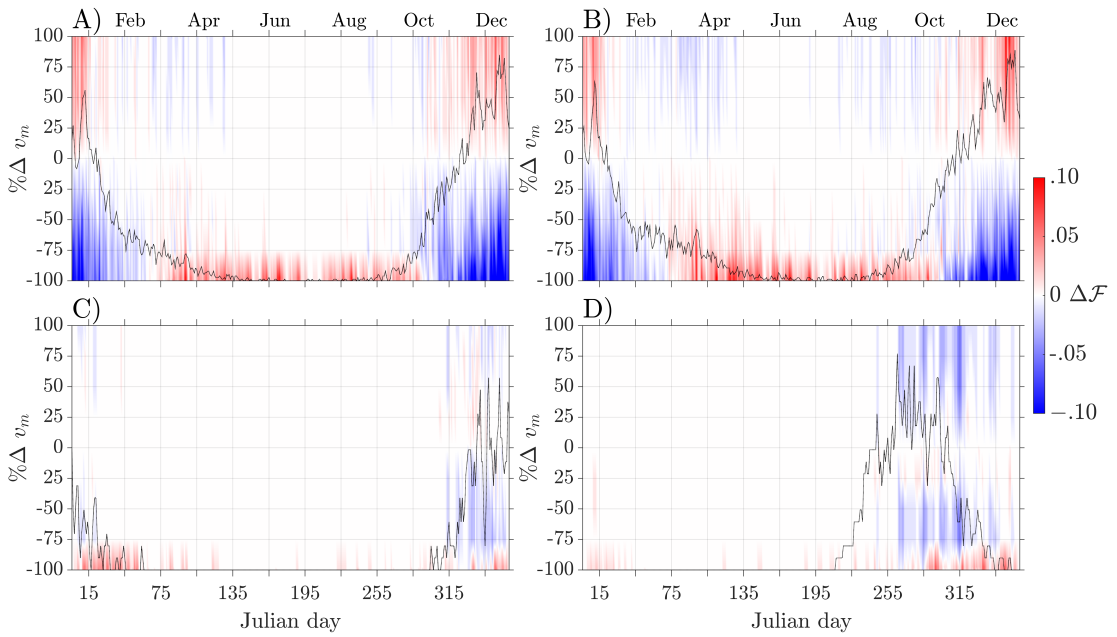

(a) $\Delta\mathcal{F}$ of specific growth rate (v_m) sensitivity runs. A) upper shelf. B) upper slope. C) lower shelf. D) lower slope.

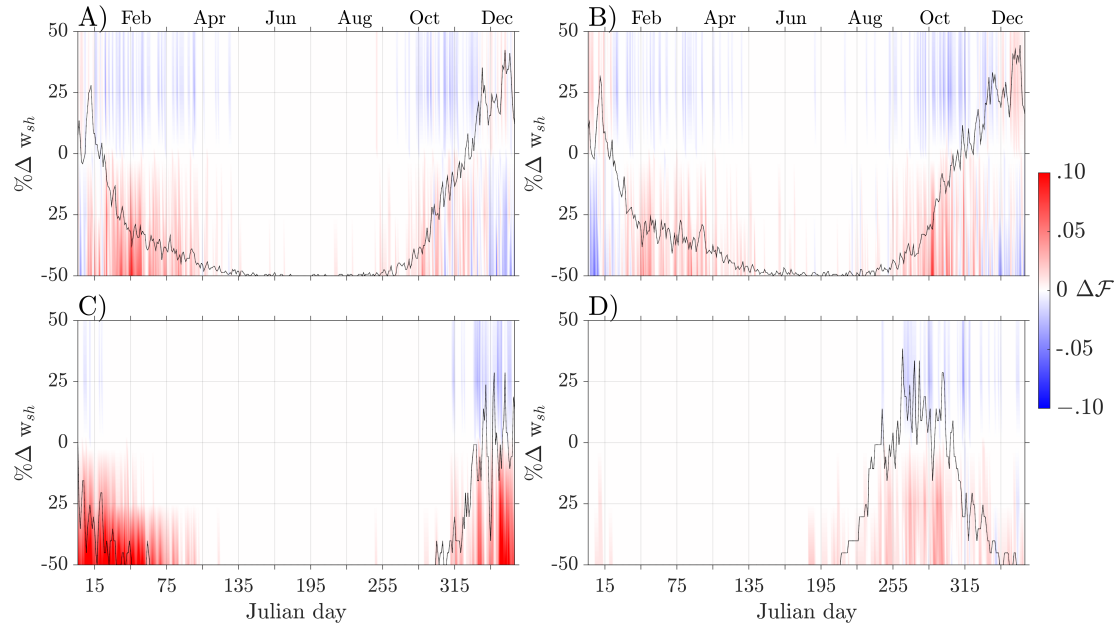

(b) $\Delta\mathcal{F}$ of shelf width (w_{sh}) sensitivity runs. A) upper shelf. B) upper slope. C) lower shelf. D) lower slope.

Figure 5.7: The difference in the number of days with joint DIC – O_2 extremes in the baseline and that of the sensitivity model runs. The $\mathcal{F}$ curves from the baseline run are shown on top of each plot.

sensitivity to the two types of physical forcing separately. DIC appears to be more sensitive to changes in remote forcing than does O_2. The low frequency remote wind forcing allows air-sea fluxes driven by local high frequency forcing to adjust O_2 but not DIC.

Sensitivity tests show upper layer DIC and oxygen are mostly controlled by physical processes although biological processes offset the control to some extent. Biological processes are more important in subsurface layers. These results corroborate the results I found in chapter 4.

In the lower layers the response to changes in v_m by oxygen extremes is not linear. Near zero growth rate maintains the oxygen level while moderately low growth rate causes a decrease in $q_{05(O_2)}$. This decrease is due to reduction of upper layer oxygen production and subsequent physical mixing that normally offsets the oxygen deficit following upwelling.

The sensitivity of DIC and O_2 median values to most parameter changes showed what was expected (Appendix E.1). For example, in the lower shelf box, a decrease in v_m resulted in reduced median values of DIC than the DIC extremes. This result is due to the physical and biological processes acting differently on the median and extremes. In general, the extremes are more sensitive to physical processes, while the medians are sensitive to biological processes.

A separate sensitivity test for the upwelling season only showed both DIC and O_2 extremes are more responsive to changes in almost all parameters than for full-year analyses. Finally, DIC and oxygen extremes showed negligible responses to changes in the volume and content of the VICC. This lack of response could be due to the relatively small fluxes from inner boundary (VICC) of the model compared to other fluxes such as upwelling or primary production.

The frequency of upwelling season joint DIC–O_2 extreme events does not depend on up/downwelling intensities within the upwelling season. However, there is a delayed response in the winter season to what happened in the previous summer upwelling season. Lowering summer upwelling intensities reduces the frequency

of wintertime joint DIC–O_2 extreme events because less primary production occurs to later increase DIC when more organic matter is mineralized and consume more oxygen. Increasing the summer upwelling intensities has the opposite effect on the frequency of joint extreme events.

Finally, although this quantity is not likely to change in the timescales considered in this thesis, it is worth noting that reducing the shelf width increased the frequency of wintertime joint DIC–O_2 extreme events. This knowledge can be useful when the model used in this thesis is adjusted to other domains.

Chapter 6

Conclusions

6.1 Summary of main results

This thesis explored the relative importance of different physical and biological mechanisms that affect oxygen and carbon extremes in the west coast of southern Vancouver Island. Although less appreciated in the past, coastal trapped wave mediated remote forcing of upwelling in the study region was found to be as important as locally generated upwelling. Roughly, on a time scale of a week to a month, about 40% of the current and temperature variability in the study region are explained by winds along the west coasts of California and Oregon. This contribution to upwelling variability in the study region is substantial enough to impact biogeochemical cycling in the study region.

Following the data analysis results above, I conducted a modelling study focusing on DIC and oxygen extremes, specifically the lowest 5% O_2 and highest 5% DIC concentrations that occur at present-day. The oxygen cycle has been successfully added to the original model. The model was further improved by introducing a more mechanistic mixed layer depth and allowing it to handle multiple time dependent forcing components. A stochastic model was used to generate long (1020 year long) realizations of these model forcing components. The time varying model forcing allowed for the representation of seasonal cycles and variability in modelled DIC and

O_2. Observational data were compiled from various observational datasets from the last two decades, to inform and evaluate the modelling work.

Modelled DIC and O_2 show larger interannual variability at the start and end of the upwelling season, due to variability in the start and end of upwelling season itself. The winter downwelling season shows the least interannual variability. Model simulations also show relatively high upper layer DIC during winter and a minimum late in the productive summer upwelling season. This seasonal cycle reproduces depth averaged observations.

The modelled dissolved oxygen shows an opposite signed seasonal cycle as DIC and agrees well with data. The modelled DIC and O2 are well-coupled in the lower layers, where biological processes dominate, in contrast with the surface mixed layer where physical fluxes, which may decouple O_2 and DIC tendencies, play a key role.

Statistical analyses of the long realizations of modelled DIC and O_2 were conducted. The application of stochastically generated daily resolved long-record model forcing enabled the estimation of robust statistics on DIC and O_2 extremes, which are defined as the 95^{th} and 5^{th} percentiles of modelled DIC and O_2 respectively.

In the upper mixed layer, relatively short O_2 extreme events occur more frequently than DIC extreme events. This layer also shows larger spreads among the cumulative distribution curves of DIC and O_2 when the distributions are conditioned on up/downwelling intensities. The differences between upwelling and downwelling conditioned DIC and O_2 cumulative distribution curves are also larger in the upper layer. The probability distribution functions of intense up/downwelling associated with short and long return periods of DIC and O_2 extreme events show that in the upper layer the spread between the PDFs of composite up/downwelling extreme events are noticeably different between DIC and O_2. In this layer, DIC and O_2 extreme events appear less related. Through its effect on the intensity and timing of net up/downwelling, remote wind forcing influences DIC and O_2 extreme events in the study region, primarily in the upper mixed layer.

Biological processes, like individual upwelling events, are relatively more impor-

tant in subsurface layers. These processes play a role in determining DIC and O_2 extreme events and they tend to tie the two extreme events together. Unlike physical processes, which operate at short timescales, biological process operate at intermediate to long timescales. These timescale differences are observed in some of the results found in this thesis. For example, when there are intense upwelling events early in the upwelling season, lower layer oxygen levels are kept high due to the intermediate timescale primary production (hence O_2 production) in the upper layer and vertical mixing of O_2 between layers. However, towards the end of the upwelling season, oxygen extreme events occur due to the increased biological production early in the season and the associated increase in organic matter remineralization in the lower layer. In an upwelling season where upwelling intensities are weaker and more uniform with time, the chance of having extremely low O_2 levels is therefore low.

The interaction between physical and biological processes in driving DIC and O_2 extreme events is not trivial. As I showed in Chapter 4, when there is no primary production, differences in upwelling intensities have little relevance to DIC and O_2 extreme events, especially in the lower layer. Upwelling intensity and its timing are important for the biological processes to lead to DIC and O_2 extreme events. The interdependence between these physical upwelling and biological transformations of carbon and oxygen, and the fact that they operate at different time scales, do not allow straightforward quantification of the relative contribution of each process to DIC and O_2 extreme events. Sensitivity analysis results reveal some details on how DIC and O_2 extreme events respond to these processes, through changes in model parameters.

The same parameter perturbation can have different effects on the magnitudes of the mean/median and extreme values of modelled DIC and O_2. The model's lower layer DIC extreme showed unexpected increase of up to 20 μmol kg^{-1} when atmospheric CO_2 was doubled. In contrast, increase in the mean DIC was slightly lower (up to 15 μmol kg^{-1}) A narrow shelf experiences frequent wintertime joint DIC–O_2 extreme events in both upper and lower layers. The effect of fluxes from the inner

shelf region (the Vancouver Island Coastal Current) on modelled DIC and O_2 extreme events are minor compared to other fluxes of both physical and biological origin. DIC and O_2 extreme events are more sensitive to biological parameters such as growth rate during upwelling season than across a year. A moderate decrease in phytoplankton growth rate increases the chances of model lower layer O_2 extreme events, while near-zero growth rate does not. Increased primary production, via increased phytoplankton growth rate, decreased the frequency of joint DIC–O_2 extreme events in the upper layers during the summer upwelling season, but increased it in the winter downwelling season. Changes in up/downwelling intensity do not change the frequency of joint DIC–O_2 extreme events within the upwelling season. Lowering upwelling intensities lowered the frequency of wintertime joint DIC–O_2 extreme events.

General implications

Carbon and oxygen extreme events can interact synergistically to lead to an even bigger impact on marine organisms than events of each kind would have individually. One of the main reasons for studying carbon and oxygen extreme events in the west coast of Vancouver Island (northern end of the CalCS) was because, due to the typical circulation features in the region, anthropogenically driven changes may be amplified (Feely et al., 2008). The Northeastern Pacific has one of the shallowest oxygen minimum zones, and the old subsurface water has higher carbon, than most other places do.

The strong link between local biogeochemical cycles in the study region and remote wind forcing implies that a change in those distant locations will affect future carbon and oxygen extreme events in the the west coast of Vancouver Island. Changes in wind strength, timing and general pattern are expected in a future climate (Bakun, 1990; Auad et al., 2006). Furthermore, the global ocean continues to absorb more CO_2 and heat from the warming atmosphere (Carter et al., 2019).

The increased heat uptake will tend to decrease the ocean mixed layer depth

through increases in ocean stratification on a global-scale. Some of the consequences of a shallower mixed layer is that nutrient resupply from deeper depths will likely become more difficult. Ventilation of the deep ocean with oxygen will be less efficient (Deutsch et al., 2006; Gruber, 2011). Finally, the wave-mediated remote wind influence on local upwelling described in this thesis will likely be different in a future climate where ocean stratification is different.

The increased CO_2 uptake by the ocean will directly affect the ocean water chemistry, with more free hydrogen ions released, decreasing the ocean pH. On top of this long term decrease are the short-term episodic fluctuations, particularly common in coastal upwelling regions like the west coast of southern Vancouver Island, that will decrease the extreme low pH experienced in the region.

Most previous studies, including those in the CalCS, focused on trends and seasonal cycles of the mean states of carbon and oxygen individually (e.g., Turi (2014); Claudine Hauri (2015); Siedlecki et al. (2015)) excepting Bianucci et al. (2011). I focused on the extreme events and both tracers simultaneously. As two of the multi-stressors to marine organisms, DIC and O_2 are best studied together. Results based on the analysis of the mean state may not necessarily translate to the extreme events, which likely have higher impact on organisms.

Studying both carbon and oxygen at the same time revealed some facts which are not clear otherwise. For example, my results show that the same parameter perturbation can have different effects on DIC and O_2. The mean and extreme events of DIC and O_2 have different responses to the same change. For example, when growth rate (v_m) was reduced, the median value of DIC decreased by more than the extreme did. Since growth rate depends on temperature, it will likely change in a future climate. Another benefit of studying the two together is identifying their relationship in different environments. This thesis found that there is a tendency for the two to decouple in the upper layers. Part of this tendency can be attributed to the differences in the gas exchange rates.

Management issues

The adverse changes on the west coast of Vancouver Island are concerning not only from environmental health perspective but also for their possible negative impact on the economy of the region. The region supports multi-billion dollar industries related to fisheries, tourism and other related sectors. One of the key results of this thesis is the time and spatial dependence of extreme events. Such knowledge can be useful in resource management efforts, including where and when to start monitoring indicators. The lower shelf and slope show more year-to-year variability both in terms of DIC and oxygen extreme events than the upper shelf/slope. Historically, the lower layer is less frequently sampled but these short records are less representative of the range of variability than in the upper layers. It is, therefore, suggested that the frequency of sampling in these subsurface regions be increased. A better (though expensive) solution would be deploying observing systems to continuously observe these layers for both DIC and oxygen extreme events. In terms of when to survey and forecasting, this thesis suggests monitoring upwelling proxies such as coastal wind upwelling indices from as far south as Oregon earlier in the summer upwelling season to better anticipate late summer extreme events, particularly of oxygen.

Organisms in the upper shelf/slope region are more likely to experience frequent low oxygen events than high DIC events. One consequence of the statistical definition of extreme events in this thesis is that frequent events will necessarily have shorter duration. Oxygen extreme events of short duration could still have great impact on aerobic organisms (Hofmann et al., 2013). Organisms in the lower shelf/slope are most impacted by both high carbon and low oxygen events during late summer.

This thesis has also produced a model climatology with its variability that is a valuable resource where data are scarce and costly to collect. Future modelling studies, particularly those focusing on interactions between higher trophic levels, can use this climatology to construct boundary conditions.

6.2 Future Work

By construction, the model forcing variables in the stochastic model were more accurate in representing mean and variances but not the extremes. Improving the external forcing by including information about extremes in the stochastic model could change the responses of carbon and oxygen extremes to the external forcing. Observational data used to construct the stochastic model could also be longer and more representative of atmospheric variability.

Adding more layers to the model to increase vertical resolution could reduce biases in the extremes. In its current form spatial averaging likely reduces the magnitudes of extremes relative to what is seen in observed profiles.

The model has a highly simplified biological component. For example, it does not have a representation of the denitrification process. Under low dissolved oxygen conditions microbes in the ocean use nitrate (NO_3^-) as a substitute oxidant for O_2. Loss of NO_3^-, a limiting nutrient, may decrease local and global primary production, and thus, the ability of the ocean to be a major atmospheric CO_2 sink.

Global mean atmospheric temperature is increasing and will continue to increase due to climate change. This warming exerts a strong control over air-sea gas exchange processes. This model uses a seasonally prescribed temperature. Developing the model further so that it would predict temperature would allow experiments concerning temperature and its impact on extremes.

This thesis did not explicitly model tidal processes. Although tidal mixing is implicit in the eddy diffusivities, the fact that these are constant neglects the observed 18.6-year modulation of the tidal cycle which has been found to be relevant for decadal oxygen variability in the offshore water (Crawford and Peña, 2013). A future study will benefit from including the effects of long period tidal cycles on the exchange coefficients and on oxygen and carbon variability on the isopycnal used in this study to better represent deep ocean boundary conditions for the model.

Finally, this thesis used a relatively simple approach in analyzing extremes. A

more formal approach would be to apply the extreme value theory, which involves fitting generalized extreme values distributions.

Appendices

Appendix A

Multitaper Method for Coherence

A.1 Application of the Multitaper Method

The multitaper method formally introduced by Thomson (1982) is a non parametric method that aims to address the two problems of bias and variance reductions of spectral estimates (Babadi and Brown, 2014). The method is ideal for revealing low frequency processes in a seasonally bounded geophysical data such as mine because it does not reduce the limit on the lowest frequency that can be resolved. In the multitaper method, the time series are multiplied by taper functions before the discrete Fourier transform is computed. The data tapers, h, used in Thomson (1982) are given by the Slepian sequences. The number and nature of these sequences are determined by the sample size, N, and by the required frequency resolution, $R = \frac{2p}{N\Delta}$, where p is a time-half bandwidth product that determines the number of tapers to be used for the required R; Δ is the time interval between observations. In this study, the total sample length, N, is 976 and 968 for summer and winter, respectively, and Δ is 3 hr. Generally, the first k$\ll 2p-1$ tapers are useful. I set $p = 4$ so R is about 0.0027 hr^{-1} and the number of tapers is 7.

Introducing the tapers $h^{(i)}(t)$, where i (=1,2,..., k) is the taper number, I can write the Fourier transform, $X^{(i)}$, of each tapered data segment of a zero-mean, time-

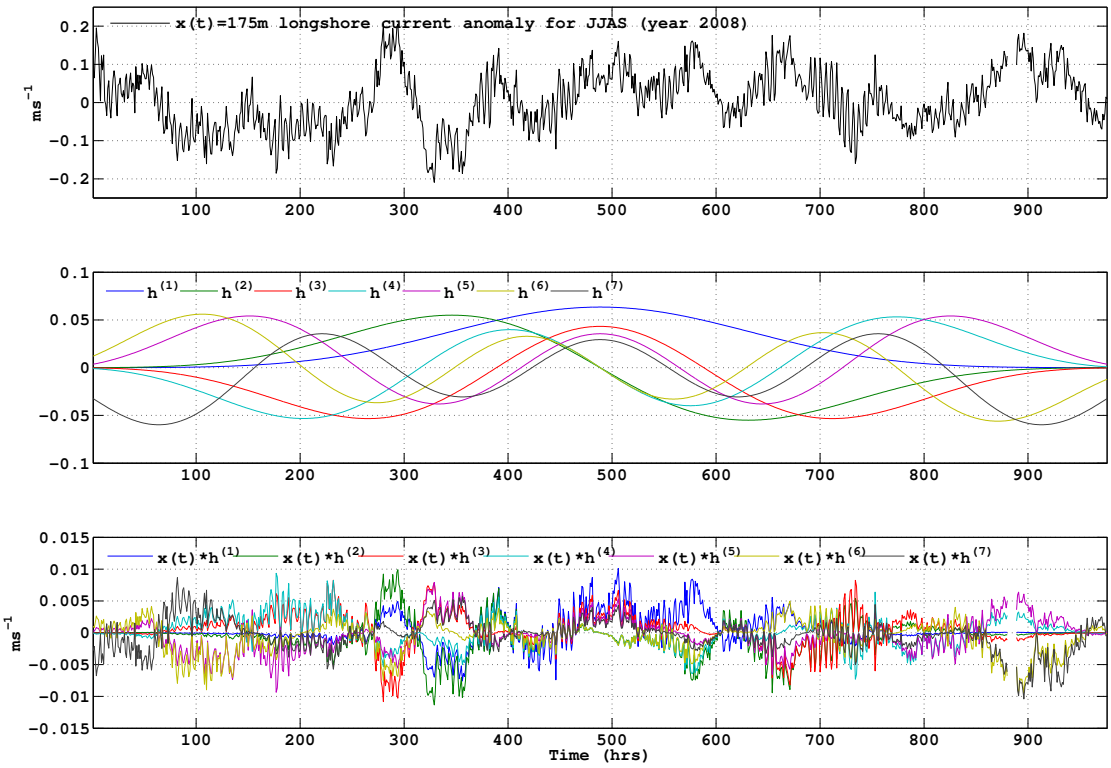

Figure A.1: An example plot showing alongshore current velocity anomaly timeseries (xt) at 175 m depth for the months of July – September (JJAS) (top), the seven tapers $h^{(i)}(t)$ used (middle) and the resulting uncorrelated tapered data segments ($x(t) * h^{(i)}(t)$) (bottom).

dependent stationary stochastic process $x(t)$ as a function of frequency f:

$$X^{(i)}(f) = \sum_{n=1}^{N} h^{(i)}(t)x(t)e^{-2j\pi fn\Delta} \tag{A.1}$$

The i^{th} tapered auto power spectrum then takes the form:

$$P_{xx}^{(i)}(f) = \frac{X^{(i)}(f)X^{(i)*}(f)}{N\Delta} \tag{A.2}$$

where X$^*(f)$ is the complex conjugate of $X(f)$.

Using k number of tapers and averaging the power estimates over the k number

of power spectra I get a better estimate, $\bar{P}_{xx}$, of the true power spectrum as

$$\bar{P}_{xx}(f) = \frac{1}{k}\sum_{i=1}^{k} P_{xx}^{(i)}(f) \tag{A.3}$$

Given a second process $y(t)$, I can also estimate the power spectrum $\bar{P}_{yy}$ as

$$\bar{P}_{yy}(f) = \frac{1}{k}\sum_{i=1}^{k} P_{yy}^{(i)}(f) \tag{A.4}$$

Furthermore, I can estimate the average cross-spectrum, $\bar{P}_{xy}$, as

$$\bar{P}_{xy}(f) = \frac{1}{k}\sum_{i=1}^{k} P_{xy}^{(i)}(f) \tag{A.5}$$

Each power spectrum entering into the averaging in Equations A.3 through A.5 is a distinct estimate because the tapers are chosen so that the tapered data are uncorrelated. Thus, the number of degrees of freedom (dof) is $2k$ and the sampling variances are reduced by a factor of $\frac{1}{k}$ relative to the raw spectra. This variance reduction, however is achieved at the cost of reduced distinction between neighbouring spectra because of the smoothing (loss of frequency resolution). The balance between this type of loss in frequency resolution and variance reduction is determined by how much resolution (R) one needs.

In my analysis, I obtain one average spectral estimate for each of m seasons and further average them. These final average spectral estimates will be denoted as $< \bar{P}_{xx}(f) >$, $< \bar{P}_{yy}(f) >$ and $< \bar{P}_{xy}(f) >$. The resulting average spectra will have $2(k+m)$ degrees of freedom and the total variance reduction factor becomes $\frac{1}{(k+m)}$. The dof in my work ranges from 38 to 52 depending on the size of gaps in the the 20 year record.

The squared coherence , $\kappa_{xy}^2(f)$, and the associated phase lag, $\phi_{xy}(f)$, are then given by

$$\kappa_{xy}^2(f) = \frac{|< \bar{P}_{xy}(f) >|^2}{< \bar{P}_{xx}(f) >< \bar{P}_{yy}(f) >} \tag{A.6}$$

$$\phi_{xy}(f) = \tan^{-1}(\frac{\text{imag}(< \bar{P}_{xy}(f) >)}{\text{real}(< \bar{P}_{xy}(f) >)}) \tag{A.7}$$

The confidence limits of the estimated magnitude coherence squared at a specified confidence level α is given by $1-\alpha^{\frac{1}{\frac{dof}{2}-1}}$ (Thompson, 1979; Thomson and Emery, 2014) for the null hypothesis of two independent stationary processes whose $\kappa^2_{xy}(f)$ at any frequency is zero.

In the above, both $x(t)$ and $y(t)$ were scalars. A general case of coherence where at least one of the time series is a vector is given by a rotary coherence (Gonella, 1972). Rotary coherences have a number of advantages over scalar coherences , as described in Thomson and Emery (2014). The primary advantage for my analysis is that it allowed us to treat the winds as vectors for reasons discussed in sub section 3.3. I will briefly discuss how I applied the rotary coherence method when needed to use wind vectors instead of just their components. First, for convenience, I generalize both the scalar time series $x(t)$ and $y(t)$ by the vector time series as:

$$\mathbf{x}(t) = x_1 + jx_2, \qquad \mathbf{y}(t) = y_1 + jy_2 \tag{A.8}$$

I can write the lag covariance, $\gamma(\tau)_{\mathbf{x(t)y(t)}}$, of the two vectors in terms of components as

$$\gamma(\tau)_{\mathbf{x}(t)\mathbf{y}(t)} = \gamma(\tau)_{x_1(t)y_1(t)} + \gamma(\tau)_{x_2(t)y_2(t)} + j[\gamma(\tau)_{x_1(t)y_2(t)} - \gamma(\tau)_{x_2(t)y_1(t)}] \tag{A.9}$$

where τ denotes the time lag between $\mathbf{x}(t)$ and $\mathbf{y}(t)$.

The Fourier transform of each term in the above equation gives the corresponding power spectrum. Thus, the cross-spectrum, $P_{\mathbf{x}(t)\mathbf{y}(t)}(f)$, becomes:

$$P_{\mathbf{x}(t)\mathbf{y}(t)}(f) = P_{x_1(t)y_1(t)}(f) + P(f)_{x_2(t)y_2(t)}(f) + j[P_{x_1(t)y_2(t)}(f) - P_{x_2(t)y_1(t)}(f)] \tag{A.10}$$

For $\mathbf{x}(t)$=$\mathbf{y}(t)$, Equation A.10 gives the rotary out-spectrum of each series. Once the cross- and auto-spectra are computed using Equation A.10, the coherence and phase lag between $\mathbf{x}(t)$ and $\mathbf{y}(t)$ are calculated in the same fashion as in Equations A.6 and A.7.

To define the rotary components I first define my coordinates. The cross-shore direction is such that it is aligned with y_1 and the longshore direction is aligned with y_2. In contrast, I take x_1 as the zonal component of the wind stress and x_2 as the meridional component. The rotary coherences between wind vectors and longshore currents were computed after dropping the y_1 subscripted terms in Equation A.10. Similarly, y_2 subscripted terms were dropped to compute rotary coherences between wind vectors and cross-shore currents. For temperatures, I dropped y_2 subscripted terms.

By convention, the auto spectra with negative frequencies ($f < 0$) make up the CW rotating components of the total rotary auto spectrum and those with positive frequency are CCW rotating components.

A.1.1 Band Averaged Coherences and Time Lags

The two main goals of using coherence analysis in this work are to (a) identify the time scales at which the wind vectors and the components of currents and temperatures show the strongest linear relationships and (b) determine the phase differences between the two time series at these time scales. Treating the winds as vectors required rotary coherence analysis. While coherences and phase relationships between two variables can easily be illustrated as functions of frequency at discrete locations (Eg. buoy locations), it is useful to visualize the spatial structure of the linear relationship between wind stresses across a wide area domain and oceanic variables measured at a given location. To this end, I defined the band averaged mean squared coherence,

$\overline{\kappa}^2_{\mathbf{x}(t)\mathbf{y}(t)}$, (following Oliver and Thompson (2010)):

$$\overline{\kappa}^2_{\mathbf{x}(t)\mathbf{y}(t)} = \frac{\sum_{f=f_1}^{f_2} \left\{ \kappa^2_{\mathbf{x}(t)\mathbf{y}(t)}(f) < \bar{P}_{\mathbf{y}(t)\mathbf{y}(t)}(f) > \right\}}{\sum_{f=f_1}^{f_2} < \bar{P}_{\mathbf{y}(t)\mathbf{y}(t)}(f) >} \tag{A.11}$$

between quantities at the mooring and wind stresses across the domain shown in Figure 3.2. From Equation A.11 it is clear that $\overline{\kappa}^2_{\mathbf{x}(t)\mathbf{y}(t)}$ does not depend on frequency. It can be interpreted as the fraction of variance of the predictand variable $\mathbf{y}(t)$ that is linearly accounted for by the predictor variable $\mathbf{x}(t)$ in a given frequency window, $[f_1, f_2]$. In my case, since the currents and temperatures are always considered the predictand variables I estimate the amount of variance that is accounted for by the winds in a given frequency interval.

I computed the band averaged mean time lag, $\overline{lag}_{\mathbf{x}(t)\mathbf{y}(t)}$, corresponding to $\overline{\kappa}^2_{\mathbf{x}(t)\mathbf{y}(t)}$ by calculating the phases, $\phi_{\mathbf{x(t)y(t)}}$, as in Equation A.7 and performing the band averaging as

$$\overline{lag}_{\mathbf{x}(t)\mathbf{y}(t)} = \frac{\sum_{i=2}^{n-1} \left\{ \kappa^2_{\mathbf{x}(t)\mathbf{y}(t)}(f_i) \Delta\Phi_{\mathbf{x}(t)\mathbf{y}(t)} f_i^{-1} \right\}}{2\pi(n-2) \sum_{i=2}^{n-1} \kappa^2_{\mathbf{x}(t)\mathbf{y}(t)}(f_i)} \tag{A.12}$$

where $\Delta\Phi_{\mathbf{x}(t)\mathbf{y}(t)} = \Phi_{\mathbf{x}(t)\mathbf{y}(t)}(f_{i+1}) - \Phi_{\mathbf{x}(t)\mathbf{y}(t)}(f_{i-1})$, and n is the number of frequencies in the window $[f_1, f_2]$.

The weighting by the $\kappa^2_{\mathbf{x}(t)\mathbf{y}(t)}(f_i)$ in Equation A.12 gives more weights to the more relevant phase lags based on the strength of the coherence squared at a given frequency. However, while this method is most accurate when looking at a relatively narrow frequency window, the resulting mean time lags for my calculations are not substantially different from those calculated without weighting (Figure A.3).

Depth (m)	**Years excluded (summer)**	**# of summer seasons used**
35	1989, 1992, 1997, 2001 & 2006	15
100	1989, 1995, 1999, 2001, 2003 & 2006	14
175	1989,1990, 1992, 2000, 2002, 2005 & 2006	13
400 (Temperature)	1989, 1997, 1998, & 2001, 2002, 2003	14
Depth (m)	**Years excluded (winter)**	**# of winter seasons used**
35	1993/1994, 1997/1998, 1998/1999 & 2005/2006	16
100	1994/1995,1998/1999, 2001/2002 & 2005/2006	16
175	1989/1990, 1991–1993, 1998–2000, 2001/2002, 2003/2004 & 2005/2006	12
400 (Temperature)	1994/1995	19

Table A.1: Number of seasons used in all coherence calculations in this study.

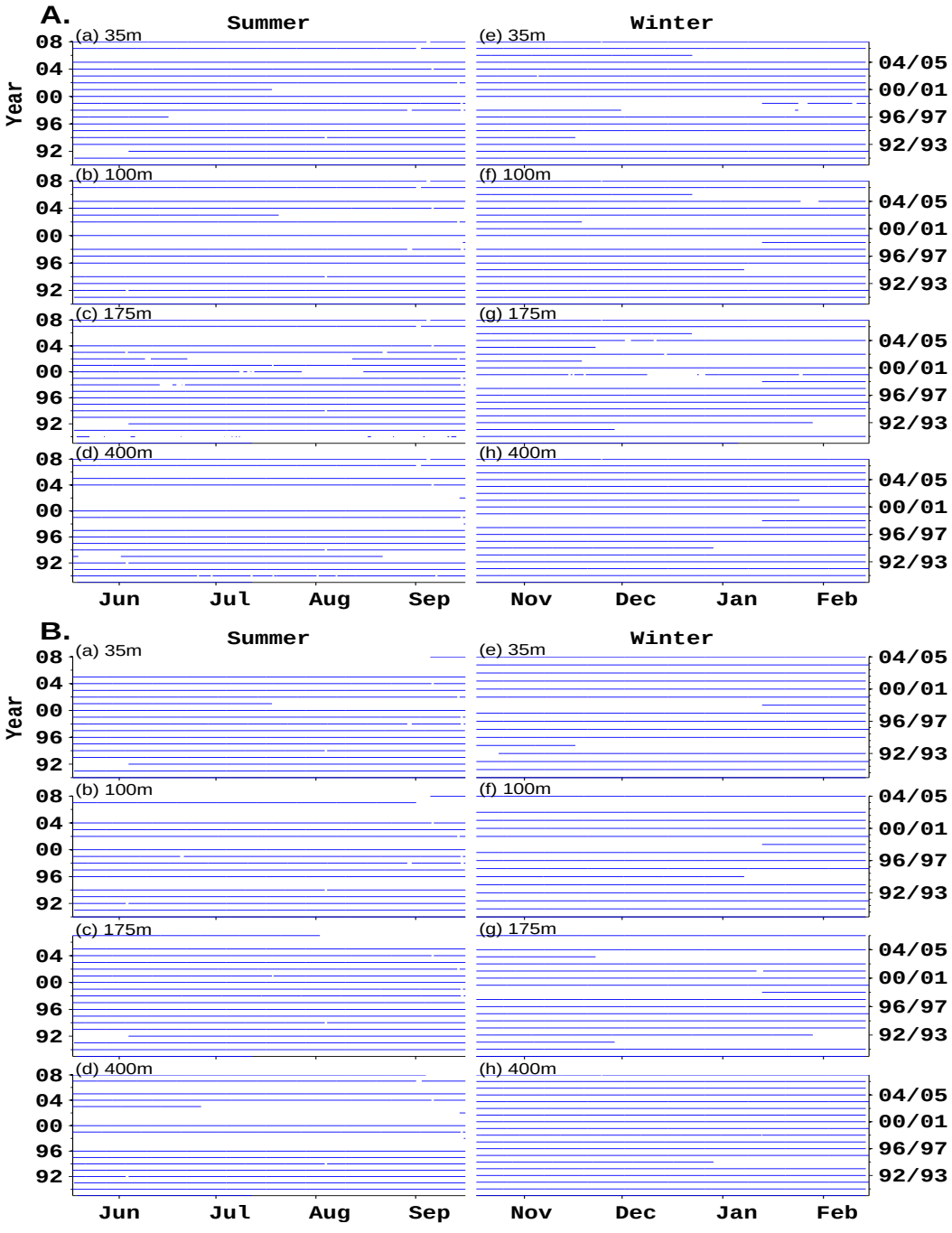

Figure A.2: A schematic showing record lengths of current meter records at the four depths used in Chapter 2: A. Current; B. Temperature. White blank spaces represent data gaps.

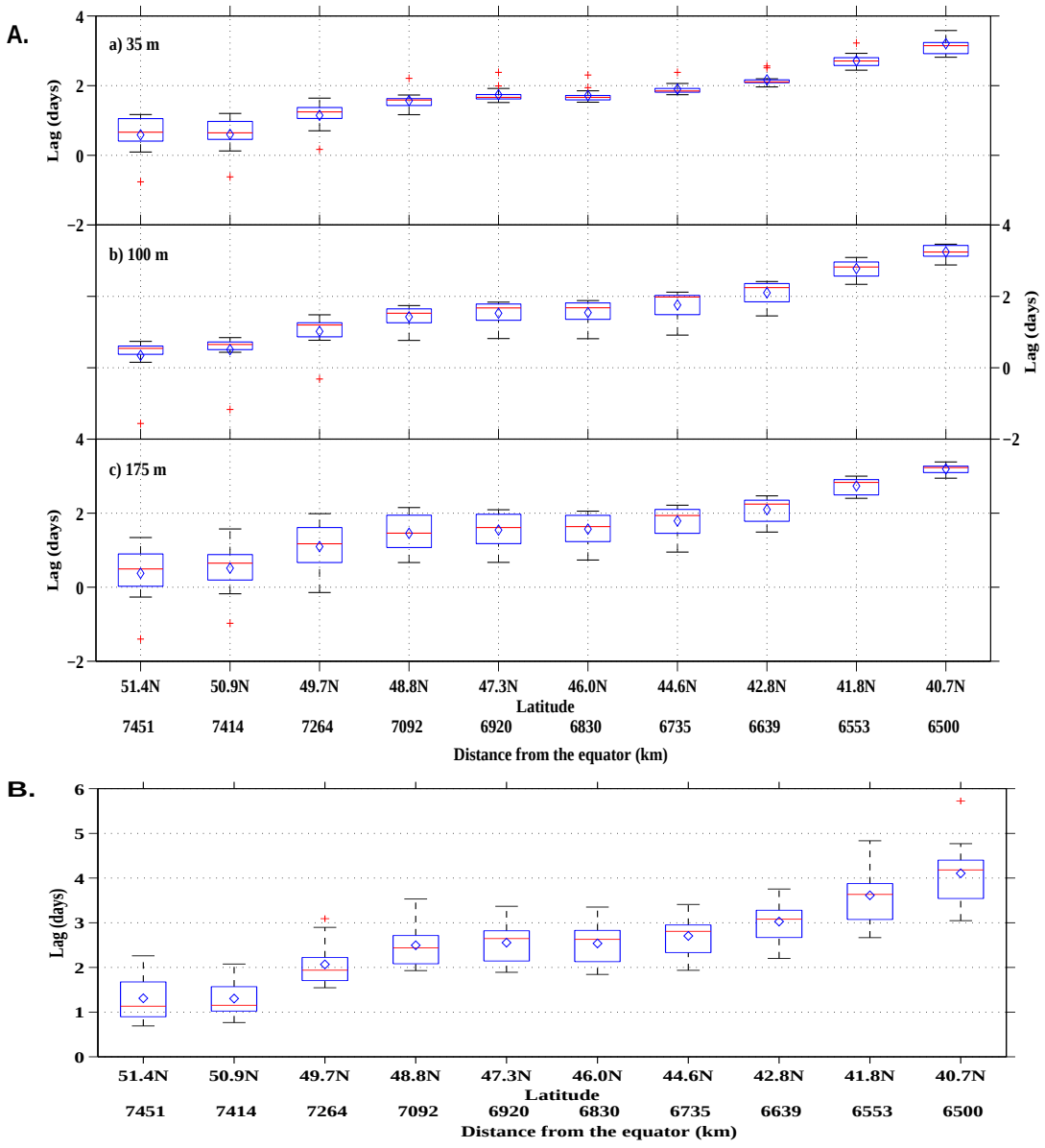

Figure A.3: Box plots for 13 frequencies over which mean time lags (blue diamonds) are estimated: A. Currents; B. 400 m Temperature. Each box corresponds to a buoy location to which NARR winds interpolated and current (temperature) vs wind stress phase differences computed (Figures 2.2(II) and 2.3(II).

Appendix B

Model Equations

B.1 The Model Equations

All model equations (more specifically the ordinary differential equations - ODEs) for the currency carbon of Ianson and Allen (2002) are listed in this appendix. Terms in upper and lower layers are referred by the subscripts u and l respectively.

For the currency Nitrogen the ODEs are similar. DIN are identical to those of DIC except there are not gas flux and excess uptake terms for DIN. POC equations are identical to those of PON.

DIC ODEs

$$\frac{dDIC_u}{dt} = -PP - PC + r_d DOC_u + \frac{G^*}{h_u} + X + V + H \tag{B.1}$$

$$\frac{dDIC_l}{dt} = r_d DOC_l + r_p POC_l + X + V + H \tag{B.2}$$

POC ODEs

$$\frac{dPOC_u}{dt} = PP - s(POC_u\beta) + X + H \tag{B.3}$$

$$\frac{dPOC_l}{dt} = \frac{sph_u\beta}{h_t - h_u} POC_u - r_p POC_l + X + H \tag{B.4}$$

DOC ODEs

$$\frac{dDOC_u}{dt} = [(1-p)sPOC_u\beta] + PC - rdDOC_u + V + X + H \tag{B.5}$$

$$\frac{dDOC_l}{dt} = -r_d DOC_l + V + X + H \tag{B.6}$$

Excess carbon uptake, PC

$$PC = chl_r(v_m p_o \overline{\gamma} - PP) \tag{B.7}$$

Fraction of living POC, p_o:

$$p_o = PO\{1 - exp[-0.1W^{-1}m^2(I_0(noon) - 43\ W^{-1}m^2)]\} \tag{B.8}$$

Exponential saturation curve for light limitation:

$$\gamma = 1 - exp(-\alpha I_{PAR}(\frac{z}{v_m})) \tag{B.9}$$

Maximum growth rate, v_m:

$$v_m = v_{m0}\ \exp(0.069\mathrm{K}^{-1}\mathrm{T}) \tag{B.10}$$

Uptake per I_{PAR} at low light intensity, α:

$$\alpha = \frac{v_m(T)}{I_{\text{sat}}} \tag{B.11}$$

Dimensionless POC decay (loss) flux function β:

$$\beta = MAX\left(9 - \left(8\frac{DIN}{DIN + K_{SN}^2}\right), 6 - \left(5\frac{\overline{\gamma}^2}{\overline{\gamma}^2 + K_{sl}^2}\right)\right) \tag{B.12}$$

Vertical mixing, V, using a tracer q is given by

$$V_{i,j}(q) = \left(\frac{M_v d_m}{h_{i,j}(h_{i,pp} - h_{i,u})_i} + e_{i,j}\right)(q_{i,k} - q_{i,j}) \tag{B.13}$$

Where $k = l$ if $j = u$ and vice versa.

The entrainment rates $e_{i,j}$ are

In the upper layer

$$e_{i,u} = MAX\left(\frac{dh_{i,u}}{dt}\left(h_{i,pp} + h_{i,u}\right)^{-1}, 0\right) \tag{B.14}$$

In the lower layer

$$e_{i,l} = MIN\left(\frac{dh_{i,u}}{dt}\left(2h_{i,t} - h_{i,pp} - h_{i,u}\right)^{-1}, 0\right) \tag{B.15}$$

where $j = pp$ and $j = t$ represent the permanent pycnocline and depth of the total water column, respectively. These terms arise from the vertical structure described in section 2.3.2 of IA02. Note that the vertical mixing coefficient (M_v) is multiplied by $d_m(h_{i,pp} - h_{i,u})^{-1}$ for $(h_{i,u} \leq (h_{i,pp}d_m))$ so that mixing occurs between the upper layer and the fluid centered at a depth of d_m below the interface. In the above formulation of entrainments the unit is per day (d^{-1}).

Horizontal mixing, H, using a tracer q is given by:

$$H_{i,j}(q) = \frac{M_H}{w_i}\frac{h_{i-1,j}}{h_{i,j}}\left(q_{i-1,j} - q_{i,j}\right)\delta_{i,sl} + \frac{M_H}{w_i}\left(q_{i+1,j} - q_{i,j}\right) \tag{B.16}$$

where $\delta_{i,sl} = 1$ for i=sl and 0 otherwise.

In the revised model (this thesis) the mixed layer depths ($h_{i,u}$) and their rate of change ($\frac{dh_{i,u}}{dt}$) are calculated offline (Appendix C.1) rather than as a prescribed climatotology as in IA02. The model interpolates (using a polynomial fit) both the time series ($h_{i,u}$ and $\frac{dh_{i,u}}{dt}$) to obtain the correct values at each time step. The permanent pycnocline, $h_{i,pp}$, values for shelf and slope are given in Table 3.1.

The four advective, X, terms:

Upper shelf:

$$X_{sh,u} = \frac{A}{h_{sh,u}}\left(q_{sh,l} - q_{sh,u}\right) + \frac{D}{h_{sl,u}}\left(q_{sl,u} - q_{sh,u}\right) + B_{sh} \tag{B.17}$$

Lower shelf:

$$X_{sh,l} = \frac{A}{h_{sh,l}}\left(q_{sl,l} - q_{sh,l}\right) + \frac{D}{h_{sh,l}}\left(q_{sh,u} - q_{sh,l}\right) \tag{B.18}$$

Upper slope:

$$X_{sl,u} = \frac{A}{h_{sl,u}}\left(q_{sh,u} - q_{sl,u}\right) + \frac{D}{h_{sl,u}}\left(q_{o,u} - q_{sl,u}\right) + B_{sl} \tag{B.19}$$

Lower slope:

$$X_{sl,l} = \frac{A}{h_{sl,l}}\left(q_{o,l} - q_{sl,l}\right) + \frac{D}{h_{sl,l}}\left(q_{sh,l} - q_{sl,l}\right) \tag{B.20}$$

Buoyancy, B, Fluxes:

Shelf box:

$$B_{sh} = \frac{P}{h_{sh,u}}\left(q_p - q_{sh,u}\right) + \frac{R}{h_{sh,u}}\left(q_r - q_{sh,u}\right) + \frac{C}{h_{sh,u}}\left(q_c - q_{sh,u}\right) \tag{B.21}$$

Slope box:

$$B_{sl} = \frac{P}{h_{sl,u}}\left(q_p - q_{sl,u}\right) \tag{B.22}$$

where P, R, and C are flux per length of coastline for rainfall, terrigenous runoff, and VICC. P, R and C are given as follows:

$$P = 0.029 \exp\left\{-0.5\left[3.5 - 2\cos\left(\frac{2\pi}{365}\left(t + 20 \text{ days}\right)\right)\right]\right\} \text{m d}^{-1} \tag{B.23}$$

$$R = 0.05 \exp\left\{-0.5\left[3.5 - 2\cos\left(\frac{2\pi}{365}\left(t + 20 \text{ days}\right)\right)\right]\right\} \text{m d}^{-1} \tag{B.24}$$

$$C = 0.05 \exp\left\{-0.6\left[5 - 2\cos\left(\frac{2\pi}{365}\left(t + 150 \text{ days}\right)\right)\right]\right\} \text{m d}^{-1} \tag{B.25}$$

pCO_2 is calculated from DIC and alkalinity (ALK), which is empirically determined from salinity, S, as

$$\text{ALK} = 52.85S + 470.13 \ \mu\text{eq kg}^{-1}; (r^2 = 0.929, n = 709); (S <= 33.85; S = 30.3 - 33.85) \tag{B.26}$$

Name	Description	Unit
PP	Primary Production	μM d^{-1}
DOC	Dissolved Organic Carbon	μM
PC	Excess Carbon uptake	μM C d^{-1}
r_d	DOC remineralization rate	d^{-1}
G^*	gas flux	μM d^{-1}
V	Vertical mixing and entrainment	d^{-1}
X	advection	m d^{-1}
H	horizontal mixing	d^{-1}
p_o	fraction of living POC	n/a
I_{sat}	saturation light intensity at which v_m is reached	W m^{-1}
I_{PAR}	photosyntheticlly available radiation	W m^{-1}
I_o(noon)	I_{PAR} at noon	W m^{-1}
chl_r	factor to account for reduction of cellular chlorophyll (chl) relative to carbon	n/a
β	dimensionless POC decay flux function	n/a
p	fraction of β that sinks	n/a
s($\text{POC}_u\beta$)	decay of upper layer (living) POC	
s	decay rate of POC pool	d^{-1}
r_p	POC remineralization rate	d^{-1}
K_{sn}	Half saturation constant for PO decay due to nitrogen limitation	μM
K_{sl}	Half saturation constant for PO decay due to light limitation	μM
v_{m0}	maximum growth rate at 0 K temperature	d^{-1}
v_m	maximum growth rate at average upper layer temperature in K unit	d^{-1}

Table B.1: Model parameters.

Appendix C

Model Mixed Layer and Boundary Conditions

C.1 Model Mixed Layer

Because the model I used has only two main layers, I considered a two layer ocean to derive the mixed layer model that is applicable only during mixed layer deepening (Figure C.1).

Temperature in either layer will be controlled by air-sea fluxes and entrainment of fluid into that layer. These two effects are mathematically represented as follows:

$$\frac{dT}{dt} = \frac{Q_{net}}{\rho h c_p} - \frac{\Delta T}{h}\frac{\partial h}{\partial t} \tag{C.1}$$

where $\rho = 1024\text{kgm}^{-3}$ is density of sea water, Q_{net} is the net heating at the surface of a mixed layer of depth h. ΔT is the difference between the upper (mixed) and lower layers and $c_p = 4200$ $\text{Jkg}^{-1}\text{k}^{-1}$ is specific heat capacity of water.

Assuming no velocity shear in the mixed layer, the rate of mechanical energy input by the wind is $m_o \rho_a C_D U^3(t)$, where m_o is a fraction of the wind energy that goes into doing work on the stratification. Thompson (1976) used 0.0001 as the value of m_o. In this work, half of that value gave more realistic results. Air density, ρ_a=1.2 kg m^{-3},

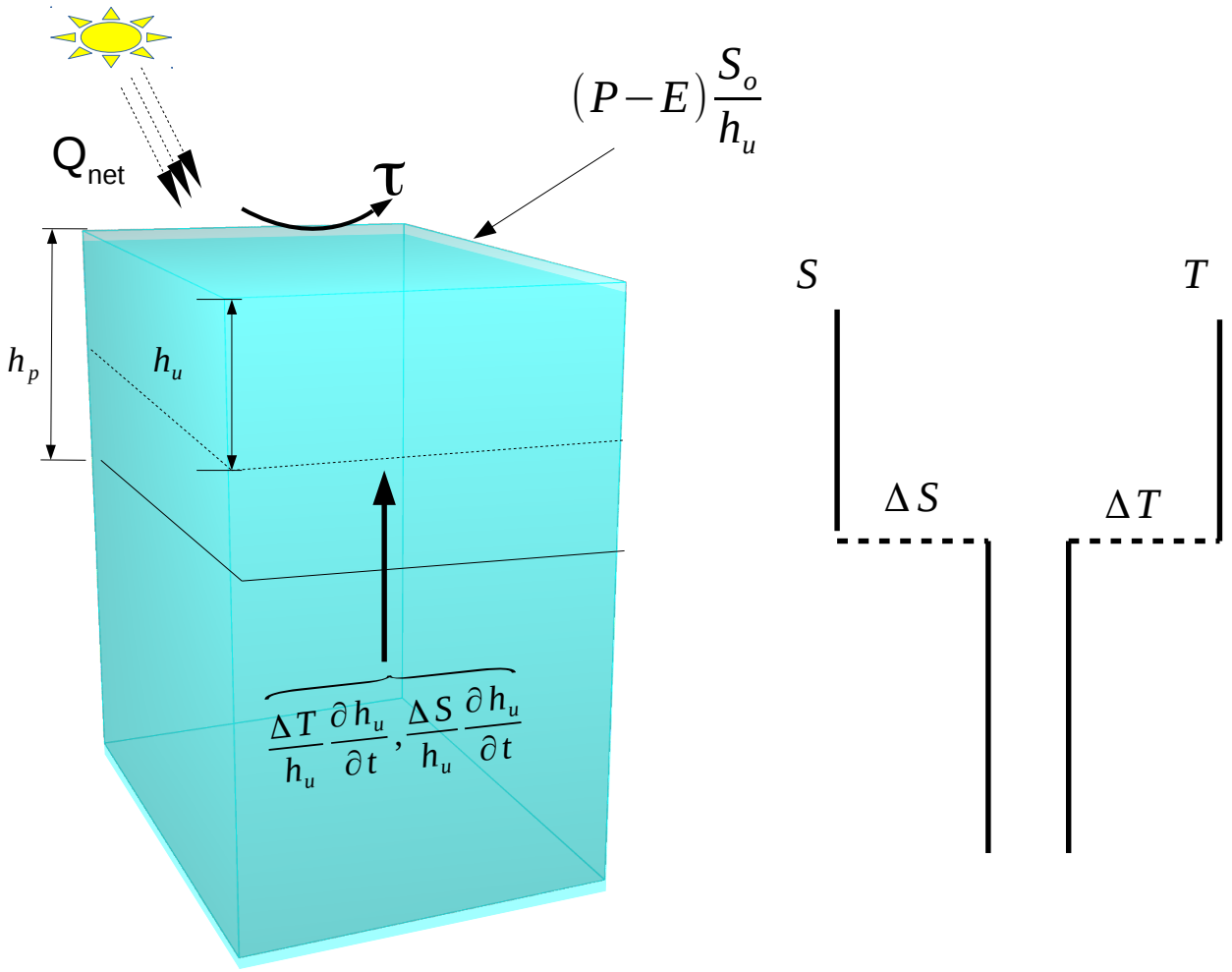

Figure C.1: Model mixed layer schematics. Left - The two layer mixed layer is shown with relevant termes labelled. Right - The temperature and salinity profiles as represented in this mixed layer model are shown.

and the surface drag coefficient, C_D, as calculated in Equation 3.1 are used. U is stochastically generated local wind speed. The rate of wind mixing is the same as the rate of change of potential energy of a fluid column of density ρ. Mathematically, this rate of change of potential energy is expressed as $-\frac{gh^2}{2}\frac{d\rho}{dt}$, where g is acceleration due to gravity. Hence, I can write

$$-\frac{gh^2}{2}\frac{d\rho}{dt} = m_o \rho_a C_D U^3(t) \tag{C.2}$$

Thermal expansion and salt contraction are the two causes of sea water density change. Their combined effect on density is given by the expression:

$$\frac{d\rho}{dt} = -\alpha\rho\frac{dT}{dt} + \beta\rho\frac{dS}{dt} \tag{C.3}$$

where α and β are the coefficients of thermal expansion and salt contraction of sea water. I calculate these coefficients following Kraus and Businger (1994) and from seasonally varying prescribed upper and lower layer temperatures (T_u and T_l) as

$$\alpha = (77.5 + 8.70 \times \frac{T_u + T_l}{2}) \times 10^{-6} \tag{C.4}$$

$$\beta = (779.1 - 1.66 \times \frac{T_u + T_l}{2}) \times 10^{-6} \tag{C.5}$$

The rate of change of salt ($\frac{dS}{dt}$) inside a water column of depth h is dependent on the difference between surface evaporation and precipitation rates and on the entrainment rate. Mathematically, the above rate of change in S can be represented as

$$\frac{dS}{dt} = \frac{(E-P)}{h}S_o + \frac{\Delta S}{h}\frac{\partial h}{\partial t} \tag{C.6}$$

where E and P are evaporation and precipitation rates in m s^{-1} units. S_o is a reference sea surface salinity (33 psu) and ΔS represents the salinity jump between the two layers. When I substitute the above expression of $\frac{dS}{dt}$ and the expression for

$\frac{dT}{dt}$ from equation C.1 into equation C.3, the expression for $\frac{d\rho}{dt}$ in equation C.3 will take the form

$$\frac{d\rho}{dt} = -\alpha\rho\left(\frac{Q_{net}}{\rho h c_p} - \frac{\Delta T}{h}\frac{\partial h}{\partial t}\right) + \beta\rho\left(\frac{(E-P)}{h}S_o + \frac{\Delta S}{h}\frac{\partial h}{\partial t}\right) \tag{C.7}$$

To finalize the mixed layer depth formulation, I substitute this expression into equation C.2 and collect like terms. The final equation of the mixed layer model is shown (Equation C.8).

$$\underbrace{m_o\rho_a C_D U^3}_{\text{Wind mixing term}} + \underbrace{\frac{\rho g h_u}{2}\left(\alpha\Delta T + \beta\Delta S\right)\frac{\partial h_u}{\partial t}}_{\text{Entrainment term}} - \underbrace{\frac{\rho g h_u}{2}\left(\frac{\alpha Q_{net}}{\rho c_p} + \beta\left(P-E\right)S_o\right)}_{\text{Buoyancy term}} = 0 \tag{C.8}$$

The simple mixed layer model is useful to incorporate the effects of surface processes and fluxes (both mass and energy) into the mixed layer.

There are not simple bulk models of the oceanic mixed layer that can diagnose shoaling. Instead, I experimented with various time scales of relaxation back to a stratified state. Therefore, during deepening, the predicted mixed layer depth, h_u(t+Δt) is given by the first case ($h_u(t) \leq h_u(t+\Delta t)$) in Equation C.9.

$$h_u(t{+}\Delta t) = \begin{cases} h_u(t) + \left[\frac{\alpha Q(t) + c_p\rho\beta(P-E)S_o}{c_p\rho(\alpha\Delta T(t)+\beta\Delta S(t))} - \frac{2m_o\rho_a C_D U^3(t)}{\rho g(\alpha\Delta T(t)+\beta\Delta S(t))h_u(t)}\right]\Delta t, & (h_u(t) \leq h_u(t+\Delta t)) \\ h_u(t) + \Delta t\frac{(h_{min}-h_u(t))}{\tau}, & (h_u(t) \geq h_u(t+\Delta t)) \end{cases} \tag{C.9}$$

During shoaling, I use the second case ($h_u(t) \geq h_u(t+\Delta t)$) of Equation C.9 where I use a simple exponential function with a decay time scale of τ and h_{min} is the minimum h_u can get. Observational data suggest this minimum is about 5–10 m on both shelf and slope. Thus, I set a limit for MLD shoaling of 10 m. The time scale τ is 10 days. The shelf h_u results are shown in Figure C.2.

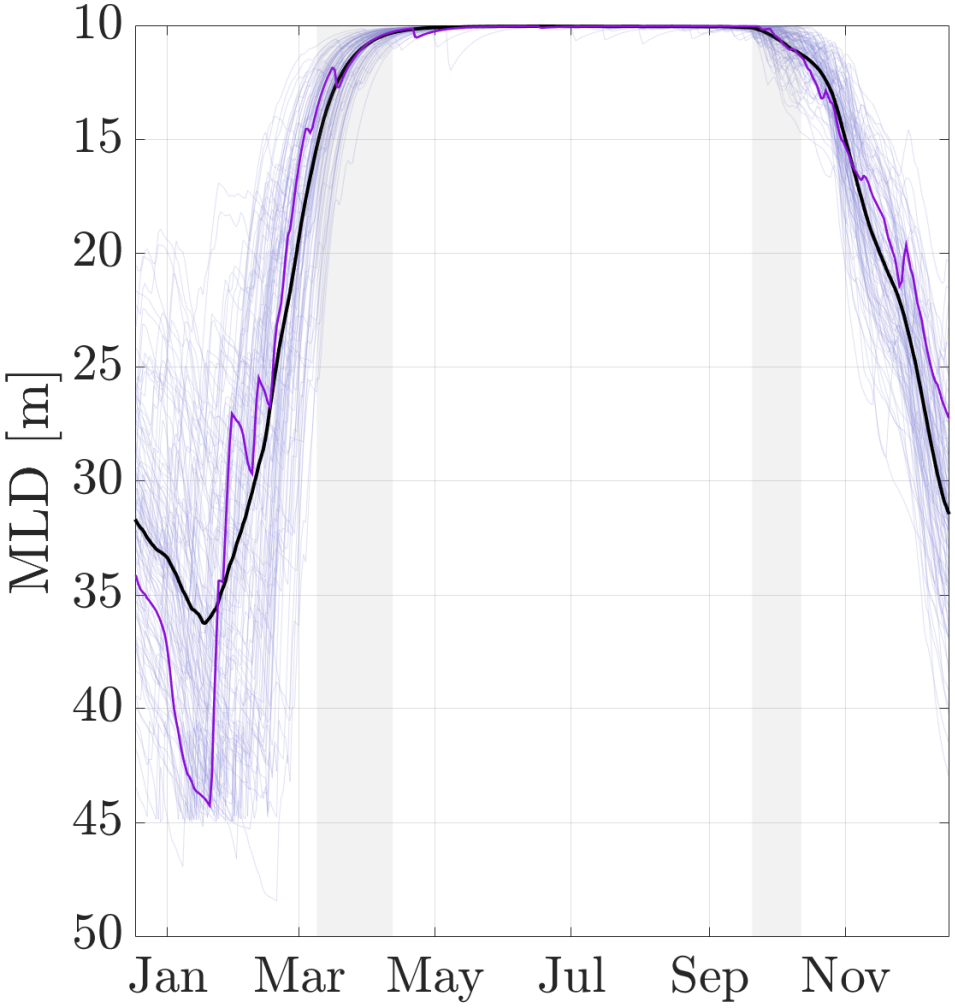

Figure C.2: Estimated shelf mixed layer depths (h_u). Light purple curves are for the individual year. Heavy purple curve highlights a randomly selected year. Solid black curve is long term average MLD. Note that the start and end of upwelling seasons shown in gray vertical shading pass through the shoulders of the MLDs.

C.2 Model Outer Boundary Conditions

The outer model boundary conditions were set after experimenting with different long term average observed quantities on density surfaces. The best model-observation agreements were obtained when the density surface $\sigma_\theta = 26.6$ was chosen. This isopycnal was also found to be the density surface that is more likely to reach the surface during upwelling, bringing in its characteristic properties to the surface (Unpublished data, Ianson, D.). Just outside the slope, the $\sigma_\theta = 26.6$ surface sits on a depth range of 200 – 300 m, which is considered the depth range of upwelling source water. Since the observed profiles, especially bottle sampled quantities do not have high depth resolutions I calculated weighted averages of quantities as follows. First, for each year, values were computed as σ_θ weighted averages between the $\sigma_\theta \pm .25$ and those weighted averages were further averaged across years. For example, for DIC the averages across n number of σ_θ surfaces in the $\sigma_\theta \pm .25$ range are given by

$$\overline{DIC} = \frac{\sum_{i=1}^{n} \sigma_{\theta i} * DIC_i}{\sum_{i=1}^{n} \sigma_{\theta i}} \tag{C.10}$$

Table C.1: Model deep ocean boundary values for the months where data are available.

Month	S [psu]	T [^oC]	DIC [μmole kg^{-1}]	O_2 [μmole kg^{-1}]	DIN [μM]	Depth [m]
1	33.843	6.178	2191.601	147.904	29.373	214.119
2	33.840	6.372	2199.274	138.014	32.352	216.067
3	-	-	-	-	-	-
4	33.925	6.738	2228.777	99.333	29.860	209.483
5	33.909	6.760	2223.381	104.313	32.826	216.285
6	33.880	6.457	2221.176	116.663	32.677	216.384
7	-	-	-	-	-	-
8	33.901	6.517	2218.761	112.782	33.089	231.642
9	33.923	6.695	2233.370	95.690	33.793	231.483
10	33.934	6.627	2221.607	108.796	32.836	224.734

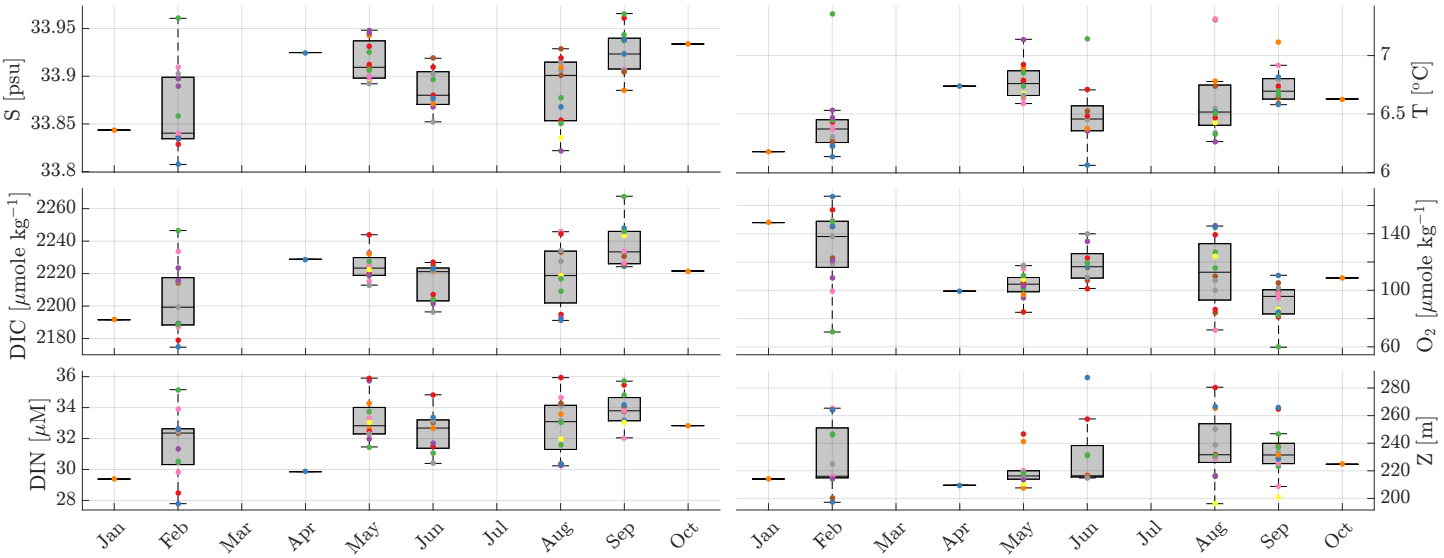

Figure C.3: Open ocean observed values from isopycnal $\sigma_\theta = 26.6$. Different colors represent weighted averages of observed quantities from the different years where data are available.

Appendix D

Stochastic Model

D.1 Stochastic model forcing

Monahan and Denman (2004) used a stochastic method to produce long realizations of atmospheric variability that were used as drivers of a coupled ecosystem model. A similar stochastic method was used to generate over a thousand year long model forcing in this work. The method is described here. I start by considering a stochastic process $\mathbf{x}(\mathrm{t}) \in R^N$ that is the solution to the stochastic differential equation

$$\frac{d\mathbf{x}}{dt} = A\mathbf{x} + B\dot{\mathbf{W}} \tag{D.1}$$

where A and B are square matrices of length N and $\dot{\mathbf{W}} \in R^N$ is a vector of Gaussian white noise processes (i.e., its autocorrelation function $\phi_{\dot{\mathbf{W}}}(\tau)$ is zero for nonzero lag, τ.)

In order for $\mathbf{x}(\mathrm{t})$ to be the solution to Equation D.1, it has to be Gaussian with stationary mean of zero and stationary covariance $C(0) = \left\langle \mathbf{x}\mathbf{x}^T \right\rangle$, where the $\langle . \rangle$ is a time averaging operator.

Determining A and B using the relatively short observed data time series and generating the stochastic forcing time series used in this work is an inverse problem. To solve this problem, I analyzed the observed time series, $\mathbf{y}_l(t)$ of dimension 6×2920

(i.e., 6 variables of each record length 2920 = 365 × 8 days, corresponding to the eight years 1995 – 2002). This time period is used as it is the period in which data for all forcings are available .

$$\mathbf{y}_l(t) = (Q_{net}(t), E(t) - P(t), u_1(t), v_1(t), u_2(t), v_2(t)) \tag{D.2}$$

where Q_{net} is the surface heat flux, $E - P$ is evaporation minus precipitation, and (u_i , v_i) are respectively the zonal and meridional wind components at the i$^{\text{th}}$ location (i=1,2 corresponding respectively to local and remote winds), so that $\mathbf{y}_l(t)$ possesses the properties of $\mathbf{x}$(t) described above.

First, I estimated the seasonal cycle of the mean, $\mu_l(t)$, using harmonic analysis.

$$\mu_l(t) = \sum_{m=1}^{N_h} \left[a_{lm} cos(\frac{2\pi mt}{T}) + b_{lm} sin(\frac{2\pi mt}{T}) \right] \tag{D.3}$$

where $T = 365$ days is one year and N_h is the number of harmonics considered. For my analysis, I used N_h =2 so the seasonal cycle is composed of an annual and a semiannual cycle. The coefficients a_{lm} and b_{lm} are determined by linear regression to $\mathbf{y}_l(t)$. The deseasonalized observed time series,

$$\mathbf{y}'(t) = \mathbf{y}_l(t) - \mu_l(t) \tag{D.4}$$

is thus obtained. Some of the variables (e.g., E and P or their difference) in $\mathbf{y}'(t)$ were not Gaussian enough and required transforming to assume more Gaussian form. The nonlinear mapping

$$\tilde{y}_j = \begin{cases} \alpha_{j-1} \tanh\left(\frac{y'_j - \alpha_j}{\alpha_{j+1}}\right), & j = 2 \\ y'_j, & j \neq 2 \end{cases} \tag{D.5}$$

was used to transform the time series of variables. The α's here are optimized to map quantiles of $y'_j \in \mathbf{y}'(t)$ to Gaussian quantiles. To further stationarize the anomalies, $\tilde{y}_j(t)$, I normalized them by a smoothly-varying estimate of the standard

deviation seasonal cycle, $\sigma_l(t)$, to get

$$x^{obs}(t) = \frac{\tilde{y}_j(t)}{\sigma_l(t)} \tag{D.6}$$

which forms the Gaussian stationary vector time series of observations. $x^{obs}(t)$ and the variables in $\mathbf{y}'(t)$ that did not need any further transformation made up the Gaussian stationary vector time series of observations, $\mathbf{x}^{obs}(t)$. Using properties of the stationary lagged-covariance, $C(\tau) = \left\langle \mathbf{x}(t-\tau)^{obs}(\mathbf{x}(t-\tau)^{obs})^T \right\rangle$, associated with solutions to Equation D.1 I write

$$AC(0) + C(0)A^T + BB^T = 0 \tag{D.7}$$

$$C(\tau) = e^{A\tau}C(0) \tag{D.8}$$

Matrix A was estimated from Equation D.8 by setting $\tau = 1$ day. Then, matrix B was estimated from Equation D.7.

After I estimated A and B, I used Equation D.1 to generate realizations of $\mathbf{x}$(t) of arbitrary length. To obtain realizations of the desired quantities ('raw' synthetic data), I reversed the order of pre-processing carried out to estimate A and B. First I multiplied $\mathbf{x}$(t) by the smooth estimate of the seasonal cycle of standard deviation, σ(t). Next, the inverse of the nonlinear transformation Equation D.5 was applied to the vector components that required transforming. Finally, the seasonal cycle of the means was added. An example of these realizations (a hundred year long Q_{net}) used in this work is shown in Figure D.1.

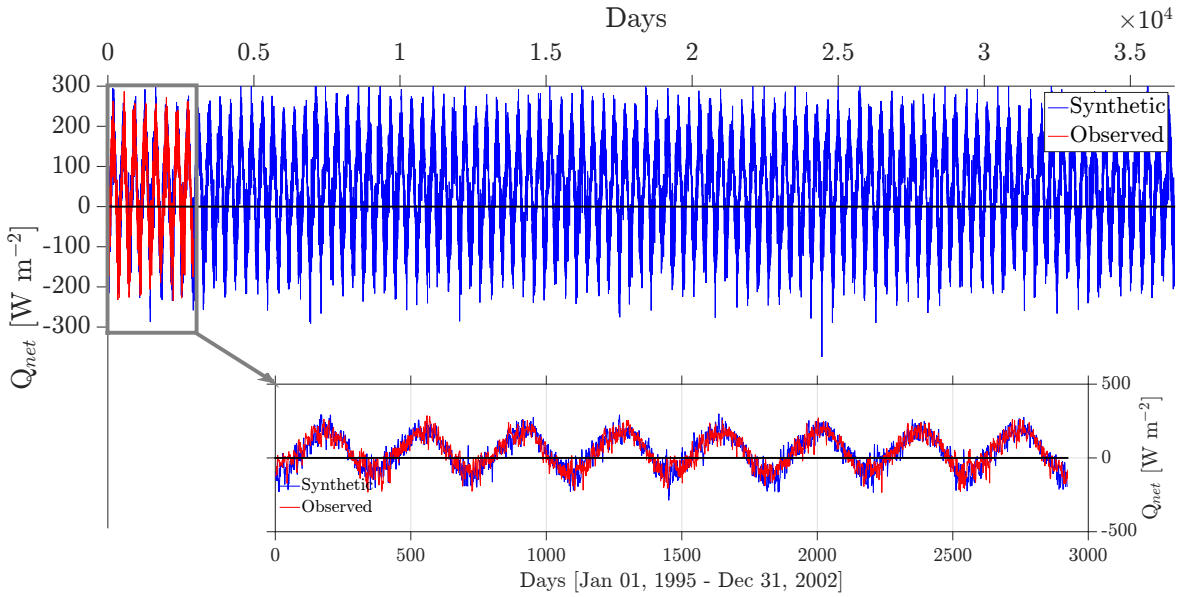

Figure D.1: A realization of the stochastically generated (synthetic) net surface heating, Q_{net}, (blue line) and the observed net surface heating data (red line) are shown. The inset shows the agreement between the two time series.

Appendix E

Additional Sensitivity Analyses

E.1 Sensitivity During Upwelling Season

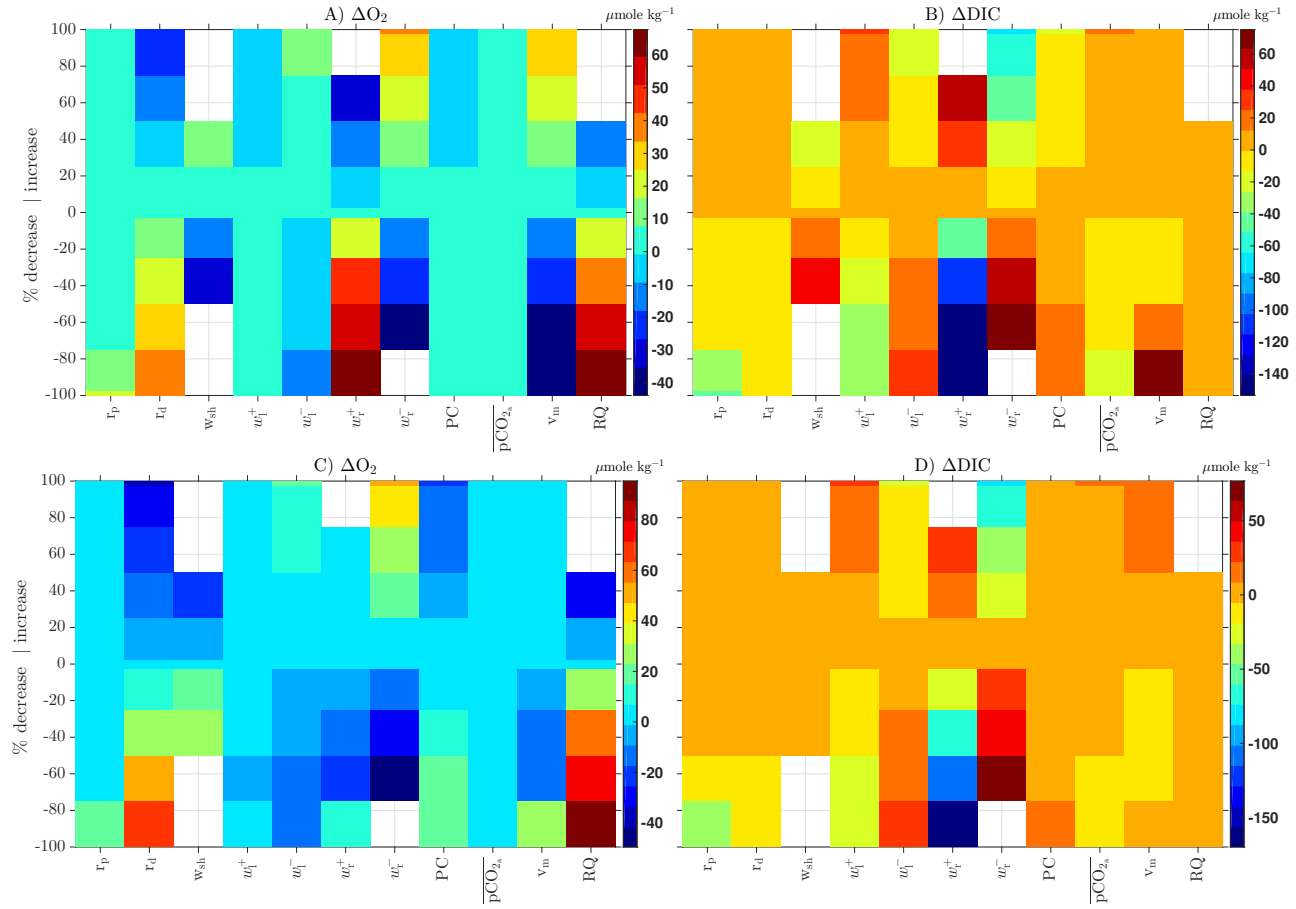

Figure E.1: Differences between the 5^{th} O_2 (95^{th} DIC) percentiles of the 12 sensitivity runs and the baseline run 5^{th} O_2 (95^{th} DIC) percentiles of upwelling seasons only. A) Upper shelf O_2. B) Upper shelf DIC. C) Lower shelf O_2. D) Lower shelf DIC.

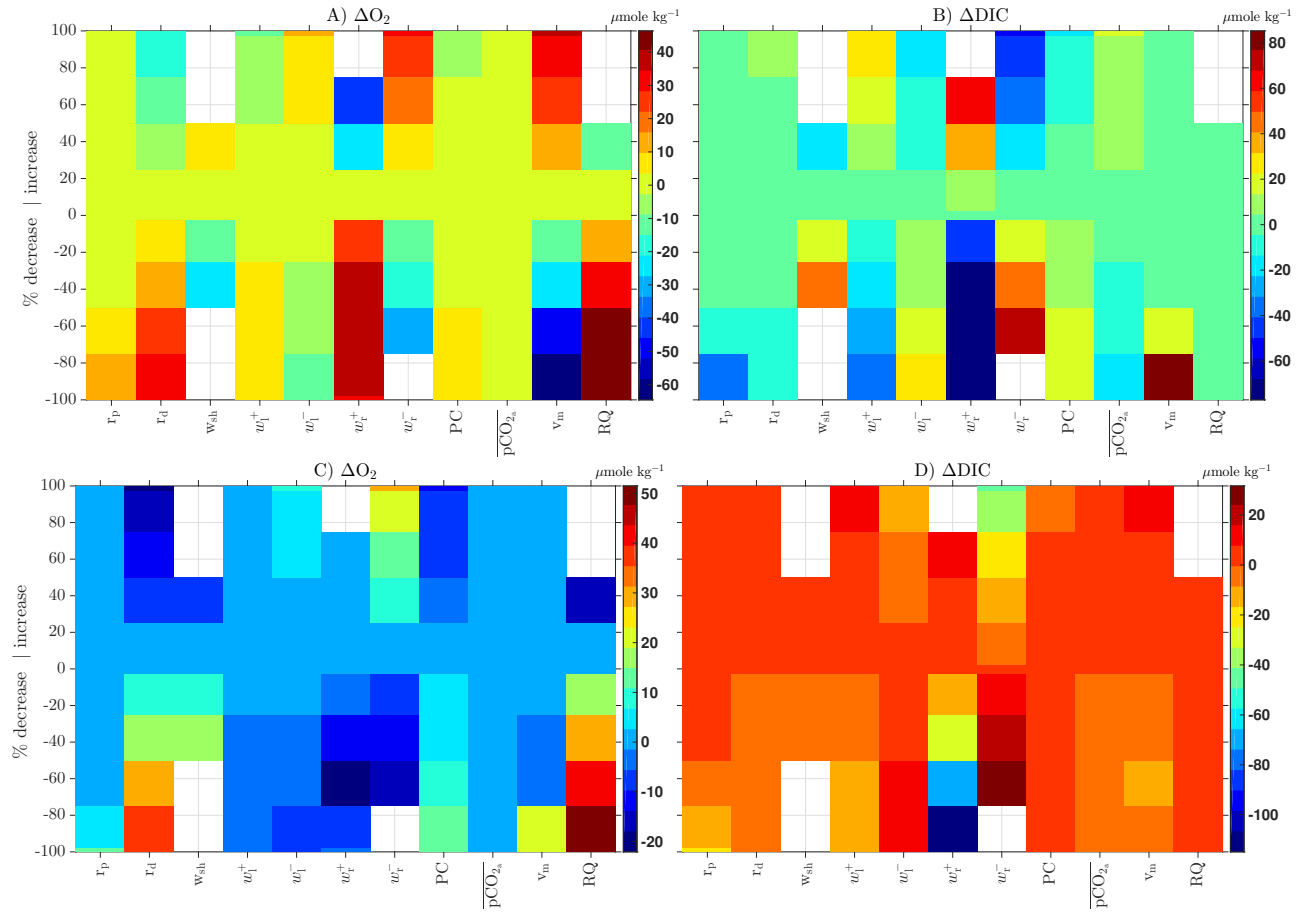

Figure E.2: Differences between the 5^{th} O_2 (95^{th} DIC) percentiles of the 12 sensitivity runs and the baseline run 5^{th} O_2 (95^{th} DIC) percentiles of upwelling seasons only. A) Upper slope O_2. B) Upper slope DIC. C) Lower shelf O_2. D) Lower shelf DIC.

E.2 Sensitivity of the 50$^{\text{th}}$ percentile

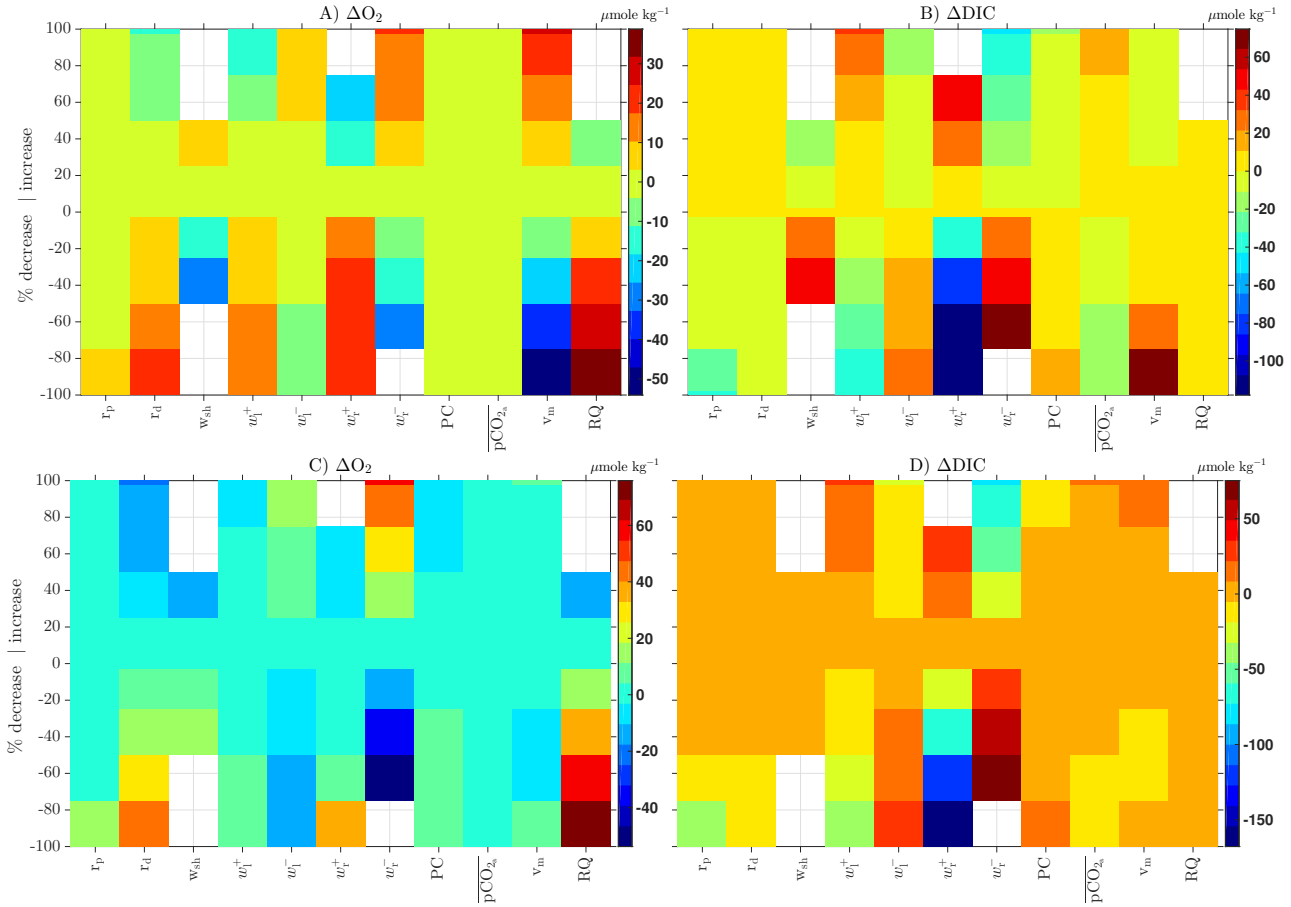

Figure E.3: Differences between the 50th O_2 (50th DIC) percentiles of the 12 sensitivity runs and of the baseline model run 50th O_2 (50th DIC) percentiles . A) Upper shelf O_2. B) Upper shelf DIC. C) Lower shelf O_2. D) Lower shelf DIC. Here the sensitivity tests done on model inner boundary values.

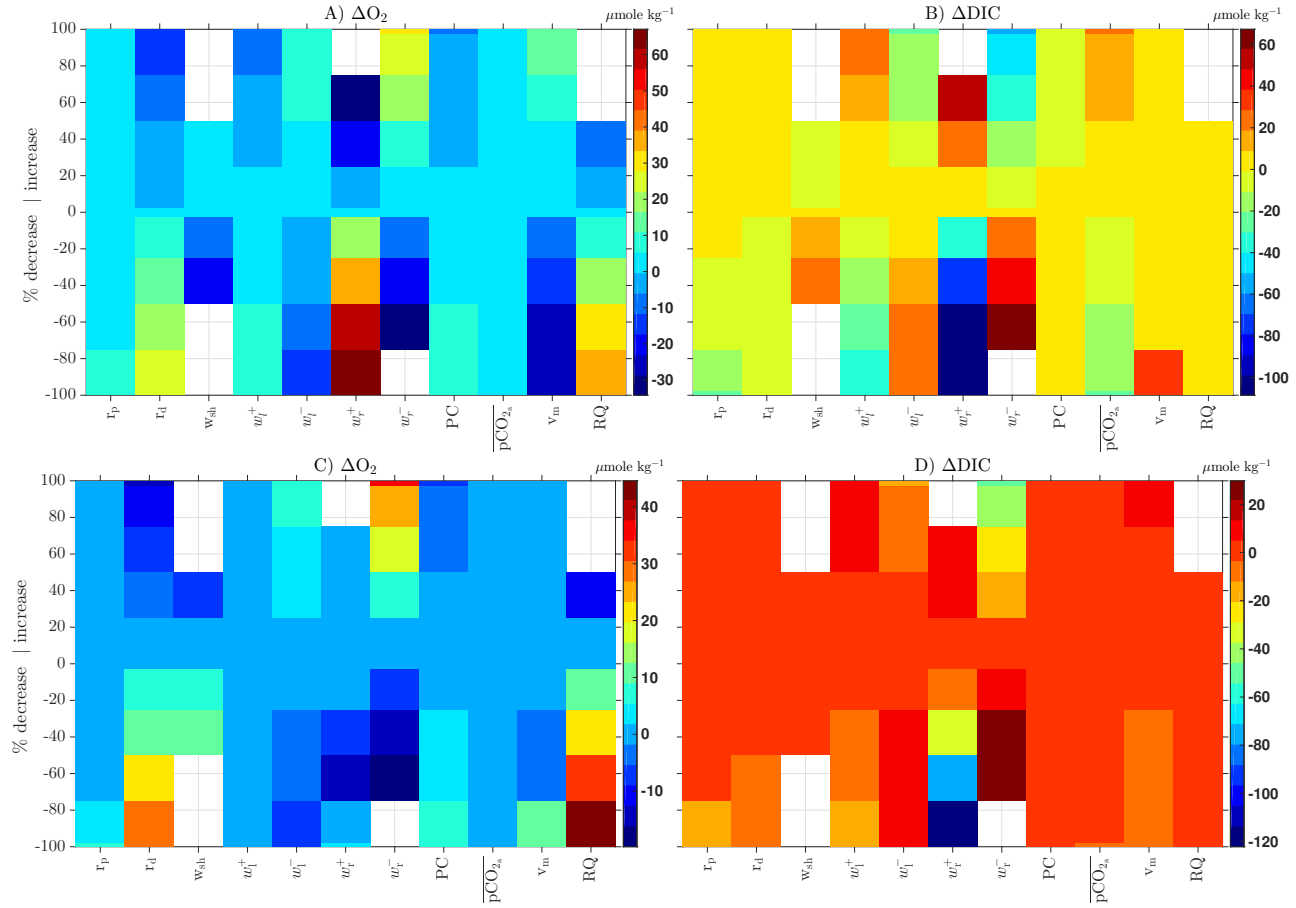

Figure E.4: Differences between the 50^{th} O_2 (50^{th} DIC) percentiles of the 12 sensitivity runs and of the baseline model run 50^{th} O_2 (50^{th} DIC) percentiles . A) Upper slope O_2. B) Upper slope DIC. C) Lower slope O_2. D) Lower slope DIC. The parameters labeled in the x-axes were varied by 12 different percentages (see main text).

Bibliography

Allen, J. S. and Denbo, D. W. Statistical characteristics of the large-scale response of coastal sea level to atmospheric forcing. *J. Phys. Oceanogr.*, 14(6):1079–1094, 1984. ISSN 0022-3670. doi: 10.1175/1520-0485(1984)014⟨1079:SCOTLS⟩2.0.CO;2.

Anderson, T. and Williams, P. B. Modelling the Seasonal Cycle of Dissolved Organic Carbon at Station E1 in the English Channel. *Estuarine, Coastal and Shelf Science*, 46(1):93 – 109, 1998. ISSN 0272-7714. doi: https://doi.org/10.1006/ecss.1997.0257. URL http://www.sciencedirect.com/science/article/pii/S0272771497902572.

Auad, G., Miller, A., and Di Lorenzo, E. Long-term forecast of oceanic conditions off California and their biological implications. *Journal of Geophysical Research: Oceans*, 111(C9), 2006. doi: 10.1029/2005JC003219. URL https://agupubs.onlinelibrary.wiley.com/doi/abs/10.1029/2005JC003219.

Babadi, B. and Brown, E. N. A Review of Multitaper Spectral Analysis. *IEEE Transactions on Biomedical Engineering*, 61(5):1555–1564, May 2014. ISSN 0018-9294. doi: 10.1109/TBME.2014.2311996.

Bakun, A. Coastal upwelling indices, west coast of North America. *U.S. Dept. of Commerce, NOAA Tech. Rep.*, 2:NMFS SSRF–671, 103p., 1973.

Bakun, A. Global Climate Change and Intensification of Coastal Ocean Upwelling. *Science*, 247(4939):198–201, 1990. doi: 10.1126/science.247.4939.198. URL http://www.sciencemag.org/content/247/4939/198.abstract.

Barth, J. A., Menge, B. A., Lubchenco, J., Chan, F., Bane, J. M., Kirincich, A. R., McManus, M. A., Nielsen, K. J., Pierce, S. D., and Washburn, L. Delayed upwelling alters nearshore coastal ocean ecosystems in the northern California current. *Proceedings of the National Academy of Sciences*, 104(10):3719–3724, 2007. ISSN 0027-8424. doi: 10.1073/pnas.0700462104. URL https://www.pnas.org/content/104/10/3719.

Battisti, D. S. and Hickey, B. M. Application of remote wind-forced coastal-trapped wave theory to the Oregon and Washington coasts. *J. Phys. Oceanogr.*, 14(5):887–903, 1984. ISSN 0022-3670. doi: 10.1175/1520-0485(1984)014⟨0887:AORWFC⟩2.0.CO;2.

Bianucci, L. and Denman, K. L. Carbon and oxygen cycles: Sensitivity to changes in environmental forcing in a coastal upwelling system. *J. Geophys. Res.*, 117:G01020, 2012.

Bianucci, L., Denman, K. L., and Ianson, D. Low oxygen and high inorganic carbon on the Vancouver Island Shelf. *Journal of Geophysical Research: Oceans (1978–2012)*, 116(C7), 7 2011. ISSN 2156-2202. doi: 10.1029/2010JC006720. URL http://https://doi.org/10.1029/2010JC006720.

Billé, R., Kelly, R., Biastoch, A., Harrould-Kolieb, E., Herr, D., Joos, F., Kroeker, K., Laffoley, D., Oschlies, A., and Gattuso, J.-P. Taking Action Against Ocean Acidification: A Review of Management and Policy Options. *Environmental Management*, 52(4):761–779, 2013. ISSN 0364-152X. doi: 10.1007/s00267-013-0132-7. URL http://dx.doi.org/10.1007/s00267-013-0132-7.

Bograd, S. J., Castro, C. G., Lorenzo, E. D., Palacios, D. M., Bailey, H., Gilly, W., and Chavez, F. P. Oxygen declines and the shoaling of the hypoxic boundary in the California Current. *Geophys. Res. Lett.*, 35:L12607, 2008.

Bograd, S. J., Schroeder, I., Sarkar, N., Qiu, X., Sydeman, W. J., and Schwing, F. B. Phenology of coastal upwelling in the California Current. *Geophysical Research*

Letters, 36(1):L01602, 2009. ISSN 1944-8007. doi: 10.1029/2008GL035933. URL http://dx.doi.org/10.1029/2008GL035933.

Booth, J. A. T., Woodson, C. B., Sutula, M., Micheli, F., Weisberg, S. B., Bograd, S. J., Steele, A., Schoen, J., and Crowder, L. B. Patterns and potential drivers of declining oxygen content along the southern California coast. *Limnology and Oceanography*, 59(4):1127–1138, 2014. ISSN 1939-5590. doi: 10.4319/lo.2014.59.4.1127. URL http://dx.doi.org/10.4319/lo.2014.59.4.1127.

Bopp, L., Resplandy, L., Orr, J. C., Doney, S. C., Dunne, J. P., Gehlen, M., Halloran, P., Heinze, C., Ilyina, T., Séférian, R., Tjiputra, J., and Vichi, M. Multiple stressors of ocean ecosystems in the 21^{st} century: projections with CMIP5 models. *Biogeosciences*, 10(10):6225–6245, 2013. doi: 10.5194/bg-10-6225-2013. URL http://www.biogeosciences.net/10/6225/2013/.

Breitburg, D., Levin, L. A., Oschlies, A., Grégoire, M., Chavez, F. P., Conley, D. J., Garçon, V., Gilbert, D., Gutiérrez, D., Isensee, K., Jacinto, G. S., Limburg, K. E., Montes, I., Naqvi, S. W. A., Pitcher, G. C., Rabalais, N. N., Roman, M. R., Rose, K. A., Seibel, B. A., Telszewski, M., Yasuhara, M., and Zhang, J. Declining oxygen in the global ocean and coastal waters. *Science*, 359(6371), 2018. ISSN 0036-8075. doi: 10.1126/science.aam7240. URL http://science.sciencemag.org/content/359/6371/eaam7240.

Buchwald, V. T. and Adams, J. K. The Propagation of Continental Shelf waves. *Proceedings of the Royal Society of London A: Mathematical, Physical and Engineering Sciences*, 305(1481):235–250, 1968. ISSN 0080-4630. doi: 10.1098/rspa.1968.0115.

Burnett, L. E. The challenges of living in hypoxic and hypercapnic aquatic environments. *American Zoologist*, 37(6):633–640, 1997. doi: 10.1093/icb/37.6.633. URL http://dx.doi.org/10.1093/icb/37.6.633.

Bylhouwer, B., Ianson, D., and Kohfeld, K. Changes in the onset and intensity of

wind-driven upwelling and downwelling along the North American Pacific coast. *Journal of Geophysical Research: Oceans*, 118, 2013. doi: 10.1002/jgrc.20194.

Byrne, J. V. *GEOMORPHOLOGY OF THE OREGON CONTINENTAL TERRACE SOUTH OF COOS BAY*, volume 25. The ORE BIN, 1963.

Canadell, J. G., Le Quéré, C., Raupach, M. R., Field, C. B., Buitenhuis, E. T., Ciais, P., Conway, T. J., Gillett, N. P., Houghton, R. A., and Marland, G. Contributions to accelerating atmospheric CO_2 growth from economic activity, carbon intensity, and efficiency of natural sinks. *Proceedings of the National Academy of Sciences*, 104(47):18866–18870, 2007. ISSN 0027-8424. doi: 10.1073/pnas.0702737104. URL https://www.pnas.org/content/104/47/18866.

Carter, B. R., Feely, R. A., Wanninkhof, R., Kouketsu, S., Sonnerup, R. E., Pardo, P. C., Sabine, C. L., Johnson, G. C., Sloyan, B. M., Murata, A., Mecking, S., Tilbrook, B., Speer, K., Talley, L. D., Millero, F. J., Wijffels, S. E., Macdonald, A. M., Gruber, N., and Bullister, J. L. Pacific anthropogenic carbon between 1991 and 2017. *Global Biogeochemical Cycles*, 33(5):597–617, 2019. doi: 10.1029/2018GB006154. URL https://agupubs.onlinelibrary.wiley.com/doi/abs/10.1029/2018GB006154.

Carton, J. A. and Philander, S. G. H. Coastal Upwelling Viewed as a Stochastic Phenomenon. *J. Phys. Oceanogr.*, 14(9):1499–1509, 1984. ISSN 0022-3670. doi: 10.1175/1520-0485(1984)014⟨1499:CUVAAS⟩2.0.CO;2.

Chan, F., Barth, J. A., Lubchenco, J., Kirincich, A., Weeks, H., Peterson, W. T., and Menge, B. A. Emergence of anoxia in the California current large marine ecosystem. *Science*, 319(920), 2008.

Ciais, P., Sabine, C., Bala, G., Bopp, L., Brovkin, V., Canadell, J., Chhabra, A., DeFries, R., Galloway, J., Heimann, M., Jones, C., Quéré, C. L., Myneni, R., Piao, S., and Thornton, P. *Carbon and Other Biogeochemical Cycles. In: Climate Change*

2013: The Physical Science Basis. Contribution of Working Group I to the Fifth Assessment Report of the Intergovernmental Panel on Climate Change [Stocker, T.F., D. Qin, G.-K. Plattner, M. Tignor, S.K. Allen, J. Boschung, A. Nauels, Y. Xia, V. Bex and P.M. Midgley (eds.)]. Cambridge University Press, Cambridge, United Kingdom and New York, NY, USA, 2013.

Clarke, A. J. Observational and Numerical Evidence for Wind-Forced Coastal Trapped Long Waves. *J. Phys. Oceanogr.*, 7(2):231–247, 1977. ISSN 0022-3670. doi: 10.1175/1520-0485(1977)007⟨0231:OANEFW⟩2.0.CO;2.

Clarke, A. J. On the generation of the seasonal coastal upwelling in the Gulf of Guinea. *Journal of Geophysical Research: Oceans*, 84(C7):3743–3751, 1979. ISSN 2156-2202. doi: 10.1029/JC084iC07p03743. URL http://dx.doi.org/10.1029/JC084iC07p03743.

Claudine Hauri, G.-K. P. S. A. R. A. F. B. H. P. A. W., Nicolas Gruber. Ocean Acidification in the California Current System. *Oceanography*, 22, 2015. URL https://doi.org/10.5670/oceanog.2009.97.

Codiga, D. *Unified Tidal Analysis and Prediction Using the UTide Matlab Functions*. Graduate School of Oceanography, University of Rhode Island, Narragansett, RI. 59pp, 2011.

Connolly, T. P., Hickey, B. M., Geier, S. L., and Cochlan, W. P. Processes influencing seasonal hypoxia in the northern California Current System. *Journal of Geophysical Research: Oceans*, 115(C3), 2010. ISSN 2156-2202. doi: 10.1029/2009JC005283. URL http://dx.doi.org/10.1029/2009JC005283.

Connolly, T. P., Hickey, B. M., Shulman, I., and Thomson, R. E. Coastal Trapped Waves, Alongshore Pressure Gradients, and the California Undercurrent*. *J. Phys. Oceanogr.*, 44(1):319–342, 2014. ISSN 0022-3670. doi: 10.1175/JPO-D-13-095.1. URL http://dx.doi.org/10.1175/JPO-D-13-095.1.

Crawford, W. R. and Thomson, R. E. Continental shelf waves of diurnal period along Vancouver Island. *Journal of Geophysical Research: Oceans*, 87(C12):9516–9522, 1982. ISSN 2156-2202. doi: 10.1029/JC087iC12p09516. URL http://dx.doi.org/10.1029/JC087iC12p09516.

Crawford, W. R. and Peña, M. A. Declining oxygen on the British Columbia Continental Shelf. *Atmosphere-Ocean*, 51(1):88–103, 2013. doi: 10.1080/07055900.2012.753028. URL http://dx.doi.org/10.1080/07055900.2012.753028.

Crawford, W. R. and Thomson, R. E. Physical oceanography of the western Canadian continental shelf. *Continental Shelf Research*, 11(810):669 – 683, 1991. ISSN 0278-4343. doi: http://dx.doi.org/10.1016/0278-4343(91)90073-F. URL http://www.sciencedirect.com/science/article/pii/027843439190073F. Proceedings of the Canadian Continental Shelf Seabed Symposium (C2S3).

Cushman-Roisin, B. and Beckers, J.-M. *Introduction to Geophysical Fluid Dynamics: Physical and Numerical Aspects, 2nd edn.* Elsevier, Amsterdam, 2011.

Denbo, D. W. and Allen, J. S. Large-scale response to atmospheric forcing of shelf currents and coastal sea level off the west coast of North America: May-July 1981 and 1982. *Journal of Geophysical Research: Oceans*, 92(C2):1757–1782, 1987. ISSN 2156-2202. doi: 10.1029/JC092iC02p01757. URL http://dx.doi.org/10.1029/JC092iC02p01757.

DePasquale, E., Baumann, H., and Gobler, C. Vulnerability of early life stage Northwest Atlantic forage fish to ocean acidification and low oxygen. *Mar Ecol Prog Ser*, 523:145 – 156, 2015. doi: https://doi.org/10.3354/meps11142.

Deutsch, C., Emerson, S., and Thompson, L. Fingerprints of climate change in North Pacific oxygen. *Geophysical Research Letters*, 32(16), 2005. doi: 10.1029/2005GL023190. URL https://agupubs.onlinelibrary.wiley.com/doi/abs/10.1029/2005GL023190.

Deutsch, C., Emerson, S., and Thompson, L. Physical-biological interactions in North Pacific oxygen variability. *Journal of Geophysical Research: Oceans*, 111 (C9), 2006. doi: 10.1029/2005JC003179. URL https://agupubs.onlinelibrary.wiley.com/doi/abs/10.1029/2005JC003179.

Di Lorenzo, E., Schneider, N., Cobb, K. M., Franks, P. J. S., Chhak, K., Miller, A. J., McWilliams, J. C., Bograd, S. J., Arango, H., Curchitser, E., Powell, T. M., and Rivire, P. North Pacific Gyre Oscillation links ocean climate and ecosystem change. *Geophysical Research Letters*, 35(8), 2008. ISSN 1944-8007. doi: 10.1029/2007GL032838. URL http://dx.doi.org/10.1029/2007GL032838. L08607.

Doney, S. C., Fabry, V. J., Feely, R. A., and Kleypas, J. A. Ocean Acidification: The Other CO_2 Problem. *Annual Review of Marine Science*, 1(1):169–192, 2009. doi: 10.1146/annurev.marine.010908.163834. URL http://dx.doi.org/10.1146/annurev.marine.010908.163834. PMID: 21141034.

Druon, J., Mannino, A., Signorini, S., McClain, C., Friedrichs, M., Wilkin, J., and Fennel, K. Modeling the dynamics and export of dissolved organic matter in the Northeastern U.S. continental shelf. *Estuarine, Coastal and Shelf Science*, 88(4):488 – 507, 2010. ISSN 0272-7714. doi: https://doi.org/10.1016/j.ecss.2010.05.010. URL http://www.sciencedirect.com/science/article/pii/S0272771410001976.

Edmond, J. M. and Gieskes, J. On the calculation of the degree of saturation of sea water with respect to calcium carbonate under in situ conditions. *Geochimica et Cosmochimica Acta*, 34(12):1261 – 1291, 1970. ISSN 0016-7037. doi: http://dx.doi.org/10.1016/0016-7037(70)90041-4. URL http://www.sciencedirect.com/science/article/pii/0016703770900414.

Ekstrom, J. A., Moser, S. C., and Margaret, T. Barriers to Climate Change Adaptation: A Diagnostic Framework. *California Energy Commission*, (CEC-500-2011-004):669 – 683, 2011.

Emerson, S. R. and Hedges, J. I. *Chemical Oceanography and the Marine Carbon Cycle*. Cambridge University Press, 2008. ISBN ISBN-13 978-0-511-39855-1 eBook (EBL).

Emerson, S., Watanabe, Y. W., Ono, T., and Mecking, S. Temporal Trends in Apparent Oxygen Utilization in the Upper Pycnocline of the North Pacific: 1980–2000. *Journal of Oceanography*, 60(1):139–147, Feb 2004. ISSN 1573-868X. doi: 10.1023/B:JOCE.0000038323.62130.a0. URL https://doi.org/10.1023/B:JOCE.0000038323.62130.a0.

Enfield, D. B. and Allen, J. S. On the Structure and Dynamics of Monthly Mean Sea Level Anomalies along the Pacific Coast of North and South America. *J. Phys. Oceanogr.*, 10(4):557–578, 1980. ISSN 0022-3670. doi: 10.1175/1520-0485(1980)010⟨0557:OTSADO⟩2.0.CO;2.

Engida, Z., Monahan, A., Ianson, D., and Thomson, R. E. Remote forcing of subsurface currents and temperatures near the northern limit of the California Current System. *Journal of Geophysical Research: Oceans*, 121(10):7244–7262, 2016. ISSN 2169-9291. doi: 10.1002/2016JC011880. URL http://dx.doi.org/10.1002/2016JC011880.

Feely, R. A., Sabine, C. L., Lee, K., Berelson, W., Kleypas, J., Fabry, V. J., and Millero, F. J. Impact of Anthropogenic CO_2 on the $CaCO_3$ System in the Oceans. *Science*, 305(5682):362–366, 2004. doi: 10.1126/science.1097329. URL http://www.sciencemag.org/content/305/5682/362.abstract.

Feely, R. A., Sabine, C. L., Hernandez-Ayon, J. M., Ianson, D., and Hales, B. Evidence for Upwelling of Corrosive "Acidified" Water onto the Continental Shelf. *Science*, 320(5882):1490–1492, 2008. doi: 10.1126/science.1155676. URL http://www.sciencemag.org/content/320/5882/1490.abstract.

Feely, R. A., Alin, S. R., Newton, J., Sabine, C. L., Warner, M., Devol, A., Krembs, C., and Maloy, C. The combined effects of ocean acidification, mixing, and

respiration on pH and carbonate saturation in an urbanized estuary. *Estuarine, Coastal and Shelf Science*, 88(4):442 – 449, 2010. ISSN 0272-7714. doi: http://dx.doi.org/10.1016/j.ecss.2010.05.004. URL http://www.sciencedirect.com/science/article/pii/S027277141000185X.

Feely, R. A., Okazaki, R. R., Cai, W.-J., Bednarek, N., Alin, S. R., Byrne, R. H., and Fassbender, A. The combined effects of acidification and hypoxia on pH and aragonite saturation in the coastal waters of the California current ecosystem and the northern Gulf of Mexico. *Continental Shelf Research*, 152:50 – 60, 2018. ISSN 0278-4343. doi: https://doi.org/10.1016/j.csr.2017.11.002. URL http://www.sciencedirect.com/science/article/pii/S0278434317303643.

Feller, W. .-. *An introduction to probability theory and its applications*. New York : Wiley, c1950–1966., 1966.

Foreman, M. G. G., Pal, B., and Merryfield, W. J. Trends in upwelling and downwelling winds along the British Columbia shelf. *Journal of Geophysical Research: Oceans*, 116(C10), 2011. ISSN 2156-2202. doi: 10.1029/2011JC006995. URL http://dx.doi.org/10.1029/2011JC006995. C10023.

Freeland, H., Crawford, W., and Thomson, R. Currents along the Pacific coast of Canada. *Atmosphere-Ocean*, 22(2):151–172, 1984. doi: 10.1080/07055900.1984.9649191. URL http://dx.doi.org/10.1080/07055900.1984.9649191.

Frischknecht, M., Münnich, M., and Gruber, N. Remote versus local influence of ENSO on the California Current System. *Journal of Geophysical Research: Oceans*, 120(2):1353–1374, 2015. ISSN 2169-9291. doi: 10.1002/2014JC010531. URL http://dx.doi.org/10.1002/2014JC010531.

Garcia, H. E. and Gordon, L. I. Oxygen solubility in seawater: Better fitting equations. *Limnology and Oceanography*, 37(6):1307–1312, 1992,1993. doi: 10.4319/lo.1992.37.6.1307. URL https://aslopubs.onlinelibrary.wiley.com/doi/abs/10.4319/lo.1992.37.6.1307.

Ghashghaie, J., Badeck, F.-W., Lanigan, G., Nogués, S., Tcherkez, G., Deléens, E., Cornic, G., and Griffiths, H. Carbon isotope fractionation during dark respiration and photorespiration in c_3 plants. *Phytochemistry Reviews*, 2(1):145–161, Jan 2003. ISSN 1572-980X. doi: 10.1023/B:PHYT.0000004326.00711.ca. URL https://doi.org/10.1023/B:PHYT.0000004326.00711.ca.

Gill, A. E. and Schumann, E. H. The Generation of Long Shelf Waves by the Wind. *J. Phys. Oceanogr.*, 4(1):83–90, 1974. ISSN 0022-3670. doi: 10.1175/1520-0485(1974)004⟨0083:TGOLSW⟩2.0.CO;2.

Gobler, C. J. and Baumann, H. Hypoxia and acidification in ocean ecosystems: coupled dynamics and effects on marine life. *Biology Letters*, 12(5), 2016. ISSN 1744-9561. doi: 10.1098/rsbl.2015.0976. URL http://rsbl.royalsocietypublishing.org/content/12/5/20150976.

Gobler, C. J., DePasquale, E. L., Griffith, A. W., and Baumann, H. Hypoxia and Acidification Have Additive and Synergistic Negative Effects on the Growth, Survival, and Metamorphosis of Early Life Stage Bivalves. *PLOS ONE*, 9(1):1–10, 01 2014. doi: 10.1371/journal.pone.0083648. URL https://doi.org/10.1371/journal.pone.0083648.

Gonella, J. A rotary-component method for analysing meteorological and oceanographic vector time series. *Deep Sea Research and Oceanographic Abstracts*, 19 (12):833 – 846, 1972. ISSN 0011-7471. doi: 10.1016/0011-7471(72)90002-2. URL http://www.sciencedirect.com/science/article/pii/0011747172900022.

Grantham, B., Chan, F., Nielsen, K. J., Fox, D., Barth, J., Huyer, A., and J. Lubchenco, a. B. A. M. Upwelling-driven nearshore hypoxia signals ecosystem and oceanographic changes in the northeast Pacific. *Nature*, 429:749–754, 2004.

Gruber, N. Warming up, turning sour, losing breath: ocean biogeochemistry under global change. *Philosophical Transactions of the Royal Society*, (369):1980–

1996, 2011. doi: doi:10.1098/rsta.2011.0003. URL http://doi.org/10.1098/rsta.2011.0003.

Gruber, N., Hauri, C., Lachkar, Z., Loher, D., Frölicher, T. L., and Plattner, G.-K. Rapid progression of ocean acidification in the California current system. *Science*, 337(6091):220–223, 2012. ISSN 0036-8075. doi: 10.1126/science.1216773. URL https://science.sciencemag.org/content/337/6091/220.

Haigh, R., Ianson, D., Holt, C. A., Neate, H. E., and Edwards, A. M. Effects of Ocean Acidification on Temperate Coastal Marine Ecosystems and Fisheries in the Northeast Pacific. *PLoS One*, 10(2), 2015. ISSN 1932-6203. doi: doi:10.1371/journal.pone.0117533.

Hernández-León, S. and Ikeda, T. A global assessment of mesozooplankton respiration in the ocean. *Journal of Plankton Research*, 27(2):153–158, 2005. doi: 10.1093/plankt/fbh166. URL http://dx.doi.org/10.1093/plankt/fbh166.

Hickey, B. M. The California current system–hypotheses and facts. *Progress in Oceanography*, 8(4):191–279, 1979. ISSN 0079-6611. doi: http://dx.doi.org/10.1016/0079-6611(79)90002-8. URL http://www.sciencedirect.com/science/article/pii/0079661179900028.

Hickey, B. *Coastal Oceanography of Western North America from the tip of Baja California to Vancouver Island*. 345393 in The Sea, Vol. 11, K.H. Brink and A.R. Robinson, eds., Wiley and Sons, Inc., New York, NY, 1998.

Hickey, B. and Banas, N. Why is the northern end of the California Current System so productive? *Oceanography*, 21(4):90–107, 2008. URL http://dx.doi.org/10.5670/oceanog.2008.07.

Ho, D. T., Law, C. S., Smith, M. J., Schlosser, P., Harvey, M., and Hill, P. Measurements of air-sea gas exchange at high wind speeds in the southern ocean: Implications for global parameterizations. *Geophysical Research Letters*, 33(16), 2006.

Hoblit, F. M. *Gust Loads on Aircraft: Concepts and Applications*. AIAA Education Series. American Institute of Aeronautics and Astronautics, 1988. ISBN 978-0-930403-45-4.

Hoegh-Guldberg, O., Mumby, P. J., Hooten, A. J., Steneck, R. S., Greenfield, P., Gomez, E., Harvell, C. D., Sale, P. F., Edwards, A. J., Caldeira, K., Knowlton, N., Eakin, C. M., Iglesias-Prieto, R., Muthiga, N., Bradbury, R. H., Dubi, A., and Hatziolos, M. E. Coral Reefs Under Rapid Climate Change and Ocean Acidification. *Science*, 318(5857):1737–1742, 2007. ISSN 0036-8075. doi: 10.1126/science.1152509. URL https://science.sciencemag.org/content/318/5857/1737.

Hofmann, A. F., Peltzer, E. T., and Brewer, P. G. Kinetic bottlenecks to chemical exchange rates for deep-sea animals - Part 2: Carbon dioxide. *Biogeosciences*, 10: 2409–2425, 2013. doi: 10.5194/bg-10-2409-2013.

Hofmann, M. and Schellnhuber, H.-J. Oceanic acidification affects marine carbon pump and triggers extended marine oxygen holes. *Proceedings of the National Academy of Sciences*, 106(9):3017–3022, 2009. ISSN 0027-8424. doi: 10.1073/pnas.0813384106. URL https://www.pnas.org/content/106/9/3017.

Hönisch, B., Ridgwell, A., Schmidt, D. N., Thomas, E., Gibbs, S. J., Sluijs, A., Zeebe, R., Kump, L., Martindale, R. C., Greene, S. E., Kiessling, W., Ries, J., Zachos, J. C., Royer, D. L., Barker, S., Marchitto, T. M., Moyer, R., Pelejero, C., Ziveri, P., Foster, G. L., and Williams, B. The geological record of ocean acidification. *Science*, 335(6072):1058–1063, 2012. ISSN 0036-8075. doi: 10.1126/science.1208277. URL https://science.sciencemag.org/content/335/6072/1058.

Hoshijima, U., Wong, J., and GE, H. Additive effects of pCO_2 and temperature on respiration rates of the Antarctic pteropod limacina helicina antarctica. *Conservation physiology*, 5(1), 2017. ISSN 5(1): cox064. doi: 10.1093/conphys/cox064.

Hsieh, W. W., Ware, D. M., and Thomson, R. E. Wind-induced upwelling along the west coast of North America, 1899–1988. *Canadian Journal of Fisheries and*

Aquatic Sciences, 52(2):325–334, 1995. doi: 10.1139/f95-033. URL http://dx.doi.org/10.1139/f95-033.

Huffman, G. J., Adler, R. F., Morrissey, M. M., Curtis, S., Joyce, R., McGavock, B., and Susskind, J. Global precipitation at one-degree daily resolution from multi-satellite observations. *J. Hydrometeor.*, 2:36–50, 2001.

Ianson, D. and Allen, S. E. A two-dimensional nitrogen and carbon flux model in a coastal upwelling region. *Global Biogeochemical Cycles*, 16(1):11–1–11–15, 2002. ISSN 1944-9224. doi: 10.1029/2001GB001451. URL http://dx.doi.org/10.1029/2001GB001451.

Ianson, D., Allen, S. E., Harris, S. L., Orians, K. J., Varela, D. E., and Wong, C. S. The inorganic carbon system in the coastal upwelling region west of Vancouver Island, Canada. *Deep Sea Research Part I: Oceanographic Research Papers*, 50(8):1023 – 1042, 2003. ISSN 0967-0637. doi: http://dx.doi.org/10.1016/S0967-0637(03)00114-6. URL http://www.sciencedirect.com/science/article/pii/S0967063703001146.

Ianson, D., Feely, R., Sabine, C., and Juranek, L. Features of coastal upwelling regions that determine net air-sea CO_2 flux. *Journal of Oceanography*, 65(5):677–687, 2009. ISSN 0916-8370. doi: 10.1007/s10872-009-0059-z. URL http://dx.doi.org/10.1007/s10872-009-0059-z.

Keeling, R. F., Kärtzinger, A., and Gruber, N. Ocean deoxygenation in a warming world. *Annu. Rev. Mar. Sci.*, 2:199–229, 2010.

Kleypas, J. A., Buddemeier, R. W., Archer, D., Gattuso, J.-P., Langdon, C., and Opdyke, B. N. Geochemical Consequences of Increased Atmospheric Carbon Dioxide on Coral Reefs. *Science*, 284(5411):118–120, 1999. doi: 10.1126/science.284.5411.118. URL http://www.sciencemag.org/content/284/5411/118.abstract.

Krassovski, M. V. *Investigation of the California Undercurrent off the west coast of Vancouver Island, M.Sc. thesis*. University of Victoria, Victoria, B. C., Canada., 2008.

Kraus, E. B. and Businger, J. A. *Atmosphere-ocean interaction. Second edition*. Oxford University Press, ISBN 0 19 506618 9, 362 pp., 1994.

Lachkar, Z. Effects of upwelling increase on ocean acidification in the California and Canary Current systems. *Geophysical Research Letters*, 41(1):90–95, 2014. doi: 10.1002/2013GL058726. URL https://agupubs.onlinelibrary.wiley.com/doi/abs/10.1002/2013GL058726.

Lara-Espinosa, A. Determination of the acidication state of canadian pacic coastal waters using empirical relationships with hydrographic data. *Univ. of Victoria*, Victoria(Canada):Masters thesis, 2013.

Laws, E. A. Photosynthetic quotients, new production and net community production in the open ocean. *Deep Sea Research Part A. Oceanographic Research Papers*, 38(1):143 – 167, 1991. ISSN 0198-0149. doi: https://doi.org/10.1016/0198-0149(91)90059-O. URL http://www.sciencedirect.com/science/article/pii/019801499190059O.

LeBlond, P. H. and Mysak, L. A. *Waves in the Ocean*. Elsevier Scientific Pub. Co., Amsterdam-Oxford, NY, 1978.

Lentz, S. J. The surface boundary layer in coastal upwelling regions. *J. Phys. Oceanogr.*, 22(12):1517–1539, 1992. ISSN 0022-3670. doi: 10.1175/1520-0485(1992)022⟨1517:TSBLIC⟩2.0.CO;2.

Leth, O. and Middleton, J. F. A numerical study of the upwelling circulation off central Chile: Effects of remote oceanic forcing. *Journal of Geophysical Research: Oceans*, 111(C12), 2006. ISSN 2156-2202. doi: 10.1029/2005JC003070. URL http://dx.doi.org/10.1029/2005JC003070. C12003.

Mackas, D. L., Thomson, R. E., and Galbraith, M. Changes in the zooplankton community of the British Columbia continental margin, 1985–1999, and their covariation with oceanographic conditions. *Canadian Journal of Fisheries and Aquatic Sciences*, 58(4):685–702, 2001. doi: 10.1139/f01-009. URL https://doi.org/10.1139/f01-009.

Mackas, D. L. Seasonal Cycle of Zooplankton off Southwestern British Columbia: 197989. *Canadian Journal of Fisheries and Aquatic Sciences*, 49(5):903–921, 1992. doi: 10.1139/f92-101. URL https://doi.org/10.1139/f92-101.

Manning, M. R. *Seasonal Cycles in Atmospheric CO_2 Concentrations. Heimann, Martin(ed.), The Global Carbon Cycle. pp. 65–94.* Springer Berlin Heidelberg, 1993. ISBN 978-3-642-84608-3.

Mantua, N. J., R., H. S., Zhang, Y., Wallace, J. M., and Francis, R. C. A Pacific Interdecadal Climate Oscillation with Impacts on Salmon Production. *Bull. Amer. Meteor. Soc.*, 78(6):1069–1079, 1997. doi: 10.1175/1520-0477(1997)078⟨1069:APICOW⟩2.0.CO;2. URL http://dx.doi.org/10.1175/1520-0477(1997)078<1069:APICOW>2.0.CO;2.

Marchesiello, P. and Estrade, P. Upwelling Limitation by Onshore Geostrophic Flow. *Journal of Marine Research*, 68:37–62, 2010. ISSN 0022-2402. URL http://www.documentation.ird.fr/hor/fdi:010052909.

Masson, D. Seasonal Water Mass Analysis for the Straits of Juan de Fuca and Georgia. *Atmosphere-Ocean*, 44(1):1–15, 2006. doi: doi:10.3137/ao.440101. URL https://doi.org/10.3137/ao.440101.

Matear, R. J. and Hirst, A. C. Long-term changes in dissolved oxygen concentrations in the ocean caused by protracted global warming. *Global Biogeochemical Cycles*, 17 (4), 2003. doi: 10.1029/2002GB001997. URL https://agupubs.onlinelibrary.wiley.com/doi/abs/10.1029/2002GB001997.

McCormick, L. R. and Levin, L. A. Physiological and ecological implications of ocean deoxygenation for vision in marine organisms. *Philosophical Transactions of the Royal Society A: Mathematical, Physical and Engineering Sciences*, 375(2102):20160322, 2017. doi: 10.1098/rsta.2016.0322. URL https://royalsocietypublishing.org/doi/abs/10.1098/rsta.2016.0322.

Mesinger, F., DiMego, G., Kalnay, E., Mitchell, K., Shafran, P. C., Ebisuzaki, W., Jovic, D., Woolen, J., Rogers, E., Berbery, E. H., Ek, M. B., Fan, Y., GruhPaine, R., Higgins, W., Li, H., Lin, Y., Manikin, G., Parrish, D., and Shi, W. North American regional reanalysis. *Bull. Amer. Meteor. Soc.*, 87:343–360, 2006.

Monahan, A. H. and Denman, K. L. Impacts of atmospheric variability on a coupled upper-ocean/ecosystem model of the subarctic Northeast Pacific. *Global Biogeochem. Cycles*, 18(GB2010), 2004.

Moore, D., Hisard, P., McCreary, J., Merle, J., O'Brien, J., Picaut, J., Verstraete, J.-M., and Wunsch, C. Equatorial adjustment in the eastern Atlantic. *Geophysical Research Letters*, 5(8):637–640, 1978. doi: 10.1029/GL005i008p00637. URL https://agupubs.onlinelibrary.wiley.com/doi/abs/10.1029/GL005i008p00637.

Moore, G. W. K., Pickart, R. S., and Renfrew, I. A. Buoy observations from the windiest location in the world ocean, Cape Farewell, Greenland. *Geophys. Res. Lett.*, 35:L18802, 2008. doi: 10.1029/2008GL034845.

Oliver, E. C. J. and Thompson, K. R. Madden-Julian Oscillation and sea level: Local and remote forcing. *Journal of Geophysical Research: Oceans*, 115(C1), 2010. ISSN 2156-2202. doi: 10.1029/2009JC005337. URL http://dx.doi.org/10.1029/2009JC005337.

Orr, J. C., Fabry, V. J., Aumont, O., Bopp, L., Doney, S. C., Feely, R. A., Gnanadesikan, A., Gruber, N., Ishida, A., Joos, F., Key, R. M., Lindsay, K., Matear, R., Monfray, P., Mouchet, A., Najjar, R. G., Plattner, G.-K., Rodgers, K. B.,

Sabine, C. L., Sarmiento, J. L., Schlitzer, R., Slater, R. D., Totterdell, I. J., Weirig, M.-F., Yamanaka, Y., and Yool, A. Anthropogenic ocean acidification over the twenty-first century and its impact on calcifying organisms. *Nature*, 437(7059):681–686, 2005. ISSN 0028-0836. doi: 10.1038/nature04095. URL http://dx.doi.org/10.1038/nature04095.

Pawlowicz, R. and Farmer, D. M. Diagnosing vertical mixing in a two-layer exchange flow. *Journal of Geophysical Research: Oceans*, 103(C13):30695–30711, 1998. doi: 10.1029/1998JC900024. URL https://agupubs.onlinelibrary.wiley.com/doi/abs/10.1029/1998JC900024.

Pörtner, H.-O. Ecosystem effects of ocean acidification in times of ocean warming: a physiologist's view. *Mar. Ecol. Prog. Ser.*, 373:203–217, 2009. doi: 10.3354/meps07768.

Pörtner, H. O. and Farrell, A. P. Physiology and Climate Change. *Science*, 322 (5902):690–692, 2008. ISSN 0036-8075. doi: 10.1126/science.1163156. URL http://science.sciencemag.org/content/322/5902/690.

Pörtner, H. O., Langenbuch, M., and Michaelidis, B. Synergistic effects of temperature extremes, hypoxia, and increases in CO_2 on marine animals: From Earth history to global change. *Journal of Geophysical Research: Oceans*, 110 (C9), 2005. doi: 10.1029/2004JC002561. URL https://agupubs.onlinelibrary.wiley.com/doi/abs/10.1029/2004JC002561.

Price, J. F., Weller, R. A., and Pinkel, R. Diurnal cycling: Observations and models of the upper ocean response to diurnal heating, cooling, and wind mixing. *Journal of Geophysical Research: Oceans*, 91(C7):8411–8427, 1986. ISSN 2156-2202. doi: 10.1029/JC091iC07p08411. URL http://dx.doi.org/10.1029/JC091iC07p08411.

Pringle, J. M. and Riser, K. Remotely forced nearshore upwelling in Southern California. *Journal of Geophysical Research: Oceans*, 108(C4), 2003. ISSN 2156-2202.

doi: 10.1029/2002JC001447. URL http://dx.doi.org/10.1029/2002JC001447. 3131.

Raven, J., Caldeira, K., Elderfield, H., O., H.-G., Liss, P., Riebesell, U., Shepherd, J., Turley, C., and Watson, A. Ocean acidification due to increasing carbon dioxide. *The Royal Society*, 12/05:ISBN 0 85403 6192, 2005.

Rice, S. O. "Mathematical Analysis of Random Noise: Part III Statistical Properties of Random Noise Currents". *Bell System Technical Journal*, 24(1):46 – 156, 1945.

Sabine, C. L., Feely, R. A., Gruber, N., Key, R. M., Lee, K., Bullister, J. L., Wanninkhof, R., Wong, C. S., Wallace, D. W. R., Tilbrook, B., Millero, F. J., Peng, T.-H., Kozyr, A., Ono, T., and Rios, A. F. The oceanic sink for anthropogenic CO_2. *Science*, 305(5682):367–371, 2004. ISSN 0036-8075. doi: 10.1126/science.1097403. URL http://science.sciencemag.org/content/305/5682/367.

Sarmiento, J. L., Hughes, T. M. C., Stouffer, R. J., Stouffer, R. J., and Manabe, S. Simulated response of the ocean carbon cycle to anthropogenic climate warming. *Nature*, 393(8):245–, 1998. URL https://doi.org/10.1038/30455.

Sarmiento, L., Jorge and Gruber, N. *Ocean Biogeochemical Dynamics*. Princeton University Press, ISBN: 0-691-01707-7, 526 pp., 2006.

Schwing, F. B., Bond, N. A., Bograd, S. J., Mitchell, T., Alexander, M. A., and Mantua, N. Delayed coastal upwelling along the u.s. west coast in 2005: A historical perspective. *Geophysical Research Letters*, 33(22), 2006. doi: 10.1029/2006GL026911. URL https://agupubs.onlinelibrary.wiley.com/doi/abs/10.1029/2006GL026911.

Siedlecki, S. A., Banas, N. S., Davis, K. A., Giddings, S., Hickey, B. M., MacCready, P., Connolly, T., and Geier, S. Seasonal and interannual oxygen variability on the Washington and Oregon continental shelves. *Journal of Geophysical Research:*

Oceans, 120(2):608–633, 2015. ISSN 2169-9291. doi: 10.1002/2014JC010254. URL http://dx.doi.org/10.1002/2014JC010254.

Smith, R. L. The physical processes of coastal ocean upwelling systems. In Summerhayes, C. P., Emeis, K.-C., Angel, M. V., Smith, R. L., and Zeitzschel, B., editors, *Upwelling in the ocean: Modern processes and ancient records*, pages 39 – 64. Wiley and Sons Ltd., 1994.

Solomon, S., Plattner, G.-K., Knutti, R., and Friedlingstein, P. Irreversible climate change due to carbon dioxide emissions. *Proceedings of the National Academy of Sciences*, 106(6):1704–1709, 2009. ISSN 0027-8424. doi: 10.1073/pnas.0812721106. URL http://www.pnas.org/content/106/6/1704.

Tcherkez, G., Nogués, S., Bleton, J., Cornic, G., Badeck, F., and Ghashghaie, J. Metabolic Origin of Carbon Isotope Composition of Leaf Dark-Respired CO_2 in French Bean. *Plant Physiology*, 131(1):237–244, 2003. ISSN 0032-0889. doi: 10.1104/pp.013078. URL http://www.plantphysiol.org/content/131/1/237.

Teeter, L., Hamme, R. C., Ianson, D., and Bianucci, L. Accurate estimation of net community production from o2/ar measurements. *Global Biogeochemical Cycles*, 32(8):1163–1181, 2018. doi: 10.1029/2017GB005874. URL https://agupubs.onlinelibrary.wiley.com/doi/abs/10.1029/2017GB005874.

Thompson, R. O. R. Y. Climatological Numerical Models of the Surface Mixed Layer of the Ocean. *Journal of Physical Oceanography*, 6(4):496–503, 1976. doi: 10.1175/1520-0485(1976)006⟨0496:CNMOTS⟩2.0.CO;2. URL https://doi.org/10.1175/1520-0485(1976)006<0496:CNMOTS>2.0.CO;2.

Thompson, R. O. R. Y. Coherence Significance Levels. *J. Atmos. Sci.*, 36(10):2020–2021, 1979. ISSN 0022-4928. doi: 10.1175/1520-0469(1979)036⟨2020:CSL⟩2.0.CO;2. URL http://www.po.gso.uri.edu/~codiga/utide/utide.htm.

Thomson, D. Spectrum estimation and harmonic analysis. *Proceedings of the IEEE*, 70(9):1055–1096, Sept 1982. ISSN 0018-9219. doi: 10.1109/PROC.1982.12433.

Thomson, R. E. and Fine, I. V. Estimating mixed-layer depth from oceanic profile data. *J. Atmos. Ocean. Tech.*, 20:319–329, 2003.

Thomson, R. and Emery, W. *Data Analysis Methods in Physical Oceanography (3rd Edition)*. Elsevier Science, Amsterdam, 2014.

Thomson, R. E. and Krassovski, M. V. Poleward reach of the California Undercurrent extension. *Journal of Geophysical Research*, 115:C09027, 2010. doi: 10.1029/2010JC006280.

Thomson, R. E. and Krassovski, M. V. Remote alongshore winds drive variability of the California Undercurrent off the British Columbia-Washington coast. *Journal of Geophysical Research: Oceans*, 2015. ISSN 2169-9291. doi: 10.1002/2015JC011306. URL http://dx.doi.org/10.1002/2015JC011306.

Thomson, R. E. and Ware, D. M. A current velocity index of ocean variability. *Journal of Geophysical Research: Oceans*, 101(C6):14297–14310, 1996. ISSN 2156-2202. doi: 10.1029/96JC01055. URL http://dx.doi.org/10.1029/96JC01055.

Thomson, R. E., Heesemann, M., Davis, E. E., and Hourston, R. A. S. Continental microseismic intensity delineates oceanic upwelling timing along the west coast of North America. *Geophysical Research Letters*, 41(19):6872–6880, 2014. ISSN 1944-8007. doi: 10.1002/2014GL061241. URL http://dx.doi.org/10.1002/2014GL061241. 2014GL061241.

Turi, L. Z. G. N., G. Spatiotemporal variability and drivers of pCO_2 and airsea CO_2 fluxes in the California current system: an eddy-resolving modeling study. *Biogeosciences*, 11(3):671–690, 2014. doi: 10.5194/bg-11-671-2014. URL https://www.biogeosciences.net/11/671/2014/.

Vargas, C. A., de la Hoz, M., Aguilera, V., Martn, V. S., Manrquez, P. H., Navarro, J. M., Torres, R., Lardies, M. A., and Lagos, N. A. CO_2-driven ocean acidification reduces larval feeding efficiency and changes food selectivity in the mollusk Concholepas concholepas. *Journal of Plankton Research*, 35(5):1059–1068, 2013. doi: 10.1093/plankt/fbt045. URL http://plankt.oxfordjournals.org/content/35/5/1059.abstract.

Volk, T. and Hoffert, M. *Ocean carbon pumps: analysis of relative strengths and efficiencies in ocean-driven atmospheric CO_2 changes.*, pages 99–110. American Geophysical Union; Geophysical Monograph 32, 1985.

Waldbusser, G. G. and Salisbury, J. E. Ocean Acidification in the Coastal Zone from an Organism's Perspective: Multiple System Parameters, Frequency Domains, and Habitats. *Annual Review of Marine Science*, 6(1):221–247, 2014. doi: 10.1146/annurev-marine-121211-172238. URL http://dx.doi.org/10.1146/annurev-marine-121211-172238. PMID: 23987912.

Wang, D., Gouhier, T. C., Menge, B. A., and Ganguly, A. R. Intensification and spatial homogenization of coastal upwelling under climate change. *Nature*, 518 (7539):390–394, 2015. ISSN 0028-0836. doi: 10.1038/nature14235. URL http://dx.doi.org/10.1038/nature14235.

Wang, D.-P. and Mooers, C. N. K. Coastal-Trapped Waves in a Continuously Stratified Ocean. *Journal of Physical Oceanography*, 6(6):853–863, 1976. doi: 10.1175/1520-0485(1976)006⟨0853:CTWIAC⟩2.0.CO;2. URL http://dx.doi.org/10.1175/1520-0485(1976)006<0853:CTWIAC>2.0.CO;2.

Wang, D.-P. and Mooers, C. N. K. Long Coastal-Trapped Waves off the West Coast of the United States, Summer 1973. *J. Phys. Oceanogr.*, 7(6):856–864, 1977. ISSN 0022-3670.

Wanninkhof, R. Relationship between wind speed and gas exchange over the ocean. *Journal of Geophysical Research*, 97, 1992. doi: doi:10.1029/92JC00188.

Ward, J. K. and Kelly, J. K. Scaling up evolutionary responses to elevated CO_2: lessons from arabidopsis. *Ecology Letters*, 7(5):427–440, 2004. doi: 10.1111/j.1461-0248.2004.00589.x. URL https://onlinelibrary.wiley.com/doi/abs/10.1111/j.1461-0248.2004.00589.x.

Ware, D. M. and Thomson, R. E. Bottom-up ecosystem trophic dynamics determine fish production in the Northeast Pacific. *Science*, 308:1280–1284, doi: 10.1126/science.1109049, 2005.

Ware, D. M. and Thomson, R. E. Link Between Long-Term Variability in Upwelling and Fish Production in the Northeast Pacific Ocean. *Canadian Journal of Fisheries and Aquatic Sciences*, 48(12):2296–2306, 1991. doi: 10.1139/f91-270. URL http://dx.doi.org/10.1139/f91-270.

Weiss, R. F. Carbon dioxide in water and seawater: the solubility of a non-ideal gas. *Marine Chemistry*, 2(3):203 – 215, 1974. ISSN 0304-4203. doi: https://doi.org/10.1016/0304-4203(74)90015-2. URL http://www.sciencedirect.com/science/article/pii/0304420374900152.

Whitney, F. and Tortell, P. Fifty years of ocean observations in the Pacific Northeast. *Eos, Transactions American Geophysical Union*, 87(49):551–555, 2006. doi: 10.1029/2006EO490005. URL https://agupubs.onlinelibrary.wiley.com/doi/abs/10.1029/2006EO490005.

Williams, R. G. and Follows, M. J. *Ocean Dynamics and the Carbon Cycle*. Number 404. Cambridge University Press, 2011. ISBN 978-0-521-84369-0 Hardback.

Yao, T., Freeland, H. J., and Mysak, L. A. A Comparison of Low-Frequency Current Observations off British Columbia with Coastal-Trapped Wave Theory. *J. Phys. Oceanogr.*, 14(1):22–34, 1984. ISSN 0022-3670. doi: 10.1175/1520-0485(1984)014⟨0022:ACOLFC⟩2.0.CO;2.

Yelland, M. and Taylor, P. K. Wind Stress Measurements from the Open Ocean. *J. Phys. Oceanogr.*, 26(4):541–555, 1996. ISSN 0022-3670. doi: 10.1175/1520-0485(1996)026⟨0541:WSMFTO⟩2.0.CO;2.

Zeebe, R. and Wolf-Gladrow, D. *CO_2 IN SEAWATER: EQUILIBRIUM, KINETICS, ISOTOPES*, volume 65 of *Oceanography Series*. Elselvier, 2001. ISBN 0444509461.